X-ray and neutron topography observations of domains aim dislocations

Graham Fraser Clark

X-RAY AND NEUTRON TOPOGRAPHY OBSERVATIONS OF DOMAINS AND DISLOCATIONS

by

Graham Fraser Clark. B.Sc., M.Sc.

A thesis submitted to the University of Durham in candidature for the Degree of Doctor of Philosophy

September 1980

Abstract

A brief introduction to the theory of magnetism and magnetic domains is given which is followed by a review of X-ray topography techniques and an outline of the theory and contrast mechanisms necessary for the interpretation of the topographs.

Results are presented on the perfection of flux grown rare-earth germanate crystals which clearly indicate the usefulness, to the crystal grower, of synchrotron X-ray topography for rapid routine assessment of a large number of crystals.

The techniques of neutron topography are described and some of the more important results obtained are reviewed. Results obtained with neutron topography on the possible correlation between surface vicinal features and dislocations in holmium galium garnet are presented. These results, although not conclusive, provide further evidence of a probable correlation.

Previous work reported on the antiferromagnetic $KCoF_3$ is described with particular reference to the limited number of domain observations. Previous work on the motion of antiferromagnetic domain walls under an applied magnetic field has been extended by considering the case of the motion of these walls under an applied stress using both synchrotron X-ray topography and rocking curve measurements. The critical stress achieved was in reasonable agreement with that predicted from the magnetic field data. These results also confirm that data obtained in torque magnetometry and linear dichroism experiments may be explained by the motion of antiferromagnetic domain walls under stress.

Work on the magnetic properties of terbium is reviewed, particularly work relating to measurements of magnetostriction. An X-ray technique for measuring the magnetostriction of high magnetostriction materials without resorting to absolute lattice parameters is described and the results obtained on using this technique to measure the magnetostriction of terbium are presented. These results are fitted to a two-ion interaction model.

Work on the highly magnetostrictive $Tb_{.27}Dy_{.73}Fe_2$ is described and results are presented on the observation of magnetic domains in this material in an applied magnetic field. Calculations of the domain wall energies and widths are presented which enabled the domain structure to be interpreted.

Acknowledgements

It is a pleasure for me to make the following acknowledgements.

I would like to thank Professors A.W. Wolfendale and B.H. Bransden for permitting me to use the facilities of the Physics Department of Durham University for researching this work. I would also like to thank the Science Research Council for a studentship for the greater part of the work and Durham University for the financial assistance which made it possible for it to be completed.

My thanks also go to Dr W.D.Corner, Head of the Solid State Physics Group, for many useful discussions. In particular, it is a pleasure for me to express my gratitude to Dr B.K.Tanner for his unstinting enthusiasm, encouragement and guidance on all aspects of this work and without whom it would never have been completed.

I would like to thank the Director and staff of the S.R.C. Daresbury Laboratory for the provision of synchrotron radiation facilities and for making it possible for me to use the synchrotron radiation facilities at the DESY Laboratory, West Germany. To the Director and staff of this laboratory I also extend my gratitude.

My thanks also to the Director and staff of the Institute Laue Langevin for the provision of the neutron beam facility and to the S.R.C.Rutherford Laboratory who made my visit possible. In particular I would like to thank Drs M. Schlenker and J.Baruchel who allowed me to use their neutron topography camera and provided me with considerable assistance and many useful discussions on

this and other work.

I would like to thank Mrs B.M.Wanklyn, who provided me with crystals of garnets, germanates and $KCoF_3$, Dr H.T.Savage who provided the $Tb_{.27}Dy_{.73}Fe_2$ crystal and Dr D.Jones and his colleagues who provided the terbium crystal.

I would like to acknowledge the technical assistance of Mr K.Moulson the group technician, Mr J.Scott the glassblower, Mr W.Leslie, Mr D.Jobling, Mr T.Jackson and their staffs in the Department's workshops, also Mr M.Lee and his staff for some of the photographs and diagrams.

My thanks also go to past and present members of the Solid State Group for assistance and helpful discussions, including Mr R.D.Hawkins for his assistance in proof reading and Dr A.Joraide , who used the computer program of Dr J.Welford, to fit the magnetostriction data on terbium to a two-ion interaction model. Finally I would like to thank my mother Mrs A.E.Clark for typing this thesis.

List of Publications

X-ray Topographic Studies Using Synchrotron Radiation.

Tanner B.K., Safa M., Midgely D., MacCormack I.B. and Clark G.F.

Fourth European Crystalographic Meeting (1977) 110

A Simple Automatic Cassette for X-ray Synchrotron Topography

Buckley-Golder I.M., Tanner B.K. and Clark G.F.

J. Appl. Cryst. (1977) 10 509

Domain Configurations in Single Crystal Tb Fe_2 and $Tb_{.27}Dy_{.73}Fe_2$

Ser y R.S., Savage H.T., Tanner B.K. and Clark G.F.

J. Appl. Phys. (1978) 49 2010

Stress Induced Displacement of Antiferromagnetic Domain Walls in $KCoF_3$

Clark G.F. and Tanner B.K.

Europhysics Conference Abstracts (1978) 2G 111

The Magnetization Process in Rare-earth Iron Laves Phase Compounds

Clark G.F., Tanner B.K., Ser y R.S. and Savage H.T.

J. de Phys. Suppl. (1979) C5 183

X-ray Topographic Assessment of Flux Grown Crystals of Rare-earth Germanates $R_2Ge_2O_7$

Clark G.F., Tanner B.K. and Wanklyn B.M.

J. Mater. Sci. (1980) 15 1328

Antiferromagnetic Domain Wall Motion Under External Stress.

Clark G.F., Tanner B.K.

Phys. Stat. Sol. (a) (1980) 59 241

CONTENTS

CHAPTER ONE

MAGNETIC ORDER

1.1 Introduction

1.2 Diamagnetism

1.3 Paramagnetism

1.4 Ferromagnetism

1.5 Ferrimagnetism

1.6 Antiferromagnetism

1.7 Magnetic Domains

CHAPTER ONE

MAGNETIC ORDER

1.1 Introduction

The existence of magnetic phenomenon has been known for many years, the earliest reference is to lodestone in Greek writings about 800 BC, and has long been the subject of experimental observation. No detailed understanding of magnetism was possible before the introduction of quantum mechanical ideas in the early part of this century. Magnetism is probably the most common manifestation of the quantum mechanical nature of matter and is inseparable from it, for it is impossible for a classical system in thermal equilibrium to exhibit a magnetic moment.

There are three sources of the magnetic moment of a free atom. These are the spin angular momentum of an electron, the orbital angular momentum of an electron about a nucleus and changes in the orbital moment induced by an applied magnetic field. The first two effects give a paramagnetic contribution to the magnetization and the latter a diamagnetic contribution. The quantised nature of the motion of electrons gives rise to a fundamental unit of magnetic dipole moment, the Bohr magneton μ_B . Several different types of magnetism exist and these will be briefly discussed here. A fuller introdu ction may be found in standard texts on magnetism e.g. Chikazumi (1964), Morrish (1965), Kittel (1971), Bleaney and Bleaney (1976) and Crangle (1977).

1.2 Diamagnetism

Diamagnetic substances have a negative magnetic susceptibility. All materials have a diamagnetic term which is usually weak and often masked by a larger paramagnetic term. For solids the diamagnetic volume susceptibility is typically -10^{-6} cgs units per mole. The diamagnetic susceptibility arises from the effect of a magnetic field on the motion of the inner electrons of an atom. The magnetic field causes a change in flux through the electron orbits which induces an e.m.f. This e.m.f. causes a change in the electron orbits which induces a magnetic moment in the atom which, from Lenz's law, opposes the change in flux through the atom. Hence the induced magnetization and the susceptibility are negative. Type one superconductors are perfectly diamagnetic, the induced e.m.f. remaining for as long as the field is applied.

The induced magnetic moment and the susceptibility were first calculated classically by Langevin, the theory being outlined by Kittel (1971). The results agree with the quantum mechanical derivation of Van Vleck (1932). The induced magnetic moment, is given by

$$\mu_{dia} = -\frac{Z e^2 B}{4 m c^2}\langle \rho^2 \rangle \qquad (1.1)$$

where Z is the atomic number

e is the electronic charge

m is the electronic mass

B is the magnetic flux density

$\langle \rho^2 \rangle$ is the mean square of the perpendicular distance of the electron from the field axis through the nucleus. For a spherically symmetrical charge distribution we have

$$\langle r^2 \rangle = \frac{3}{2} \langle \rho^2 \rangle$$

where $\langle r^2 \rangle$ is the mean square distance of the electrons from the nucleus.

If N is the number of atoms per unit volume the diamagnetic susceptibility per unit volume is

$$\chi_{dia} = \frac{N\mu_{dia}}{B} = -\frac{NZe^2}{6mc^2}\langle r^2 \rangle \qquad (1.2)$$

Apart from very small changes in $\langle r^2 \rangle$ with temperature this expression is temperature independent and clearly indicates that all materials exhibit a diamagnetic susceptibility which is always negative.

1.3 Paramagnetism

Paramagnetism occurs in materials where the atoms or molecules have a permanent magnetic moment. Paramagnetic materials have a small positive susceptibility independent of any external field but with a simple temperature dependence.

In a magnetic field an atom with angular momentum quantum number J has a magnetization given by

$$M = Ng J \mu_B B_J(x) \qquad (1.3)$$

where

$$x = \frac{gJ\mu_B}{k_B T} \qquad (1.4)$$

where g is the Landé splitting factor

$$\mu_B = \frac{e\hbar}{2mc} \qquad (1.5)$$

and B_J is the Brillouin function

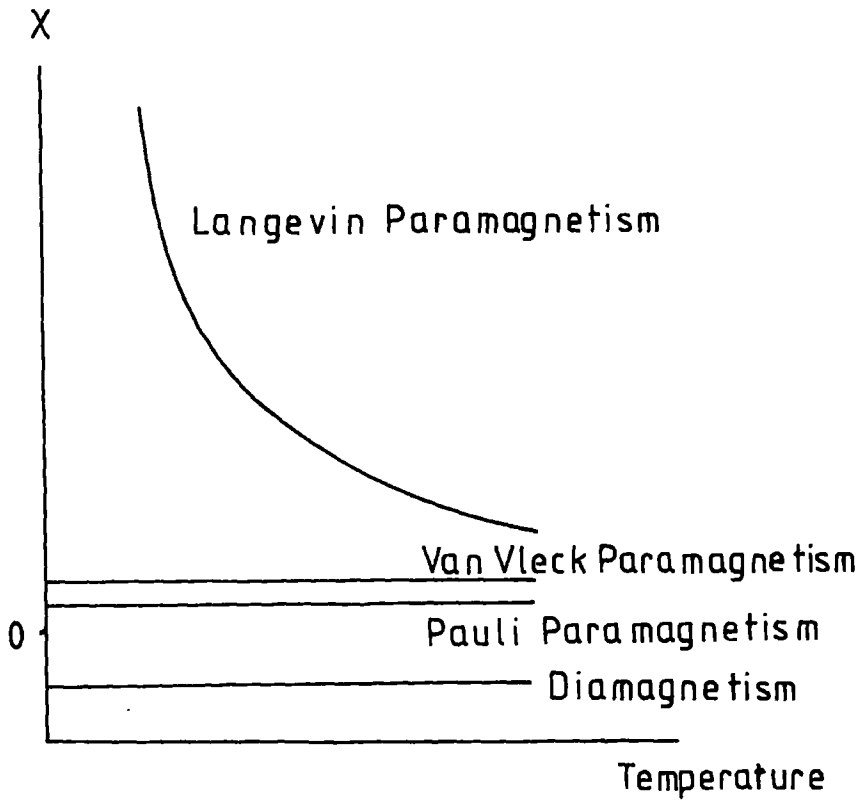

Fig. 1.1 Characteristic Magnetic Susceptibilities

$$B_j(x) = \frac{2J+1}{2J}\,\mathrm{ctnh}\left[\frac{(2J+1)x}{2J}\right] - \frac{1}{2J}\,\mathrm{ctnh}\left[\frac{x}{2J}\right] \quad (1.6)$$

where

$$\mathrm{ctnh}\, x = \frac{1}{x} + \frac{x}{3} - \frac{x^3}{45} \cdots\cdots \quad (1.7)$$

The susceptibility then becomes

$$\chi = \frac{NJ(J+1)g^2\mu_B^2}{3k_BT} = \frac{C}{T} \quad (1.8)$$

the Curie law; where the effective number of Bohr magnetons is given by

$$p = g[J(J+1)]^{1/2} \quad (1.9)$$

and k_B is Boltzman's constant.

Magnetization results from the orientation of the magnetic moments in an applied magnetic field, but thermal disorder resists the tendency of the field to order the moments. The Curie law applies only in the limit $\mu_B B \ll k_B T$. The magnetic susceptibilities of paramagnetic and diamagnetic materials versus temperature are shown in fig 1.1.

Nuclear paramagnetism arises from nuclear magnetic moments which are of the order of 10^{-3} times smaller than electron magnetic moments.

Not all paramagnetic materials obey the Curie law, for these the susceptibilities follow the Curie-Weiss law

$$\chi = \frac{C'}{T-\theta} \quad (1.10)$$

where θ and C' are constants.

The paramagnetic contribution to the susceptibility is of the order of 10^{-2} to 10^{-4} cgs units per mole considerably larger than

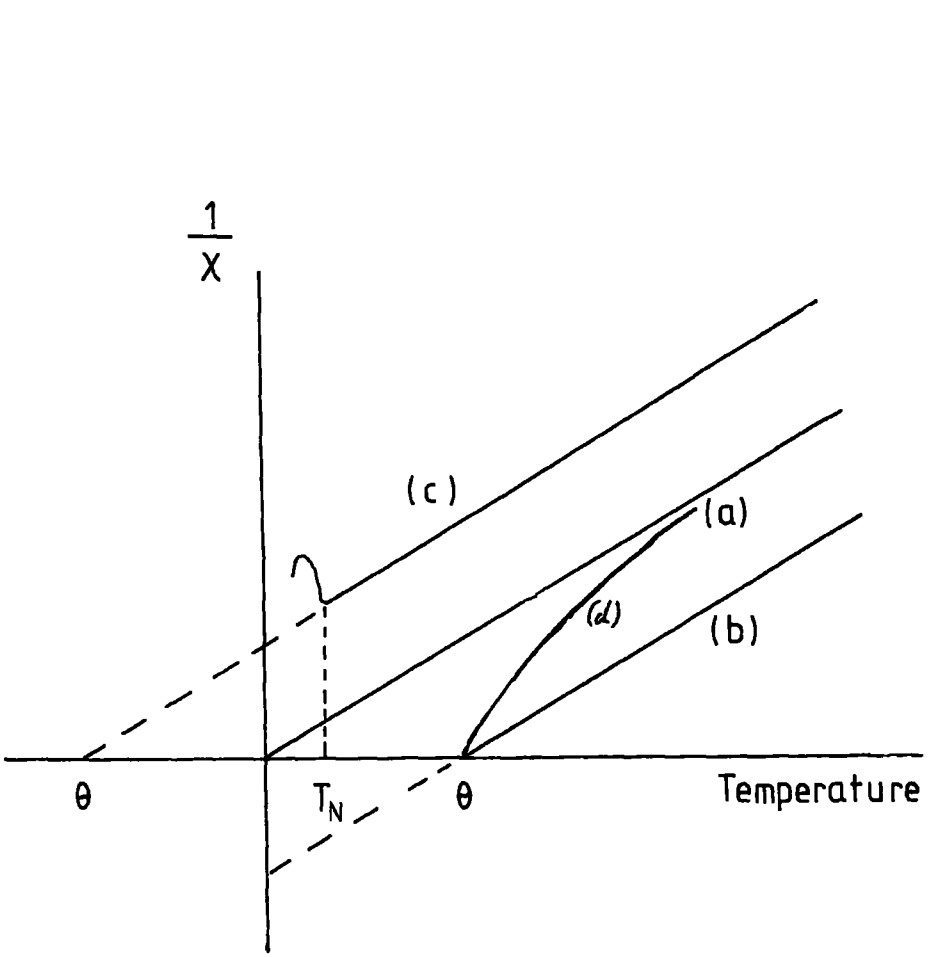

Fig. 1.2 Reciprocal Susceptibilities

(a) Curie Paramagnet

(b) Curie-Weiss Ferromagnet

(c) Curie-Weiss Antiferromagnet

(d) Curie-Weiss Ferrimagnet

the diamagnetic susceptibility. A positive value of θ gives rise to ferromagnetism or ferrimagnetism, while a negative value corresponds to antiferromagnetism. (see fig 1.2)

Van Vleck paramagnetism arises from a positive term in the quantum mechanical derivation of the diamagnetic susceptibility for atoms which have zero magnetic moment in the ground state, but exhibit a magnetic moment in an excited state. When the energy gap between states is greater than $k_B T$ only a small proportion of the atoms can be in the excited state, hence the term is small.

Pauli paramagnetism is found in metals when conduction electrons 'flip' their spin to align with an applied field. This effect is again small since only electrons within about $k_B T$ of the Fermi energy may make the transition.

1.4 Ferromagnetism

Below their Curie temperatures ferromagnets possess a spontaneous magnetization. The susceptibility of ferromagnets is field and temperature dependent. In general these materials are saturated by low fields. Above their Curie temperatures they behave as paramagnets, but their Curie temperatures may be raised by the application of a magnetic field. Ferromagnetic ordering is shown in fig 1.3.

These characteristics can be explained by assuming that below their Curie temperatures they possess a spontaneous Weiss molecular field proportional to the magnetization which is temperature dependent. This field is found experimentally to be of the order of 10^3 Tesla. This is four orders of magnitude

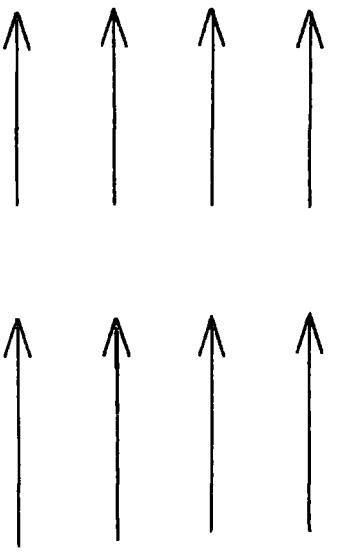

Fig. 1.3 Ferromagnetic Order

larger than that obtainable from a dipole - dipole interaction between individual magnetic moments, Heisenberg (1928) suggested that this field arose from a quantum mechanical exchange interaction. The exchange potential between two atoms with spins S_i and S_j is

$$W_{ij} = - 2\mathcal{J}\underline{S}_i.\underline{S}_j \qquad (1.11)$$

where $\mathcal{J}$ is the exchange integral. If the exchange integral is positive the lowest energy configuration occurs when the two spins are parallel.

1.5 Ferrimagnetism

Ferrimagnetic materials show ferromagnetic behaviour, but the saturation magnetization at T = OK does not correspond to parallel alignment of the constituent ions. Ferrimagnetic materials have two or more lattice sites on which the magnetic ions exist. The magnetic moments on equivalent sites order parallel to each other and anti-parallel to the moments on non-equivalent sites. The exchange integral is positive for the interaction between ions on equivalent sites and negative for the interaction between ions on non-equivalent sites. If the magnitude of the magnetic moments on different sites, or the number of the different sites are unequal, then ferrimagnetic behaviour is exhibited. The susceptibility of ferrimagnets is shown in fig 1.2. The curvature is explained by the interaction between the different sites. Ferrimagnetic ordering is shown schematically in fig 1.4.

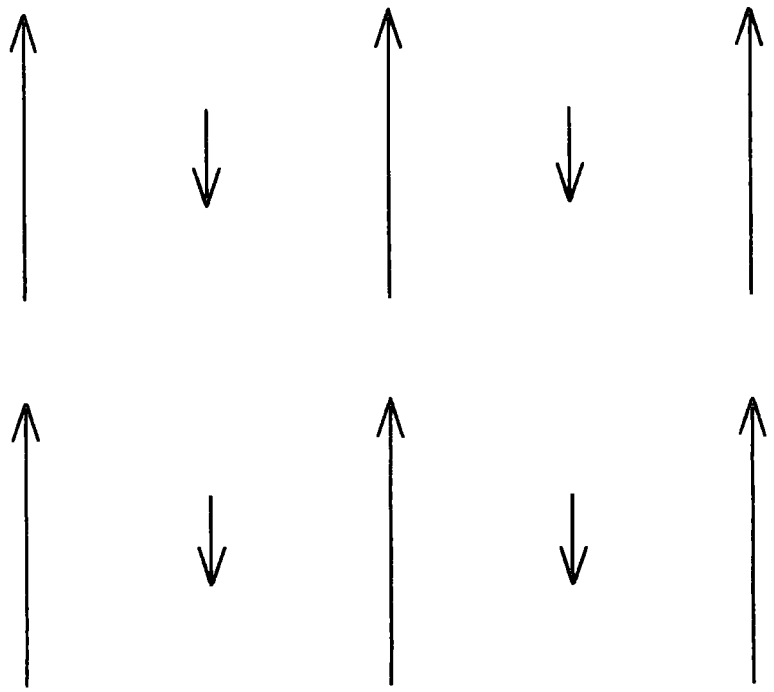

Fig. 1.4 Ferrimagnetic Order

The best known example of a ferrimagnet is magnetite Fe_3O_4 which is composed of two types of iron ions Fe^{2+} and Fe^{3+}. Neutron diffraction studies show that the Fe^{3+} ions are split into two groups which are aligned antiparallel. The Fe^{2+} ions are aligned parallel to one site giving a net magnetic moment of $4.1\,\mu_B$ compared with a possible maximum of $14\,\mu_B$.

One of the technologically important types of magnetic materials are garnets which are currently being exploited as magnetic bubble memory devices. These are ferrimagnetic materials.

1.6 Antiferromagnetism

The concept of antiferromagnetism was first proposed by Néel (1932). If the exchange integral of equation 1.11 is negative for the interaction between the equivalent magnetic sites then the minmum energy corresponds to antiparallel alignment of the moments. If the moments are equal there is no magnetic moment and the material is antiferromagnetic. This is a special case of ferrimagnetism where the two sublattice magnetizations are equal in magnitude.

Antiferromagnets were originally envisaged as being composed of two sublattices which, below their Néel temperature, are magnetized in opposite directions.

Antiferromagnetic ordering is shown in fig 1.5. If the directions of the magnetization within the two sublattices are not exactly antiparallel but are equal in magnitude the canting of the

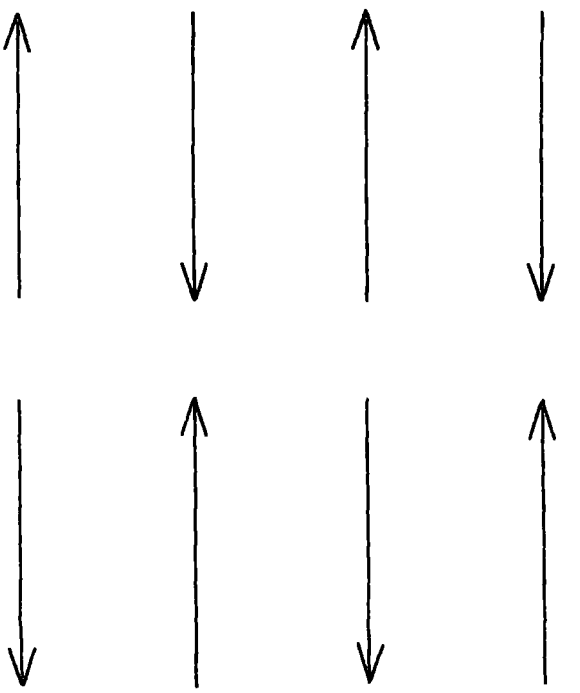

Fig. 1.5 Antiferromagnetic Order

moments leads to a net spontaneous magnetization and the material behaves as a weak ferromagnet. Haematite is an example of a canted antiferromagnet. The type of ordering is shown in fig 1.6.

Many of the rare-earth elements exhibit an antiferromagnetic behaviour believed to arise from the spiral spin structure shown in fig 1.7. The direction of the magnetization lies within the basal plane, however there is an angular displacement of the magnetization between adjacent layers, resulting in zero net magnetization within a bulk crystal. Kramers (1934) pointed out that it is possible to have exchange spin-coupling via intermediate non-magnetic ions. Anderson (1950) developed the theory of super-exchange for MnO and showed that this is stronger between atoms on opposite sides of the negative oxygen ion. S hull et al. (1951) found strong coupling between next nearest neighbour manganese ions indicating that the super-exchange between the manganese ions via the oxygen ions may be stronger than the direct exchange interaction.

Antiferromagnetic domains have recently been reviewed by Tanner (1979). Due to the fact that there is no net magnetization many of the techniques capable of imaging ferromagnetic domains are inapplicable. There are in fact only three techniques capable of imaging antiferromagnetic domains which are polarized light microscopy and X-ray and neutron diffraction topography.

Antiferromagnetic domains were first shown to exist in NiO by Roth (1960) and Slack (1960). Antiferromagnetic domains have also been observed in $KCoF_3$. These results are reported more fully in chapter six where further information relating to antiferromagnets may be found.

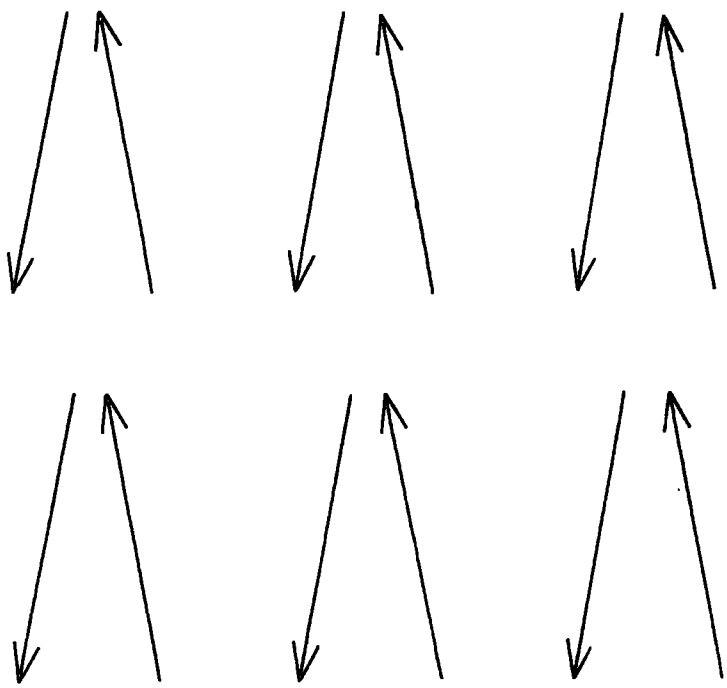

Fig. 1.6 Canted Antiferromagnetic Order

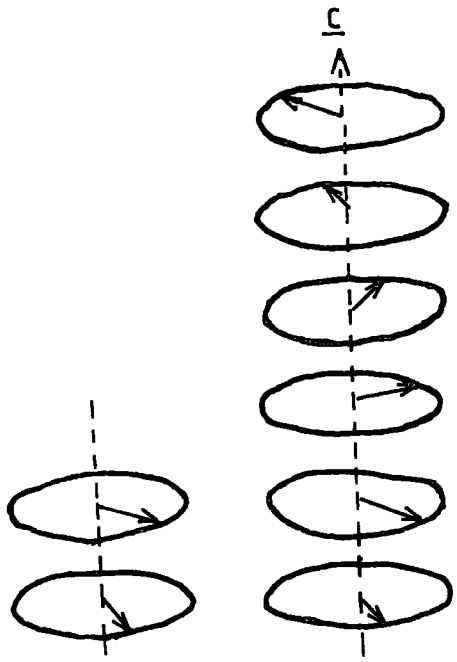

Fig. 1.7 Helical Antiferromagnetic Order

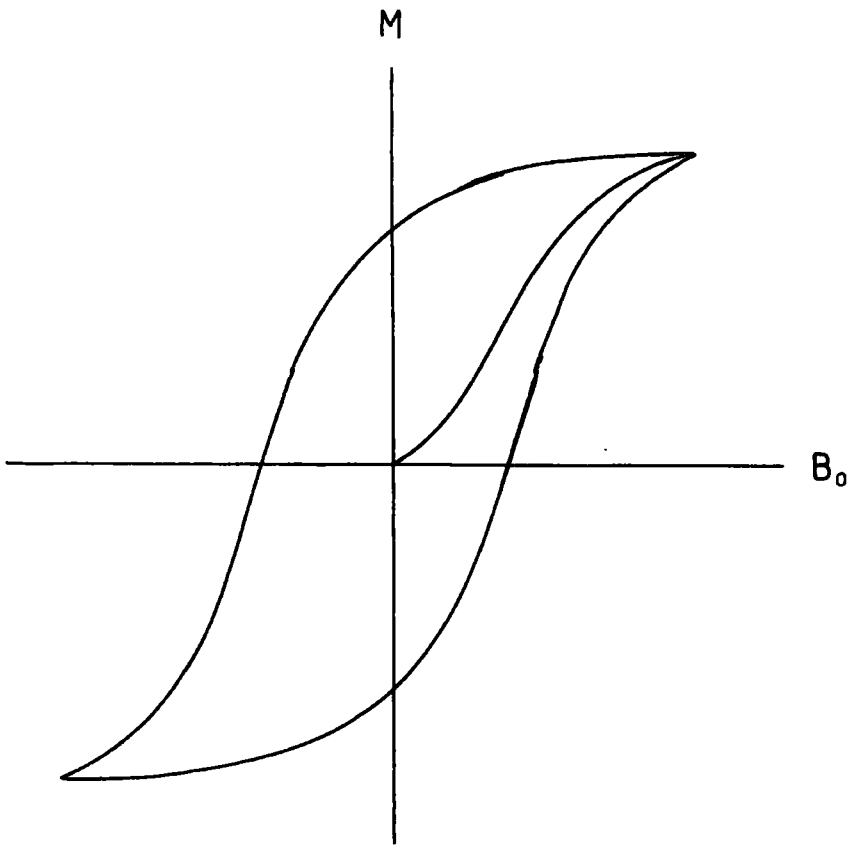

Fig. 1.8 Magnetisation Curve

1.7 Magnetic Domains

A typical magnetization curve for a ferromagnet is shown in fig 1.8. The ability of the ferromagnet to exist in the demagnetized state and the existence of hysteresis in the magnetization cycle provided initial problems with the idea of an internal molecular field. Weiss (1907) suggested that ferromagnets were subdivided into small domains and magnetized to saturation by the molecular field. The direction of magnetization within these domains may differ allowing a net zero magnetization. The application of a magnetic field enables domains preferentially aligned to the field to grow at the expense of other domains until saturation is reached. Upon reducing the field the presence of defects, grain boundaries and inclusions may prevent the domains returning to their original state. Magnetic domains have since been shown to exist. Carey and Isaac (1966) describe many techniques for their observation. In addition to the colloid technique, magneto-optical techniques, electron beam techniques and probe techniques which they describe, X-ray topography has been employed, (Polcarova 1969) and the neutron techniques described in chapter five have also been employed.

The domain structures observed depend on many factors, Landau and Lifshitz (1935) showed that domains were a natural consequence of the minimization of free energy. The theory of ferromagnetic domains has been reviewed by Kittel (1949). Calculations of ferromagnetic domain wall energies and widths are given in chapter eight, hence the factors associated

with the domain structure will only be outlined here.

When the magnetization of a sample is measured as a function of magnetic field it is found that it is easier to saturate the sample along certain directions. The difference in energy required to saturate a sample along a hard direction compared with an easy direction is known as the anisotropy energy.

The magneto-crystalline anisotropy is due to the symmetry of the crystal lattice resulting from the spin-orbit interaction with the crystal field. Hexagonal crystals are known with easy directions along the a, b and c axes. Cubic materials are known with easy axes along the <100>and <111> directions. The majority of ferromagnets have easy axis along low index crystallographic directions.

The demagnetizing field of a sample is obviously related to the presence of free magnetic poles on the surface of a sample. Hence a long thin rod with easy directions along its axis and perpendicular to its axis may be magnetized more easily along its axis. This is known as shape anisotropy.

A magnetostrictive anisotropy can be produced by applying a mechanical stress to a sample. This is related to the magneto-striction and magnetoelastic energy of the sample. It is found experimentally that ferromagnetic materials undergo a small change in dimension when they are magnetized.

Several types of domain wall exist, the first is the Bloch wall. This type of wall exists in bulk samples. The perpendicular component of the magnetization remains constant throughout the domain wall and on either side of the wall. This

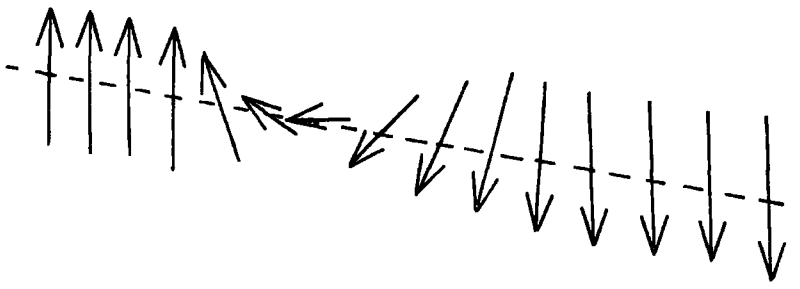

Fig. 1.9 Bloch Wall

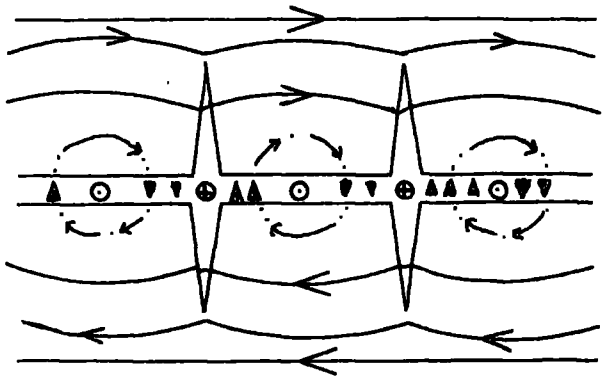

Fig. 1.10 Cross-tie Wall (Huber et al. 1958)

prevents the formation of free magnetic poles on the wall plane. The wall then remains uncharged and there is no magnetostatic energy associated with it. Rotation of the direction of the magnetization between domains occurs via rotation of the component of the magnetization lying in the plane of the wall. Fig 1.9 shows a Bloch wall which is the type of wall discussed in chapter 8.

The second type of domain wall is the Néel wall. Néel (1955) showed that in thin films, where the domain wall width approaches the specimen thickness, the magnetostatic energy, associated with free poles when a Bloch wall intersects the surface of a sample, becomes important. In low anisotropy energy material this may be the most important energy term resulting in the magnetization remaining in the plane of the thin film. Free poles are thus present on the wall plane instead of on the sample surface.

Huber et al, (1958) observed a new type of 180^{o} wall called a cross-tie wall. The main wall is cut at right angles by short regularly spaced cross-ties. The structure is interpreted as shown diagrammatically in fig 1.10. The plane of the spin rotation varying along the length of the wall.

The energy associated with the various types of domain wall have been calculated by Middelhoek (1963) and are shown in fig 1.11. From these calculations it appears Bloch walls are expected for specimens thicker than about 900 Å and cross-tie walls for thinner specimens. This has been confirmed experimentally (Methfessel et al 1960). Experimentally Middelhoek (1963) found

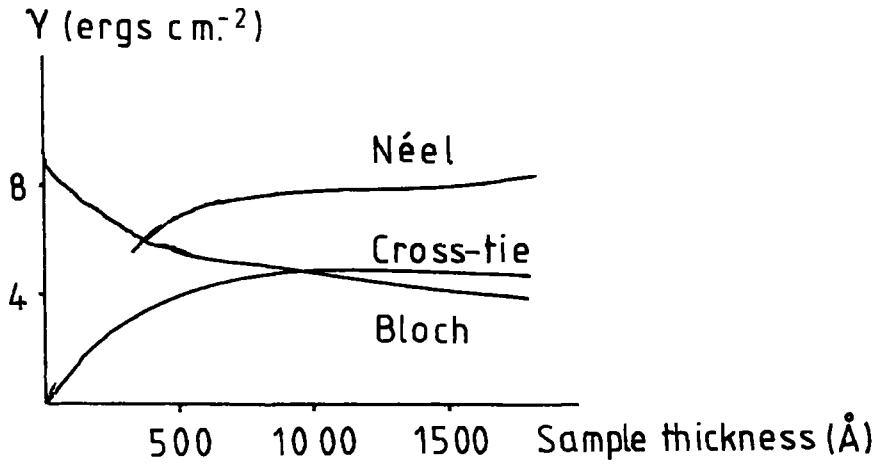

Fig. 1.11 Domain Wall Energies (Middelhoek 1963)

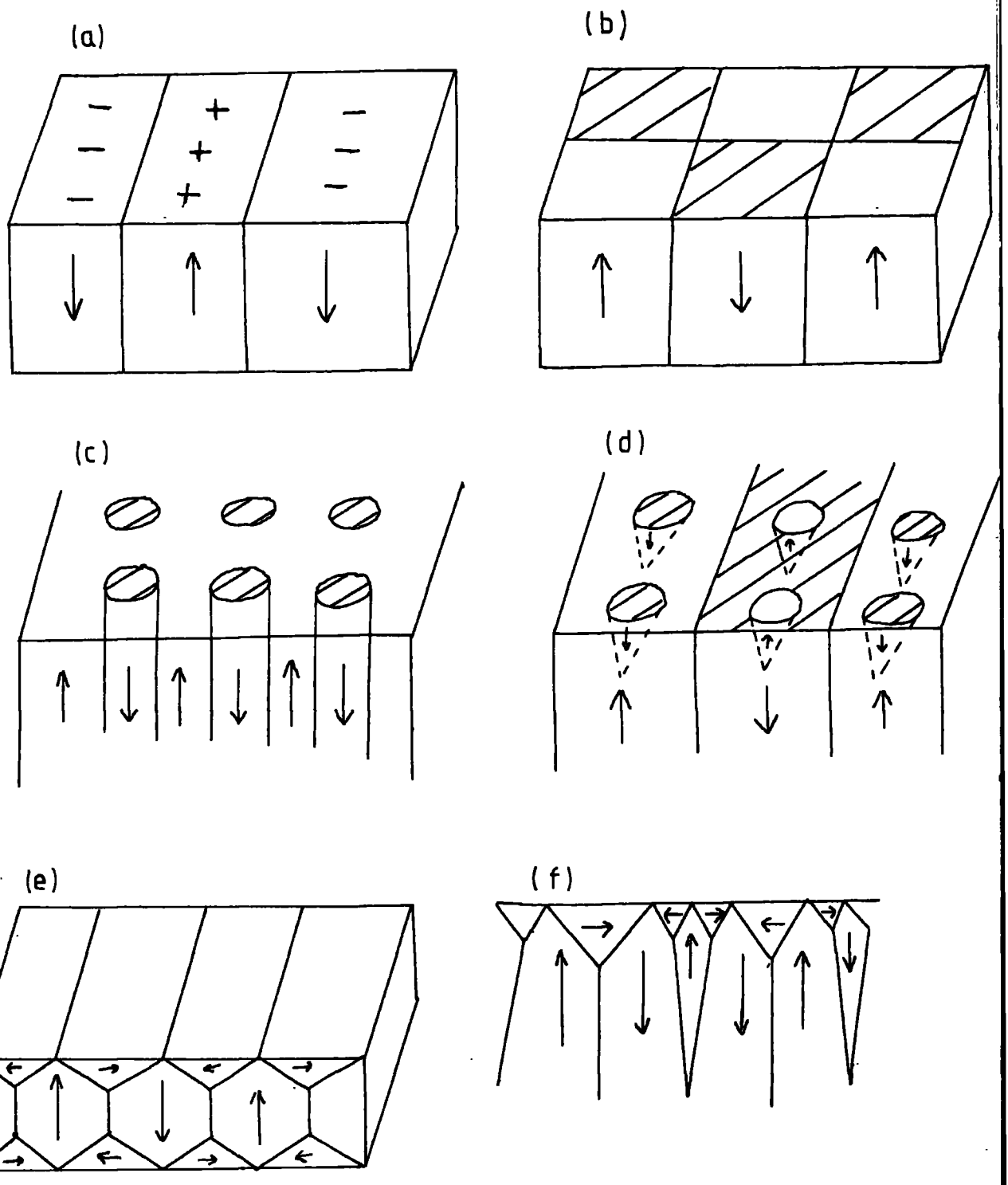

Fig.1.12 Uniaxial Domain Structures

that for samples less than 200 Å thick normal Néel walls are always seen, however the theoretical calculations show that cross-tie walls are expected. The discrepancy is probably due to the approximations necessary to calculate the cross-tie wall energy.

The domain structures present within an unstressed ferromagnet depend upon its shape, its saturation magnetization, the effective anisotropy and the exchange energy. The domain structure is determined by the necessity to minimise the total free energy, i.e. the sum of the wall energy and domain energy. In practice it is difficult to make accurate predictions, hence it is usual to minimise the magnetostatic energy present in a domain model.

Fig 1.12 shows a variety of domain models proposed for uniaxial materials. For a uniaxial material only 180° domain walls are possible. The simplest possible structure is shown in fig.1.12 a. In large anisotropy energy materials the formation of closure domains is not expected and possible domain structures are those shown in fig 1.12 a, b, c and d. In fig 1.12 d reverse dagger or spike domains are shown to reduce the surface magnetostatic energy with only a small increase in wall energy. This structure was proposed by Goodenough (1956). For lower anisotropy energy materials closure domains are expected to enclose the flux totally within the sample. Fig 1.12 e shows the simplest closure structure. Lifshitz (1944) proposed the structure shown in fig 1.12 f extending the model of Landau and Lifshitz (1935) to take into account thick crystals. Magnetic bubbles are an example of the domain structure in a uniaxial ferromagnet with a domain structure

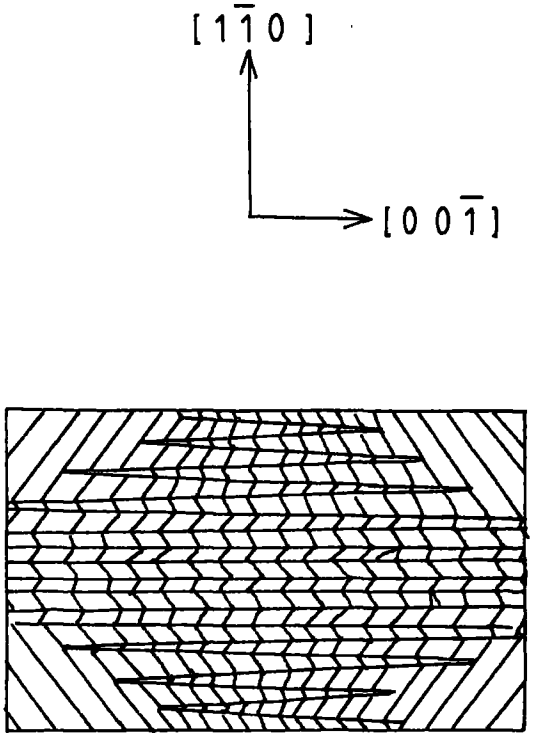

Fig. 1.13 Parallelogram-net in Nickel
(Yamamoto and Iwata 1953)

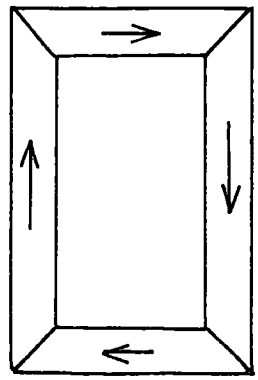

(a)

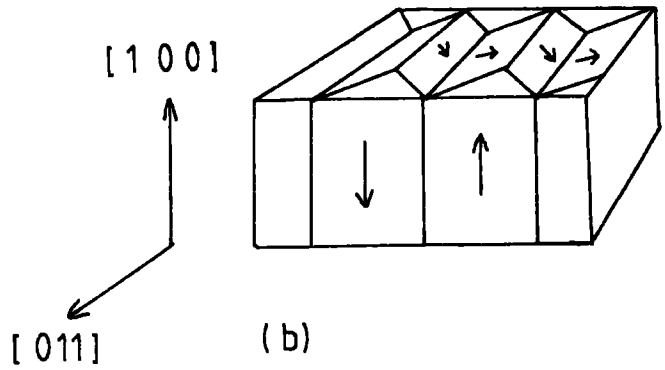

(b)

Fig. 1.1 4 Closure Domain Structures

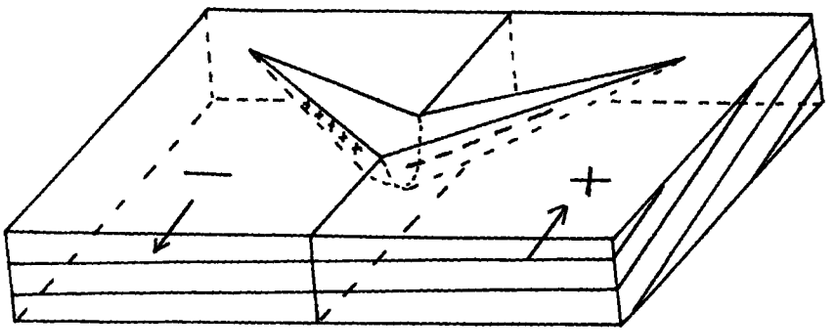

Fig. 1.15 Fir Tree Domain

similar to that shown in fig 1.12 c. Jones (1976) has given an introduction to magnetic bubbles.

In non-uniaxial materials the domain structure becomes more complicated. A possible domain structure for hexagonal terbium with its b axis easy is given in chapter seven and a discussion on a possible domain structure on a (110) surface sample of terfernol a <111> easy axis material is given in chapter eight. Fig 1.13 shows the parallelogram domain structure from a surface close to (110) in nickel which has <111> easy directions.

Williams and Shockley (1949) studied the domain structures in a (100) surface "picture frame" sample of silicon iron which has <100> easy directions. The domain structure observed is shown in fig 1.14 a and represents a perfect closure structure. Fig 1.14 b shows the domain structure for (110) and (100) surfaces of a <100> easy axis material. This structure was confirmed by Bates and Neale (1949, 1950). On an inclined (100) plane a "fir tree" pattern is observed (fig 1.15) the tree pattern appearing for an inclination between 0.65^{o} and 1.3^{o}. This tree pattern is a superficial surface structure which reduces the magnetostatic energy by producing partial flux closure.

CHAPTER TWO

X-RAY TOPOGRAPHY

CHAPTER TWO

X-RAY TOPOGRAPHY

2.1 Introduction

X-ray topography comprises a variety of X-ray diffraction techniques used to determine variations within a crystal from the ideal crystal. These techniques are complementary to electron microscopy techniques compared with which X-ray topography has an inferior resolution. However it is capable of imaging large areas of samples up to several millimetres thick, depending on the material, compared with the small areas of specimens a few hundred angstroms thick required for electron microscopy. It is also, in general, non-destructive. This latter point makes it possible to take repeated topographs of the same sample without encountering problems due to radiation damage and enables such examinations to be inserted between other types of experiment on the same sample. X-ray topography is concerned with point to point variations in the intensities or directions of an X-ray beam diffracted from a crystal according to Bragg's law.

$$\lambda = 2d_{hkl}\sin\theta \qquad (2.1)$$

where λ is the wavelength,

d_{hkl} is the lattice spacing for the hkl reflection,

θ is the Bragg angle.

These variations give rise to extinction and orientation contrast respectively. By recording the diffracted beam a direct mapping of the lattice plane topography is obtained. The variations within the diffracted beam allow the defect structure of the crystal to be studied.

A variety of review articles have appeared describing experimental techniques and results. These include articles by Lang (1970), Bonse Hart and Newkirk (1967), Austermann and Newkirk (1967), Isherwood and Wallace (1974), Armstrong and Wu (1975) and Tanner (1977). In addition information is obtained from a book Tanner (1976) and information on synchrotron X-ray topography is obtainable from a separate review article, Tanner (1977). An outline of the various experimental techniques will be given here and a description of contrast mechanisms and the relevant diffraction theory will be given in the next chapter.

2.2 Berg-Barrett Topography

This is a technique originally developed by Berg (1931) and improved by Barrett (1945). The principles are outlined in fig 2.1 in reflection and fig 2.2 in transmission. This is a characteristic radiation method employing an extended source and is most commonly used in reflection. A single crystal is set to Bragg reflect characteristic radiation from a chosen set of lattice planes. Bragg reflection takes place over an angle of approximately one degree due to the extended nature of the source. This implies it is simple to set up and insensitive to orientation contrast for small specimens to plate distances or for regions misorientated by less than one degree. The apparatus is fairly simple with no moving parts required. However a problem is present owing to the doublet nature of the K_α line. This will result in a double image, the $K_{\alpha 1}$ and $K_{\alpha 2}$ lines resulting in diffracted beams travelling in different directions.

Considering the reflection case first, from fig 2.1 it can be seen that by using an extended source with the crystal inclined at an oblique angle to the X-ray beam, a fairly large area of the crystal

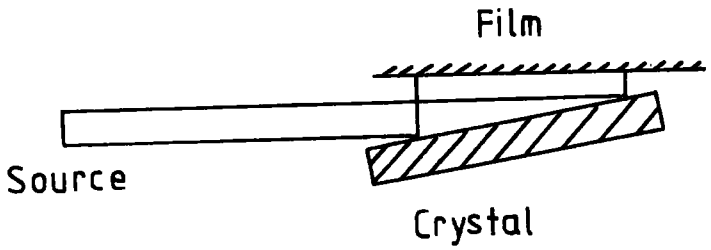

Fig. 2.1 Berg-Barrett Topography (Reflection)

can be imaged, typically several millimetres square. By using a specimen with suitable geometry, careful choice of asymmetric reflecting planes and X-ray wavelength enables the diffracted beam to be almost normal to the crystal surface. It is then possible to place the film very close to the crystal severely limiting the divergence between the $K_{\alpha 1}$ and $K_{\alpha 2}$ lines and avoiding the formation of double images. This enables a resolution of one micrometre to be achieved.

With the film very close to the sample it must be very nearly parallel to the crystal surface, hence geometric distortion is not a problem. However it is not always possible for the film to be perpendicular to the diffracted beam. Loss of resolution due to the diffracted beam passing through the film at an angle can be minimised by using very thin emulsions (10 micrometres). Use of such emulsions is not normally a problem as their lower absorption efficiency is compensated for by using more easily absorbed soft radiation.This is often convenient as these give large Bragg angles for low index reflections.

As this technique is a surface reflection technique, only a thin surface layer of the crystal is examined. It is thus suitable for examining materials with relatively high dislocation densities (10^6 cm^{-2}) compared with the lower maximum (10^4 cm^{-2}) which can be studied with transmission techniques.

Two modifications have been employed to image larger areas of the crystal. In the first by Wooster and Wooster (1945), the specimen and film are fixed relative to each other and are rocked through an angle sufficiently large for all areas of the crystal to diffract the characteristic X-ray line. This simulates a continuous radiation topograph and is sensitive to extinction contrast only.

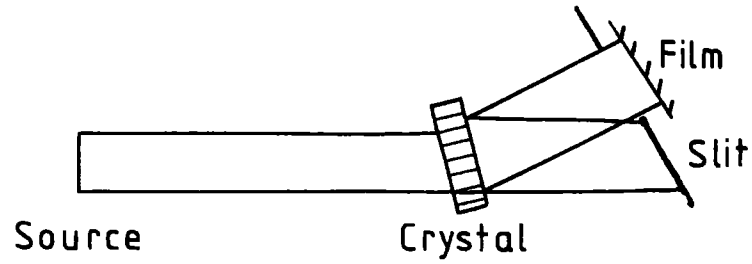

Fig. 2.2 Barth - Hosemann Topography (Transmission)

The second method by Merlini and Guinier (1957) is sensitive to both orientation and extinction contrast.The film is placed parallel to the specimen surface. The film and plate are translated together so that an extended area of the specimen can be scanned by a finely collimated incident ribbon X-ray beam which gives good angular resolution.

In transmission, (Barth-Hosemann(1958) geometry) fig 2.2, it is not usually possible to place the film close to the specimen due to the overlapping between direct and diffracted beams. Thus the film must be separated from the specimen and a slit used to block the direct beam. Unfortunately this leads to problems associated with the angular dispersion between the $K_{\alpha 1}$ and $K_{\alpha 2}$ beams. Dionne (1967) used the K_{β} line to overcome this where the $K_{\beta 2}$ line is very weak compared with the $K_{\beta 1}$ line. Unfortunately the K_{β} line is much weaker than the K_{α} line and there is a considerable cost in terms of exposure time. Tanner and Humphreys (1970) overcame this by use of the WL_{α} line. Hosoya (1968) used filtered silver radiation, the A_g $K_{\alpha 1}$ line being removed by a rubidium filter. Roessler(1967) used a very thick crystal in which anomalous transmission, the Borrman effect, occurred. The direct beam was attenuated by the sample enabling the film to be placed in contact with the specimen.

Use of an extended source makes the technique relatively insensitive to orientation contrast, hence enabling topographs of bent crystals to be taken. However the high background of scattered radiation reduces the sensitivity to extinction contrast.

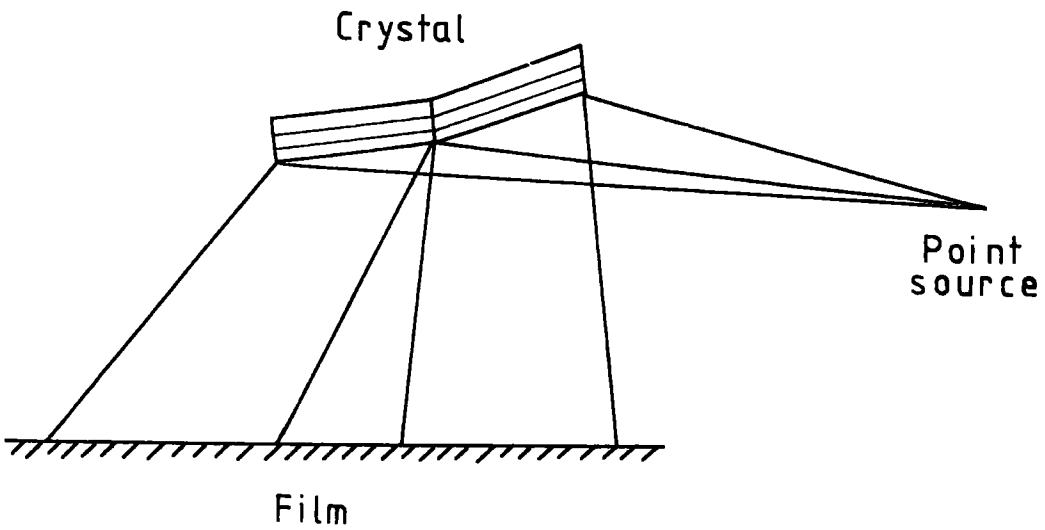

Fig. 2.3 Schulz Topography (Reflection)

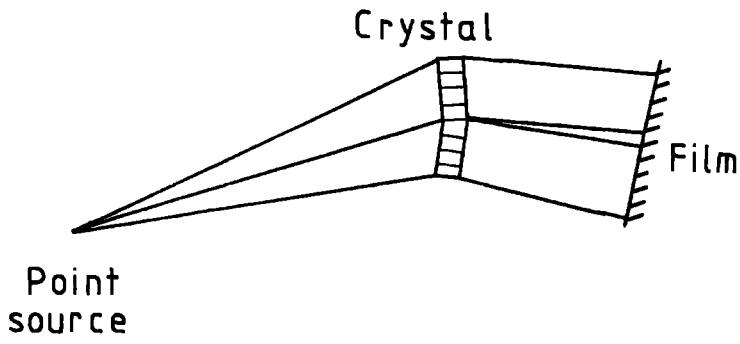

Fig. 2.4 Guinier-Tennevin Topography (Transmission)

2.3 Schulz Method

This is a reflection technique using continuous radiation, first employed by Schulz (1954), the principles of which are outlined in fig 2.3. It employs a microfocus X-ray source with dimensions of typically 25 micrometres. White X-rays diverge from this point source to be diffracted by the crystal and recorded on film. The polychromaticity of the source enables images from several different sets of reflecting planes or from different grains to be recorded on one film. In practice, the source to specimen and specimen to film distances are about equal and hence a microfocus source is essential for high resolution. This technique is sensitive to both orientation and extinction contrast with a resolution dependent upon the geometry employed in the experiment.

Guinier and Tennevin (1949) employed a similar technique in transmission, fig 2.4, with white X-rays diverging from a point source. These two techniques are the basis of the white radiation experiments performed in synchrotron X-ray topography. They are simple to set up as there is no need for precise angular adjustment to obtain Bragg reflection.

2.4 Lang Method

The most widely used method of transmission X-ray topography is that developed by Lang initially in the form of the section topograph Lang (1958) and modified into the projection topograph, Lang (1959). A fine focus target is collimated to a sufficiently

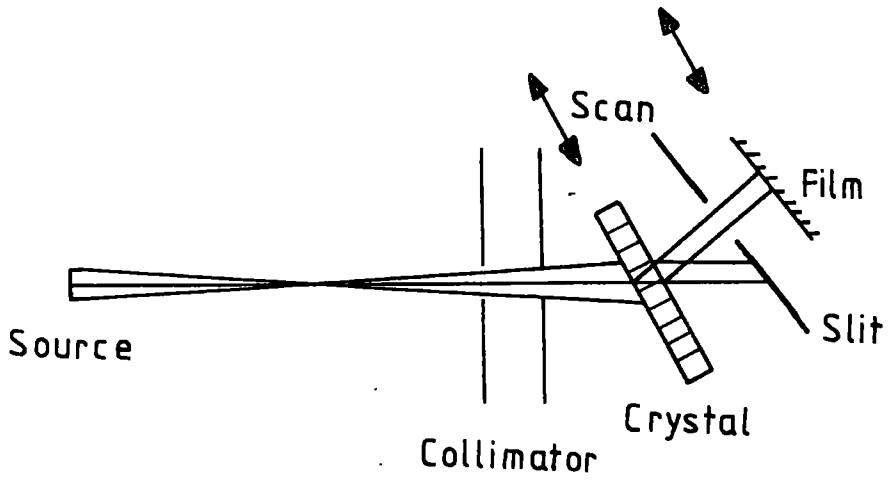

Fig. 2.5 Lang Topography

small horizontal angular divergence that the crystal will not simultaneously diffract both the $K_{\alpha 1}$ and $K_{\alpha 2}$ lines. The $K_{\alpha 1}$ line is used because of its higher intensity. The typical angular divergence of the beam is 5×10^{-4} radians which is greater than the perfect crystal reflecting range of 10^{-5} radians. Due to the high collimation of the beam the technique is sensitive to orientation contrast as well as extinction contrast. A schematic diagram of the arrangement is shown in fig 2.5 and a photograph of the apparatus employed at Durham is shown in fig 2.6.

The crystal is set up to Bragg reflect a characteristic radiation line. Slits are positioned to allow the diffracted beam to pass through onto a photographic emulsion or other recording medium, which is placed perpendicular to the diffracted beam and to stop the undiffracted beam. If the incident beam slit width is narrow compared with the base of the Borrman fan, (ie $a < 2t \sin\theta$ where t is the crystal thickness and θ the Bragg angle) an image of a section through the crystal is produced. This is the section topograph. If the crystal and film are translated together, usually parallel to the crystal surface, a projection topograph results. In this case the width of the beam need not be as narrow as that required for a section topograph. This technique requires an accurate traversing mechanism which must be capable of traversing the width of the crystal, (up to 10 cm) while retaining a constant angular setting. The traverse speed must be constant so that the crystal is uniformly exposed to X-rays or formation of vertical striations or traverse lines occurs.

Fig 2.6 Lang Camera (with Cryostat)

For a platelet sample Bragg planes are chosen to be normal or nearly normal to the crystal surface whenever possible then, for a small Bragg angle, image distortion is kept to a minimum. If a very fine microfocus tube is employed with an effective source size of a few microns, the crystal will act as its own collimator, hence making collimator slits unnecessary, (Lang 1957). However, with more normal fine focus X-ray sources collimating slits are required.

As the projection topograph is obtained by adding many section topographs this throws away information available in the more fundamental section topograph . Unfortunately in very thin crystals it is often impossible to meet the incident beam width condition for section topographs.

$$a \ll 2t\sin\theta \qquad (2.2)$$

where a is the incident beam slit width.

In practice for section topographs the slit width is about 10 microns compared with about 200 microns for a projection topograph, the effective source width in the X-ray set used at Durham. Experimentally the same apparatus is used for both with the slit width adjusted for the type of topograph required. This facilitates taking section topographs of an area of particular interest which has formed part of a projection topograph.

Section topographs are very convenient in determining the exact location or depth of a particular defect within a crystal. An alternative method which is less sensitive, but is far quicker to perform and can cover a large area of crystal is to take stereo pairs. There are two methods of doing this. The first,(Lang 1959),

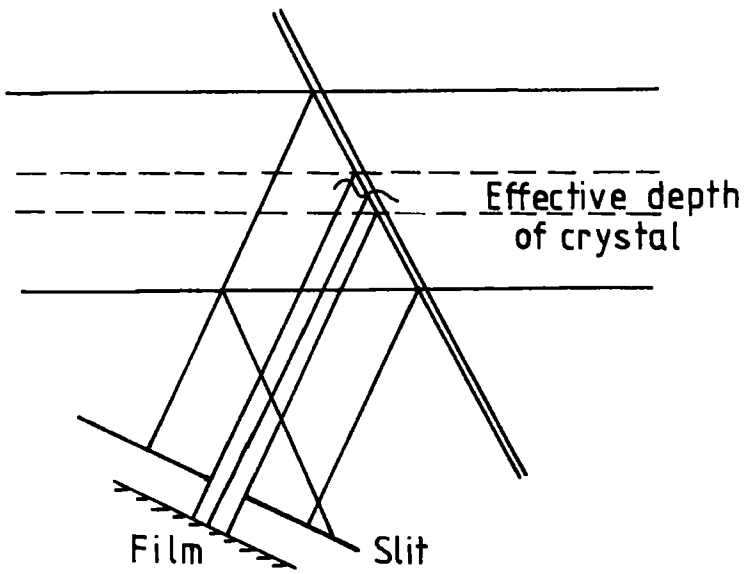

Fig. 2.7 Limited Projection Topography
(Lang 1963)

is to take a pair of hkl and $\bar{h}\bar{k}\bar{l}$ reflections. Under moderate absorption conditions this is not possible as the contrast of many defects changes between the two reflections. The second method is to take the same reflection twice, Haruta (1965) with the crystal rotated by between $\pm 2^{o}$ to $\pm 15^{o}$ about the diffraction vector. The angle employed depends upon the sample thickness and the sensitivity required.

A modification of the projection topography technique, called limited projection topography, was developed by Lang (1963) for use with crystals where it was undesirable to remove a strained surface layer. This was developed particularly for the study of natural diamond which has very low absorption. In the usual Lang topography arrangement strong diffraction from a damaged surface layer will obscure contrast due to interior defects. In limited projection topography the diffracted beam slits are arranged to cut into the diffracted beam so that diffracted beams from one or both surfaces of the sample are prevented from reaching the emulsion. Fig 2.7. This technique can be used to study a surface layer or any particular layer within a crystal. Under low absorption conditions the majority of the intensity in the image is from X-rays scattered out of the direct beam which do not exactly satisfy the Bragg condition. Thus a direct image of a defect is formed at a point across the diffracted beam corresponding to its depth within the crystal. Only defects within the effective depth of a low absorbing crystal defined by the diffracted beam slits will form an image on the film.

Lang (1963) also showed that for very high quality crystals

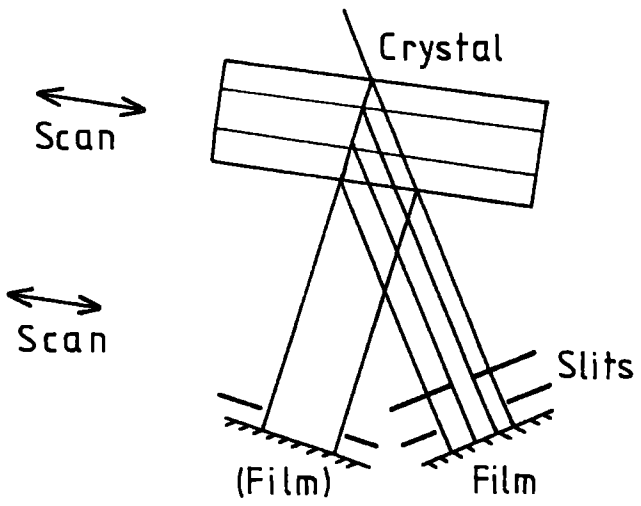

Fig. 2.8 Direct Beam Topography

(Lang 1963)

direct beam topography was also possible, fig 2.8. A screen is placed to prevent the incident beam, and if required, part of the forward diffracted beam from reaching the film. If the X-ray absorption is low, the contrast of defects in the forward diffracted beam is complimentary to that produced in the more usual diffracted beam geometry.

2.5 Double Crystal Topography

Conventional topographic techniques are at best sensitive to strains of about 1 part in 10^5. In practice they are only sensitive to long range strains of about 1 part in 10^3. As for slow variations in the lattice parameter the diffracted intensity is equivalent to the integrated intensity because of the large angular divergence of the X-ray beam. However by using a double crystal technique (Bond and Andrus 1952; Bonse and Kappler 1958) as shown in fig 2.9, variations in lattice parameter of a few parts in 10^8 have been detected. (Hart 1968; Aldred and Hart 1973).

The technique uses two successive Bragg reflections from two crystals of similar lattice parameter which in practice are often the same material and must be the same material for maximum sensitivity. Fig 2.9 shows the successive reflection of X-rays from two crystals in the (+-) parallel arrangement. In this setting the two crystal technique is at its most sensitive to variations in lattice parameter orientation or distortion. The rocking curve obtained by rotating either of the two crystals is very narrow closel y approaching the perfect crystal reflecting curve width, being a convolution of two perfect crystal reflecting curves. The arrangement is non-dispersive as all wavelengths satisfying the Bragg condition are simultaneously

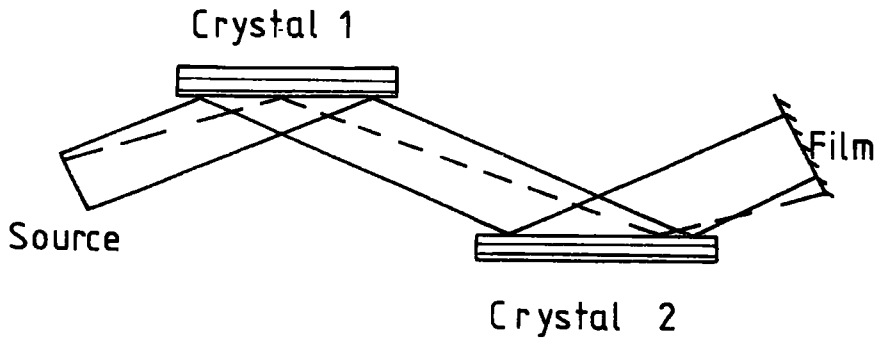

Fig. 2.9 Double Crystal Topography (+-)Parallel Setting

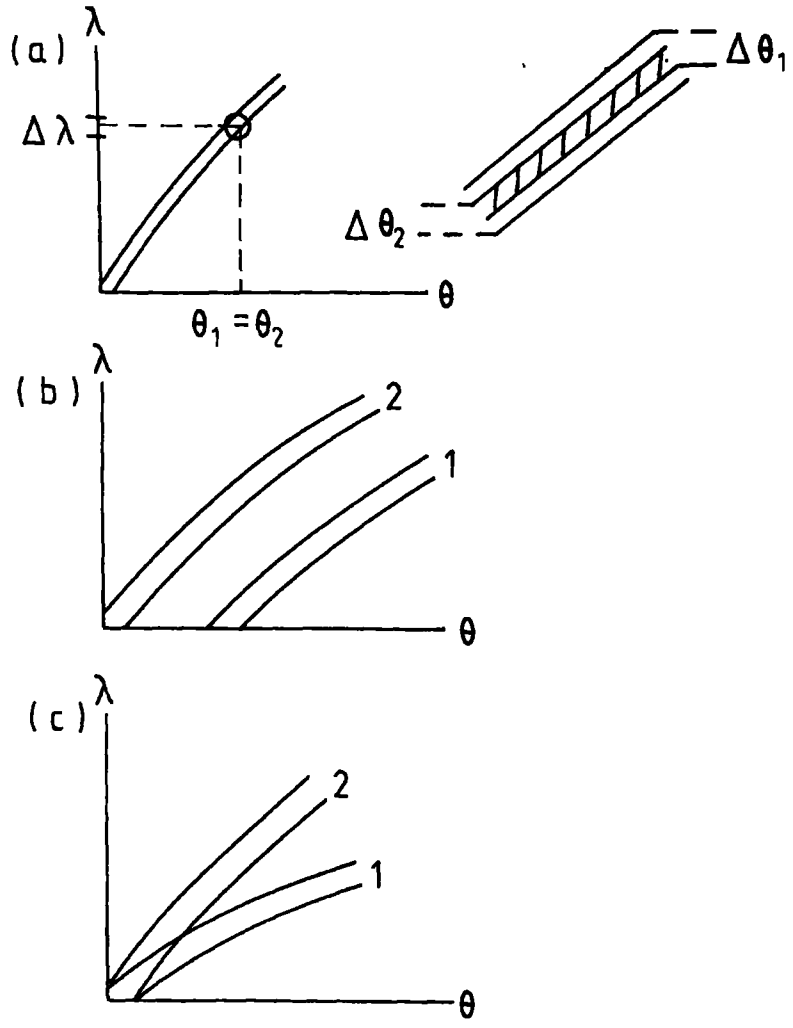

Fig. 2.10 DuMond Diagram (+-) Parallel Setting

(a) Two Perfect Crystals

(b) Local Lattice Rotation

(c) Local Lattice Dilation

diffracted. Any local misorientation of the lattice will result in a loss of intensity. This can be explained easily by considering the DuMond diagram, fig 2.10.

The DuMond diagram shows the angle at which diffraction occurs for a given set of Bragg planes. For two identical perfect crystals in the (+-) parallel setting the two curves overlap. Simultaneous diffraction takes place only over the wavelengths at which the curves do overlap. Any misorientated or distorted region in one crystal causes a displacement of the curve as shown and local loss of diffracted intensity will result.

If the second crystal is set on the steep flank of the rocking curve the slope of the rocking curve at this point can be taken to be linear. Then the lattice distortion is given by (Bonse 1962)

$$\frac{\Delta I}{I} = K\left(\tan\theta\frac{\Delta d}{d} \pm \underline{n}_g.\underline{n}_t\,\Delta\theta\right) \qquad (2.3)$$

where I is the intensity of the diffracted beam,

K is the slope of the rocking curve,

θ is the Bragg angle,

d is the lattice parameter,

$\underline{n}_g$ is a unit vector normal to the incident beam,

$\underline{n}_t$ is a unit vector parallel to the tilt axis.

Due to the angular dispersion present with two identical crystals, images of defects produced by different wavelengths are not found at the same point. Defects within the first crystal produce diffuse images, due to the large separation of this crystal from the photographic plate and hence are not usually a problem. If some wavelength dispersion is introduced by using crystals with slightly

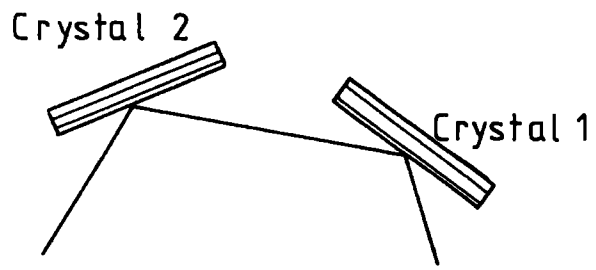

Fig. 2.11 Double Crystal Topography (++) Setting

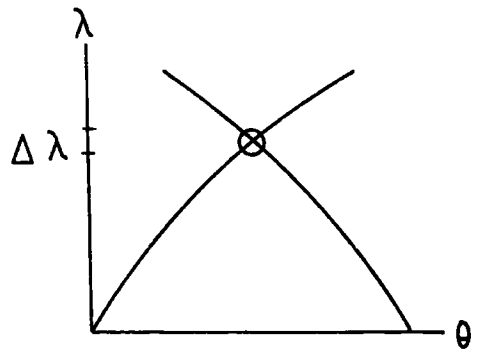

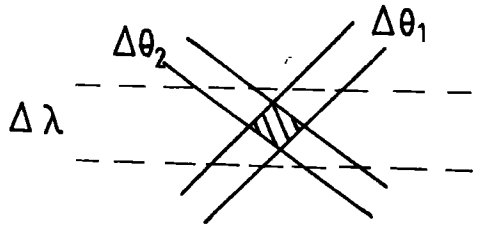

Fig. 2.12 DuMond Diagram (++) Setting

different lattice parameters only a small range of wavelengths are diffracted and the problem is at least partly overcome.

An alternative is to use the (++) setting, fig 2.11. Again we have two crystals with equal spacing of Bragg planes, but these are no longer parallel. For any relative orientation of the crystal only a narrow range of wavelengths will be diffracted as can be seen from the DuMond diagram fig 2.12. The range of wavelengths diffracted by both crystals is less than the natural linewidth of a characteristic line. Hence marked changes in contrast only occur for regions sufficiently misorientated not to diffract the characteristic line. The sensitivity is thus much less than that achievable in the (+-) setting and comparable with that of the Lang technique.

2.6 Synchrotron X-ray Topography

The principal problems with conventional X-ray topography techniques are that exposure times are long, ranging from a few hours to a few days. They are tricky to set up usually requiring precise angular adjustments and due to geometrical constraints on resolution only certain types of experiments are possible. Thus, in spite of the techniques being available and successfully exploited for some time, their use has not been widespread in crystal growth assessment or as part of other experimental programmes. Synchrotron topography overcomes many of these problems as was first shown by Tuomi et al. (1974) who showed that by placing a crystal in a synchrotron radiation beam and recording the diffracted beams images of the crystal could be obtained in seconds with relatively crude angular adjustments.

Their experiment effectively employed the Guinier-Tennevin technique.

2.6 a Synchrotron Radiation

The instantaneous power of electromagnetic radiation generated by a relativistic electron undergoing centripetal acceleration was first calculated classically by Liénard (1898) to be

$$P = \frac{2}{3}\frac{e^2 c \beta^4}{R^2}\left[\frac{E}{m_0 c^2}\right]^4 \qquad (2.4)$$

where the electron is assumed to be moving in a circular orbit of radius R and the rate of change of energy is assumed to be negligibly small compared with the rate of change of momentum. e, m_0 and v are the charge, rest mass and velocity of the electron which has a total energy E and $\beta = \frac{v}{c}$

Schwinger (1946, 1949) developed a more complete relativistic treatment and showed that for circular motion the radiation was distributed among the harmonics of the orbital motion. However, betatron oscillations of the electron beam smear out the line structure and the spectrum appears as a continuum. For low electron velocities the radiation would be emitted as a toroid, but for relativistic electrons the spatial distribution of the radiation is peaked in the instantaneous direction of the electron's motion, fig 2.13. A further consequence of the relativistic motion is that as the electron energy increases the power radiated extends into higher harmonics of the orbital frequency and hence into the X-ray region.

Schwinger's original formula is rather cumbersome and has

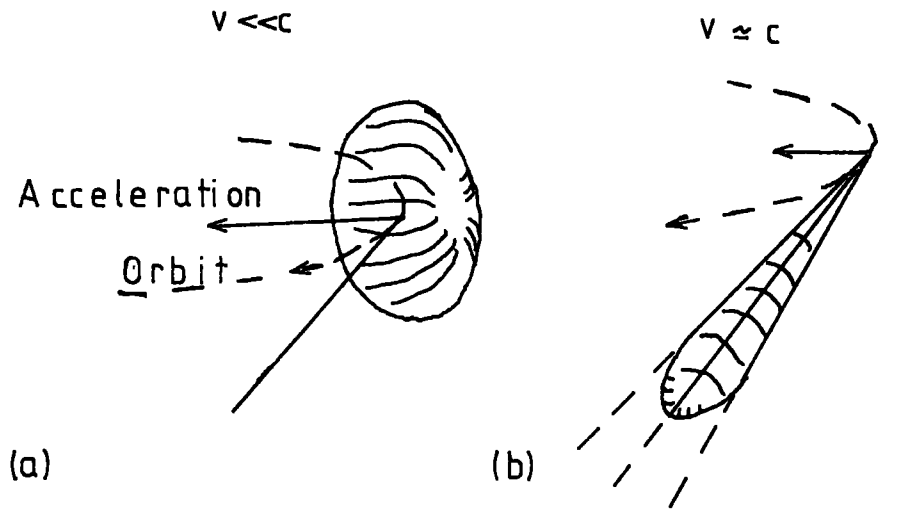

Fig. 2.13 Synchrotron Radiation from Non-relativistic and Relativistic Electrons

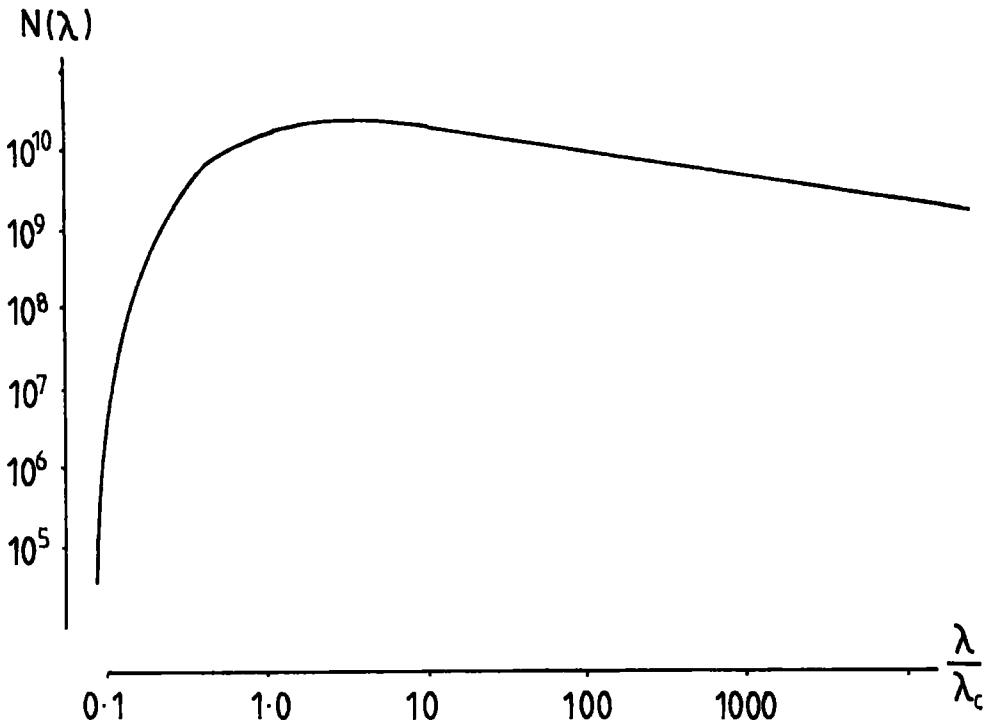

Fig. 2.14 "Universal" Spectral Curve

been rearranged by Suller (1973) to

$$N(\lambda) = 2.46\times10^{10}\left(\frac{\lambda}{\lambda_c}\right)^2 E\ G\left(\frac{\lambda}{\lambda_c}\right) \qquad (2.5)$$

where λ_c is the critical wavelength (in angstroms)

$$\lambda_c = \frac{5{\cdot}6\,R}{E^3} = \frac{18{\cdot}6}{BE^2} \qquad (2.6)$$

where E is the energy in GeV,

R is the radius in metres,

B is the magnetic field in Tesla,

λ is the wavelength in angstroms,

$$G\left(\frac{\lambda}{\lambda_c}\right) = \left(\frac{\lambda_c}{\lambda}\right)^3 \int_{\frac{\lambda_c}{\lambda}}^{\infty} K_{5/3}(u)\,du \qquad (2.7)$$

where $K_{5/3}$ is a modified Bessel function and

$N(\lambda)$ is the number of photons /s/mrad/ma in a 0.1% bandwidth calculated over the full height of the beam.

Equation 2.5 has been used by Thompson et al.(1975) to calculate a 'universal' spectral curve, fig 2.14 which along with equation 2.6 can be used to determine the spectrum of any machine. Fig 2.15 shows the spectrum of several machines and compares them with conventional X-ray sources. The characteristic wavelength determines the cut-off and peak of the spectrum. The peak occurs at about twice λ_c below this the fall off is approximately exponential hence usable intensity is available down to about $\lambda_c/10$. It is implicit from Schwinger's formula that the radiation lying in the plane of the orbit is 100% polarised. Out of the orbit plane the polarisation decreases as the wavelength and angle are increased.

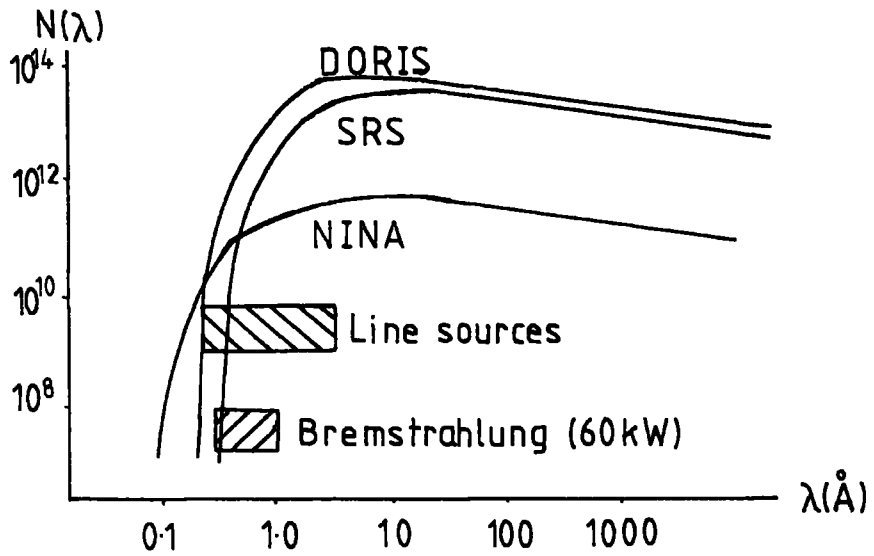

Fig. 2.15 Source Spectra

The cone angle, ψ of the radiation is given approximately by

$$\psi = \frac{m_0 c^2}{E} \qquad (2.8)$$

which is about 10^{-4} radians for machines of a few GeV giving synchrotron radiation a natural collimation. Parallel to the plane of the orbit the distribution of wavelength with angle is isotropic with contributions from all points on the orbit superimposing. Perpendicular to the orbit the angular distribution is a function of wavelength, but at the critical wavelength is focused into the angle ψ given by equation 2.8. Below λ_c the angle is less than ψ, while above λ_c the angle is greater than ψ. More information concerning the theory of synchrotron radiation can be found in the review of Codling(1973).

2.6 b Synchrotron Topography

The important characteristics of synchrotron X-ray topography are as follows:-

1. It is a white radiation technique which enables imperfect crystals to be imaged. Any misorientated regions of the lattice will select their own wavelength from the incident beam. Hence all of the crystal will be imaged with one setting.

2. The very high natural collimation allows large, typically 50 metres, source to specimen distances without undue loss of intensity. This also permits the entire crystal to be imaged without the necessity of scanning and enables large specimen to plate distances, 10 cm, to be employed without loss of resolution. The result of this is that a considerable quantity of apparatus can be placed around the sample,(for example, electromagnet, cryostat, straining jig, enviromental stage) enabling experiments to be performed which

would be difficult or impossible to carry out with conventional topographic techniques. Typical examples of the types of experiment which are now feasable are the effects of a magnetic field on the antiferromagnets $KCoF_3$ and $KNiF_3$ with fields up to 1·4T and temperatures down to 4·2K Safa (1977), Tanner et al.(1976), Safa and Tanner (1977, 1978), the work of MacCormack and Tanner (1978) on the re-crystallization of silicon-iron with temperatures up to 1000°C and the work of Jordan and Gastaldi (1979) on the re-crystallization of aluminium.

3. The high intensity of the source results in short exposure times permitting quasidynamical experiments on a realistic time scale. The experiments mentioned above took account of this property as also does the work of Bordas et al (1975).

Double crystal synchrotron topography experiments have been performed at L.U.R.E. The high intensity of synchrotron radiation has allowed Miltat and Kleman (1979) to study the interaction of moving ferromagnetic domain walls with lattice imperfections. The work involved synchronising the opening of an X-ray shutter with an oscillating magnetic field. Further double crystal topography work is included in reviews by Sauvage and Petroff (1979) and Sauvage (1979).

Single crystal experimental techniques used in synchrotron topography are the Schulz technique in reflection and Guinier-Tennevin technique in transmission. The low divergence white radiation beam results in a Laue pattern of the crystal being recorded, fig 2.16. Each set of reflecting planes selects its own wavelength from the incident beam and each 'spot' is an image of the crystal which

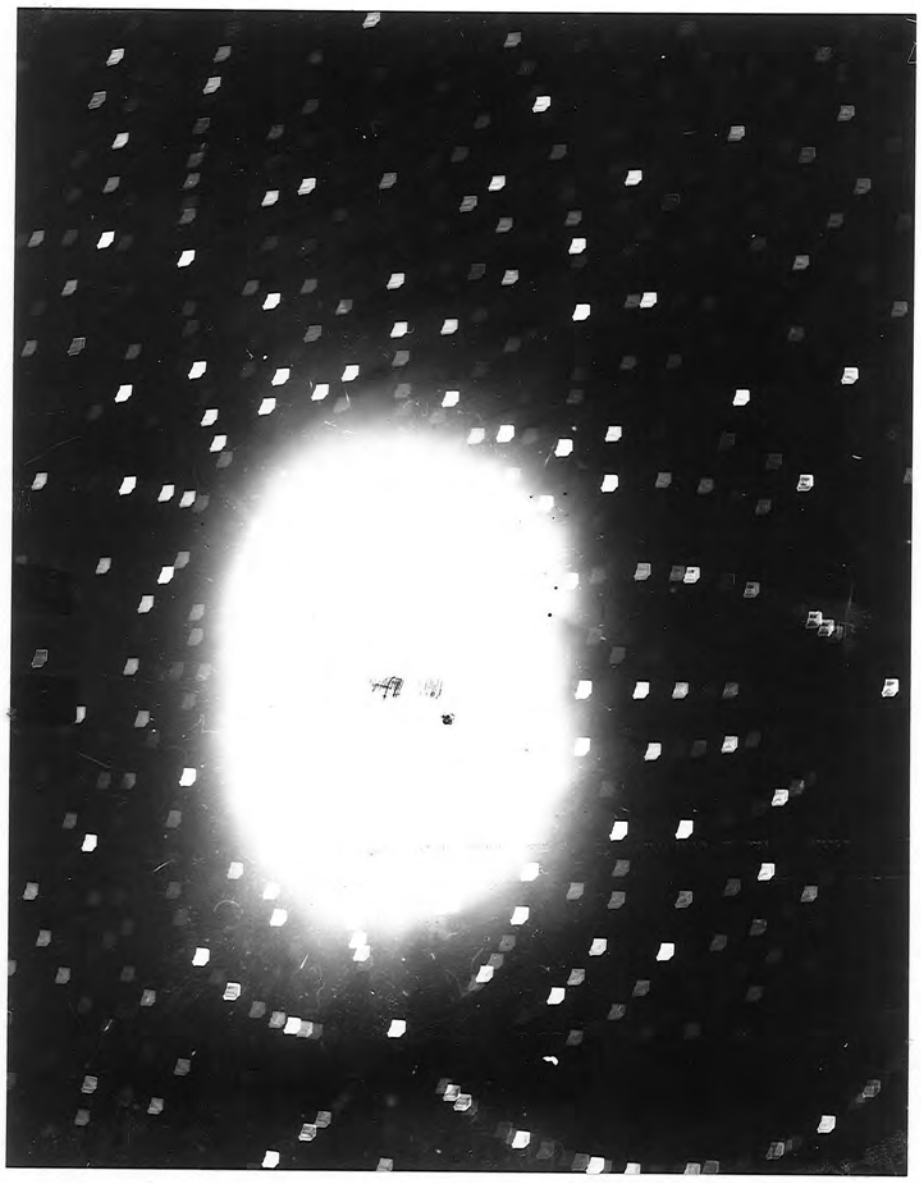

Fig 2.16 Synchrotron "Laue" Pattern of $Tb_2Ge_2O_7$
(DESY 9ma 7 Gev 6min 10μm L4)

may contain several orders of reflection.

The first experiment of Tuomi et al.(1974) gave a resolution of 5-10 microns, however Hart (1975) achieved a resolution of 1-2 microns in surface reflection topographs of silicon when working with a synchrotron of smaller source size and larger source to specimen distance. This was achieved with a specimen to plate distance of 16 cm. Hart pointed out that synchrotron topographs are more sensitive to strain than Lang topographs and that images obtained in different diffraction orders may differ due to the different extinction depths. Consequently, there may be some displacement between the images from these different orders of reflection and the contrast of a synchrotron topograph may differ from that of a Lang topograph. Tanner et al. (1977) showed that by suitable choice of diffracting planes and wavelength synchrotron topographs could be obtained which were almost indistinguishable from Lang topographs.

Tuomi et al. (1974) calculated the intensity of the diffracted beams for Laue reflections to be proportional to

$$I_{hkl} \propto P(\lambda)\, F_{hkl} \frac{\lambda^3}{\sin^2\theta} \exp(-\mu t) \qquad (29)$$

where $P(\lambda)$ is the radiated power of the source per unit wavelength

F_{hkl} is the structure factor of the hkl reflection

μ is the absorption coefficient of the crystal.

This expression neglects any polarisation losses and neglects the effects of temperature on the intensity of the diffracted beam. Hart (1975) derived essentially the same result, but pointed out that the effects of air absorption and the variation of film sensitivity with X-ray wavelength were also important factors.

Consideration of these factors enables the optimum diffracting conditions to be chosen so that the majority of the diffracted intensity belongs to only one order of reflection.

The experimental arrangement for white radiation synchrotron topography is very simple. The radiation propagates in an evacuated beam pipe and passes through a beryllium window. A collimator and scatter shield is used to limit the beam size. A schematic representation of a collimator successfully employed is shown in fig.2.17.The beam first passes through a hole drilled in a lead block. It then passes through a slightly wider aperture in steel and finally through a hole in an aluminium plate. The aluminium and steel absorb the scattered and fluorescent radiation from the lead collimator. Anything placed in a synchrotron beam will scatter radiation, hence it is important that the scatter shield does not cut into the main beam.

Due to the almost complete polarisation of the beam, wherever possible the crystal is orientated so that diffraction takes place in the vertical plane. This maximises the intensity of the diffracted beam. Rotation of the specimen about a horizontal axis normal to the beam is sufficient to choose the desired Bragg planes and wavelength.

The crystal is positioned in a laser beam which has previously been aligned with the synchrotron beam. The crystal can be mounted on a standard X-ray goniometer head or on a simple sample holder. It is preferable to mount the crystal on a plastic support. If a metal support is used and cuts into the synchrotron beam unwanted scatter will result in fogging of the nuclear emulsion plates. For optimum resolution care should be taken to ensure the nuclear

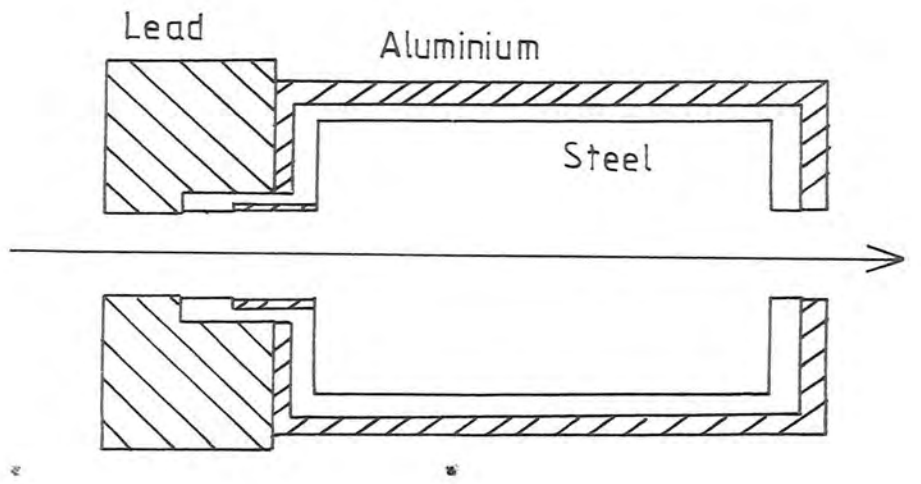

Fig. 2.17 Collimator and Scatter Shield

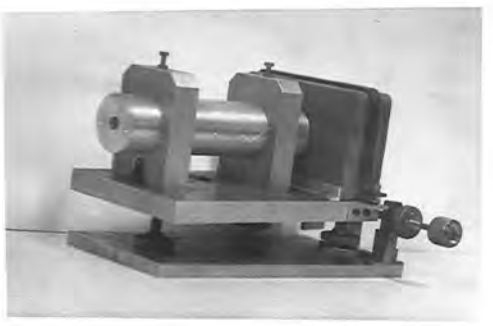

Collimator Constructed for use at DESY

emulsion plates are perpendicular to the required diffracted beam. If several reflections are required it is not possible to have the emulsion perpendicular to all the diffracted beams. Under these circumstances very thin, 10 micron, emulsions are used. The increased exposure times compared with those achieved with the usual 25 micron emulsions is more than compensated for by obtaining several usable reflections at once.

2.7 Cryogenic Topography

Many materials undergo phase transitions below room temperature. X-ray topography is one technique which may usefully be used to study these transitions. The first low temperature X-ray topography experiment was performed by Saito et al. (1966) using the Berg-Barrett technique to observe antiferromagnetic domains in CoO. They employed a specially designed cryostat with the goniometer acting as a cold finger. A plastic window allowed X-rays to reach the sample and enabled the specimen chamber to be evacuated to improve thermal insulation. This cryostat using liquid air as a coolant was capable of reaching an estimated temperature of 123K. Mathiot et al. (1973) employed a cryostat designed by MERIC of Arpajon, France, to perform topographic experiments down to 4·2K. Safa (1977) and Tanner et al. (1977) describe four cryostats successfully employed. Three of these cryostats, two with significant modifications, have been used in this work and will be described in some detail.

The fourth cryostat was a thin walled, narrow tailed glass immersion cryostat designed for use at a fixed temperature. The narrow

tailpiece was a requirement to enable the cryostat to be placed in the narrow gap between the pole pieces of an electromagnet. X-ray absorption in the glass walls of the cryostat and in the liquid nitrogen resulted in a reduction in the intensity of the diffracted beam by a factor of about twenty. The cryostat was thus suitable for use only with synchrotron radiation.

2.7 a Polystyrene Immersion Cryostat

The simplest cryostat employed has been an expanded polystyrene trough with a mylar window to facilitate alignment of the crystal. This cryostat was employed for stress experiments on $KCoF_3$ which will be described later. The sample can either be held by an external support or on a support held within the cryostat.

Essentially the cryostat operates only at fixed temperatures. The fixed temperature can be changed by changing the cooling agent. The cryostat suffered from a fairly high boil off rate and required topping up every twenty minutes, however with the high intensity of synchrotron radiation it was possible to obtain several topographs in the time. The relaxation of geometrical constraints for synchrotron topography enabled this crude cryostat to be used without serious loss of resolution, in spite of the high scatter from the liquid nitrogen causing rather large (10-20 cm) specimen to plate distances to be used. This high scatter makes the use of small Bragg angles undesirable. The tunable nature of synchrotron radiation allows a suitable wavelength to be chosen to give the desired Bragg angle. The attenuation

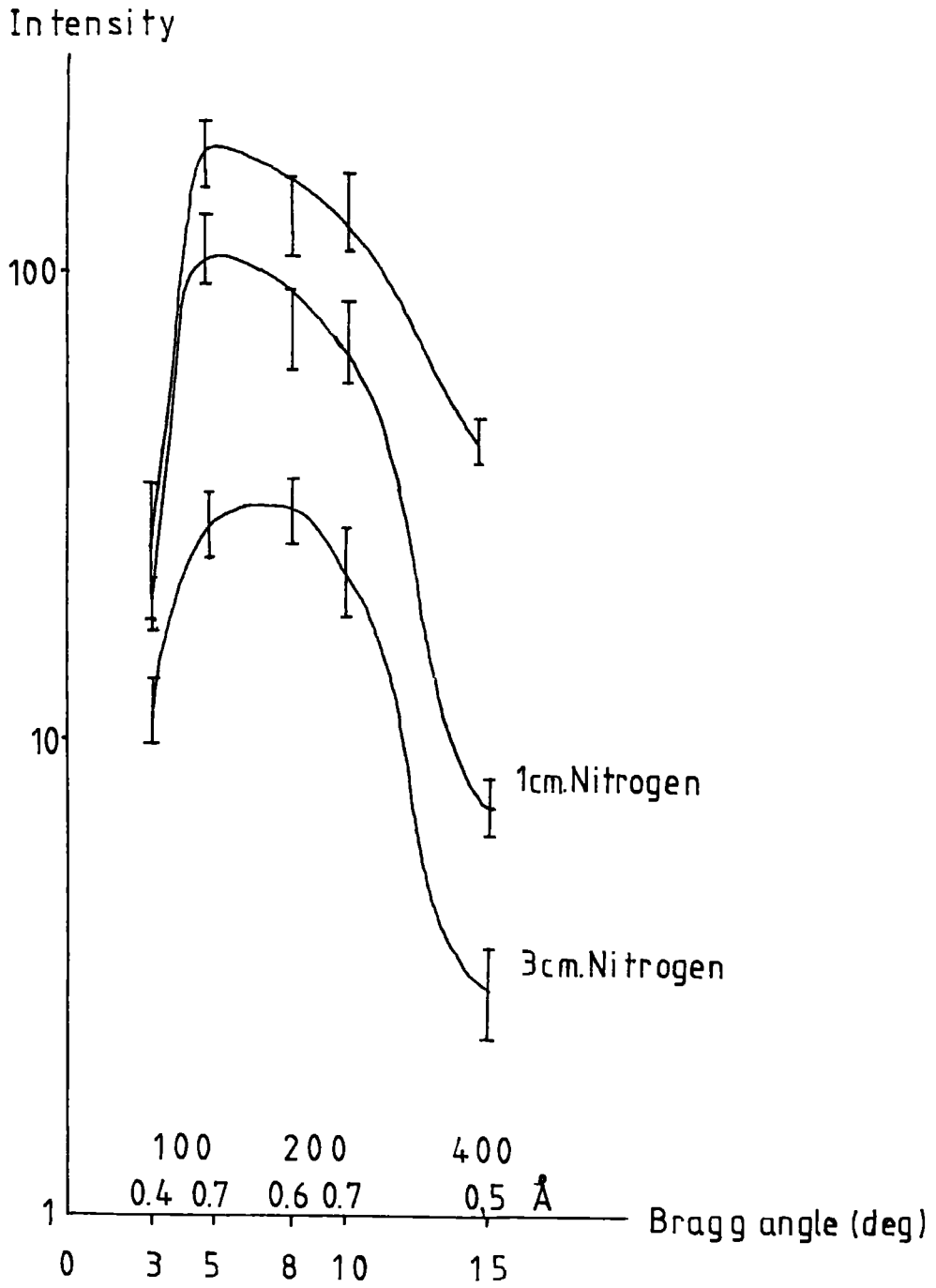

Fig. 2.18 Liquid Nitrogen Absorption (after Tanner et al. 1977)

of the X-ray beam by 3cm of liquid nitrogen is typically by a factor of about five, while the expanded polystyrene gives very little attenuation, hence the overall attenuation is not unacceptable, see fig 2.18.

This cryostat was also employed for rocking curve experiments on $KCoF_3$ using the Lang camera and rotating anode X-ray source. The intensity available was sufficient for this purpose although it was insufficient for Lang topography. Here the exposure times would have been impossibly long and the resolution achievable would not have been acceptable.

2.7 b Glass Cryostat with Cold Finger

This cryostat was designed by Midgley (1978) and has been modified by the inclusion of a new tailpiece and cold finger sample holder. These modifications were carried out in order to enable the experiments on terbium to be performed. The design of the MERIC cryostat described in the next section, made it impossible to obtain a diffracted beam for any Bragg reflection of reasonable intensity with the available characteristic wavelengths.

The cold finger is connected through a glass to metal seal to a reservoir of liquid nitrogen. Wrapped around the cold finger is a heating coil to enable the temperature to be varied. Temperature measurement is achieved via a silicon diode thermometer mounted on the cold finger as near to the sample as possible. The specimen is mounted on a metal screw to enable it to be rotated in the vertical plane. A thin walled, circular perspex tailpiece

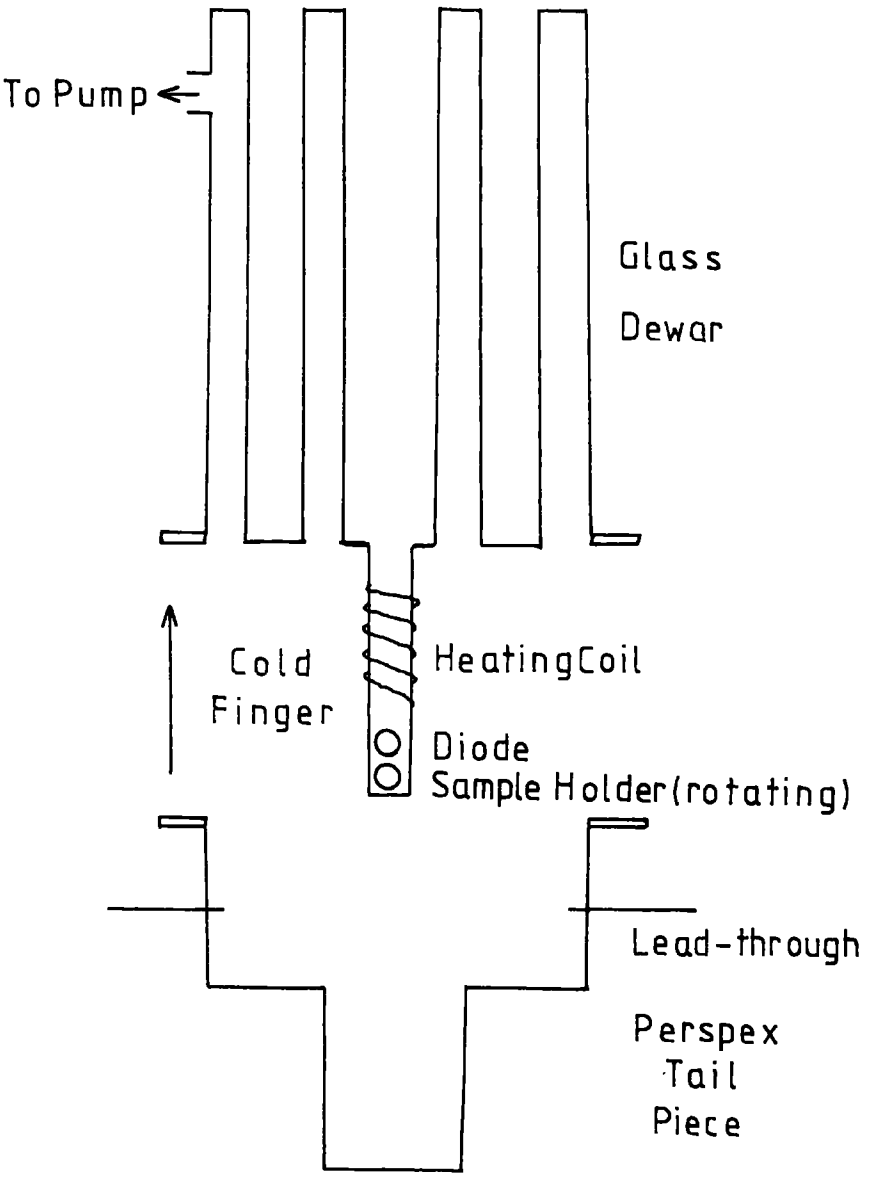

Fig. 2.19 Glass Cryostat with Cold Finger

surrounds the sample and cold finger. The sample chamber thus formed is connected to the dewar wall and the whole of this enclosure can be continuously pumped in order to reduce heat loss. The cryostat is shown schematically in fig. 2.19. The lowest temperature recorded is 135K.

The perspex tailpiece contains four epoxy sealed lead-throughs to permit current to be applied to the heating coil and to enable the temperature to be measured. The thin walls of the tail-piece enabled the incident and diffracted beam to pass through at any desired angle. For surface reflection from the terbium sample this was more convenient than using mylar windows in a glass tail-piece. The intensity of the diffracted beam with copper K_α radiation was reduced by a measured factor of about three by passage through the perspex.

The difference in temperature of the sample to that measured by the thermometer is estimated to be less than 0·5K. This estimate is based on the close agreement of the Curie temperature between different experimental runs, betweens runs on cooling and warming through the Curie temperature and the agreement of this temperature with that measured by other techniques Palmer (1979) Crangle (1979). In addition the splittings recorded at particular temperatures for different specimen mountings and for cooling and warming to those temperatures were in good agreement.

2.7 c MERIC Cryostat

This variable temperature cryostat was designed and

manufactured by MERIC specifically for Lang topography in the temperature range 2-300K. see fig 2.20. The cryostat consists of a central specimen chamber and reservoirs for both liquid nitrogen and liquid helium surrounded by the necessary vacuum jackets. Cooling is achieved by passage of helium gas drawn from the reservoir through a needle valve by a reciprocater pump. Temperatures above helium temperatures may be obtained by use of an electrical heater incorporated within the heat exchanger. Temperature stability can be within 0·02K. Temperature measurement and control is achieved via a gallium arsenide diode thermometer mounted on the specimen holder. The capacity of the helium reservoir is sufficient to maintain a temperature of 4·2K for about ten hours.

The tail of the cryostat containing the specimen is about $1\frac{1}{4}$ cm thick and two beryllium windows allow transmission of X-rays through the cryostat and crystal. When used for transmission Lang topography employing small Bragg angles it is possible to place the film and diffracted beam slits within 1 cm of the sample. When used in reflection Bragg angles in excess of 45^{o} must be used. The maximum angle between incident and diffracted beams which can be accommodated by the window is 90^{o}, hence difficulties can be and were, encountered when setting up such experiments.

The sample may be rotated through 360^{o} about the beam axis via a worm screw arrangement while maintained at a low temperature. This arrangement, although not very accurate, enables topographs of differing diffraction vectors to be taken without remounting or warming the crystal.

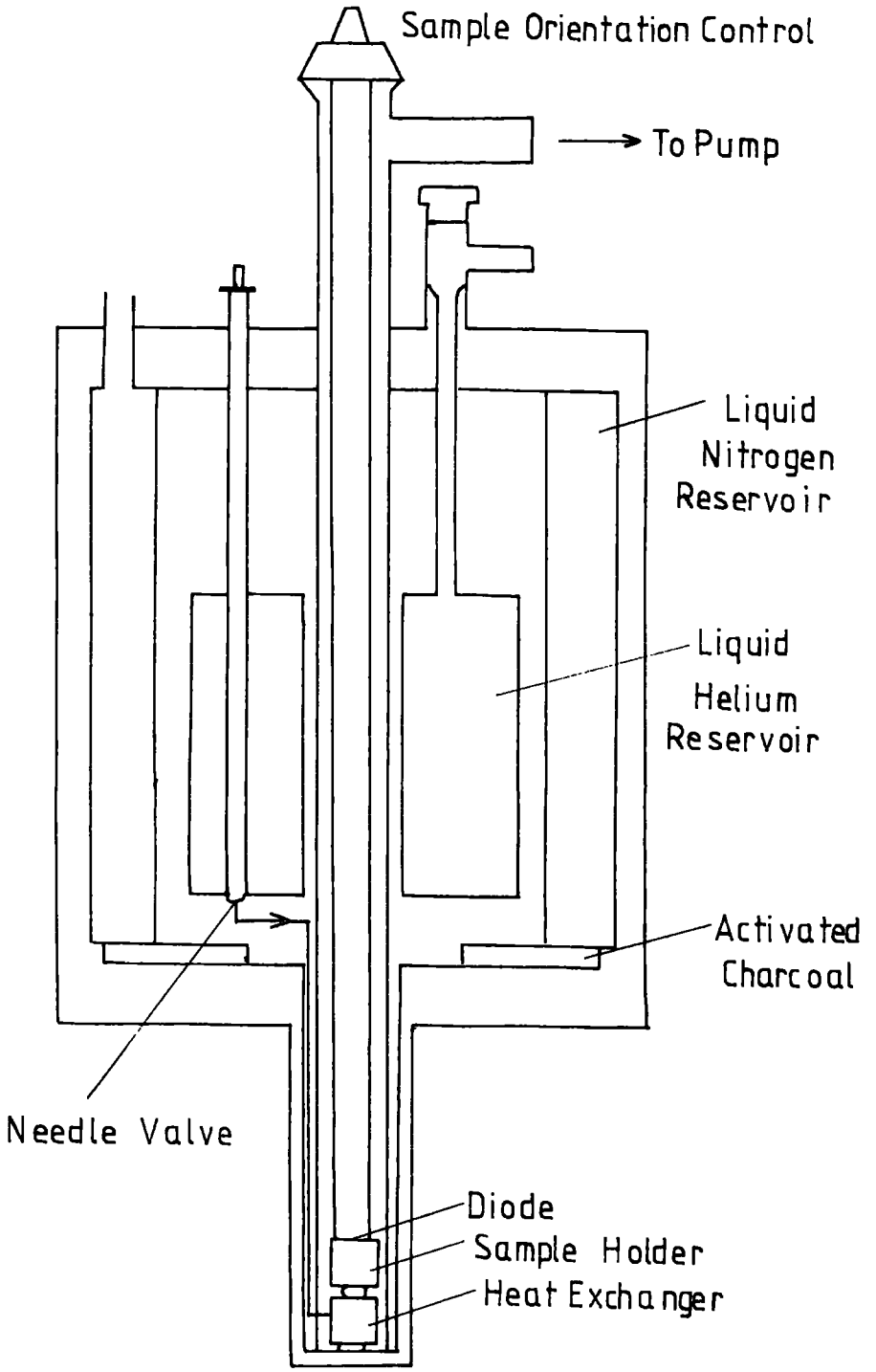

Fig. 2.20 MERIC Cryostat

2.8 Topographic Resolution

Several factors combine to determine the resolution achievable in X-ray topographs. These include the resolution achievable by the recording medium, (although with Ilford L 4 plates this is not a limiting factor) the geometrical resolution, resolution associated with the width of the X-ray line, resolution determined by the width of the dislocation images and the resolution associated with simultaneous diffraction of both K_{α} lines. The effects associated with the recording medium will be discussed in the next section. The resolution associated with any of the techniques can be degraded by vibration of the source, specimen or film hence it is essential to reduce all vibrations to a minimum.

The geometrical resolution associated with point source continuous radiation techniques is given by

$$\delta = \frac{SL}{D + L} \qquad (2.10)$$

where S is the source dimension,

L is the specimen to plate distance,

D is the source to specimen distance.

This can be arrived at by simple geometrical considerations of the arrangements shown in figs 2.3 and 2.4 for the Schulz and Guinier-Tennevin techniques and is applicable for synchrotron topography experiments. It results from the fact that X-rays from all points on the source are responsible for forming the image.

In the Lang technique no diffraction takes place in the vertical plane and resolution in the vertical direction is thus given by, (see fig 2.21)

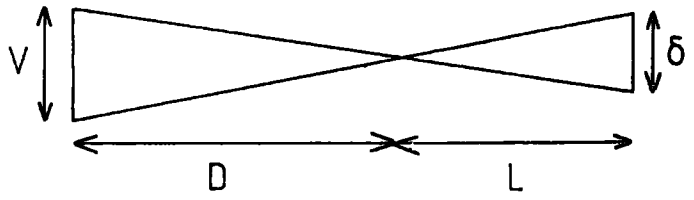

Fig. 2.21 Vertical Resolution Criteria

$$\delta = \frac{L\,V}{D} \qquad (2.11)$$

where V is the projected height of the source.

The effects of wavelength spread can be determined simply by differentiation of Braggs law.

$$\Delta\theta = \tan\theta \frac{\Delta\lambda}{\lambda} \qquad (2.12)$$

where $\Delta\lambda$ is the wavelength spread corresponding to the full width of the rocking curve at half of the maximum diffracted intensity. $\Delta\theta$ is the corresponding Bragg angle range. The image of a point on the crystal will then be spread over a distance.

$$\Delta x = L\Delta\theta \qquad (2.13)$$

This will be of most importance for large Bragg angles.

If simultaneous diffraction of both $K_{\alpha 1}$ and $K_{\alpha 2}$ lines occurs a double image will result. The displacement between these images is given by equation 2.13 where $\Delta\theta$ is now the difference in Bragg angles between the $K_{\alpha 1}$ and $K_{\alpha 2}$ lines. The angular separation of the diffracted beams between these two lines for any type of tube is between 10^{-3} and 10^{-4} radians. The separation between the two images is significant for the smallest specimen to plate distances, hence for high resolution work it is essential to ensure only one image is recorded.

The width of a dislocation image is an intrinsic property of the crystal. The perfect crystal reflecting range for symmetric

reflections is

$$\Delta\theta_{1/2} = 2C \frac{e^2}{m_0 c^2} \frac{(F_g F_{\bar{g}})^{1/2}}{\pi V \cos\theta} \lambda \qquad (2.14)$$

where C is a polarisation factor which is either 1 or $|\cos(2\theta)|$ for σ and π polarisation states

F_g and $F_{\bar{g}}$ are the structure factors of the g and $\bar{g}$ reflections

g is a reciprocal lattice vector and

V is the volume of the unit cell.

$\Delta\theta_{1/2}$ is typically 10^{-5} radians. The extinction distance is given by

$$\xi_g = \frac{2}{g \Delta\theta_{1/2}} \qquad (2.15)$$

hence for high resolution strong, low order reflections employing long wavelengths should be used.

2.9 Recording Media

2.9 a Photographic Emulsions

The most useful emulsions for high resolution X-ray topography are Ilford L 4 nuclear emulsions. These contain a very high concentration of silver halide so that high stopping power is achieved with minimum thickness. They are available in a variety of thicknesses. A thickness of 100 microns is required to absorb half the intensity of silver $K\alpha$ radiation and 25 microns for copper $K\alpha$ radiation. If the loss of resolution due to inclined rays is to be less than one micron then the emulsion must be within $\frac{1}{2}^\circ$ of perpendicular for 100 micron emulsions and 2° for 25 micron emulsions. In practice 50 micron

emulsions are employed for hard radiations because of the shorter processing times. Processing times for these thick emulsions are rather long. In order to obtain uniform development pre-soaking the emulsion and processing at low temperature is necessary. The process has been described in detail by Lang (1970).

The undeveloped grain size is about 0.15 microns and the developed grain size about 0.25 microns, well below the resolution limit of topography. The range of ionisation events for a photon varies from about one micron for CuK_α to three microns for silver K_α radiation. Statisical variations in the number of developed grains per unit area gives the image an apparent granularity. This granularity is worse for hard radiation than for soft radiation and, together with the ionisation spread determines the maximum enlargement of a topograph.

2.9 b Direct Viewing Systems

Several direct viewing systems have been developed in recent years to improve the time resolution of the topographic technique. The available systems have been reviewed by Hartmann (1977) and Green (1971, 1977).

Chikawa (1974) produced the following expression for the signal to noise ratio of an imaging system

$$R = \varepsilon C(\eta_0 V_p t)^{1/2} \qquad (2.16)$$

where ε is the dimension of the square picture element,

V_p is the number of photons per second per mm^2

η_o is the absorption efficiency of the X-ray sensitive layer,

t is the integration time,

C is the contrast of the defect

$$C = \frac{S_d - S_p}{S_p} \qquad (2.17)$$

where S_d is the signal level of the defect,

S_p is the mean signal level of each pixel of the perfect crystal.

Thus for high resolution we require:-

1. A high detection efficiency. Thick targets give a high absorption efficiency but are themselves responsible for a deterioration of resolution. Hence a compromise must be reached.

2. A long integration time will result in higher resolution. However this will be limited in the case of dynamical experiments.

3. A high X-ray intensity. The highest intensities currently available are from synchrotron sources.

There are two basic methods of direct imaging. The first method employs an X-ray sensitive vidicon which converts the topographic image into an electronic charge which can be read by a scanning electron beam. Systems of this type have been reported by Chikawa and Fujimoto (1968), Rozgonyi et al. (1970) and Chikawa (1979).

Chikawa's system employs a vidicon with a 15 micron thick lead oxide screen. The limiting spatial resolution is about 25 microns. In order to obtain Lang topographs an electronic slit is moved in synchronism with the crystal traverse mechanism.

Rozgonyi's system employs a target containing a silicon diode array and is capable of achieving a 15 micron spatial resolution, but has very poor efficiency for hard radiation.

The second imaging technique employs multiple stage imaging. The X-ray image is first converted into visible light by a fluorescent screen. This image is then optically coupled by a lens or fibre optic plate to the photo cathode of a low light level camera. Optical magnification occurs at this stage otherwise the limiting resolution would be that achievable by the camera.

Hashizume et al.(1971) were the first to use such a system with good spatial resolution employing a screen of Zn S and (Zn,Cd) S activated by Ag with a fibre optically coupled orthicon tube. The spatial resolution was limited by the fluorescent screen. Reasonable resolution could only be achieved by detecting a magnified X-ray image at some distance from the crystal, produced by placing the crystal very near to a point source.

Hartmann et al. (1975) reported on a similar system, however by employing a very thin phosphor of $Zn_2 Si O_4$ 10-15 microns thick with a very small particle size, 2 microns, they were able to achieve a resolution of about 10 microns. Problems due to the low absorption of the screen have since been reduced by employing rare earth oxysulphide phosphors. Electronic image processing has been incorporated into this system and enables spatial resolution to be improved at the cost of time resolution.

CHAPTER THREE

Diffraction Theory and Contrast Mechanisms

CHAPTER THREE

Diffraction Theory and Contrast Mechanisms

3.1 Introduction

The X-ray topography techniques described in the previous chapter are used for the study of nearly perfect crystals. The techniques rely on the difference in the X-ray intensity diffracted by deformed and perfect regions of the crystal. Very simply it can be seen how dislocations are imaged through Bragg's law

$$\lambda = 2d \sin\theta \qquad (3.1)$$

If a perfect crystal is set to diffract monochromatic radiation, then for a strong diffracted beam to emerge the above expression must be satisfied. If the crystal contains a defect where the spacing of the lattice planes, d, or the orientation of these planes varies locally, then the Bragg relation cannot be satisfied simultaneously for both the perfect and imperfect regions of the crystal. There will thus be a difference in the diffracted intensity between the two regions and an image of the defect will occur.

In order to interpret these images a knowledge of the theory of X-ray diffraction is required. There are two main diffraction theories; the approximate kinematical theory and the more fundamental dynamical theory.

3.2 Kinematical Diffraction Theory

The widely used kinematical diffraction theory is described in many texts, (e.g. James (1948), Cullity (1956) and Warren (1969). It assumes that the amplitudes of the scattered waves are small compared with the amplitude of the incident wave, i.e. the intensity of the incident X-rays falling on all the diffracting centres within the crystal are the same. Interactions between incident, and diffracted waves are neglected, resulting in a refractive index of unity. For very small crystals, or highly imperfect crystals where dislocations divide the crystals into a mosaic structure of small crystallites, the kinematical theory provides a satisfactory approximation which has been successfully employed in crystal structure determinations.

3.3 The Dynamical Diffraction Theory

In large highly perfect single crystals the amplitude of a diffracted X-ray beam becomes comparable with the amplitude of the incident X-ray beam. It is then no longer possible to neglect the interactions within the crystal between these two beams and a dynamical approach to the diffraction theory must be undertaken.

A general introduction to the dynamical theory may be found in books by James (1948), Zacharieson (1945) and Warren (1969). Batterman and Cole (1964), give a detailed mathematical treatment applicable in the X-ray case. Authier (1970), Balchin and Whitehouse (1974) and Tanner (1976), give specific reviews

relating to the interpretation of X-ray topographs. Other reviews relating to this topic are in the proceeding of a Nato A.S.I. edited by Tanner and Bowen (1980).

The theory of dynamical diffraction was put forward by Darwin (1914, 1922) and is formally identical to the theory developed by Ewald (1916, 1917) and Von Laue (1931).

The problem is to solve Maxwell's equations in a three dimensional medium with periodic susceptibility with the solutions inside the crystal matched to the boundary conditions on the crystal surface.

The Laue equation relates the diffracted beam wave-vector $\underline{K}_g$ to the wave-vector of the incident beam, $\underline{K}_o$ in reciprocal space via a reciprocal lattice vector $\underline{g}$

$$\underline{K}_g = \underline{K}_o + \underline{g} \qquad (3.2)$$

We expect solutions of Maxwell's equations for the electric displacement $\underline{D}$ to consist of linear combinations of transverse waves of the form

$$\underline{D} = \sum_g \underline{D}_g \exp(-2\pi i \underline{K}_g \underline{r}) \exp i\omega t \qquad (3.3)$$

This expression represents a superposition of plane waves which form a wavefield. The waves must reflect the periodicity of the lattice and hence the wave-vectors must be related by reciprocal lattice vectors. This type of wave is known as a Bloch wave.

In X-ray diffraction usually only two waves have significant amplitudes; the refracted wave $\underline{K}_o$ and the Bragg reflected wave $\underline{K}_g$, equation 3.3 then reduces to

$$\underline{D} = \exp i\omega t [\underline{D}_o \exp(-2\pi i \underline{K}_o \underline{r}) + \underline{D}_g \exp(-2\pi i \underline{K}_g \underline{r})] \qquad (3.4)$$

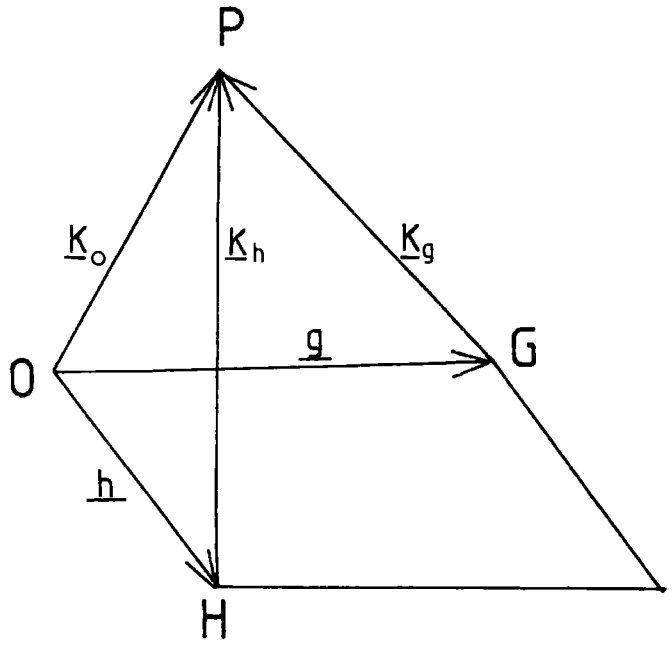

Fig 3.1 Tie-point Construction in Reciprocal Space

3.3 a Tie-Points

Equation 3.2 shows that all the wave-vectors of a wave-field within a crystal can be deduced from one another by translations equal to reciprocal lattice vectors. If these are drawn (fig 3.1) they define a common point referred to as the tie-point which characterizes the wavefield geometrically.

3.3 b Dispersion Surface

Substitution of equation 3,4 into Maxwell's equations and solving for non-zero values of the incident and diffracted beam wave amplitudes taking into account the periodicity of the lattice yields

$$\alpha_o\alpha_g = \tfrac{1}{4}kC^2 X_g X_{\bar{g}} \qquad (3.5)$$

where $\alpha_o = \frac{1}{2k}[\underline{K}_o\underline{K}_o - k^2(1 + X_o)]$

$\alpha_g = \frac{1}{2k}[\underline{K}_g\underline{K}_g - k^2(1 + X_o)]$

and C is a polarization factor. $C = \underline{D}_\sigma\underline{D}_g = 1$ for σ polarization and $C = \cos 2\theta$ for π polarization.

Equation 3.5 links the incident and diffracted beam wave-vectors within the crystal and as such is the equation of the locus of the incident beam wave-vectors which give rise to a diffracted beam passing towards G and approximately satisfying the Bragg condition, i.e. the locus of the tie-point, which is known as the dispersion surface.

If k is the vacuum wave-vector then the incident beam

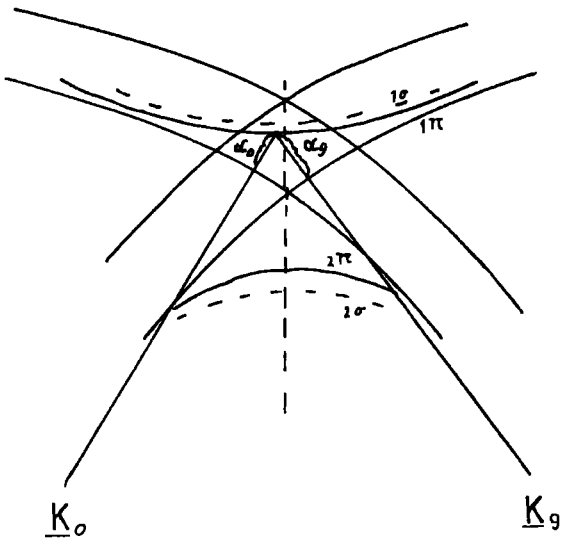

Fig 3.2 Dispersion Surface Construction

wave-vector is the product of the vacuum wave-vector and the refractive index

$$|K_o| = k(1 + \tfrac{1}{2}\chi_o) \qquad (3.6)$$

The intersection of the dispersion surface with the plane of O and G is a hyperbola. The dispersion surface being a hyperboloid Away from the Laue point there is only one wave excited in the crystal, the tail of its wave-vector $\underline{K}_o$ will fall on the sphere about O of radius $|K_o|$. When strong diffraction occurs equation 3.5 defines the relation between $\underline{K}_o$ and $\underline{K}_g$ thus the tail cannot lie on the spheres. This is shown in fig 3.2 where α_o and α_g are shown as the distances between the dispersion surface and the spheres of radii $|K_o|$ along the wave-vectors. The asymptotes of the dispersion surface are tangents to the spheres centred on O and G. Near to the Laue point the degeneracy of the dispersion surface is raised by the crystal potential and there are two branches for each polarization state with component waves either in or out of phase.

3.3 c Boundary Conditions

In order for the wave to propagate across the crystal boundary constraints must be imposed on the frequency, amplitude and wave-vector. The most important constraint is the continuity of the tangental component of the wave-vector. This implies the tie-points excited by an incident wave must lie on a normal to the crystal surface. Each plane wave excites two tie-points, fig 3.3a shows the situation for Laue geometry and fig 3.3b for

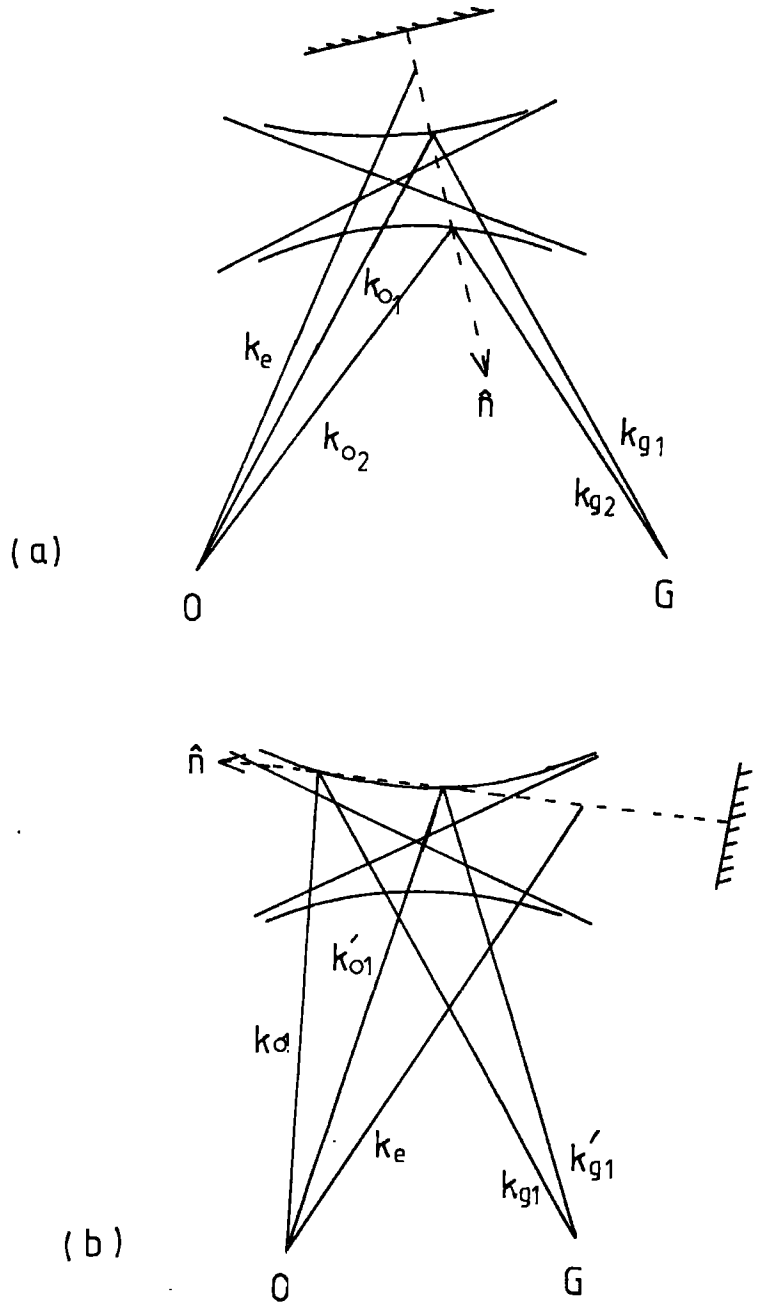

Fig 3.3 (a) Laue (b) Bragg Geometry

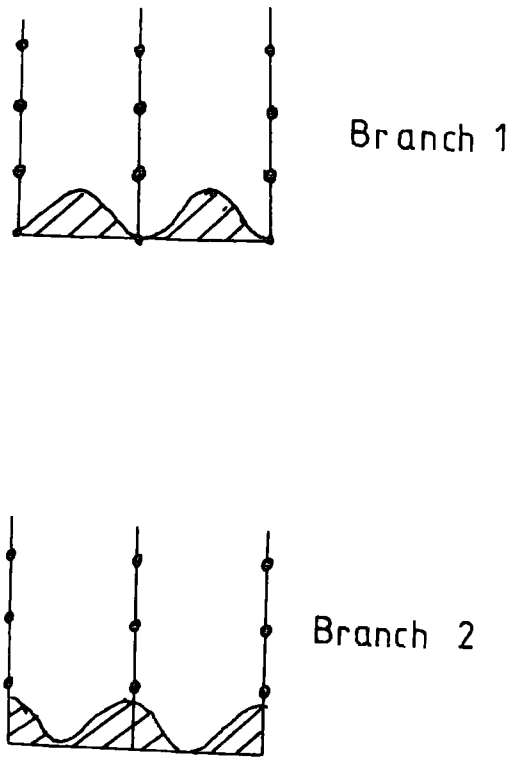

Fig 3.4 Intensity of Wavefields

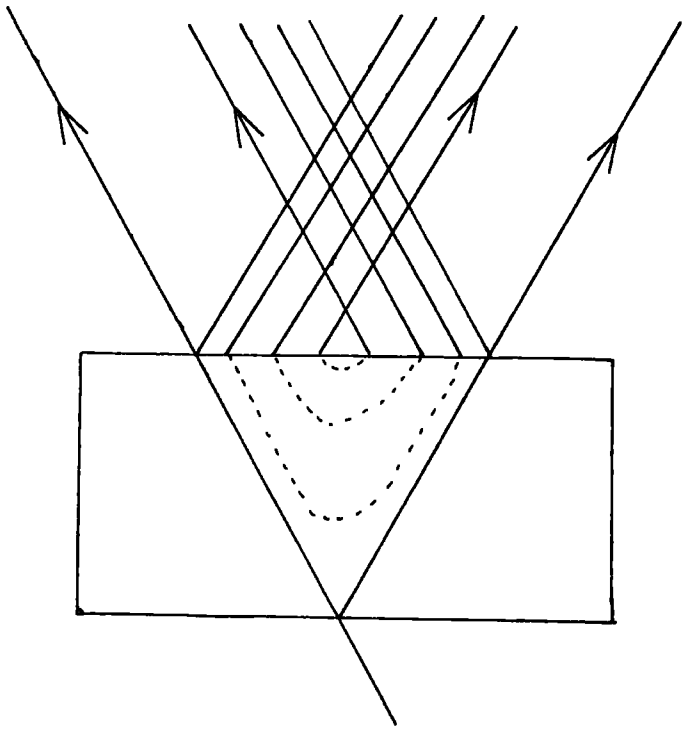

Fig 3.5 Propagation of Wavefields

Bragg geometry. The tie-points excited are on the dispersion surface where the normal to the surface defined by the tip of the incident beam wave-vector cuts the dispersion surface. When the beams reach the exit surface the two waves are decoupled giving rise to four external beams which have been seen experimentally by Authier (1961).

The second constraint relates to the amplitudes of the waves. In the X-ray region the refractive index of the crystal is close to unity, hence refraction at the boundary can be effectively ignored. The third constraint is the continuity of frequency which is implicit in the theory.

3.3 d Anomalous Transmission

Rewriting equation 3.4 and neglecting time dependence we can obtain the following expression for the intensity of the Bloch wave

$$I = D^2 = D_o^2[1 + R^2 + 2RC\cos(2\pi \underline{g}.\underline{r})] \quad (3.7)$$

where

$$R = \frac{D_g}{D_o}$$

The intensity is modulated by the cosine term which has a maxima at $\underline{g}.\underline{r} = n$ and minima at $\underline{g}.\underline{r} = (2n+1)/2$ with n integral. $\underline{g}.\underline{r} = n$ corresponds to a plane of atoms. The sign of R determines whether maxima occurs on a plane of atoms or minima. See fig 3.4.

Absorption will be greater for a Bloch wave having intensity maxima at the atomic planes for example in fig 3.4 the branch 2 wave will be more strongly absorbed than the branch 1

wave. This is known as the Borrmann effect. In a thick crystal of NaCl it is possible for the 1 0 polarized waves, (where the polarization is perpendicular to the incident plane), to be transmitted when the product of the average linear absorption coefficient and thickness of the sample is over 30. The presence of defects within the crystal will however destroy the effect.

3.3 e Pendellösung Fringes

In practice the incident beam divergence is usually large compared with the perfect crystal reflecting range. This implies that even in a section topograph it is not possible to treat the incident beam as a plane wave. The divergence of the beam thus causes all the tie-points on the dispersion surface to be excited simultaneously and X-rays propagate along all the paths within the Borrmann triangle, fig 3.5, with two wavefields, (one from each branch), propagating along any direction. Interference between the wavefields results in Pendellösung fringes due to the phase differences between the waves arriving at any point on the exit surface.

3.4 Contrast Mechanisms

Two types of contrast mechanisms can be observed in X-ray topographs. The first orientation contrast can be interpreted through simple geometrical relations, (Wu and Armstrong, 1975, Armstrong 1980). The second extinction contrast, can only be

interpreted via dynamical diffraction theory. It arises from variations in the diffracted beam intensity from the vicinity of an imperfection.

If a crystal is set to diffract a low divergence, monochromatic X-ray beam then no diffraction will occur from any region of the crystal mis-orientated by an angle greater than the divergence of the X-ray beam. This variation in diffracted beam intensity is known as orientation contrast. Orientation contrast is also visible in monochromatic divergent and continuous beams. In these cases the directions of the diffracted beams from any mis-orientated regions differ from that of the perfect crystal. Then if the film is placed sufficiently far from the crystal spatial overlap or separation of the beams results in enhanced or reduced intensity corresponding to the mis-orientated beams.

Authier (1967, 1970) described three types of images which contribute to the contrast of a dislocation. These are shown in fig 3.6.

3.4 a Direct Image

In fig 3.6 the direct beam cuts the dislocation at D In the vicinity of the dislocation there is a deformation of the lattice. Any X-ray source has a natural line width hence part of the spectrum not diffracted by the perfect crystal will be diffracted by the strained region provided that the effective mis-orientation is less than the beam divergence and greater

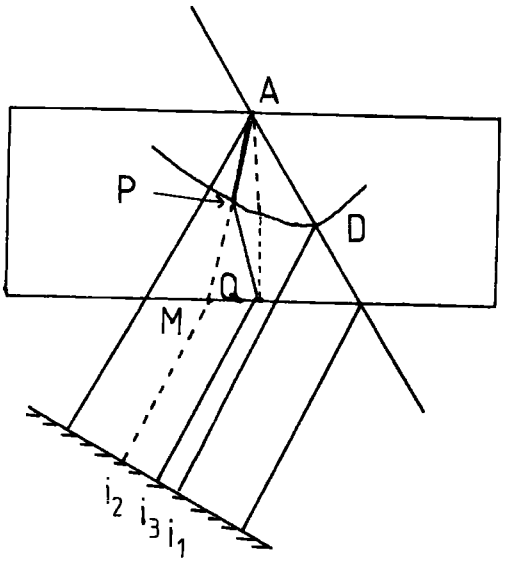

Fig 3.6 Image Formation

i_1 Direct

i_2 Dynamical

i_3 Intermediary

than the perfect crystal reflecting range

$$\Delta\theta_{\frac{1}{2}} = \frac{2 r_e \lambda^2 C (F_g F_{\bar{g}})^{\frac{1}{2}}}{\pi V \sin 2\theta} = \frac{2}{g \xi_g} \qquad (3.8)$$

Where r_e is the classical electron radius, V is the volume of the unit cell and ξ_g is the extinction distance.

This diffracted beam is received at i_1 and is known as the direct image. It is superimposed on the perfect crystal background hence the contrast appears dark. Under low absorption conditions most images are of this form.

Dislocations are in general invisible if $\underline{g}.\underline{b} = 0$. If $\underline{g}.\underline{b} \geq 2$ they can show double contrast. $\underline{g}.\underline{b} = 0$ implies the effective mis-orientation of the dislocation is zero. For a pure edge dislocation an additional second criterion is applicable that $\underline{g}.\underline{b} \times \underline{h} = 0$ where $\underline{h}$ is the line direction. If the dislocation is mixed complete invisibility never occurs.

3.4 b Dynamical Image

If a wavefield propagating along AP cuts a dislocation at P new wavefields will be excited with waves propagating along AM and PQ. Hence only part of the energy propagating along AP will propagate along PM resulting in a dynamical image at i_2 with reduced intensity.

3.4 c Intermediary Image

Wavefields created by interbranch scattering at P propagating along PQ give rise to an intermediary image i_3

These new wavefields interfere with the original wavefields resulting in oscillatory contrast.

3.5 Contrast of Magnetic Domains

Contrast of magnetic domains arises through magnetostrictive distortion and not via a direct interaction with the magnetization. It was first observed by Merz (1960) employing Berg-Barrett topography and later by Polcarova and Lang (1962) employing the Lang technique. It has been shown that domain walls are invisible if $\Delta \underline{M}.\underline{g} = 0$ this corresponds to the change in magnetization across a domain wall being perpendicular to the diffraction vector.

Polcarova and Gemperlova (1969) studied the contrast of domain walls theoretically showing that 90° walls were equivalent to a coherent twin boundary if the wall thickness is neglected, (see fig 3.7). Since domain walls are imaged by magnetostrictive distortion 180° walls which have no magnetostrictive distortion associated with them are not usually visible. However Lang (1970) has shown that under certain circumstances relaxation of the lattice at the surface of a crystal along a 180° domain wall can make these walls visible.

Polcarova and Lang (1968) showed that domain walls appear as dark bands if $\Delta \underline{M}.\underline{g} > 0$ and light bands if $\Delta \underline{M}\underline{g} < 0$. The width of the wall image depends not on the domain wall width but on the tilt of the sample about the diffraction vector, (fig 3.8). The image width being $t \sin \delta$.

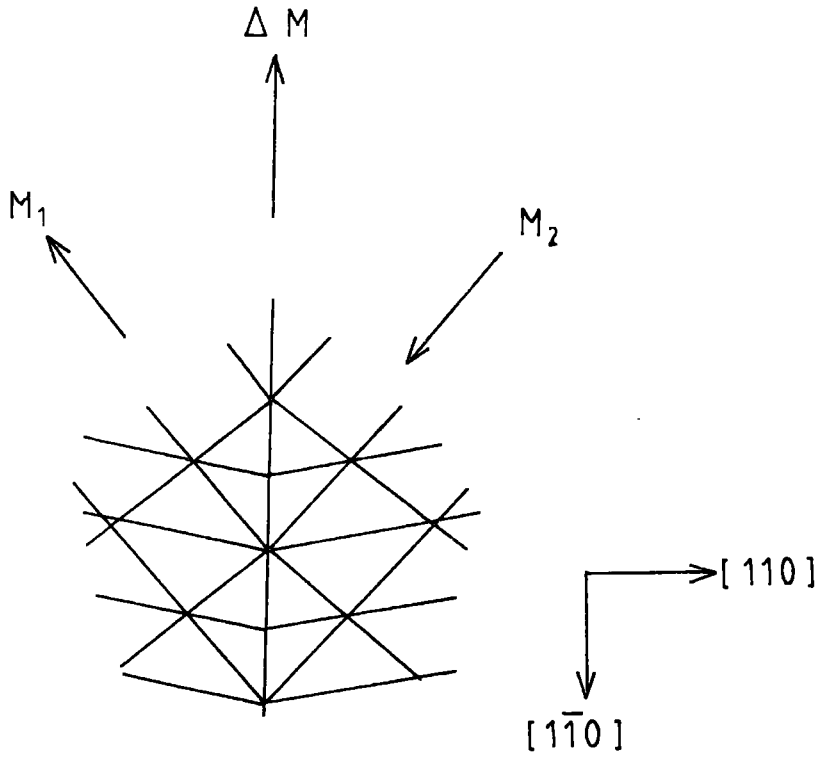

Fig 3.7 Model of a 90° Domain Wall

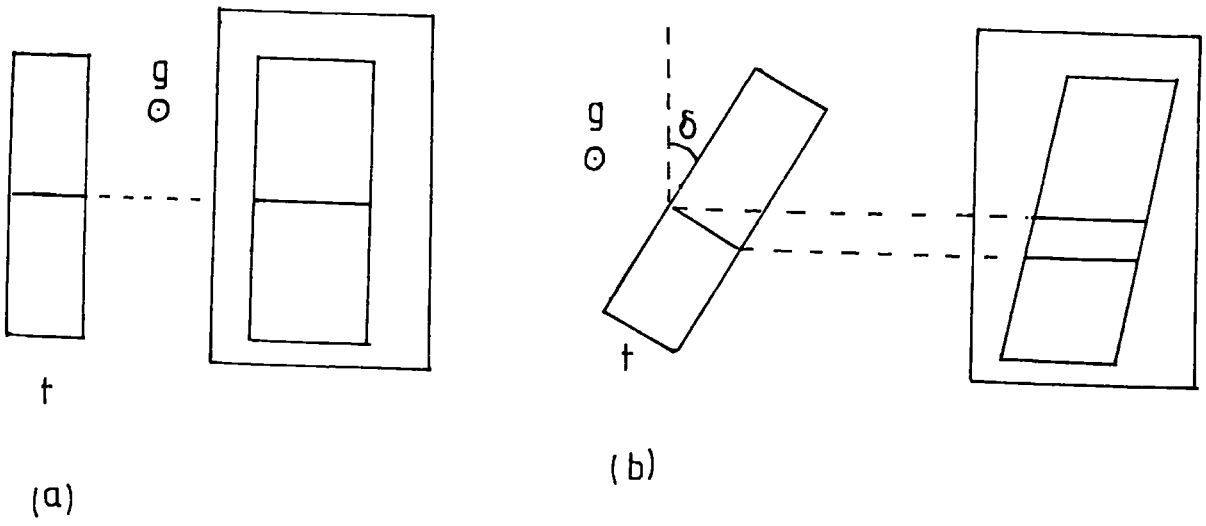

Fig 3.8 Domain Wall Image Widths

(Polcarova 1969)

Two types of contrast mechanisms enable magnetic domains to be imaged. If the magnetostriction is large,orientation contrast is observed if the mis-orientation across the boundary is greater than the beam divergence. If the mis-orientation is less than the beam divergence but greater than the perfect crystal reflecting range, the wavefields will decouple on crossing the wall and new wavefields will be excited. This results in a net change in intensity due to movement of the tie-points or in an interference effect between the newly created waves.

CHAPTER FOUR

Crystal Perfection Studies of Flux Grown Rare-earth Germanates ($R_2Ge_2O_7$)

CHAPTER FOUR

Crystal Perfection Studies of Flux Grown Rare-earth Germanates ($R_2Ge_2O_7$)

4.1 Introduction

The flux growth of single crystals of rare-earth germanates was first reported by Wanklyn (1973) from a flux of R_2O_3, PbO, PbO_2, GeO_2 and PbF_2, where R is a rare-earth (Tb to Lu). The flux was subsequently modified, Wanklyn (1978), to contain an excess of GeO_2 and MoO_3 was added. This reduced the rate of flux evaporation allowing crystals to be grown by slowly cooling the melt. Large crystals of $R_2Ge_2O_7$ were obtained up to $3x3x3mm^3$ and basal plates up to $5x5x1mm^3$ many of which were free from visible inclusions. Earlier work by Glushkova et al. (1967) and Bondar et al. (1970) on sintered samples indicated that the system contained three phases R_4GeO_8, R_2GeO_5 and $R_2Ge_2O_7$. Which phase is produced depends on the relative concentration of PbO and GeO_2. Work by Smolin (1970) indicated that $R_2Ge_2O_7$ crystals are tetragonal and should be optically active from its space group and are thus possible replacements for calcite in polarizers.

The presence of rare-earth atoms suggests that magnetic phase transitions should occur. The transition temperatures have been measured by Cooke et al. (1973) and are shown in table 4.1.

Table 4.1

Magnetic transition temperatures T(K)

Compound	T(K)
$Tb_2Ge_2O_7$	2.05 ± 0.05
$Dy_2Ge_2O_7$	2.15 ± 0.05
$Ho_2Ge_2O_7$	1.45 ± 0.05
$Er_2Ge_2O_7$	1.15 ± 0.05
$Tm_2Ge_2O_7$	
Dy_2GeO_5	2.5 ± 0.1
Ho_2GeO_5	
Er_2GeO_5	1.25 ± 0.1

After Cooke et al.(1973)

4.2 Experimental Procedures

Attempts were made to employ the Lang technique, described in chapter two, to image some of the as grown crystals of plate-like habit selected on the basis of optical perfection. These crystals were examined without cutting or polishing. Due to the thickness of these crystals and the presence of heavy elements the product of absorption coefficient and thickness, was from 2 to 10 for AgK_{α} radiation.

All the crystals examined were bent and only the crystal shown in fig 4.1 was sufficiently uniform for Lang topography and here only one reflection could be obtained. Attempts to employ a Bragg angle controller were also unsucessful due to the large amount of bending about two orthogonal axes. However assessment of these crystals was still possible by means of synchrotron X-ray topography, described in chapter two. The continuous nature of the synchrotron radiation enables each point on the crystal lattice to select its own wavelength enabling images of the entire crystal to be obtained in a very short time. In addition, numerous reflections were recorded at once (see fig 2.16). It was thus possible to examine a large number of crystals in a very short time.

The crystals were also studied with an optical microscope with light transmitted through the crystals and reflected from the crystal surfaces in order to examine the crystals for flux inclusions.

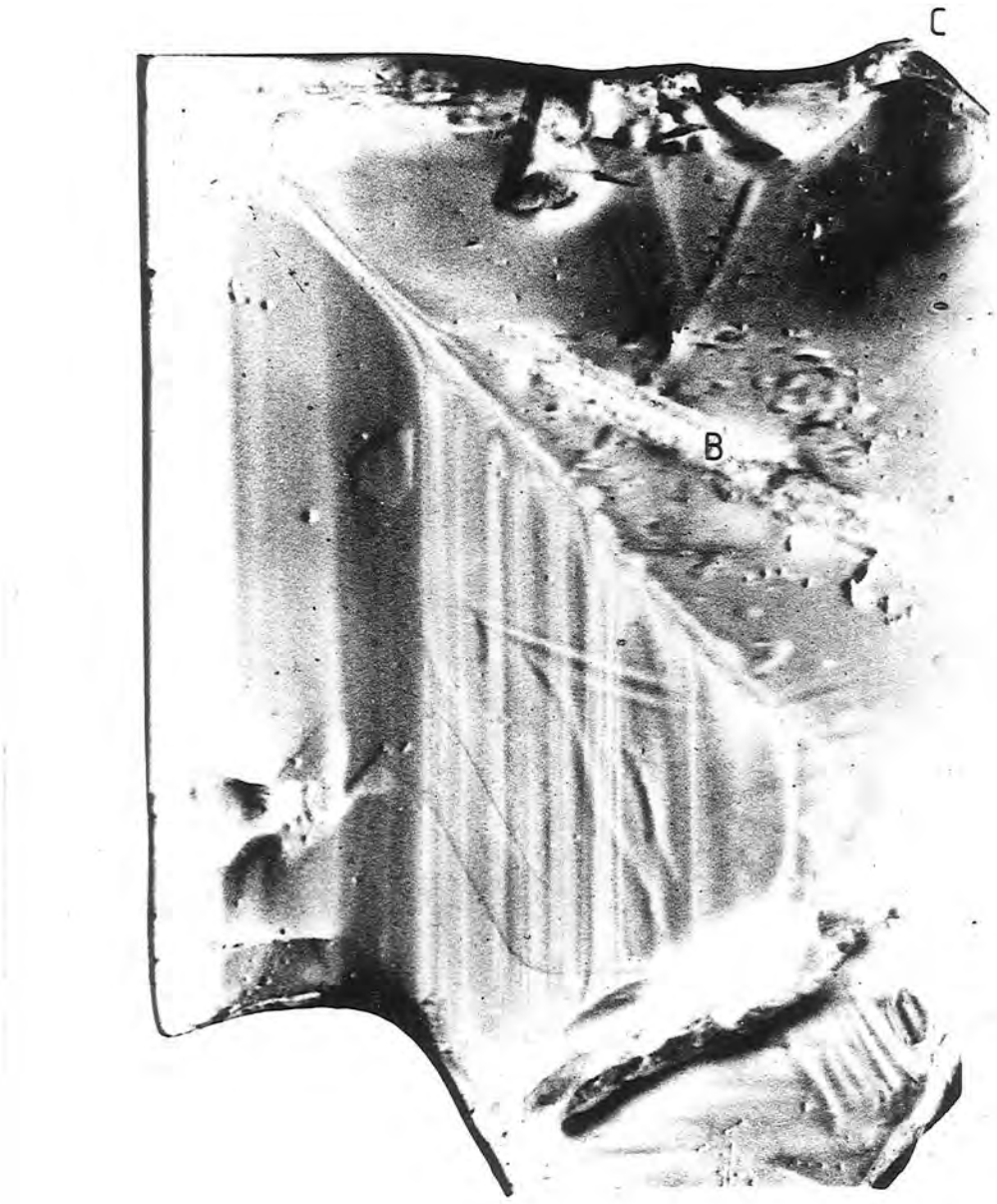

Fig 4.1 Lang Topograph of $Tb_2Ge_2O_7$ 400 Reflection Ag K_{α}

Fig 4.2 Synchroton Topograph of $Tb_2Ge_2O_7$

(DESY 7Gev 9ma 6min 10μm L 4)

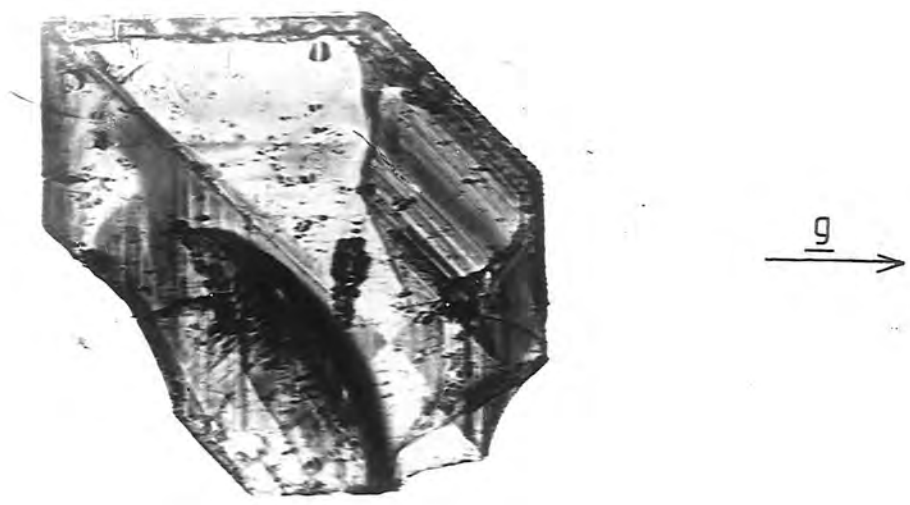

Fig 4.3 Synchrotron Topograph of $Tb_2Ge_2O_7$

Fig 4.4 Optical Micrograph of Flux Inclusions on 110 Growth Sector Boundary

growth occurred on all four $\{100\}$ faces leading to rectangular crystals with a central nucleus. It is assumed that in this crystal, nucleation took place near to the crucible wall resulting in two surfaces of the crystal being starved of solute.

Two distinct periods of growth were present in all crystals. Early growth was irregular resulting in strong growth banding, while latter growth was much more uniform. The boundary between the two regions is abrupt and the contrast near the growth sector boundary is interesting because the growth banding is curved suggesting that growth took place simultaneously on (100) and $(1\bar{1}0)$ faces.

Flux inclusions have been seen optically in this crystal. These inclusions are visible along the growth sector boundary and correspond to the precipates visible in the topograph. Flux inclusions are more pronounced where abnormalities in growth have occurred along growth sector boundaries, along growth bands, where the growth banding is curved and at C where rapid growth has taken place in the $[1\bar{1}0]$ direction.

Figures 4.2 and 4.3 are synchrotron X-ray topographs of another crystal of $Tb_2Ge_2O_7$. Growth initially took place at equal rates on all four $\{100\}$ faces. However, after initial growth, growth abruptly started on the (110) face with a growth rate comparable to that on the $\{100\}$ faces. The growth sector boundaries for the (110) growth region are non-linear, hence growth must be energetically competitive on $\{100\}$ and $\{110\}$ faces. Flux inclusions along the growth sector boundary are visible optically, fig.4.4, it is thus possible that variations in the flux composition

4.3 Experimental Results

Figure 4.1 shows a transmission Lang topograph of a 200 micron thick crystal of $Tb_2Ge_2O_7$. This is a 400 reflection from the (001) surface sample recorded on a 50 micron Ilford L4 nuclear emulsion plate with AgK_α radiation. Under the high absorption conditions, $\mu t \simeq 4$, the presence of anomalously transmitted intensity is itself an indication of high lattice perfection. Strong growth bands are visible parallel to the [010] direction in one sector of the crystal, demonstrating that fluctuations in lattice parameter took place during growth due to variations in the growth conditions. The variation in growth conditions was probably a variation in impurity content caused by convectional movement of the solution, or may be associated with temperature fluctuations during the period of crystal growth.

The growth striations correspond with steps on the crystal surface which can be seen optically indicating that variations in the growth conditions affect the growth rate in the c-direction at least. Variations in the lattice parameter only occur normal to the growth front, hence in this reflection growth bending is not visible in sector B where growth took place along on the (010) surface. However in the 040 reflection synchrotron topograph growth bending is visible in this sector.

In this crystal, growth ocurred at equal rates on two of the {100} faces. In most of the crystals examined equal

led to $\{110\}$ growth becoming dominant.

Other samples with fewer or no flux inclusions have fewer surface steps and weaker growth banding. These samples were usually thicker and growth always occurred on the $\{100\}$ faces. It thus appears that large variations in the flux composition with the formation of precipitates and strong growth banding favours growth on $\{110\}$ faces, while small variations and weak growth banding favours growth on $\{100\}$ faces.

In all the crystals examined no definite identification of a dislocation has been made. The two curved lines of fig 4.1 may be dislocations. However the large unit cell and hence Burgers vector in this structure imply a high elastic line energy and it appears no growth accident was sufficiently energetic to favour the nucleation of dislocations.

Synchrotron X-ray topography has thus enabled rapid assessment of the perfection af a large number of crystals to be made and has shown that slow cooling of a fluxed melt has resulted in highly perfect crystals.

CHAPTER FIVE

Neutron Topography Studies of Holmium Gallium Garnet ($Ho_3Ga_5O_{12}$)

5.1 Introduction

5.2 Experimental Technique

5.3 Properties of Garnet Crystals

5.4 Holmium Gallium Garnet

5.5 Neutron Topography Results

CHAPTER FIVE

Neutron Topography Studies of Holmium Gallium Garnet ($Ho_3Ga_5O_{12}$)

5.1 Introduction

The technique of X-ray topography was initiated by Berg (1931) and has been used for indirect imaging of magnetic domains through lattice distortion, Polcarova (1969). The first neutron topography experiment of Doi et al. (1971) on strained germanium followed very much later. Neutrons however, due to their magnetic interaction with matter can directly image magnetic inhomogenities and Alperin et al. (1962) made a crude one-dimensional map of antiferromagnetic domains in MnF_2. Neutron topography was subsequently developed as a technique for directly studying magnetic domains and Ando and Hosoya (1972) studied spin density wave domains in antiferromagnetic chromium, while Schlenker and Shull (1973) used polarized neutrons to study ferromagnetic domains. Results obtained by using neutron techniques to study domains have recently been reviewed by Schlenker and Baruchel (1978).

Schlenker et al. (1974) noted that in all but a very few cases the absorption coefficient for neutrons is very small. Images of crystal defects in neutron topographs can thus be expected to be predominantly by direct contrast with kinematical diffraction theory applicable. Images are produced from the distorted region around the defect where the deviation from Bragg's law is of the

order of the Darwin width in the perfect crystal. This is identical to the low absorption X-ray case described by Authier (1966, 1967).

The low absorption coefficient for neutrons enables neutron topography to be used in transmission to study thick crystals and crystals containing heavy elements which could not be imaged by transmission X-ray topography. Baruchel et al. (1978) employed the technique to investigate natural lead carbonate and Schlenker et al. (1974) employed neutron and X-ray transmission topography to study dislocations and sub-grain boundaries in iron-silicon. Differences in the images between the two techniques were partly due to resolution, the neutron technique has poorer intrinsic and instrumental resolutions, and partly due to a difference in absorption conditions resulting in a reversal of the contrast between the two cases.

5.2 Experimental Technique

The principle of neutron topography is very simple and similar to that for transmission X-ray topography. A single crystal sample is set to Bragg reflect neutrons and a neutron sensitive photographic detector is positioned to pick up the diffracted beam and avoid the transmitted beam. The detector must be as near as possible to the crystal to minimize geometrical blurring of the image due to the angular divergence of the beam. White radiation neutron topography has been performed by Boeuf et al. (1975). This is similar to the white radiation X-ray technique described in chapter two. This has been modified by incorporating the technique

of magnetic neutron Laue patterns of Marmeggi et al. (1977) by Marmeggi and Baruchel the results of which have been reported by Schlenker and Baruchel (1978). This technique enabled several neutron topographs from magnetic reflections in nickel oxide to be recorded simultaneously. The monochromatic technique will be described in some detail with particular reference to the instrument built by Schlenker at the 'Institute Laue Langevin' in Grenoble France as this was the instrument employed in this work.

The initial source of neutrons is the high flux reactor. These are moderated by a thermal moderator resulting in a Maxwellian distribution of neutrons with a peak intensity at about 1.5 Å. These are passed down a curved thermal neutron guide-tube resulting in a beam free from fast neutrons and gamma-rays. The topography station is situated eight metres from the end of the neutron guide-tube downstream from three other instruments. The primary beam divergence is cut down to a few minutes of arc by slits associated with these instruments. The incident beam was monochromated by diffraction from a mosaic single crystal of copper about 5 mm. thick. The mosaic spread of this crystal was similar to the beam divergence. The 111 reflection was employed to select a wavelength of about 1.5 Å to give a maximum flux of neutrons. The wavelength chosen depended upon the peak intensity of the neutron flux and the wavelength selected from the flux by upstream monochromators. A monochromatic flux of 3×10^4 neutrons per cm^2 per sec was obtained.

The specimen axis, (second axis), was able to rotate

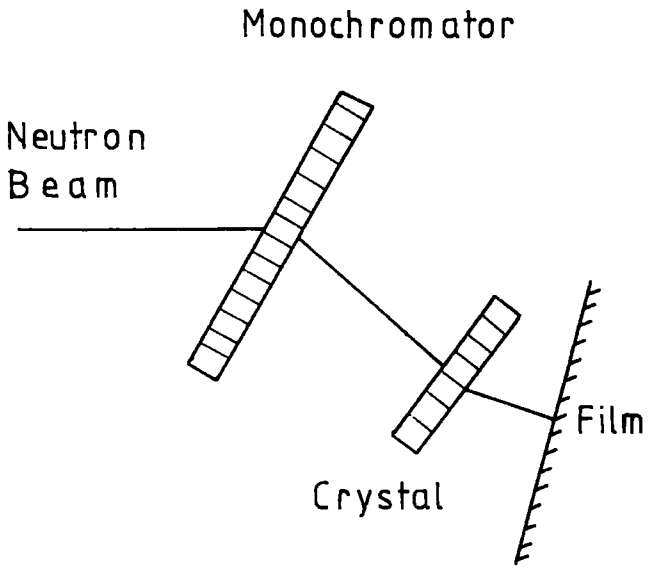

Fig. 5.1 Neutron Topography

about the monochromator axis and a standard neutron detector could rotate about the second axis. This detector, and associated counting electronics, were used to detect the first and second diffracted beams. Rotation of the axis anddetector and rotation of the second axis about the first axis were controlled by stepping motors to a precision of $\frac{1}{100}^{o}$. The arrangement is shown in fig 5.1.

Due to the low flux of neutrons the techniques for improving resolution employed in X-ray topography cannot be used as they would result in prohibitively long exposure times. The technique employed is thus analogous to the 'parallel' beam X-ray technique of Barth and Hosemann (1958). The monochromator provides a wide 'parallel beam' of neutrons with a beam divergence of several minutes of arc then for a specimen to plate distance of 10 to 20 mm a resolution of about 40 microns is achievable. Collimating slits are employed only to restrict the area of the beam to the area of the crystal of interest to reduce the background to a minimum.

Two types of photographic detector are employed;the first is a polaroid camera fitted with a LiF - ZnS phosphor screen, Wang et al. (1962), Smith (1962), which require an intensity of 3×10^5 neutrons per cm^2. This enables extremely quick exposures of very poor resolution to be obtained and is used simply to check the setting of the crystal.

The second detector consists of X-ray dental film backed by a gadolinium converter Berger (1971). The gadolinium captures neutrons and emits β particles which are recorded by the dental

film. Two types of dental film were employed. Kodak 'Ultra rapide' and Kodak 'high resolution'. The high resolution film requires an intensity of 6×10^7 neutrons per cm^2 for correct exposures and is capable of a resolution of 30 to 40 microns. The ultra rapide film requires exposures an order of magnitude lower, but has inferior resolution.

Two other approaches to the problem have been made, the first, by Berger (1973), uses boron or lithium to capture neutrons and release α particles which are recorded on track-etch materials such as cellulose nitrate. A combination of these last two techniques was used by Malgrange et al. (1976) who observed pendellösung fringes in their neutron topographs. The final approach by Davidson et al. (1974) Davidson (1976) was an attempt at a direct imaging system.

5.3 Properties of Garnet Crystals

Single crystals of garnets have been grown from the flux. The technique of flux growth has recently been reviewed by Wanklyn (1975) and the physical and chemical properties of garnets have been reviewed by Wang (1973).

Interest in garnet crystals initially stemmed from the discovery of their ferrimagnetic properties (Pauthenet 1956). from their usefulness as microwave device materials (Spencer et al. 1956), from the variety of compounds which could be produced, and more recently from their potential use in bubble memory devices

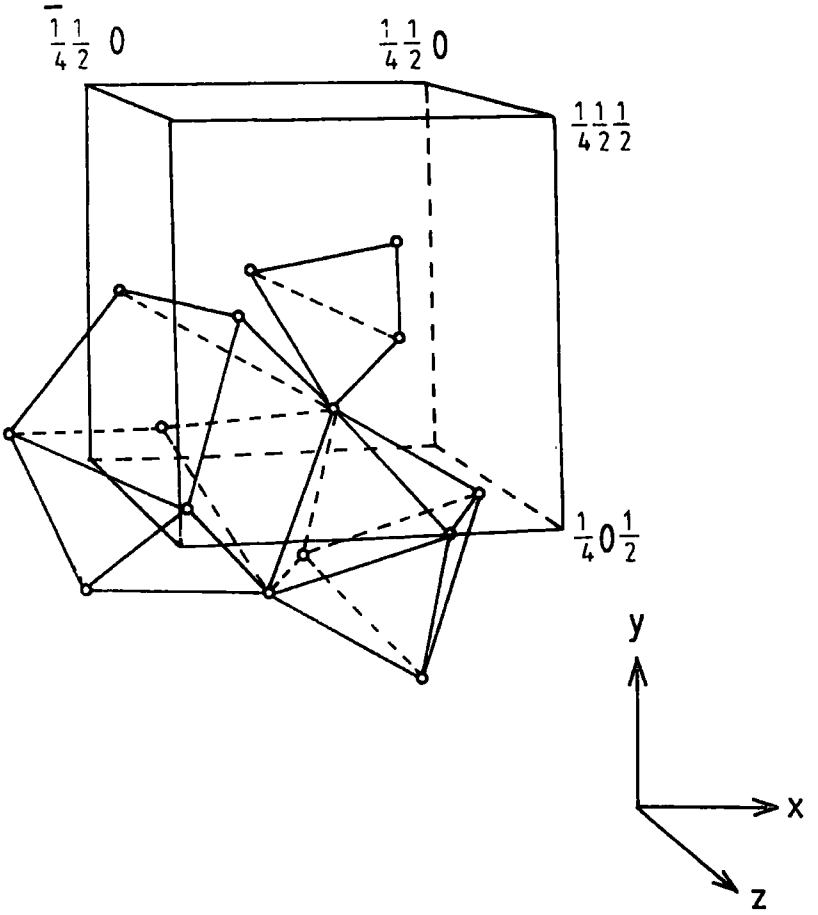

Fig. 5.2 Garnet Structure

(Bobeck 1967).

The garnet structure is shown in fig 5.2 from Wyckoff (1965). Belov (1958) showed that the most probable growth faces for the garnet structure are $\{110\}$, $\{211\}$, $\{100\}$ and $\{321\}$ faces. The possible Burgers vectors of dislocations have been found to be $<100>$ and $\frac{1}{2}<111>$ (Belt 1969). Wang (1973) reported that dislocation densities are lowest in gallium garnets and highest in iron garnets and Lang topography studies of Bardsley and Cockayne (1967) have shown the presence of growth striations within garnet crystals.

The early work on the study of growth processes within garnet crystals was performed mostly on yttrium iron garnet. Lefever et al. (1961, 1962) showed that initially dendritic growth occurred in $<100>$ and $<111>$ directions followed by layered growth on $\{110\}$ and $\{211\}$ faces. They also observed vicinal features on $\{110\}$ faces. These vicinal features are shallow pyramids the edges of which are parallel to $<110>$ and $<100>$ directions. Lefever and Chase (1962) observed growth steps on the vicinal faces. These steps possessed faces parallel to the nearest crystal face. Growth spirals were also present and from etch pit studies of dislocations they suggest that latter-stage growth involves the propogation of growth steps associated with screw dislocations. Komatsu and Sunagawa (1964) confirmed their findings by using interference contrast microscopy and etch pit studies. They showed that growth hillocks and the apex of vicinal

features were associated with dislocation outcrops. They suggest that growth hillocks are the early stage of formation of a vicinal feature.

Sunagawa (1967) observed four types of growth hillock, uniform wide and narrow spirals of monomolecular step height and non-uniform minute growth hillocks and conical growth hillocks. Komatsu et al. (1974) suggest that dislocations control the growth habit of garnets. In their studies of yttrium al uminium garnet they noted that growth hillocks were always associated with dislocation outcrops although the reverse was not necessarily true. They suggest that edge dislocations have no effect on the crystal habit whereas dislocations with a screw component do. They also measured the angle of the vicinal features and noted that they were inclined at 10 sec of arc to the (110) face.

5.4 Holmium Gallium Garnet

A crystal of holmium gallium garnet grown from the flux was supplied by Mrs B.M.Wanklyn from the Clarendon Laboratory Oxford. In this crystal growth took place predominately on $\{110\}$ faces with small $\{211\}$ faces also present. The crystal is roughly triangular in shape with edges of about 12 mm. and about 5 mm. thick. The crystal is shown in fig 5.3 with many of its faces indexed. The $(\bar{1}\bar{1}0)$ face has a slight curvature and was presumably in contact with the cruci ble during growth.

All twelve of the possible $\{110\}$ faces are present

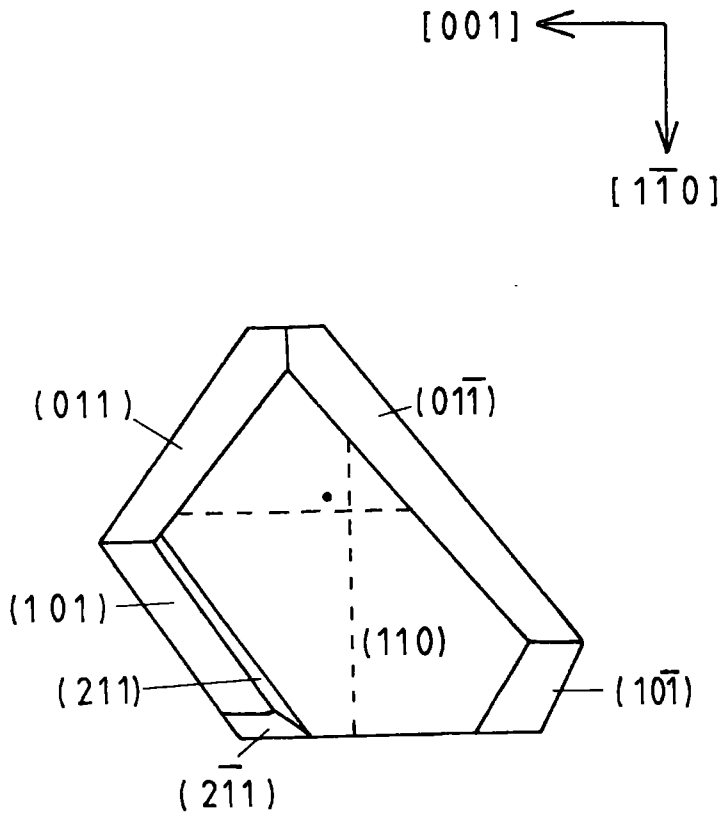

Fig. 5.3 Garnet Crystal

in this crystal and several of the $\{211\}$ faces. The $\{110\}$ faces are, in general, larger than the $\{211\}$ faces. Nine of the $\{110\}$ faces possess vicinal features either as shallow pyramids or shallow ridges. The ridges are always parallel to $<100>$ or $<110>$ directions and are inclined at angles of less than one minute to the (110) surfaces.

This crystal was examined using polarized light microscopy by Dr B.K.Tanner who observed birefringence associated with the vicinal features, but it was not clear whether the strain field pattern at the apex was that of a dislocation or not. A dislocation was observed with a $[110]$ line direction and at least some edge component in its Burger s vector. This dislocation commenced about half-way through the crystal and terminated on the (110) surface about 2 mm. from the apex of the vicinal feature on this surface.

Attempts to use surface reflection X-ray topography to observe this and any other dislocations within the crystal were unsuccessful partly due to the poor resolution achievable from the geometry necessarily employed and partly due to the high intensity of scattered radiation due to the presence of rare-earth atoms. Synchrotron radiation X-ray topography was equally unsuccessful. Due to the thickness of the crystal only anomalous transmission could be expected even with the very short wavelength available from the synchrotron source. Despite the very high perfection of this crystal, shown by optical observations and later confirmed by double crystal γ-ray diffraction with a full width at half

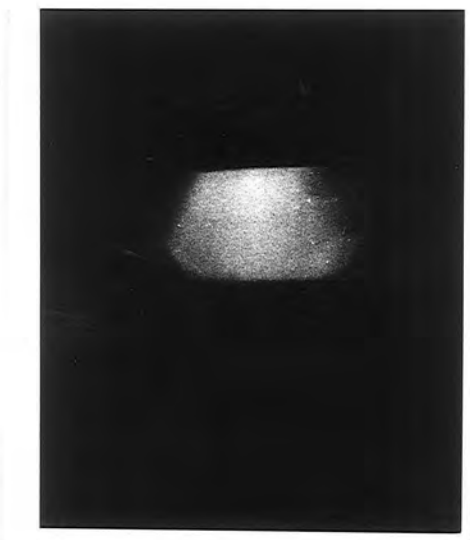

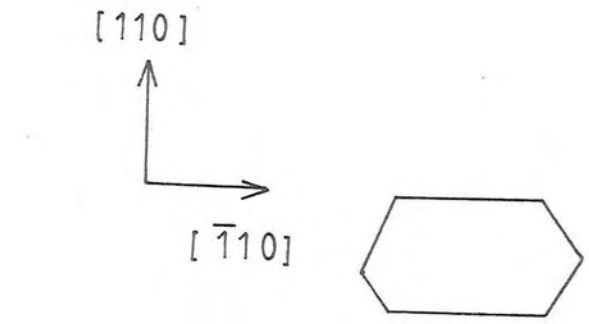

(c) 008 Reflection

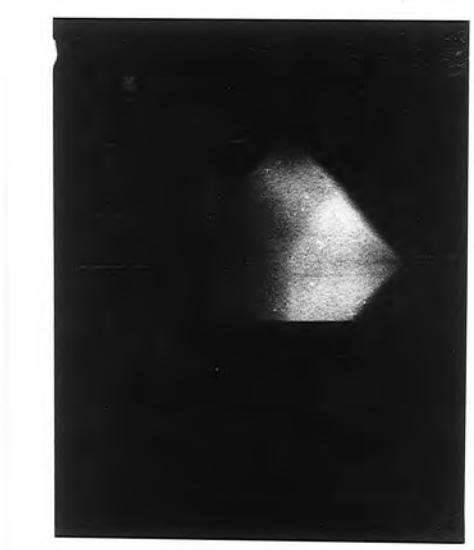

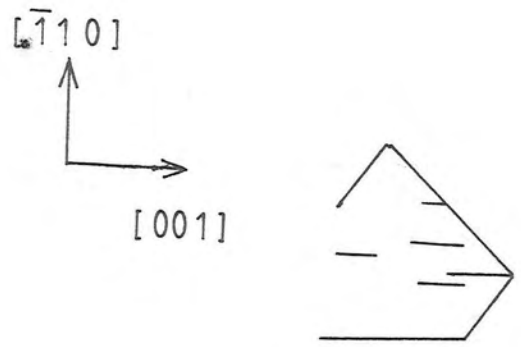

(d) 640 Reflection

Fig 5.5 Transmission Neutron Topographs (scale ×3)

maximum intensity rocking curve width of less than 11 sec of arc, no anomalous transmission occurred, probably due to the presence of strong growth banding. It was thus decided to perform neutron topography studies of this crystal in order to attempt to analyse the Burger s vector of the dislocation known to exist and to see if any other dislocations were present which could account for the observed vicinal features.

5.5 Neutron Topography Results

A variety of reflections were chosen to image the crystals on the strength of the neutron structure factors and the geometry of the crystal. Neutron rocking curves were measured on each crystal setting. Rocking curves at full width at half maximum intensity down to about 4 min of arc were recorded such as the $00\bar{8}$ reflection shown in fig 5.4 a. This is the expected rocking curve width from the divergence of the incident beam. However, many of the rocking curves were broader and were also split such as the $8\bar{8}0$ reflection in fig 5.4 b. The reasons for this splitting are unclear and recording topographs on each of the peaks did not clarify the matter.

The splittings of the neutron rocking curves were about 3 min of arc. One explanation is that this is due to a difference in lattice parameter between different growth regions or between different growth bands. A lattice parameter difference of 1 part in 10^3 would be sufficient to account for the observed splitting.

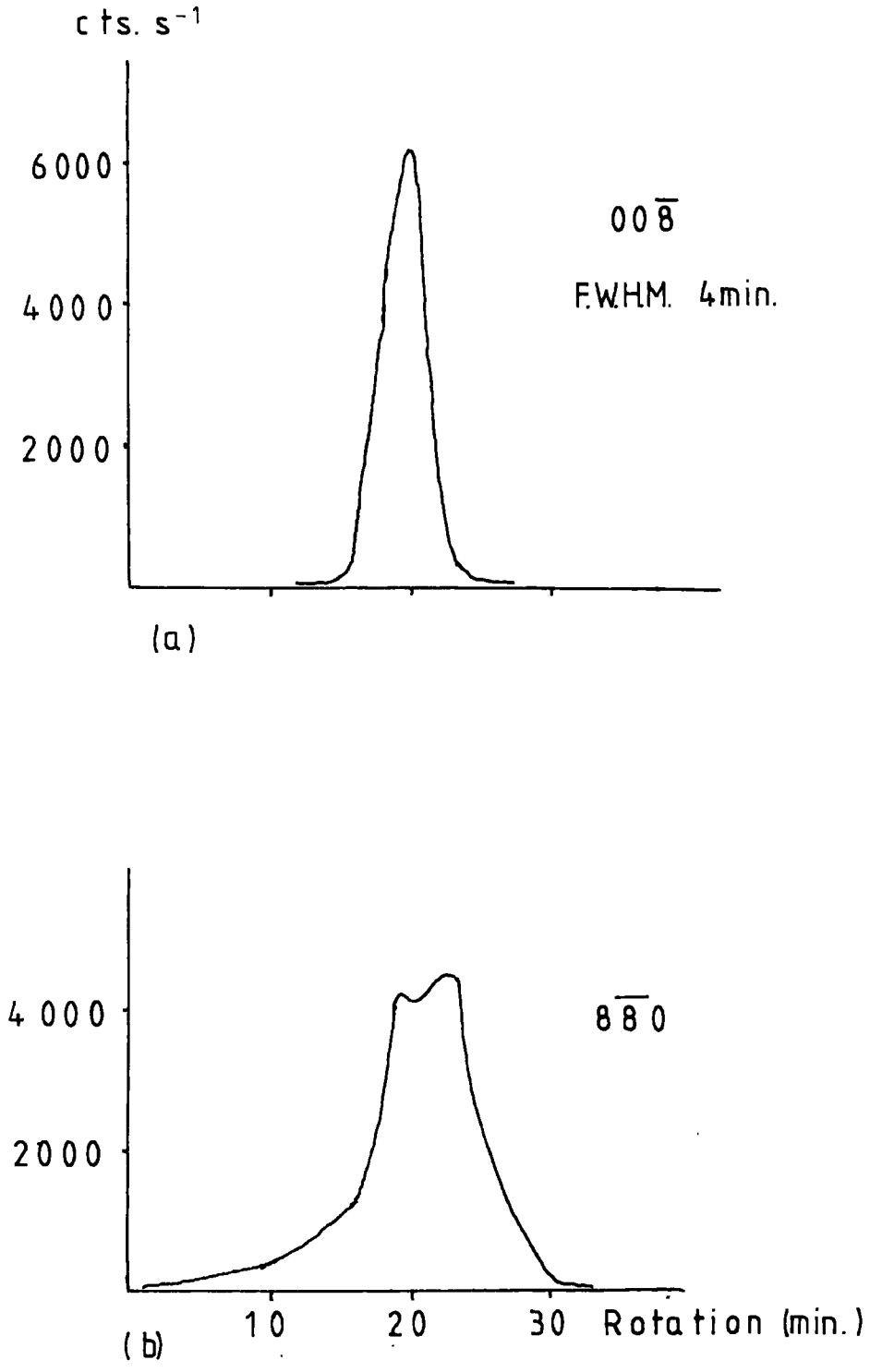

Fig. 5.4 Neutron Rocking Curves

Variations in lattice parameter, between synthetic garnets of the same composition from different sources, of this order have been reported, Donay and Odik (1973), however the difference seems a little large to occur within the same crystal. Lattice parameter variations of this order would not result in significant broadening of the double crystal gamma ray rocking curves. Due to the very short wavelength employed in the gamma ray technique it is insensitive to lattice parameter variations, but it is however highly sensitive to lattice rotations.

An alternative explanation of the splitting is that due to the very large unit cell of the garnet crystal a large number of reflections are available and the splittings may be associated with two reflections of similar Bragg angle. Several of the topographs show the presence of second weaker, reflections. The large divergence of the neutron beam may allow nearly parallel lattice planes to simultaneously satisfy the Bragg condition. However, with a highly perfect reference crystal the beam divergence in the gamma ray case would be extremely low and a mis-orientation of a few minutes of arc between reflecting planes would be sufficient to considerably reduce any second reflection. In double crystal experiments the two crystals are set with reflecting planes parallel to within one minute of arc.

Several of the neutron topographs are shown in fig 5.5, exposure times were of the order of a day. These are photographed

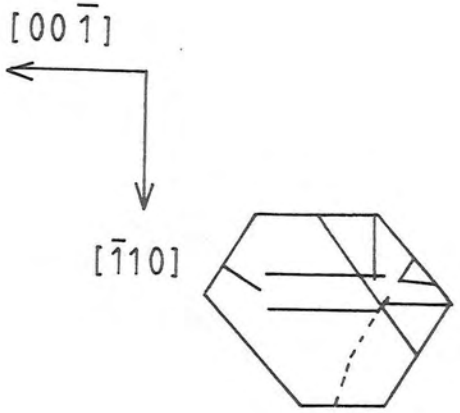

(a) 00$\bar{8}$ Reflection

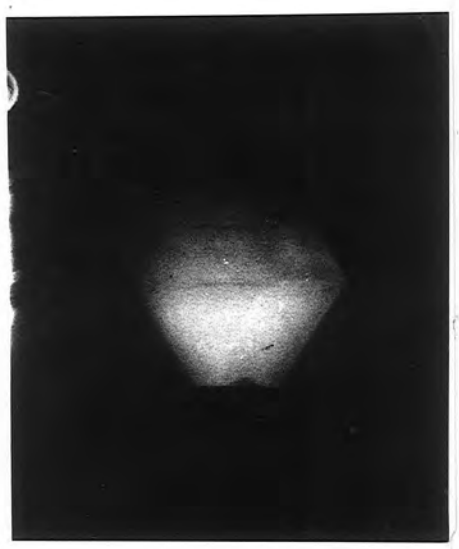

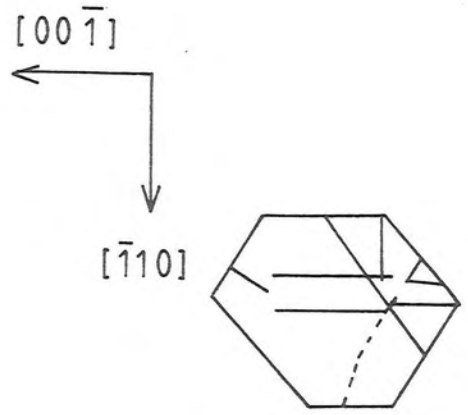

(a) 00$\bar{8}$ Reflection

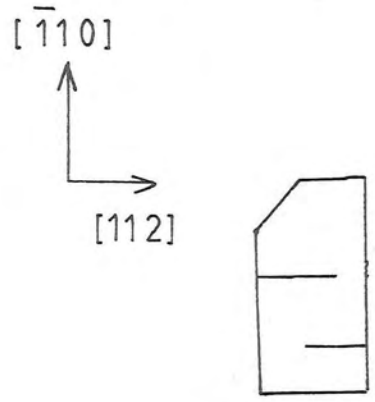

(b) $\bar{4}\bar{4}$4 Reflection

with the contrast reversed from that usual in the X-ray case. Fig 5.5a is an $00\bar{8}$ reflection. Reduced contrast images (dark in the figure) can be seen parallel to [001] , $[\bar{1}11]$, $[\bar{1}1\bar{1}]$ and close to [001] . These are probably dislocation images although the contrast of these, and other possible dislocation images seen in other topographs, is reversed from the expected kinematical images. These dislocations appear to correspond with vicinal features on the $(01\bar{1})$, (101), (011) and $(0\bar{1}1)$ faces.

A $\bar{4}\bar{4}4$ topograph is shown in fig 5.5b. A trace of a dislocation image can be seen parallel to the [112] direction which corresponds to an [001] trace dislocation seen in fig 5.5a. Fig 5.5c is an 008 reflection in which no dislocations are observable. Fig 5.5d, a 640 reflection, shows dislocation traces parallel to [001] one of these corresponds with an dislocation trace observable in fig 5.5a. There are probably five dislocations revealed in this topograph although the contrast of some of these is very weak and they are not at all clear in the reproduction. These dislocations may correspond with vicinal features on the $(01\bar{1})$, $(\bar{1}0\bar{1})$ and $(10\bar{1})$ planes.

A number of the topographs show large scale area contrast towards the edges of the crystal which is associated with the growth faces of the crystal. The dislocation with a [110] line direction observed optically is not visible on any of the topographs. In order to attempt to improve the poor resolution and see this dislocation, two section topographs were recorded corresponding to the $\bar{4}\bar{4}4$ and 640 reflections exposure times with a 0.8 mm

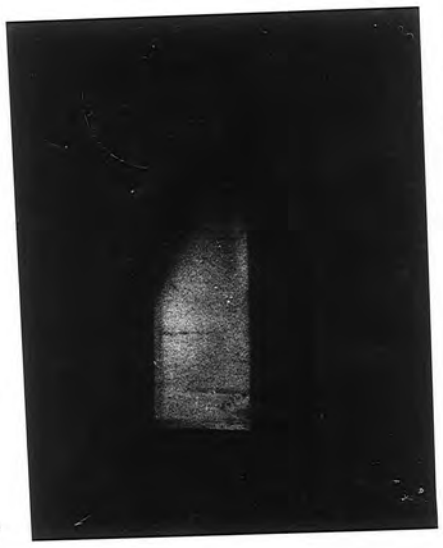

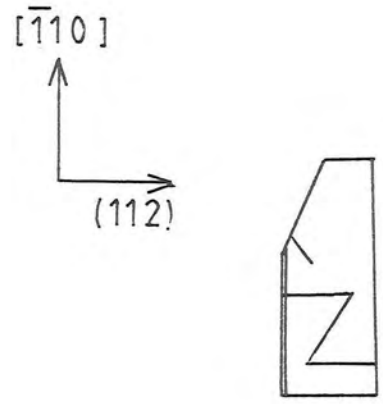

(a) $\bar{4}\bar{4}4$ Reflection

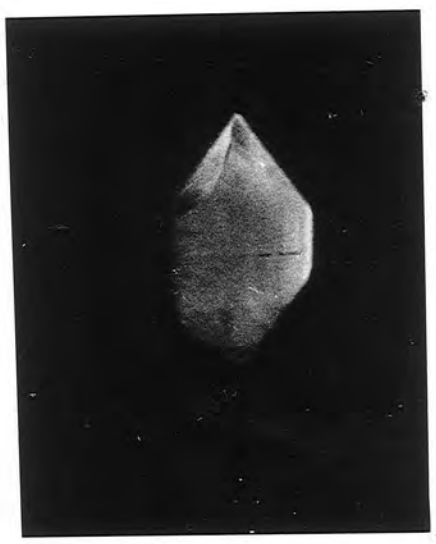

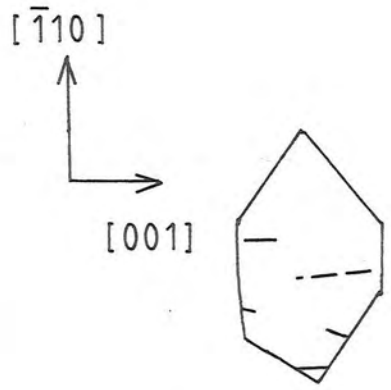

(b) 640 Reflection

Fig 5.6 Neutron Section Topographs (scale×3)

incident beam width were the order of three days.

Fig 5.6a is the $\bar{4}\bar{4}4$ reflection corresponding to fig 5.5b. The [112] trace dislocation observable in fig 5.5b can again be observed, this time much more easily. In addition, another [112] dislocation trace corresponding with the [110] line direction dislocation observed optically is visible providing evidence that the images are of dislocations. This dislocation was not definately observable in the previous wide area topograph. In addition [101], [011] and [$\bar{1}$10] traces of dislocations are observable; the latter may correspond with a vicinal feature on the (1$\bar{1}$0) surface. The 640 section topograph, fig 5.6b, again has improved resolution. An [001] dislocation trace is clearly observable which corresponds with one previously seen in fig 5.5d.

Several of the topographs show evidence for growth banding parallel to the growth faces. The presence of these strong growth bands, also observable in the birefringence micrgraphs of this crystal may in part explain the poor resolution in the majority of topographs, as the variation in lattice parameter associated with these growth bands may disrupt the diffracted waves within the very thick crystal.

Many of the dislocations observed may correlate with vicinal features on the crystal surface. In order to establish a definite correlation it is necessary to observe the dislocation in at least two non co-planar reflections. In order to determine the Burger's vector of a dislocation it is necessary to obtain

two non co-planer reflections in which the dislocation is out of contrast. Unfortunately the $\bar{4}\bar{4}4$ and 640 section topographs show that in the wide area topographs, dislocations which should be in contrast are not necessarily observed in these topographs. Hence the absence of a dislocation from a particular reflection does not necessarily imply that a dislocation is out of contrast. Thus it has not been possible to establish the Burger's vectors of any of the dislocations due to the extreme length of time, (70 hours) required for each exposure of a section topograph and the relatively short time available on the neutron topography camera at I.L.L. The experiments did however establish that a small number of dislocations were present within the crystal, several of which may correspond with vicinal features observable on the crystal surface. However, at least one dislocation did not correspond with any vicinal feature. Other vicinal features were present for which there was no correlation with any observed dislocation, but the results do not totally exclude other dislocations within the crystal which may correlate with the vicinal features.

CHAPTER SIX

Antiferromagnetic Domain Walls Motion in $KCoF_3$ Under an Applied Stress

CHAPTER SIX

Antiferromagnetic Domain Wall Motion in $KCoF_3$ under an Applied Stress

6.1 Introduction

The flux growth of crystals of KMF_3 (where M = Ni, Co, or Fe) has been reported by Wanklyn (1969, 1975) and Garrard et al. (1974, 1975). The perfection of these crystals has been studied using X-ray topography by Safa et al. (1977) . The best of the crystals have been used for static domain studies (Safa et al. 1975, and Tanner et al. 1977) and dynamic domain studies under an applied magnetic field, (Tanner et al. 1976, Safa and Tanner 1977, 1978).

$KCoF_3$, at room temperature, has the cubic perovskite structure shown in fig 6.1. This was revealed through X-ray diffraction experiments by Okazaki and Suemune (1961). Powder susceptibility measurements of Hirakawa et al. (1960) revealed that below a Néel temperature of 114K $KCoF_3$ becomes antiferromagnetic and Okazaki et al. (1959) showed that below the Néel temperature $KCoF_3$ undergoes a tetragonal distortion with $a > c$. The susceptibility data of Hirakawa et al. (1960) is shown in fig 6.2 in which a deviation from the Curie-Weiss law is seen. This arises because the lowest orbital of Co^{2+} splits into three levels with $J = \frac{1}{2}, \frac{3}{2}$ and $\frac{5}{2}$ with separations of the order of KT.

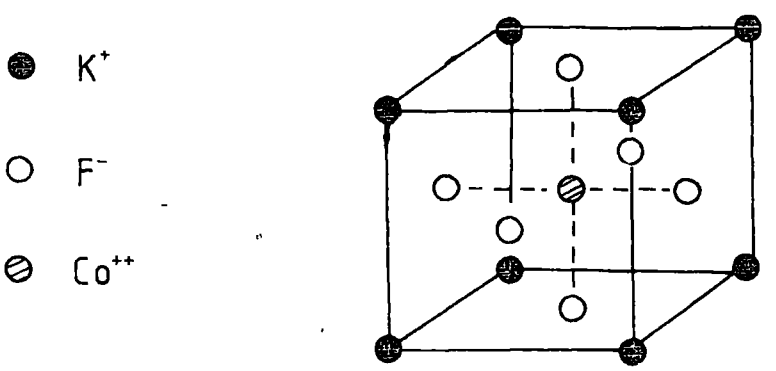

Fig. 6.1 Perovskite Structure

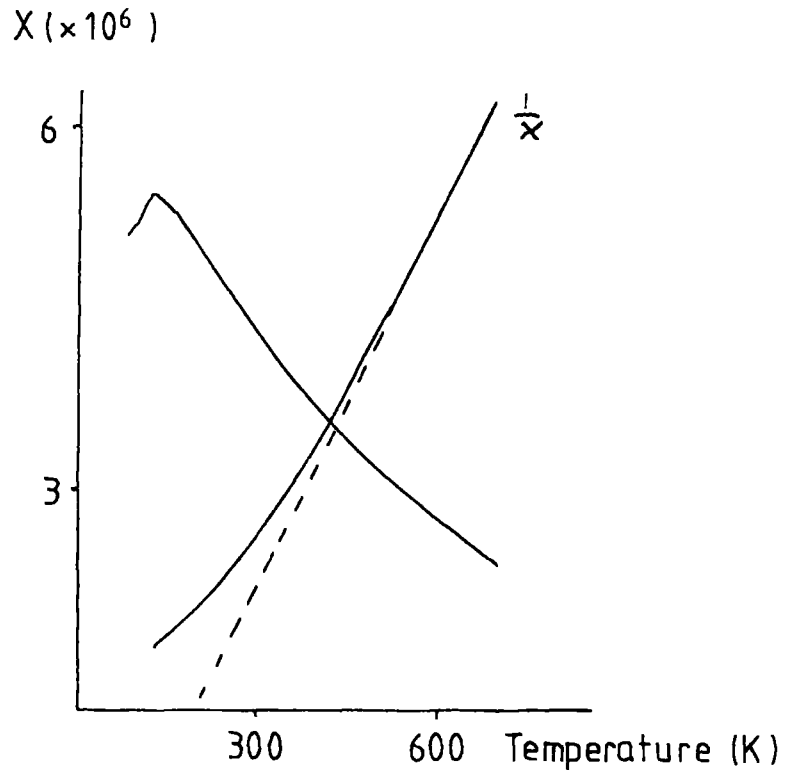

Fig. 6.2 Gram Susceptibility of $KCoF_3$

(Hirakawa et al. 1960)

Julliard and Nouet (1975) found that $KCoF_3$ underwent a magnetostrictive distortion at 117K deforming from cubic to tetragonal symmetry. Okazaki and Suemune (1961) determined the lattice constant at room temperature to be 4.069 ± 0.001 Angstroms and measured a tetragonal distortion at 114K. At liquid nitrogen temperatures they obtained values of a = 4.057 ± 0.002 and c = 4.049 ± 0.002 angstroms giving $\frac{c-a}{a} = -2\times10^{-3}$. The measured temperature dependence of the lattice constant is shown in fig 6.3.

Scatturin et al. (1961) determined the magnetic structure by neutron diffraction techniques which indicated an antiferromagnetic arrangement with the spins of all six nearest neighbours of any atom aligned antiparallel. This is the G type structure shown in fig 6.4.

Hirakawa et al. (1961) investigated the magnetic anisotropy of single crystals of $KCoF_3$ using torque magnetometry. The initial theoretical work on the interpretation of such results was performed by Nagamiya (1958) and Uchida et al. (1960). The torque data can be interpreted in two ways. Either as an anisotropy energy within the plane of easy magnetization, or as movement of walls which separate domains with different directions of magnetization. The latter interpretation, based on the ideas of Néel (1954), is favoured. Initially twofold and fourfold components were observed in the torque data. Upon application of an external stress, along one of the cube axis, the amplitude of the twofold term increased rapidly and the fourfold term diminished. From these results it was deduced that

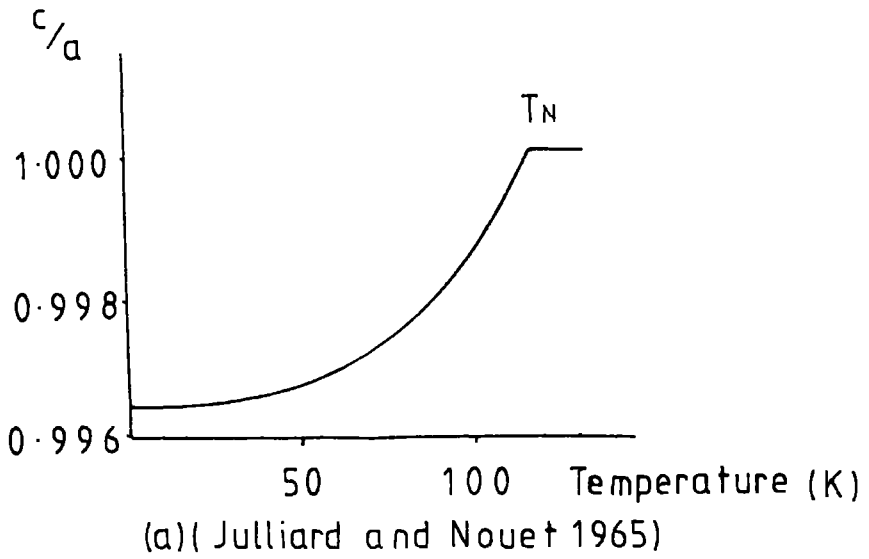

(a)(Julliard and Nouet 1965)

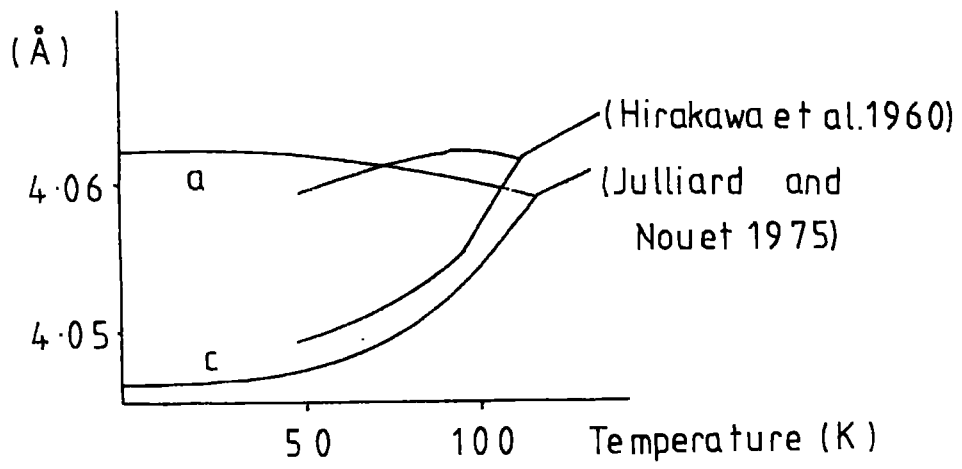

Fig. 6.3 $KCoF_3$ Lattice Parameters

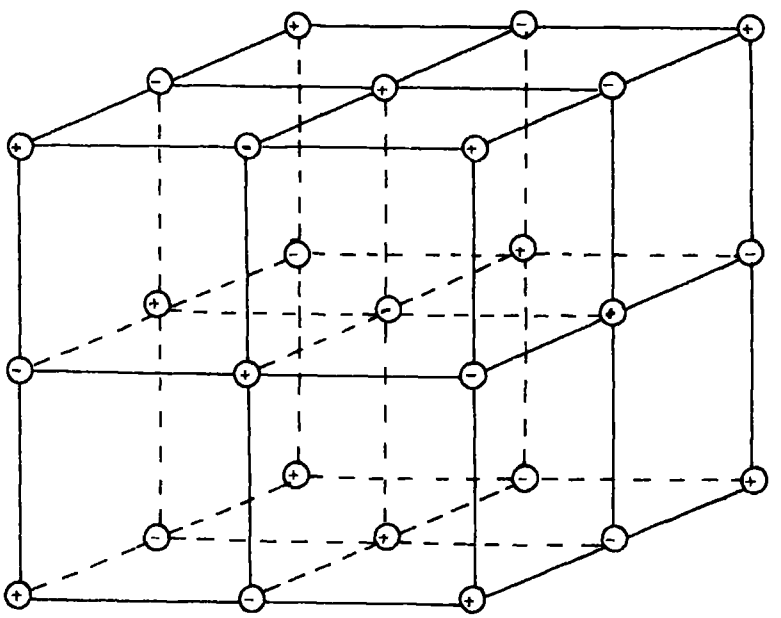

Fig. 6.4 "G" Type Antiferromagnetic Order

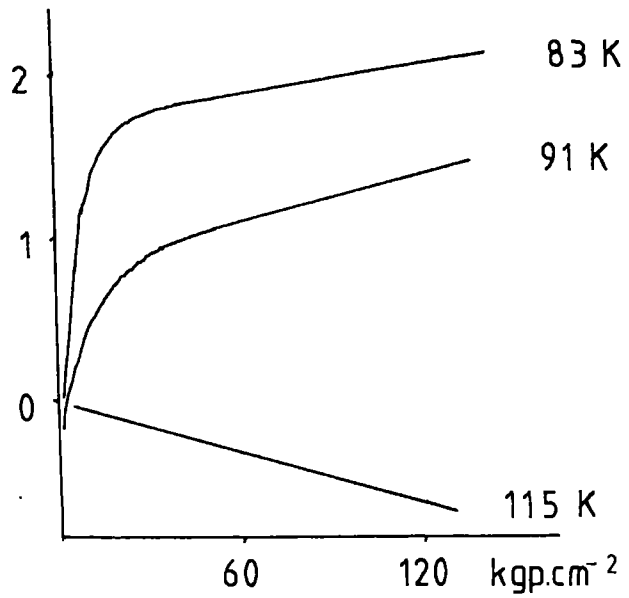

Fig. 6.5 Stress Dependence of L.D. in $RbCoF_3$

(Ferré et al. 1976)

the easy directions of magnetization were along <100> directions. The increase in the twofold term in the torque data when the crystal was stressed is interpreted as being due to the sample becoming single domain. The large negative magnetostriction should result in spins aligning along the stress direction. Further evidence of the effect of strain on the domain structure of $KCoF_3$ is available from Mossbauer studies (Morimoto and Ito 1977).

The stress dependence of linear dichroism in $KCoF_3$ (Ferré et al. 1976) has been interpreted as an effect of antiferromagnetic domain wall motion. The critical stress ($20Kgcm^{-2}$) at which samples become single domain is small compared with the stress value attributed to the spin flop phenomenon. Typical data for the stress dependence of linear dichroism in $RbCoF_3$ is shown in fig 6.5. Two parts to the curves can be seen.The initial rapid variation which is reversible is attributed to antiferromagnetic domain wall motion.

6.2 Domain Observations

The first observation of antiferromagnetic domains in $KCoF_3$ was by Schlenker et al. (1974) using X-ray topography. As expected they found three types of domains with domain walls on {110} planes which is predicted from the <100> easy directions. The possible domain walls are shown in fig 6.6 (Baruchel 1974). Schlenker et al. (1974) also showed that the domain configuration is influenced by the strain introduced on mounting the sample. Safa et al. (1975, 1978) confirmed these results with higher

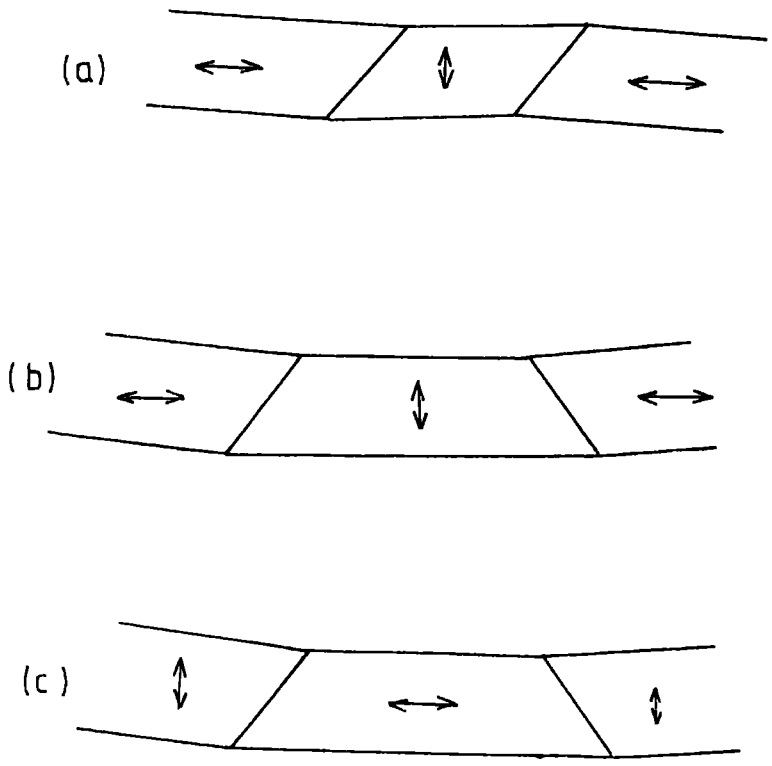

Fig. 6.6 $KCoF_3$ Domain Configurations

(Baruchel 1974)

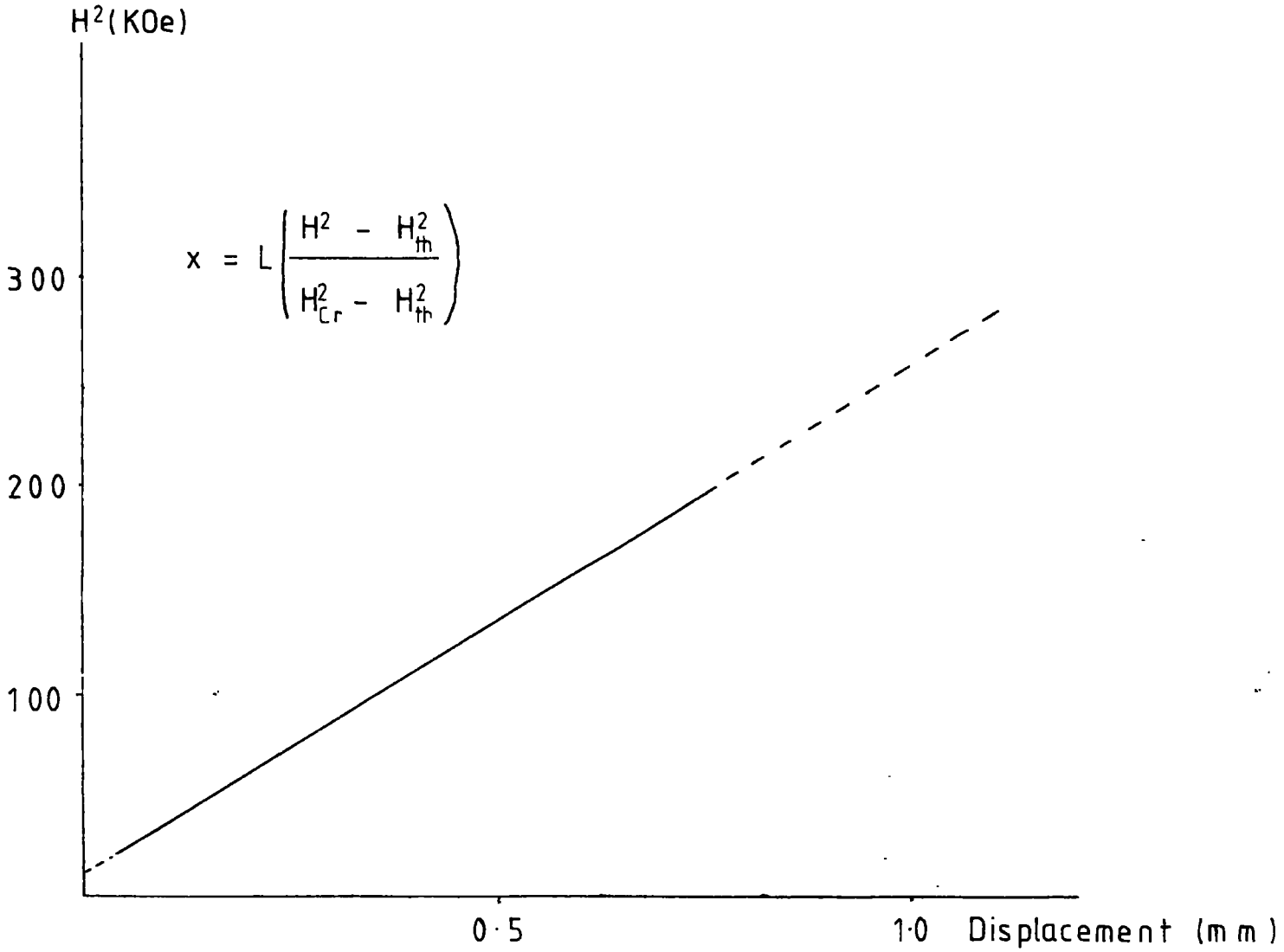

Fig. 6.7 Domain Wall Motion in KCoF (Safa and Tanner 1978)

quality crystals. By carefully mounting the sample with a very small amount of adhesive, they were able to obtain a sample which was very nearly single domain on cooling. On mounting the sample more crudely many domains were produced on cooling. This result is interpreted as being due to the effect of strain; the sample ordering below its Néel temperature in such a way as to minimize its elastic energy.

Synchrotron X-ray topography experiments on $KCoF_3$ in moderate magnetic fields, (Safa and Tanner 1978), have shown that spin flop occurs via domain wall motion. In one experiment they were able to follow the motion of a single domain wall. Excellent agreement was obtained with the theoretical predictions using the model of Néel (1954) fig 6.7.

6.3 Theory of Antiferromagnetic Domain Wall Motion Under Stress

The free energy per unit volume, F, of a crystal under an applied stress, σ, is the sum of the magnetoelastic and magnetocrystalline anisotropy energies. Thus to first order

$$\begin{aligned} F = & \tfrac{3}{2}\lambda_{100}\sigma(\alpha_1^2\beta_1^2 + \alpha_2^2\beta_2^2 + \alpha_3^2\beta_3^2) \\ & - 3\lambda_{111}\sigma(\alpha_1\alpha_2\beta_1\beta_2 + \alpha_2\alpha_3\beta_2\beta_3 + \alpha_1\alpha_3\beta_1\beta_3) \\ & + K_1(\alpha_1^2\alpha_2^2 + \alpha_2^2\alpha_3^2 + \alpha_1^2\alpha_3^2) \cdots\cdots (6.1) \end{aligned}$$

where the β_i's are the direction cosines of the stress, the α_i's

are the direction cosines of the sublattice magnetization and K_1 is the first cubic anisotropy constant. As previously mentioned X-ray topography has shown the presence of three types of domain in the unstressed crystal with magnetization along the three directions. These will be referred to as the d_x, d_y and d_z domains.

For a stress parallel to [001] we have

$$F = -\frac{3}{2}\lambda_{100}\sigma \cos^2\theta + \frac{1}{4}K \sin^2 2\theta \qquad (6.2)$$

where θ is the angle the spins make with the stress directions.

If the displacement X due to stress, of a wall between a d_z and either a d_x or d_y domain is considered and, following Néel (1954) a restoring force of the form $-Cx$ is included, where C is a constant depending on the domain configuration and including a constant force B on the wall the change in free energy due to the wall displacement is

$$\Delta F = \frac{1}{2}Cx^2 - \frac{3}{2}\lambda_{100}\sigma x(\cos^2\theta_1 + \cos^2\theta_2) - Bx + \frac{1}{4}K_1 x(\sin^2 2\theta_1 + \sin^2 2\theta_2) \qquad (6.3)$$

where θ_1 and θ_2 are the angles made by the spins with [001] in the d_z and d_x or d_y domains.

Minimizing expression 6.3 with respect to θ_1, θ_2 and X gives

$$Cx = \frac{3}{2}\sigma\lambda_{100} + B \qquad (6.4)$$

No displacement of the walls will occur below a threshold stress given by

$$\sigma_{th} = -\frac{2B}{3\lambda_{100}} \qquad (6.5)$$

Above the threshold stress wall displacement is expected to be linear with stress until the displacement reaches the original wall separation L. At this critical stress the sample will be single domain with

$$\delta L = \frac{3}{2} \lambda_{100} (\sigma_{cr} - \sigma_{th}) \qquad (6.6)$$

6.4 Experimental Procedure

In order to confirm that an applied stress caused anti-ferromagnetic domain wall motion it was necessary to design apparatus to apply a stress to a crystal maintained at liquid nitrogen temperatures and enable the crystal to be imaged by X-ray topography.

The experiment required a thin parallel sided platelet in order to keep the X-ray attenuation low and enable a uniform stress to be applied. The platelet had to be free-standing, as it was argued that use of adhesives would introduce a mounting strain, and the stress had to be applied parallel to the platelet surface.

The crystal employed was highly perfect, to keep internal strains to a minimum, and was the same sample as used in the magnetic field studies of Safa and Tanner (1978) with its opposite edges mechanically polished flat and parallel. Strain introduced by mechanically polishing the crystal was removed by chemical polishing in hydroflouric acid for several hours.

The crystal was placed in a slot in a perspex holder which was placed in the simple polystyrene cryostat described previously, fig 6.8, which could be filled with liquid nitrogen enabling the crystal to be maintained at a temperature of 77K. A compressive

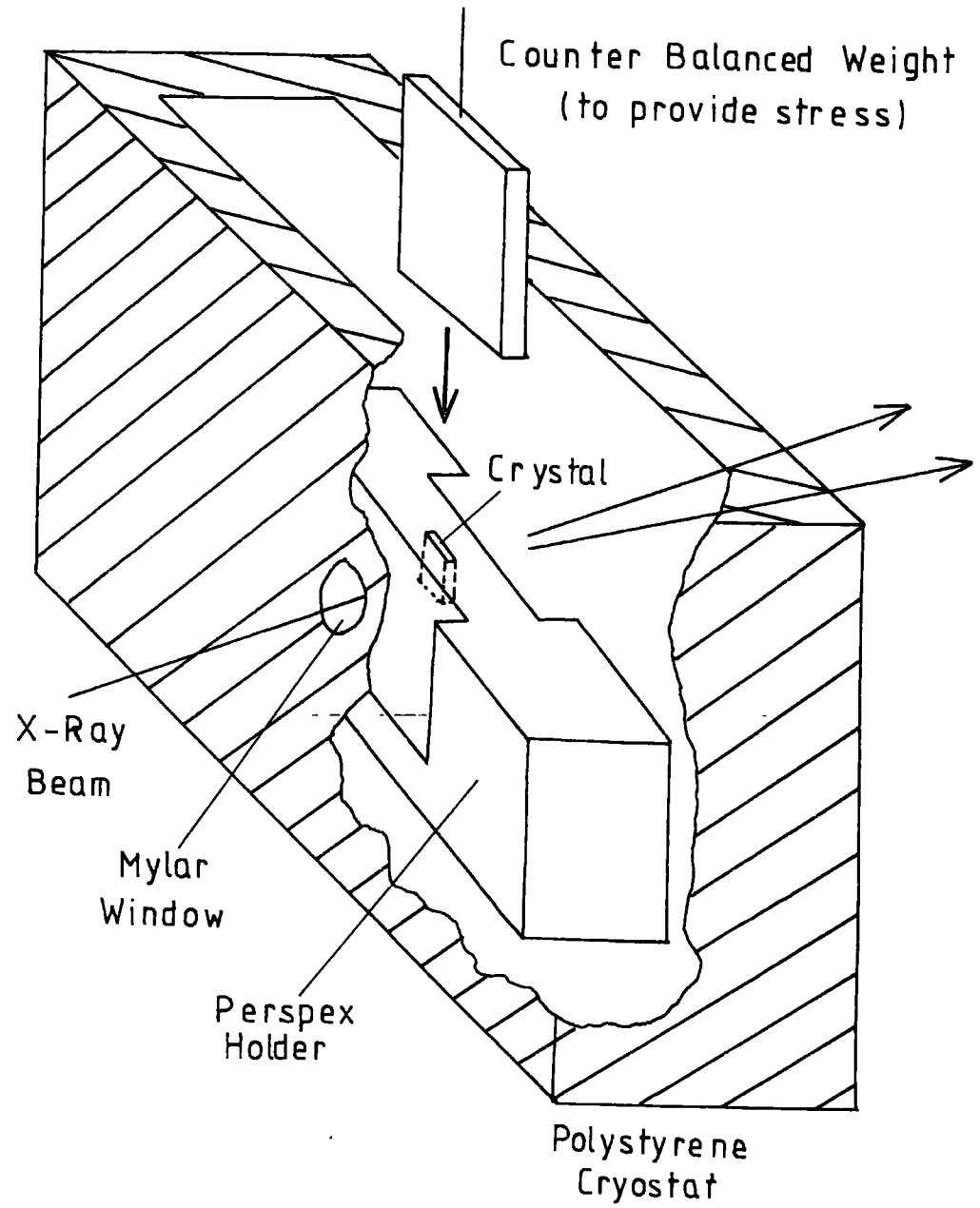

Fig. 6.8 Schematic Diagram of Stress Experiments

stress could be applied via a counter balanced weight suspended above the crystal by a pulley wheel. A known loading could be applied to the crystal, along [001], by removing weights from the counter balancing weight pan. This arrangement allowed the stress to be increased without seriously disturbing the crystal. Alignment of the crystal, with the X-ray beam was simplified by the mylar window in the cryostat. This enabled the crystal to be aligned with a laser beam which had previously been aligned with the synchrotron radiation beam and also allowed a fluorescent screen to be used to align the crystal on a conventional X-ray generator.

At a wavelength of about 0.5 Å the radiation was able to pass through the perspex holder without serious attenuation. Some attenuation resulted from the presence of liquid nitrogen. This was not a problem due to the high intensity of the synchrotron source. Radiation scattered from the liquid nitrogen was a more serious problem which was overcome by placing the nuclear emulsion about 20cm from the crystal. Due to both air absorption and to the fact that fluorescent radiation is emitted over a 4π solid angle this reduced the blackening to an acceptable level. Due to the properties of the synchrotron source the resulting loss of geometrical resolution was not serious, particularly as the experiment was designed to image the rather large domains present in the crystal. This large specimen to plate distance did however result in some image blurring due to small vibrations of the crystal in the holder.

Several images were recorded in one exposure of a few minutes although the arrangement was primarily designed to record

the 002 reflection with 0.5 Å radiation. The desired Bragg angle of about 7° was obtained by tilting the entire cryostat, diffraction taking place in the vertical plane.

Initially vibrations of the free standing crystal caused by the boiling liquid nitrogen caused problems in taking topographs of the crystal. This was overcome by supporting the crystal, in its holder, with a paper wedge. However, results indicated that this introduced a lateral stress and this practice was discontinued.

Lang topographs on a convential X-ray generator were impossible due to the hold time of the cryostat, problems with liquid nitrogen absorption and geometrical constraints. However, a sufficient understanding of the antiferromagnetic domain wall motion was obtained from the synchrotron X-ray topographs to enable additional data to be obtained from X-ray rocking curves.

The magnetostrictive deformation of the lattice results in both a mis-orientation of the lattice between domains and in lattice parameter differences. The large value of λ_{100} results in a large effective mis-orientation which can be seen as clear splittings of single crystal X-ray rocking curves. By using the 220 reflection, with Ag K_{α} radiation, the splitting due to all possible types of domain wall could be detected. The apparatus employed, apart from the cryostat was identical to that described in the chapter relating to the measurement of the magneto-striction of Terbium.

6.5 Experimental Results

Upon cooling the crystal through the Néel temperature the domain structure observed in the (100) platelet usually comprised (101) and (10$\bar{1}$) walls. (110), (1$\bar{1}$0), (011) and (0$\bar{1}$1) walls were also observed. This is in agreement with previously reported domain observations.

Part of a typical sequence of synchrotron X-ray topographs is shown in fig 6.9. Some of the domain walls mentioned above are easily deduced from the zero stress topograph. The domains are imaged by orientation contrast. The mis-orientation between domains, arising from the magnetostrictive deformation of the lattice, results in X-rays of differing wavelength being diffracted through different Bragg angles from adjacent domains. Hence diffracted beams from adjacent domains travel in different directions, either converging or diverging, depending on the sense of the mis-orientation. Divergent X-ray beams give rise to a band on the topograph devoid of diffracted intensity which can be seen clearly in the topographs shown in figs 6.9 and 6.11. Convergent beams give rise to a band of enhanced intensity which cannot clearly be seen in any of the topographs. An estimate of the magnetostriction was obtained from the width of these bands by calculating the effective mis-orientation between domains from simple geometry. The value of the magnetostriction was in agreement with the reported values of Julliard and Nouet (1975), but contained rather large errors.

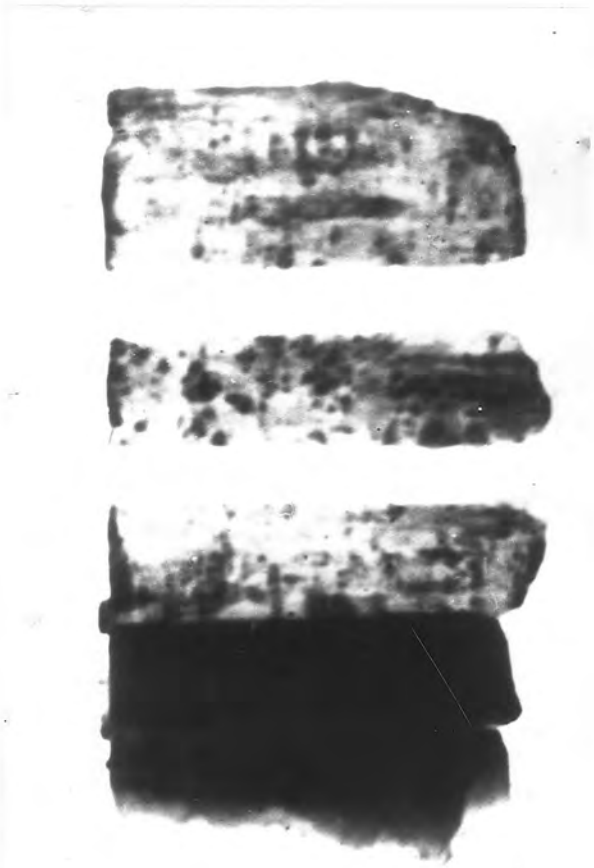

Stress 0 kg cm^{-2}

(a)

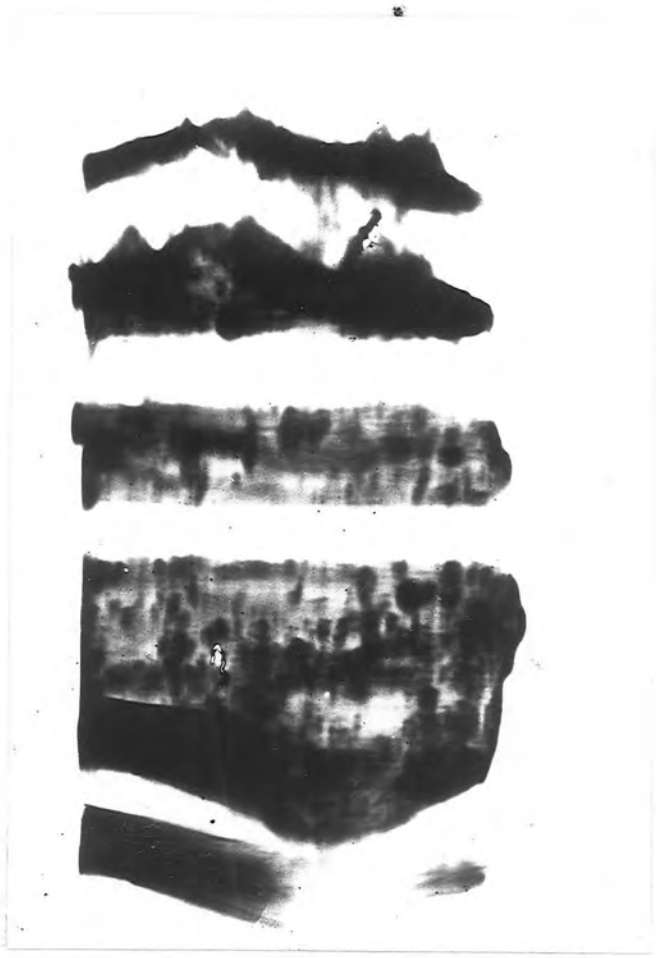

Stress 5 kg cm^{-2}

(b)

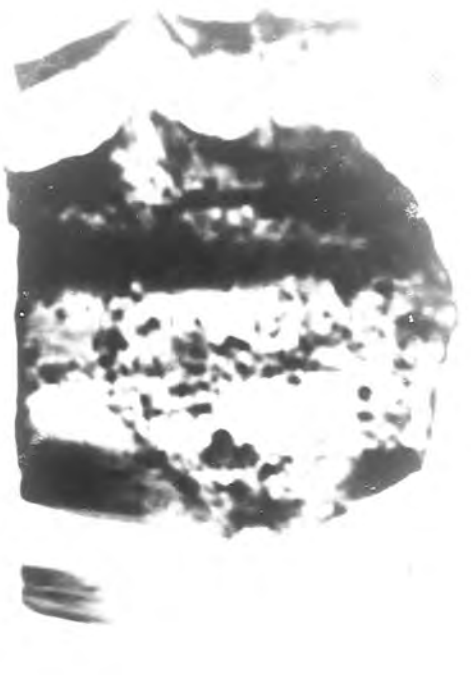

Stress 17kg cm^{-2}

(c)

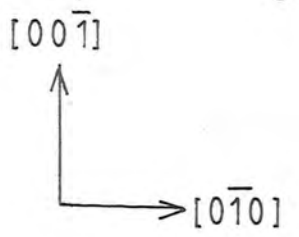

1mm

002 Reflections

Fig 6.9 Synchrotron Topographs of $KCoF_3$ under Uniaxial Stress along [001] at 77K (NINA 4.9Gev 3ma 6min 25μmL4)

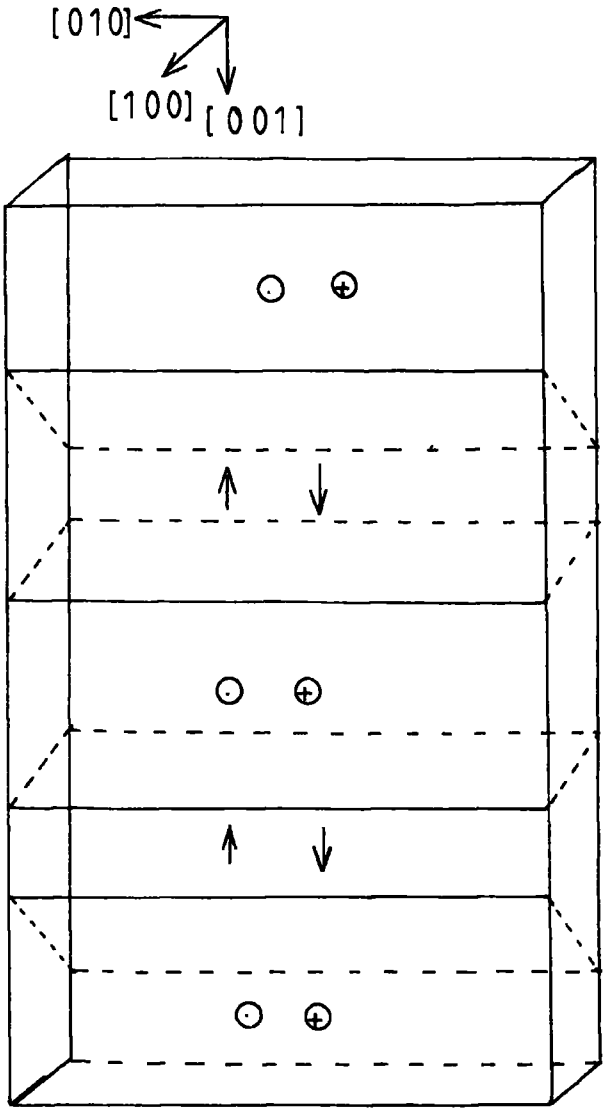

Fig 6.10 Domain Structure of fig 6.9 (a)

A possible domain structure corresponding to fig 6.9a is shown in fig 6.10. The existence of more than three divergent walls visible in other topographs implies the presence of convergent walls which cannot be definitely identified. Due to the negative magnetostriction constant (λ_{100}) we expect wall motion to occur in such a manner as to align the spins along the stress direction. (equation 6.4) This type of wall motion does occur, but the presence of a mounting stress perpendicular to the platelet surface causes the domain structure of fig 6.9a to become complex with walls no longer lying entirely on $\{110\}$ planes. In the experimental run no wall motion was apparent in the topographs below a stress of about 5 Kg cm^{-2}.

The threshold stress depended on the technique employed for holding the crystal. If the crystal was held in the slot with a supporting wedge considerable variations in the threshold stress were observed, but the difference between critical and threshold stress was constant. Without a supporting wedge considerable problems associated with specimen movement were obtained, but a very small consistent threshold stress below 0.4 Kg cm^{-2} was obtained.

Another sequence of topographs is shown in fig 6.11. A complete model of the domain configuration cannot be found. Parts of the image appear to be missing and extra walls which are not apparent from the topographs are required to explain the domain structure. The presence of $(0\bar{1}1)$ walls in this sequence, which were not usually seen, is probably a function of the way the crystal was

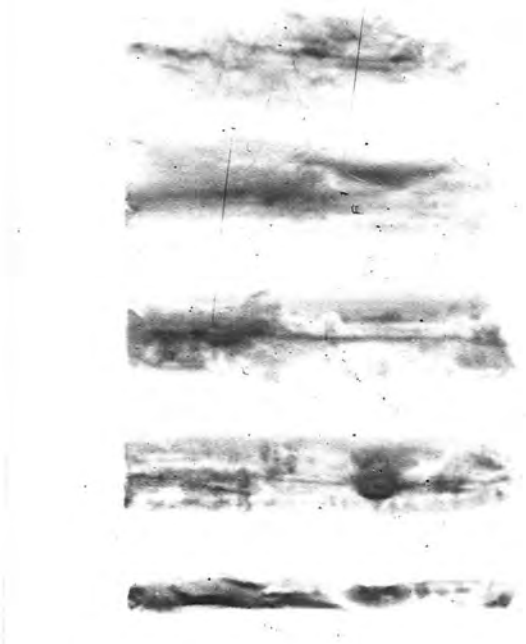

Stress Zero

(e)

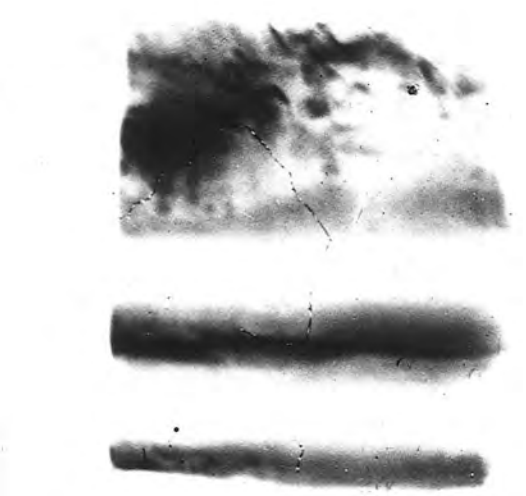

Stress $44\ kg\,cm^{-2}$

(f)

Fig 6.11 Synchrotron Topographs of $KCoF_3$ under an
[001] Stress 002 Reflections
(DESY 7Gev 10ma 90sec 25μm L4)

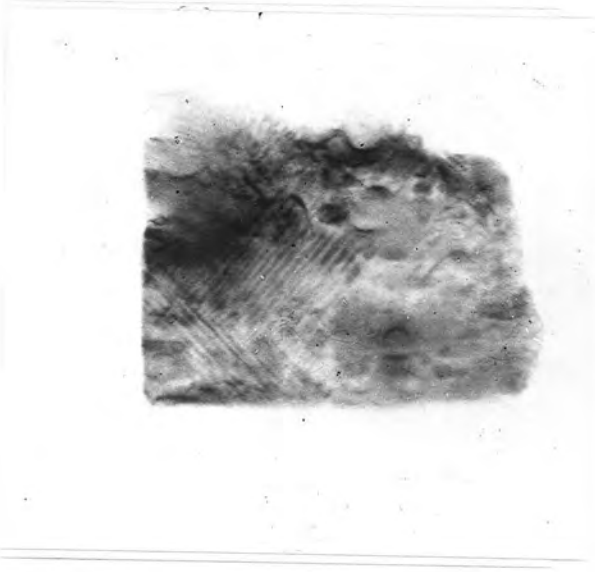

Stress 52 kg cm^{-2}

(c)

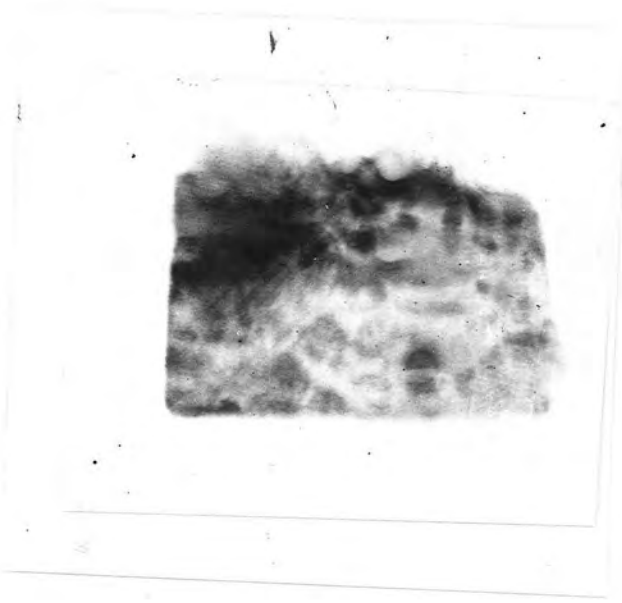

Stress 59 kg cm^{-2}

(d)

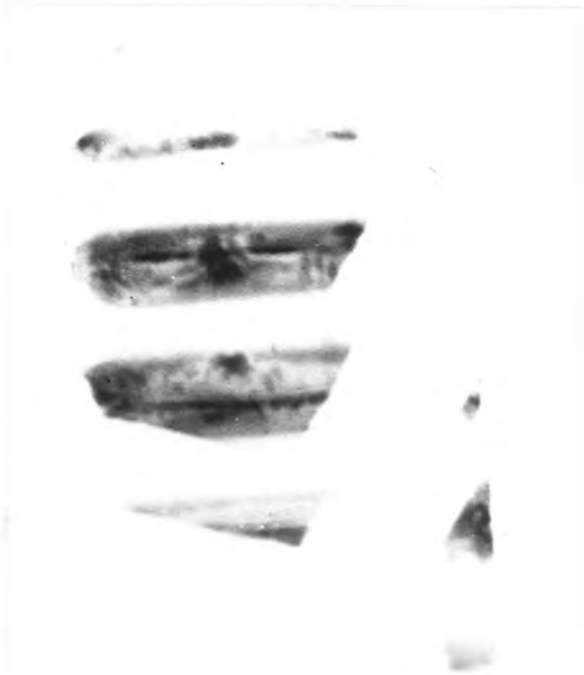

Zero Stress

[0$\bar{1}$0]

[001]

(a)

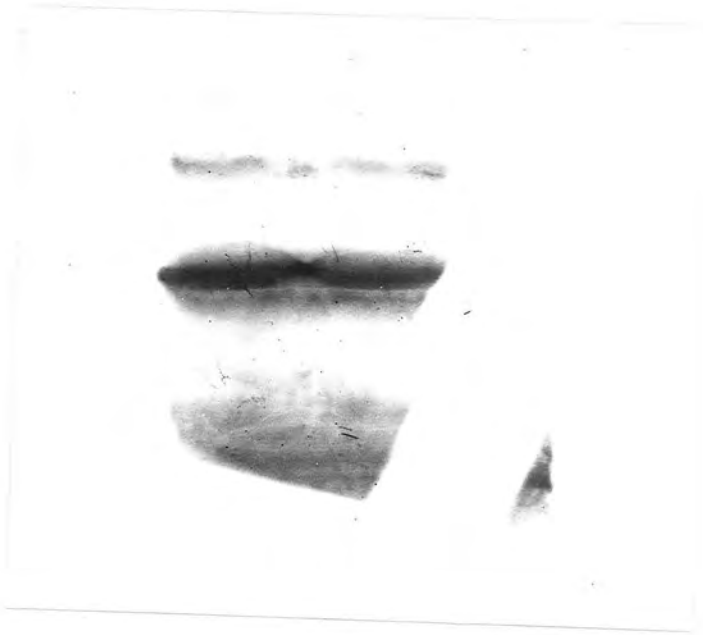

Stress 26 kg cm^{-2}

1mm

(b)

cooled. The crystal was held in tweezers and dipped into the liquid nitrogen before being placed in the slot in the perspex holder. On this experimental run the crystal was cooled corner first, whereas the domain structure shown in fig 6.9 resulted from the crystal being cooled edge first. Domain walls were never observed on a plane perpendicular to the edge which was first cooled.This supports the theory of island nucleation of domains with domain walls forming perpendicular to the temperature gradient. This sequence proceeds to a single domain via a structure containing a few small lamellae domains. On removal of the stress a simple domain configuration reforms.

Typical rocking curve data is shown in fig 6.12. In all cases rocking curve data were obtained with the crystal unsupported except by the slot in the perspex holder. A very marked change occurred between the zero stress curve and that corresponding to a small load. (fig 6.12a and 6.12b) Subsequent increments in stress resulted in a reduction of intensity in one set of peaks and an increase in intensity of the other set finally resulting in two peaks, (fig 6.12d) corresponding to $K_{\alpha 1}$ and $K_{\alpha 2}$ reflections from a single domain sample.

The rocking curve shown in fig 6.12a represents a domain structure consisting of two different types of domain. With the $K_{\alpha 1}$ and $K_{\alpha 2}$ peaks from the two domains just resolved. Although it has not been possible to reconcile completely the relative peak heights with a domain structure model the sample probably contains a mixture of d_x and d_y domains with (110) and $(1\bar{1}0)$ wall planes. Upon

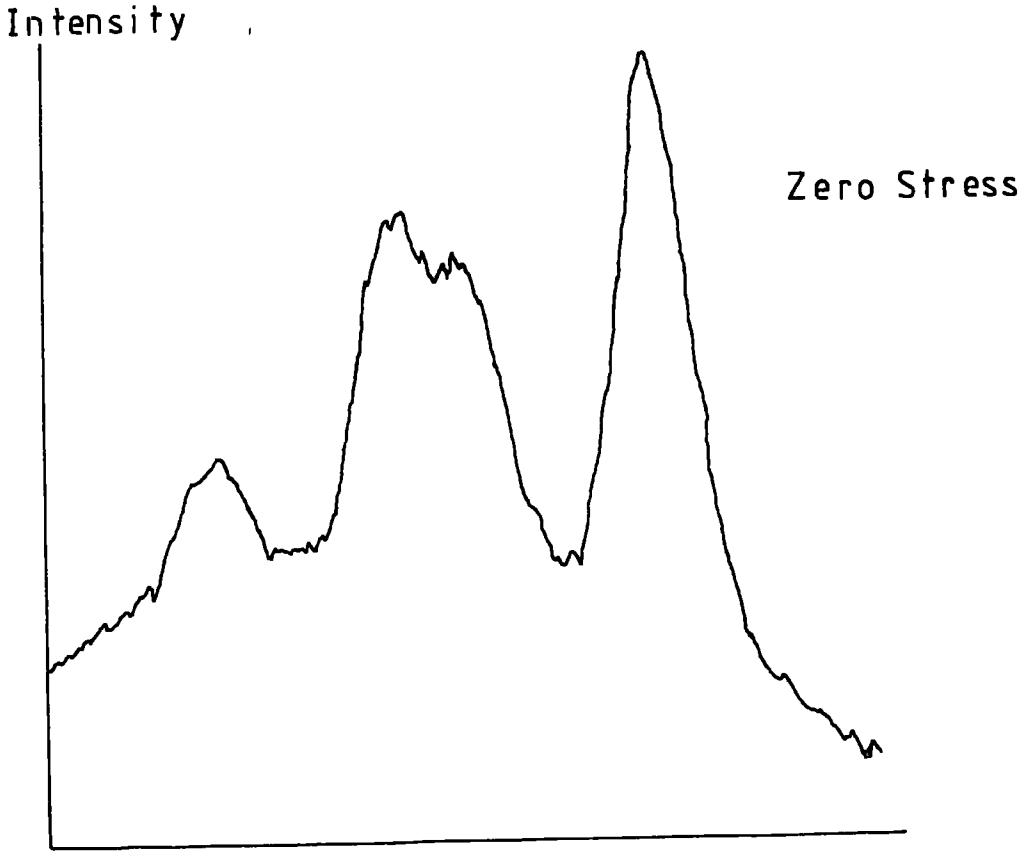

(a)

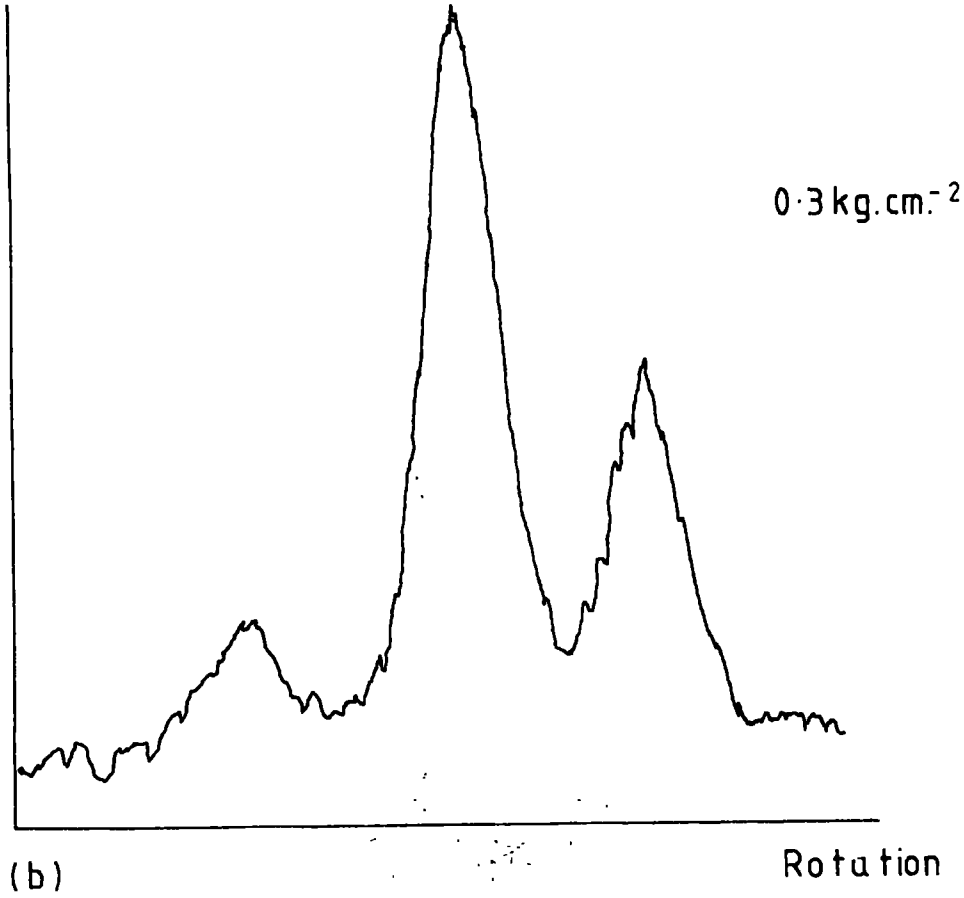

(b)

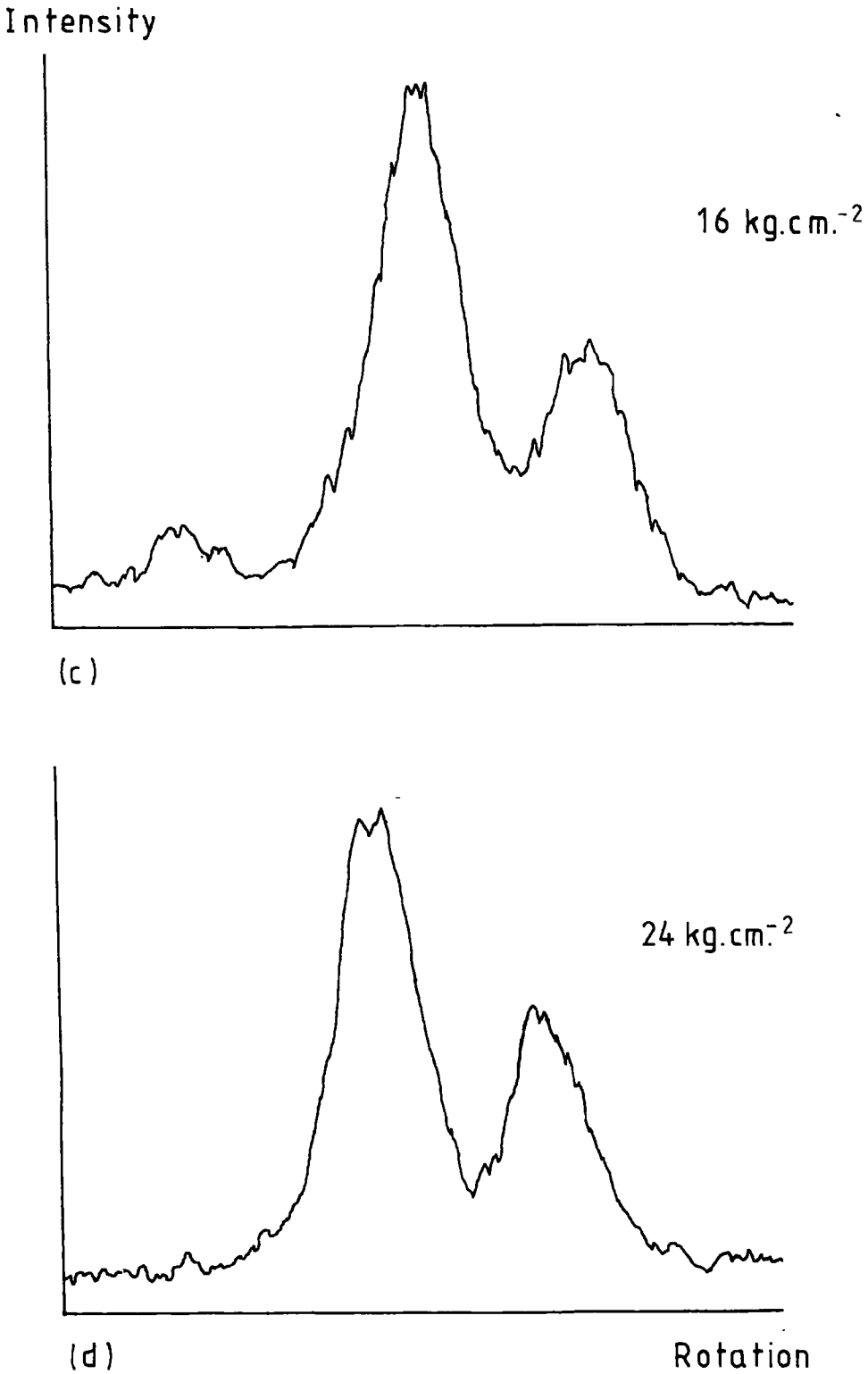

Fig. 6.12 $KCoF_3$ Rocking Curve Data

(220 Reflection Ag $K_{\alpha c}$ Radiation)

application of a stress, fig 6.12b, the sample immediately changes to a system of d_z and either d_x or d_y domains. This occurred at stresses below 0.3 Kg cm^{-2}. From a consideration of the domain structure observed in synchrotron topographs it is concluded that the domain structure consists of d_x and d_z domains with walls on (101) and $(10\bar{1})$. With subsequent loading the small angle peak gradually diminished finally leaving a single d_z domain.

The separation between the $K_{\alpha 1}$ and $K_{\alpha 2}$ peaks and their relative heights are as expected. Calculations of the magnetostriction constants from the splitting of the peaks for the assumed domain structure is in agreement with published values and the loss of the small angle peak is expected for a negative magnetostriction material. Numerical data from these experiments is presented in table 6.1.

6.6 Discussion

These results provide direct evidence that the interpretation of the stress dependant linear dichroism experiments of Ferré et al. (1976) as being due to antiferromagnetic domain wall motion at low stress is correct and that the loss of the fourfold term under stress in the torque experiments of Hirakawa et al. (1961) does result from the removal of domains. Hence the fourfold term must arise from antiferromagnetic domain wall motion.

The very small value of the threshold stress when the crystal was not wedged in the holder is in agreement with the

Table 6.1

Threshold Stress	Critical Stress	
σ_{th} (Kg cm^{-2})	σ_{cr} (Kg cm^{-2})	C_L (J m^{-3})
1.4 ± 0.4	30 ± 0.6	$4 \pm 2 \times 10^3$
< 0.4	22 ± 0.4	$5.5 \pm 2 \times 10^3$
< 0.3	24 ± 0.5	$6 \pm 2 \times 10^3$
< 0.3	27 ± 0.6	$6.7 \pm 2 \times 10^3$
Magnetic field results Safa and Tanner (1978)		$2.2 \pm 0.2 \times 10^3$
		$2.9 \pm 0.2 \times 10^3$

$\lambda_{100} = -1.9 \times 10^{-3}$ (77K) Julliard and Nouet (1975)

results of Ferré et al. (1976). When the crystal was wedged high values for both threshold and critical stresses were obtained, the differences remaining roughly constant. Wedging the crystal exerts an extra stress along the [100] direction which tends to favour d_x domains. This introduces a constant force on the domain wall tending to oppose domain wall motion due to an [001] applied stress.

The agreement between the stress and magnetic field data is only fair. This may be due to systematic errors due to the impossibility of preparing accurately parallel sided strain free thin platelets of this material. However the order of magnitude agreement suggests a common origin for the restoring force.

One suggestion for the origin of this restoring force, Safa and Tanner (1978), is that it may be associated with long range interactions between adjacent domain walls. Another possibility is from the presence of long range stresses within the crystal.

The magnitude of internal strains within the crystal can be estimated from the width of double crystal X-ray rocking curves. These have been measured at 7×10^{-5} to 11×10^{-5} radians Miriam Abdul Gani (1979) with 1×10^{-5} to 5×10^{-5} calculated from the elastic constants of Rousseau et al. (1974) and a critical stress of 24Kg cm^{-2} measured in this experiment. Internal strains and hence stresses within the crystal are thus of the required order of magnitude to provide the necessary restoring force on the domain walls.

The observed strains introduced by glueing these crystals could result in internal stress distributions large enough to account for the restoring force measured in the magnetic field experiments of Safa and Tanner (1978).

CHAPTER SEVEN

MAGNETOSTRICTION MEASUREMENTS ON TERBIUM

CHAPTER SEVEN

MAGNETOSTRICTION MEASUREMENTS ON TERBIUM

7.1 Introduction

Terbium is one element of the series of rare-earth elements or lanthanides. These elements are all in group IIIa of the periodic table and have atomic numbers from 57 to 71. They are characterized by possessing an unfilled 4f electron shell, two 6s electrons and possibly a 5d electron in addition to a xenon core. The 6s electrons and a 4f or the 5d electron usually form the conduction electrons to give a normal valency of 3. The outer electron shell remains unchanged throughout the group of rare-earth metals. This gives rise to very similar chemical properties for all the rare-earth elements and resulted in difficulties in extracting pure rare-earth metals before the development of the ion exchange method. Preparation of pure single crystals for experimental work has also been hampered by their affinity for oxygen, hydrogen and helium.

The first single crystals were produced at the Ames Laboratory U.S.A. in the early 1960's. Techniques for producing rare-earth crystals have recently been reviewed by McEwan and Touborg (1973), Jordan (1974) and Jones et al. (1977). All of the early material and most of the materially currently produced suffers from the presence of impurities probably in the form of inclusions of oxide platelets. This has resulted in anomalies in bulk magnetic measurements and in variations in results reported by different workers depending on their source of material.

In the case of magnetic anisotropy measurements on gadolinium differences have been reported in measurements of the uniaxial easy direction and in values of the anisotropy constants. Smith et al.(1977), have shown that the differences can be explained by the presence of non-magnetic inclusions in the form of platelets of the order of 1-2% by volume. Hexagonal platelets precipitated parallel to the basal plane have been observed in crystals of 3N (99.9%) gadolinium with respect to magnetic impurities. Examination of optical micrographs of this material indicate that sufficient impurities may be present in this form to explain differences in the measured anisotropy constants between material of this purity and material of much higher purity produced by the solid state electrotransport process.

Most rare-earths crystallize in either the hexagonal-close-packed structure or double hexagonal-close-packed structure. Terbium is no exception, crystallizing in the hexagonal-close-packed structure as shown in fig 7.1 which shows several of the principal planes and directions defined in terms of the Miller-Bravais indic es and an orthogonal co-ordinate system.

General reviews of the rare-earth elements, alloys and compounds and intermetallic rare-earth compounds can be found in the following references, Cooper (1968), Taylor (1970, 1971), Taylor and Darby (1972), Elliott(1972), Rhyne and McGuire (1972), Coqblin (1977) and Gschneidner and Eyring (1978).

7.2 Magnetic Properties of Rare-Earth Metals

Gadolinium was the first rare-earth metal shown to exhibit

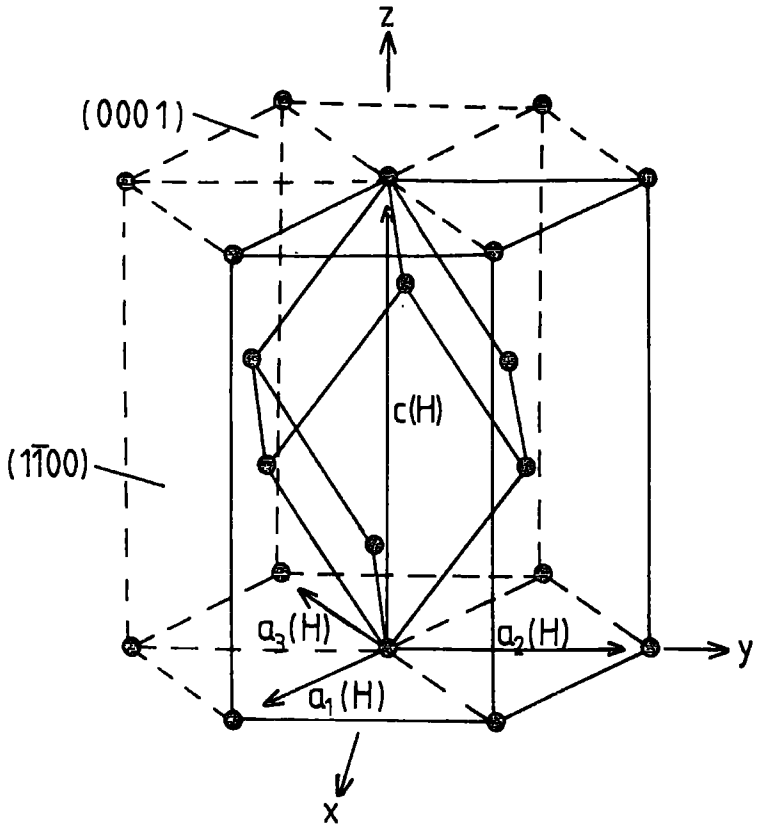

Fig. 7.1 Hexagonal-close-packed Structure

ferromagnetism by Ubain et al. (1935). Since then a wide variety of magnetic behaviour has been discovered throughout the series.

The magnetic properties of the rare-earth elements arise from the highly localised incomplete 4f electron shell. The filling of the 4f shell is in accordance with Hund's rules, thus enabling the effective number of Bohr magnetons, μ_{eff} and the paramagnetic susceptibility to be calculated. The magnetic moment is close to the value predicted for the trivalent ions of all the rare-earths except for samarium and europium. The small discrepancies in most of the rare-earths can be accounted for by consideration of the polarization of the conduction electrons. The large discrepancies in samarium and europium, can be explained by the mixing of the ground state and first excited state at room temperature - a process proposed by Van Vleck and Frank (1929).

All the rare-earths except lanthanum, ytterbium and lutetium exhibit magnetic ordering at low temperatures, all except gadolinium exhibiting an antiferromagnetic phase as well as a ferromagnetic phase. The ordering of the heavy rare-earths determined through neutron diffraction techniques is shown in Table 7.1.

The magnetic properties of the rare-earth metals are due to the 4f electrons which are screened by 5s and 5p electrons. The variety of magnetic properties exhibited by the rare-earth metals is due to the differing numbers of 4f electrons. The direct exchange interaction between 4f electrons is far too small to account for the observed magnetic ordering and hence Rudermann and Kittel (1954), Kasuya (1956) and Yosida (1957) developed a theory assuming

Summary of the magnetic structures of heavy rare earth metals. The different notations of the table are: (1) Metal. (2) Paramagnetic Curie temperature of polycrystals. (3) Paramagnetic Curie temperature of single crystals with the magnetic field applied along the $\vec{c}$-axis. (4) Paramagnetic Curie temperature of single crystals with the magnetic field in the basal plane. (5) Temperatures of the specific heat anomalies. (6) Neel temperature. (7) Structure below the Neel temperature. (8) Intermediate ordering temperature T_H (for Erbium only). (9) Structure below T_H (for Erbium only). (10) Ferromagnetic Curie temperature. (11) Structure below the Curie temperature. (12) Saturation magnetization parallel to the easy magnetization axis (in μ_B). (13) Theoretical values of the magnetic moment for the trivalent rare earths ion (in μ_B).

(1) Metal	(2) θ_p(K)	(3) $\theta_{\parallel}$(K)	(4) $\theta_{\perp}$(K)	(5) T_λ(K)	(6) T_N(K)	(7) Structure	(8) T_H(K)	(9) Structure	(10) T_c(K)	(11) Structure $T = 4.2$ K	(12) μ_{sat} (μ_B)	(13) $g_J J$ (μ_B)
Gd	317	317	317	291.8	$T_N = T_C$ 293.2	Ferromagnetic (g): ($\vec{\mu}$, $\vec{c}$) angle variable with T					7.55	7.0
Tb	237	195	239	227.7 221	229	Helix (e): $\vec{\mu} \perp \vec{c}$ $\omega_i = 20.5°$ $\omega_{f'} = 18°$			221	Ferro (f): $\vec{\mu} \perp \vec{c}$	9.34	9
Dy	153	121	169	174 83.5	179	Helix (e): $\vec{\mu} \perp \vec{c}$ $\omega_i = 43°$ $\omega_{f'} = 26.5°$			87	Ferro (f): $\vec{\mu} \perp \vec{c}$	10.2	10
Ho	87	73	88	131.6 19.4	133	Helix (e): $\vec{\mu} \perp \vec{c}$ $\omega_i = 51°$ $\omega_{f'} = 33°$			20	Cone (d) $\omega = 30°$ $\omega_f = 30°$	10.34	10
Er	40	61.7	32.5	84 53.5 19.9	80	$\vec{c}$-axis modulated with occurrence of harmonics. $\vec{\mu} \parallel \vec{c}$ (b). $\omega_i = 51.4°$	$T_H = 53$ $\omega = 51.4$	$\vec{c}$-axis modulated with occurrence of harmonics. Helix for $\mu_{\perp}$(c). $\omega_{f'} = 45°$	20	Cone (d) $\omega = 45°$ $\omega_f = 45°$	8	9
Tm	20			55	56	$\vec{c}$-axis modulated: $\vec{\mu} \parallel \vec{c}$(b) $\omega_i = 51.4°$ $\omega_{f'} = 51.4°$			38	Antiphase Ferro. 3–4 (a) $\omega_f = 51.4°$	3.4	7

TABLE 7.1 (AFTER COQBLIN(1977))

the exchange coupling of the 4f electrons involved the polarization of the conduction electrons. The simplest explanation of this theory, (Crangle 1977), is to consider a local magnetic moment surrounded by a cloud of conduction electrons. The site of the local moment then becomes favourable for conduction electrons of parallel magnetic moment and unfavourable for conduction electrons of antiparallel magnetic moment. The wave functions of the conduction electrons will distort in response to this local moment by mixing in other electron states of the same spin orientation. Electron states above the Fermi level will thus add at the local moment where they will be in phase and constructive interference will result. Since there are different electron states there will be different wave vectors and hence phase differences will be present between different wave functions as the distance from the local moment increases. The distribution of electrons with spins parallel and antiparallel to the local moment will thus be oscillatory. The overall charge density will remain constant since the effect on the wave functions of electrons with spins parallel and antiparallel to the local moment will be opposite.

7.3 Magnetic Properties of Terbium

Terbium possesses both ferromagnetic and antiferromagnetic phases. Reported values of the Néel temperature are between 226 and 230K, while reported values of the Curie temperature are between 214 and 228K. Recent experiments by Palmer (1980) employing ultra-sonic techniques on recently available high purity solid state electro-

transport terbium give a Curie temperature of 219 or 214K. Similar results were obtained on "Metals Research" terbium, (Palmer et al. 1979). Neutron diffraction experiments, (Crangle 1979), on solid state electrotransport terbium give a Curie temperature of 216K. More will be said about these results later.

Neutron diffraction experiments by Koehler et al. (1963) and Koehler (1967) established that the spin structure in the antiferromagnetic region is oscillatory although it cannot be said to be definitely helical because the structure deforms spontaneously to a planar ferromagnet when the moments are far from saturated. There is also evidence of a narrow temperature range where both the ferromagnetic and antiferromagnetic states coexist, Nagamiya (1962). Below the Curie temperature the easy directions of magnetization lie along the b directions, (Hegland et al.1963). Within the antiferromagnetic region the turn angle varies between about 16 and 21° per layer as shown in fig 7.2, (Koehler 1965, Dietrich and Als-Nielsen 1967). The nature of the spins is shown diagramatically in fig 7.3.

The transition between the antiferromagnetic region and the ferromagnetic region occurs because of the competition between the exchange interaction in the undistorted lattice favouring a spiral arrangement and the magnetostriction or the hexagonal anisotropy effects favouring ferromagnetic order. The temperature dependence of these effects differ and hence the transition occurs.

Strain introduced on mounting and cooling the crystal could result in discrepancies in the Curie temperature. The ultrasonic results on the elastic constants of Palmer et al. (1979) on two samples of "Metals Research" terbium give a Curie temperature

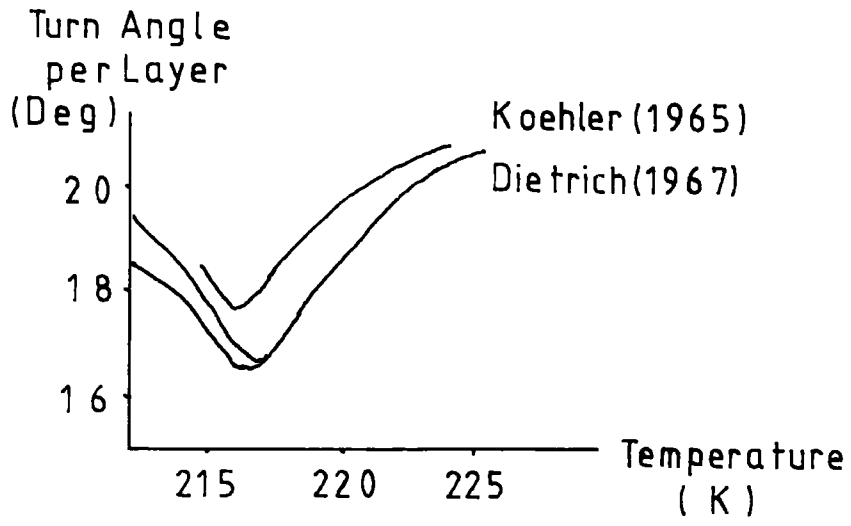

Fig. 7.2 Terbium Interplaner Turn Angles

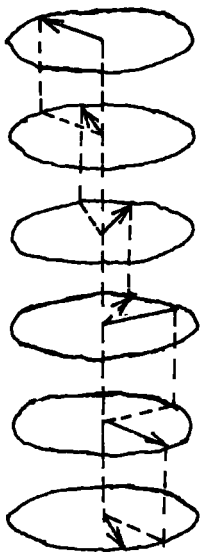

Fig. 7.3 Helical Antiferromagnetic Order

of 219K on a recently prepared sample and 214K on a similar sample which had been used extensively in previous experiments. The magnetic phase diagram for these samples are shown fig 7.4. The implication is that the previous history of the older sample had resulted in the presence of strain within this sample reducing the Curie temperature. Palmer's (1980) measurements on solid state electrotransport terbium mostly result in a Curie temperature of 219K, although on one occasion a value of 214K was obtained. These results are in excellent agreement with the values obtained from the measurement of magnetostriction to be reported here on solid state electrotransport terbium from the same source as used by Palmer. On all but one occasion the Curie temperature obtained was 219K. On the remaining occasion a value of 214K was obtained.

Measurements of the second and fourth order axial anisotropy constants have been made by Levitin and Ponomarev (1968) and are shown in fig 7.5, together with the calculated temperature dependence of Féron et al. (1970) based on the single-ion model. The basal plane anisotropy constant has been measured by Rhyne and Clark (1967) and Bly et al. (1968), and shown in fig 7.6, together with the calculated result of Cooper (1968).

The very high value of the axial anisotropy effectively constrains the magnetization to lie in the basal plane which has been shown in neutron diffraction data of Koehler (1962). Corner and Al-Bassam (1971) devised a model to explain the domain structure they observed in terbium using the dry colloid technique. This model, illustrated in fig 7.7, is based on 60^{o}, 120^{o} and 180^{o} Bloch walls

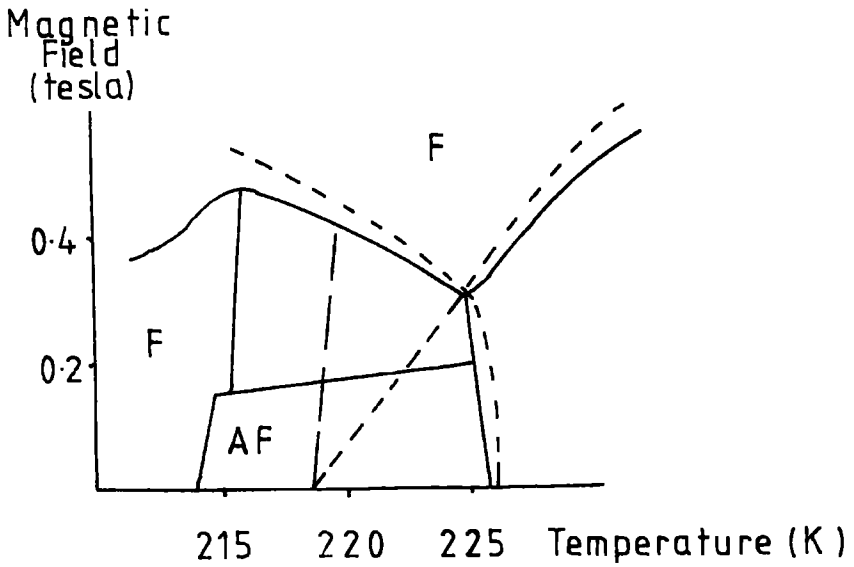

Fig. 7.4 Magnetic Phase Diagram of Terbium
(Palmer et al. 1979)

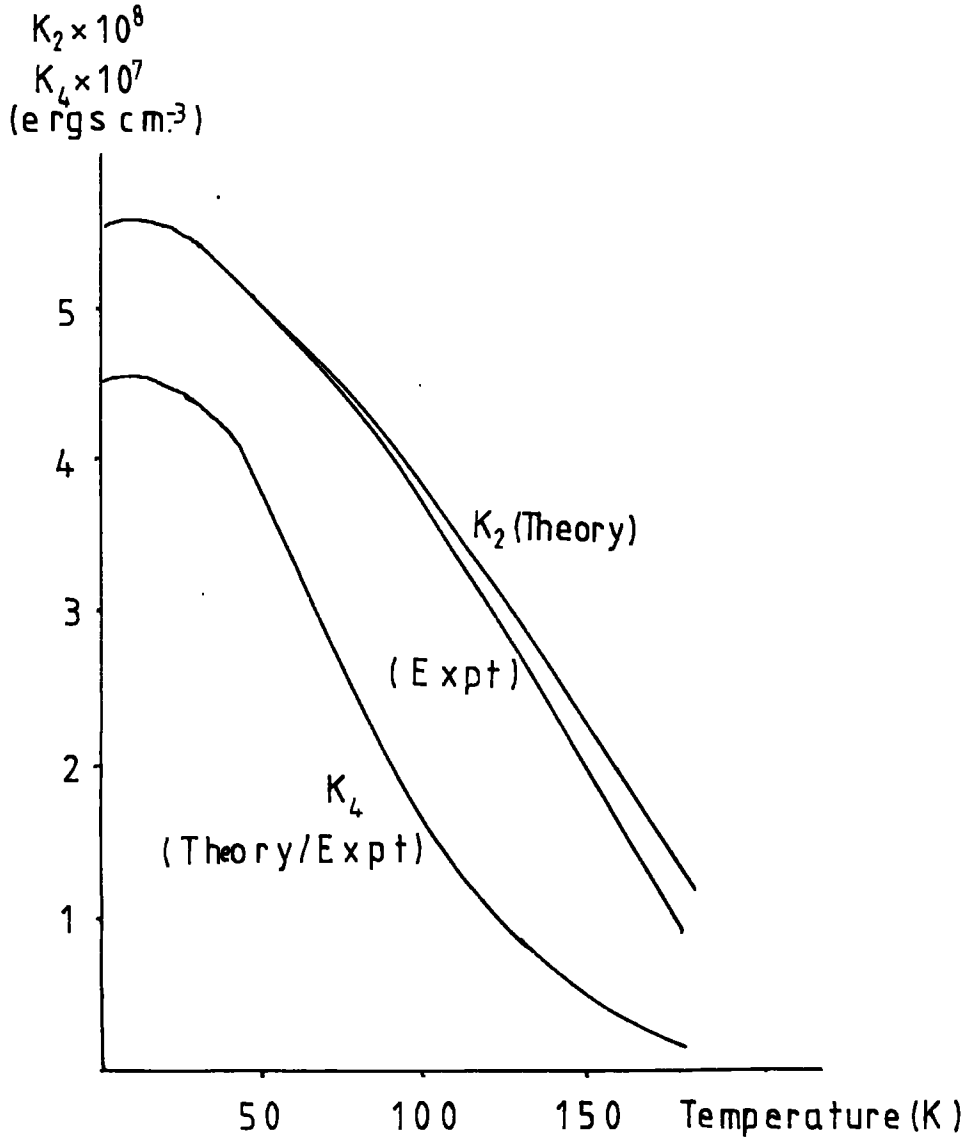

Fig. 7.5 Terbium 2nd and 4th Order Axial Anisotropy Constants

(Expt. Levetin and Ponomarev 1968

Theory Féron et al. 1970)

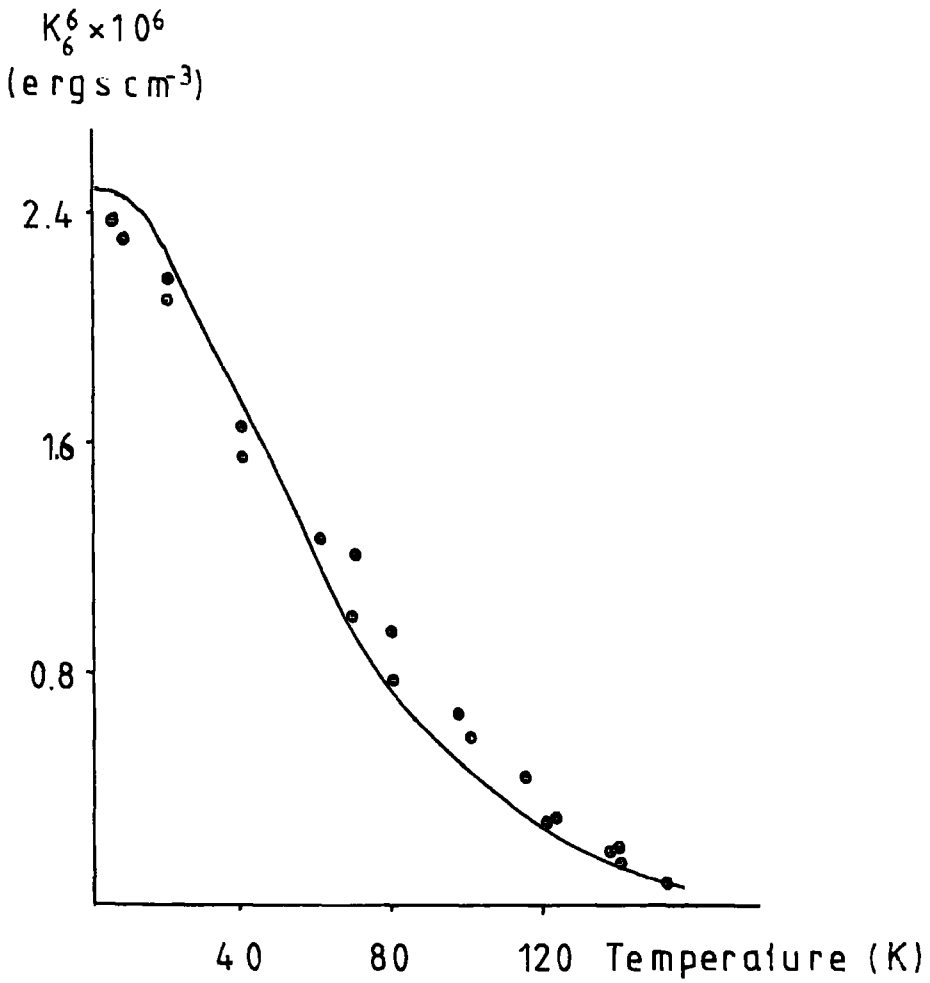

Fig. 7.6 Terbium Basal Plane Anisotropy Constant
(Expt. Rhyne and Clark 1967
Theory Cooper 1968)

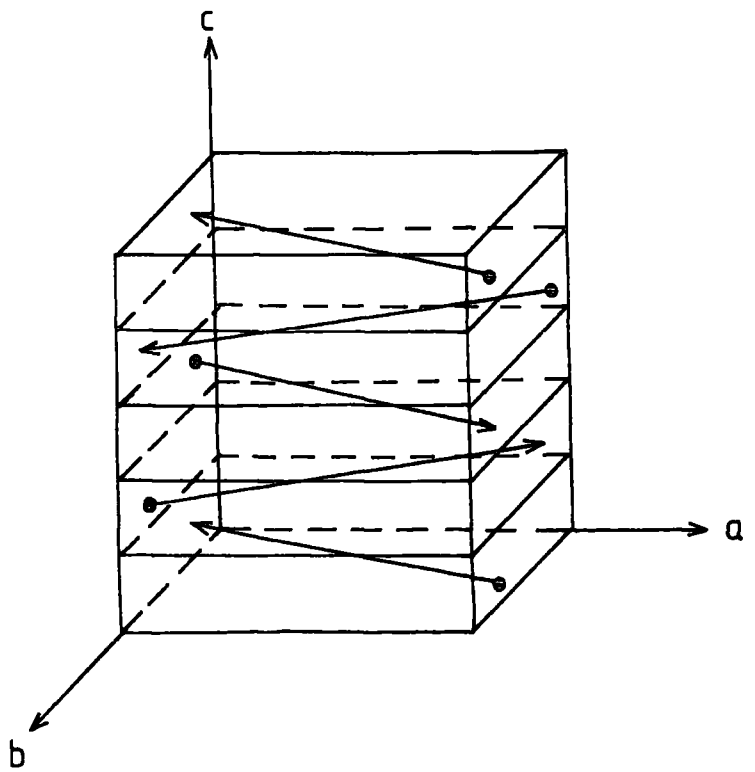

Fig. 7.7 Terbium Layer Domain Structure
(Corner and Al-Bassam 1971)

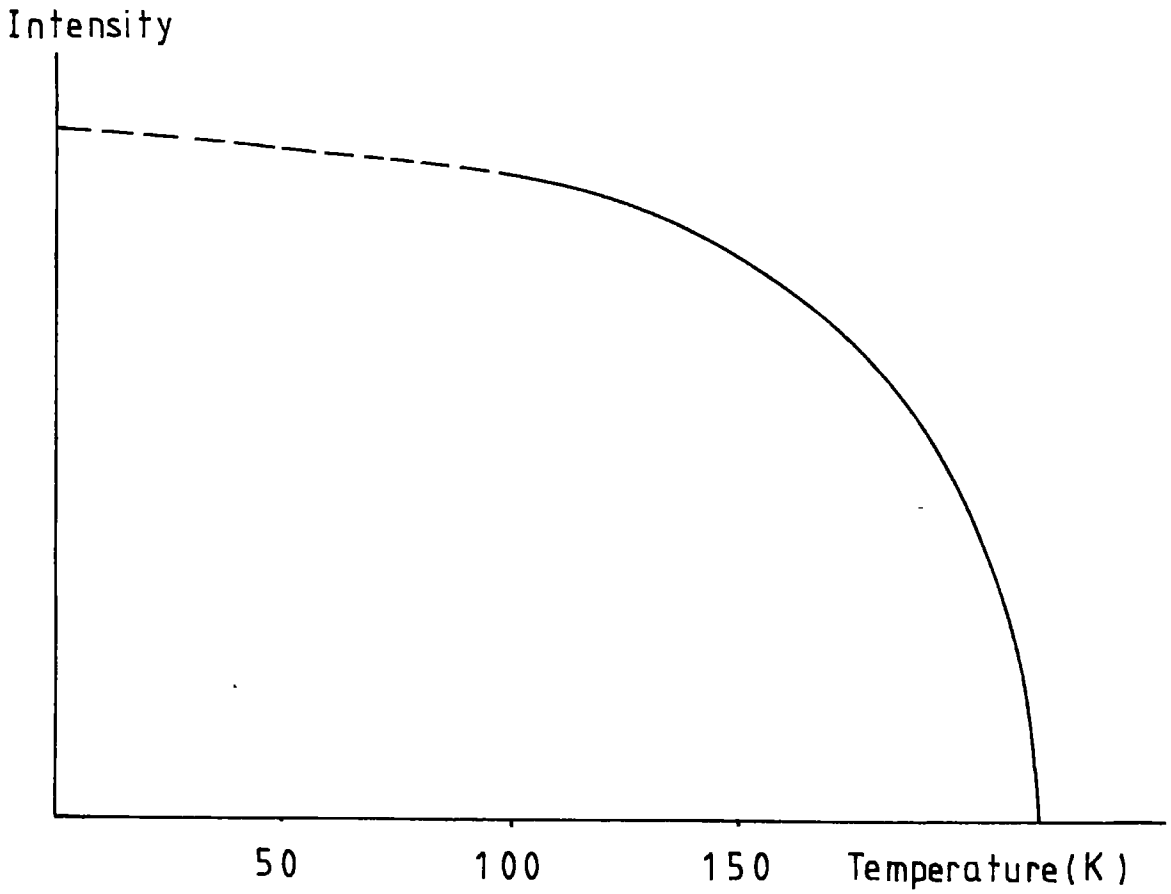

Fig. 7.8 Spontaneous Magnetisation of Terbium

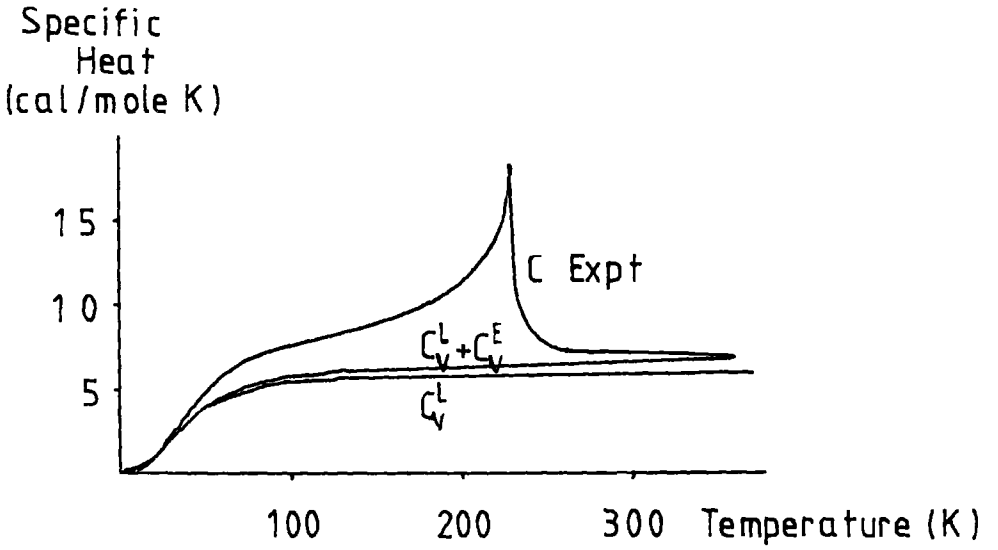

Fig. 7.9 Specific Heat of Terbium
(Houmann and Nicklow 1970)

lying parallel to the basal plane. Further limited, but confirmatory information on the domain structure of terbium has been obtained using synchrotron X-ray topography,(Tanner et al. 1977) and a structure composed of Néel walls parallel to the c axis has been observed (Herring and Jakubovics 1973).

The relative spontaneous magnetization of terbium as a function of temperature is obtainable from the results of Dietrich and Als-Nielsen (1967) and is shown in fig 7.8. Their neutron diffraction data shows that the magnetic long range order follows the characteristic temperature variation of spontaneous magnetization.

The specific heat of terbium has been measured by Houmann and Nicklow(1970) and is shown in fig 7.9 together with their calculated values. The anomaly associated with the magnetic ordering can be clearly seen.

7.4 Magnetostriction of Terbium

The magnetostriction of a material is the spontaneous distortion or change in dimensions of a material associated with its magnetic behaviour and arises from the interaction between magnetic anisotropy and exchange energies and the elastic energy. The expressions commonly used to define the magnetostriction of hexagonal crystals are;

$$\frac{\Delta L}{L} = {}^{1}\lambda_o^{\alpha} + {}^{2}\lambda_o^{\alpha}(\beta_3^2 - \tfrac{1}{3}) + {}^{1}\lambda_2^{\alpha}(\alpha_3^2 - \tfrac{1}{3})$$
$$+ {}^{2}\lambda_2^{\alpha}(\alpha_3^2 - \tfrac{1}{3})(\beta_3^2 - \tfrac{1}{3})$$
$$+ \lambda_2^{\varepsilon}[\tfrac{1}{2}(\alpha_1^2 - \alpha_2^2)(\beta_1^2 - \beta_2^2) + 2\alpha_1\alpha_2\beta_1\beta_2]$$

$$+ \quad \lambda_2^{\epsilon} 2\alpha_3\beta_3(\alpha_1\beta_1 + \alpha_2\beta_2) \; + \; {}^1\lambda_4^{\kappa}(7\alpha_3^4 - 6\alpha_3^2 + 3/5)$$

$$+ \quad {}^2\lambda_4^{\alpha}(\beta_3^2 - 1/3)(7\alpha_3^4 - 6\alpha_3^2 + 3/5)$$

$$+ \quad {}_1\lambda_4^{\gamma}[1/2(\alpha_1^2 - \alpha_2^2)(\beta_1^2 - \beta_2^2) + 2\alpha_1\alpha_2\beta_1\beta_2](\alpha_3^2 - 1/7)$$

$$+ \quad {}_2\lambda_4^{\gamma}[6\alpha_1^2\alpha_2^2 - \alpha_1^4 - \alpha_2^4)(\beta_1^2 - \beta_2^2) + 8(\alpha_1^2 - \alpha_2^2)\alpha_1\alpha_2\beta_1\beta_2]$$

$$+ \quad \lambda_4^{\epsilon} 2\alpha_3\beta_3(\alpha_1\beta_1 + \alpha_2\beta_2)(\alpha_3 - 3/7) \qquad (7.1)$$

or $$\frac{\Delta L}{L} = A[2\alpha_1\alpha_2\beta_1 + (\alpha_1^2 - \alpha_2^2)\beta_2]^2$$

$$+ \quad B\alpha_3^2[(\alpha_1\beta_1 + \alpha_2\beta_2)^2 - (\alpha_1\beta_2 - \alpha_2\beta_1)^2]$$

$$+ \quad C[(\alpha_1\beta_1 + \alpha_2\beta_2)^2 - (\alpha_1\beta_2 - \alpha_2\beta_1)^2]$$

$$+ \quad D'(1 - \alpha_3^2)(1 - \beta_3^2) + E\alpha_3^2\beta_3^2(1 - \alpha_3^2)$$

$$+ \quad F\alpha_3^2(1 - \alpha_3^2) + G'\beta_3^2(1 - \alpha_3^2)$$

$$+ \quad H\alpha_3\beta_3(\alpha_1\beta_1 - \alpha_2\beta_2) + I\alpha_3^3\beta_3(\alpha_1\beta_1 + \alpha_2\beta_2)$$

$$+ \quad J\alpha_3^2(1 - \beta_3^2) + K\alpha_3^2\beta_3^2 \qquad (7.2)$$

where the α_i's are the direction cosines of the magnetization direction and the β_i's are the direction cosines of the measuring direction. These are modifications of the original expression by Mason (1954). Darnell (1963) introducing the J and K terms. The terms D and G of Mason's expression becoming D'-J and G'-K. Neither expression uses fundamental coefficients and to do so introduces awkward numerical factors. Constants from the two expressions can be related, (Birss et al. 1978) by

$$\begin{bmatrix} J \\ K \\ G'-K \\ D'-J \\ F \\ E \\ A \end{bmatrix} = \begin{bmatrix} 1 & -\frac{1}{3} & \frac{2}{3} & -\frac{2}{9} & \frac{8}{5} & -\frac{8}{15} & 0 \\ 1 & \frac{2}{3} & \frac{2}{3} & \frac{4}{9} & \frac{8}{5} & \frac{16}{15} & 0 \\ 0 & 0 & -1 & -\frac{2}{3} & -1 & -\frac{2}{3} & 0 \\ 0 & 0 & -1 & \frac{1}{3} & -1 & \frac{1}{3} & -1 \\ 0 & 0 & 0 & 0 & -7 & \frac{7}{3} & 1 \\ 0 & 0 & 0 & 0 & 0 & -7 & -1 \\ 0 & 0 & 0 & 0 & 0 & 0 & 2 \end{bmatrix} \begin{bmatrix} {}^1\lambda_0^\alpha \\ {}^2\lambda_0^\alpha \\ {}^1\lambda_2^\alpha \\ {}^2\lambda_2^\alpha \\ {}^1\lambda_4^\alpha \\ {}^2\lambda_4^\alpha \\ {}_2\lambda_4^\gamma \end{bmatrix}$$

$$\begin{bmatrix} H \\ I \end{bmatrix} = \begin{bmatrix} 2 & -\frac{6}{7} \\ 0 & 2 \end{bmatrix} \begin{bmatrix} \lambda_2^\epsilon \\ \lambda_4^\epsilon \end{bmatrix}$$

$$\begin{bmatrix} C \\ D \end{bmatrix} = \begin{bmatrix} \frac{1}{2} & -\frac{1}{14} \\ 0 & \frac{1}{2} \end{bmatrix} \begin{bmatrix} \lambda_2^\gamma \\ {}_1\lambda_4^\gamma \end{bmatrix} \qquad (7.3)$$

The magnetostriction strain modes of order L=2 have been illustrated by Clark et al. (1963, 1965) and are shown in fig 7.10. The high axial anisotropy confines the magnetization to the basal plane, and hence $\alpha_3 = 0$ which introduces some simplification into equations 7.1 and 7.2.

Measurements of the magnetostriction of terbium have been performed by Belov et al. (1961), Darnell (1963), Rhyne and Legvold (1965) and Birss et al.(1978).

Belov et al. (1961) were unable to saturate their polycrystalline sample. Darnell (1963) employed X-ray techniques to measure the magnetostriction. Absolute values of the lattice parameter were measured above and below the Curie temperature. Temperature variations in the lattice parameter below the Curie temperature were deduced

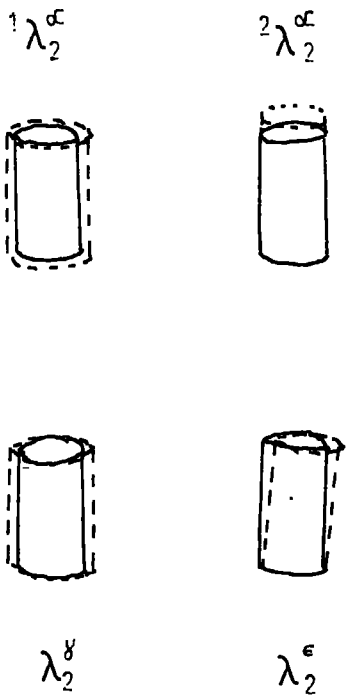

Fig. 7.10 Magnetostriction Strain Modes
(Clark et al. 1963)

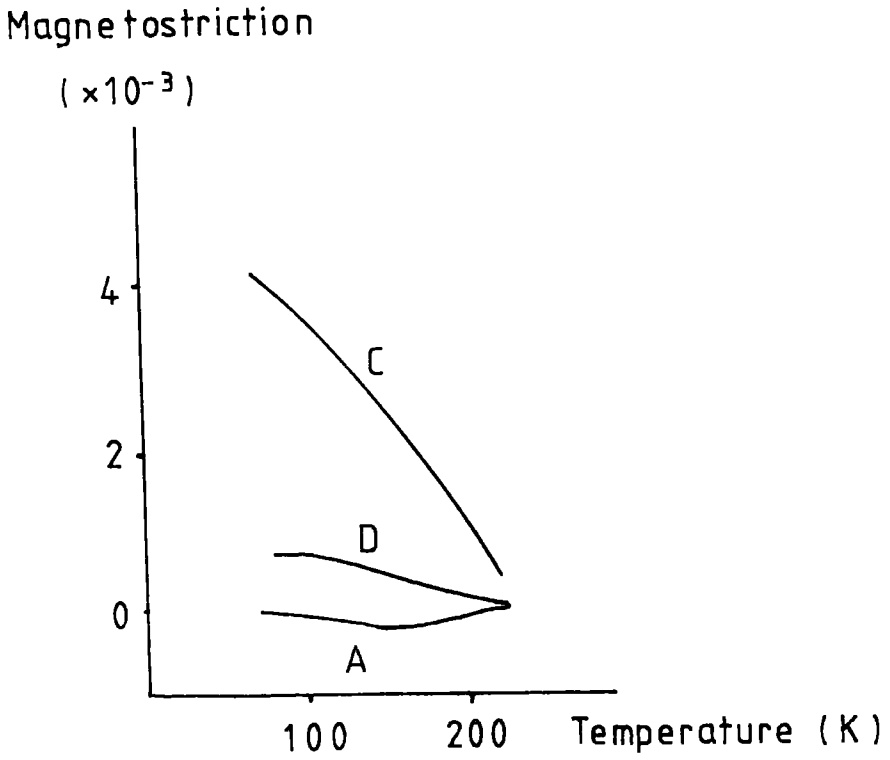

Fig. 7.11 Magnetostriction of Terbium (Darnell 1963)

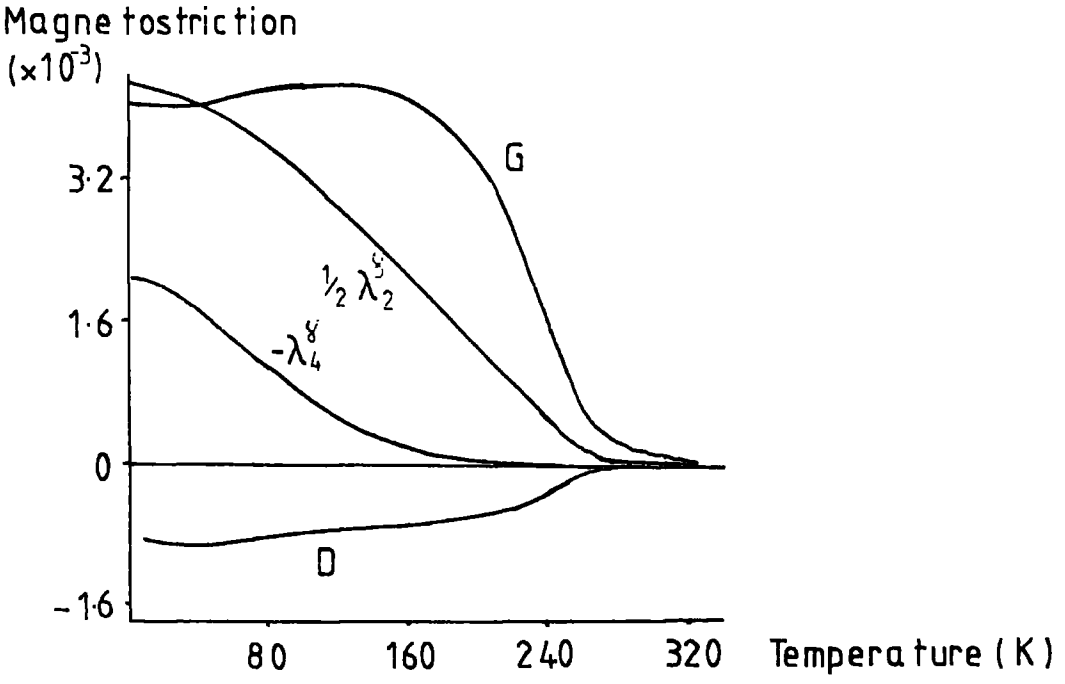

Fig. 7.12 Magnetostriction of Terbium

(Rhyne and Legvold 1965)

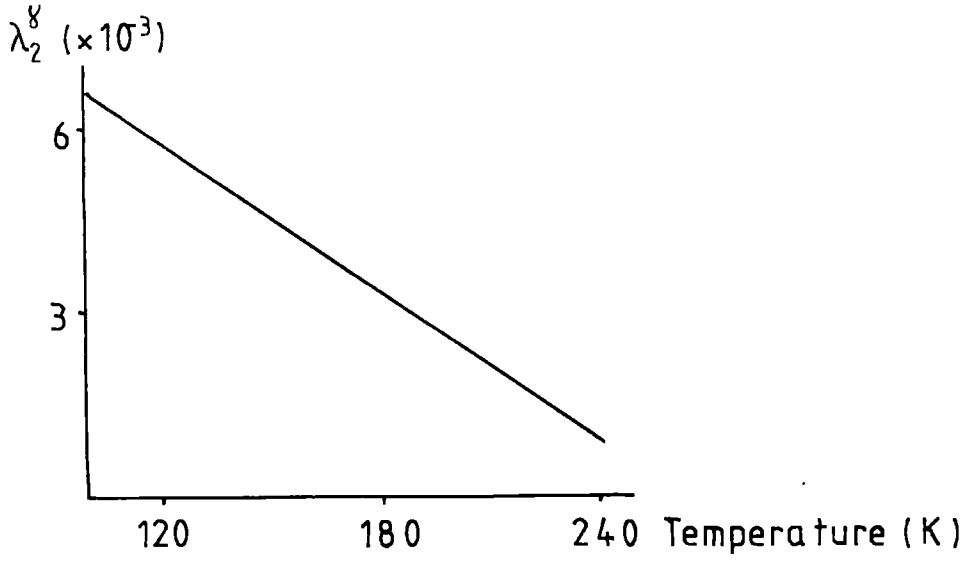

Fig. 7.13 Magnetostriction of Terbium

(Birss et al. 1978)

by extrapolating data from the paramagnetic region enabling changes in the lattice parameter due to magnetostrictive effects below the Curie temperature to be obtained. Results are shown in fig 7.11.

Rhyne and Legvold (1965) employed strain gauge techniques, originally devised by Goldman (1947) and Goldman and Smoluchowsky (1949), to measure the strain along given directions with the sample saturated, (or nearly saturated), by an applied magnetic field; the results are shown in fig 7.12. Birss et al. (1978) employed a capacitive technique to measure the dimensional changes of their sample due to an applied magnetic field; their results are shown in fig 7.13.

7.5 Experimental Procedure for Measuring the Magnetostriction of Terbium

The results described above on the measurement of the magnetostriction of terbium are measurements of the saturated magnetostriction. The presence of an applied magnetic field, typically 3 Tesla induces ferromagnetic order above the Curie temperature. Measurement of the spontaneous mis-orientation of the lattice and spontaneous differences in the lattice parameter due to magnetostrictive effects under zero applied field will give information on the spontaneous magnetostrictive constants.

Terbium possesses three easy directions of magnetization along the 3 b axes. The magnetostrictive deformation will result in a mis-orientation of the lattice, between adjacent domains magnetized along different easy directions, in order to minimise the strain

energy associated with the lattice discontinuity across the domain boundary. If a $(10\bar{1}0)$ surface sample is divided into domains magnetized along the $\pm[1\bar{1}00]$ and $\pm[01\bar{1}0]$ directions there will be no difference in lattice parameter between these domains measured along the $[10\bar{1}0]$ or $[7270]$ directions. Then any splitting of a symmetric surface reflection X-ray rocking curve will be a direct measure of the lattice mis-orientation between the domains along a direction parallel to the diffraction planes and coplanar with the incident and diffracted X-ray beam.

If an asymmetric reflection is employed the diffraction planes will no longer be parallel to the crystal surface, and differences in lattice parameter are expected between similar planes in domains with magnetization along $\pm[1\bar{1}00]$ and $\pm[01\bar{1}0]$ directions due to the magnetostrictive deformation of the lattice. This lattice parameter difference will result in differing Bragg angles. Hence the splitting of the asymmetric surface reflection X-ray rocking curve will be a measure of the lattice mis-orientation and lattice parameter difference between the domains.

The apparatus employed consisted of the GX6 X-ray generator and the Elliot Lang camera with the sample mounted in the glass cryostat with cold finger described previously. Rocking curves were obtained by rotating the sample by means of the stepping motor on the Lang camera and feeding the output of the sodium iodide scintillation counter through a ratemeter into an X-T recorder. The ratemeter time constant was sufficiently short not to distort the rocking curves, but still provided statistical averaging.

The sample employed was a b plane sample of terbium originally grown by float zone refining in ultra high vacuum at the Ames Laboratory Iowa State University and purified by the solid state electrotransport process at the Centre for Materials Science Birmingham University. The single crystal disk, about 4 mm. in diameter and 2 mm. deep,was cut from the larger crystal by means of electro-spark erosion and was kept in an atmosphere of argon or under vacuum whenever possible to reduce oxidation to a minimum.

Chemical polishing of the sample was necessary to remove surface strain introduced by the spark cutting process and light chemical polishing was performed before each experimental run to remove any oxidised surface layer which may have formed. The chemical polish employed was a mixture of 25% concentrated nitric acid, 25% glacial acetic acid and 50% analar methanol. The main chemical polishing was performed by carefully lapping the crystal on a polishing cloth moistened with this mixture. Final chemical polishing was performed by gently swabbing the surface of the crystal with this mixture with the crystal set up for an experimental run. In both cases excess chemical was removed by repeated washing in analar methanol. Repeated chemical polishing eventually revealed the presence of subgrain boundaries. Care was taken to ensure that results were obtained only from regions of the crystal where no subgrain boundaries were detectable.

After orientation by back reflection X-ray Laue photographs the crystal was mounted on a standard X-ray goniometer head with its surface coated in vacuum grease to prevent oxidation. Rocking

curves were measured in reflection using copper K_α radiation and $3\bar{1}\bar{2}0$ reflecting planes from the $(10\bar{1}0)$ surface. Chemical polishing was then repeated and rocking curves measured and topographs recorded until the surface strain was reduced to a minimum. This was indicated by a narrowing of the rocking curve width, increase in peak intensity and a reduction in the intensity of the tail and background radiation. Examples of these rocking curves are shown in fig 7.14. The two peaks shown are due to the $K_{\alpha 1}$ and $K_{\alpha 2}$ lines of the X-ray target. The splitting between the two peaks for these and all other rocking curves agreed with the splitting expected from the different wavelength of the two X-ray lines. Fig 7.15 shows the intensity of the diffracted beam as a function of position as the sample was scanned across the X-ray beam. The intensity variations relate to the shape of the sample. This together with the rocking curves of fig 7.14 indicate the exceptionally high quality of this sample for a rare-earth crystal. Fig 7.16 is a room temperature topograph imaging the entire surface of the crystal. The resolution is not good due to the geometry necessarily employed. The density of dislocations within the sample is too high for individual dislocations to be observed, but the topograph does confirm that inhomogeneous strain is not present.

The prepared sample was carefully mounted on a holder with soft wax to give as little mounting strain as possible. The sample holder was attached to the cold finger of the cryostat in such a way that the sample could be rotated about the b axis perpendicular to its surface. Additional control of the orientation

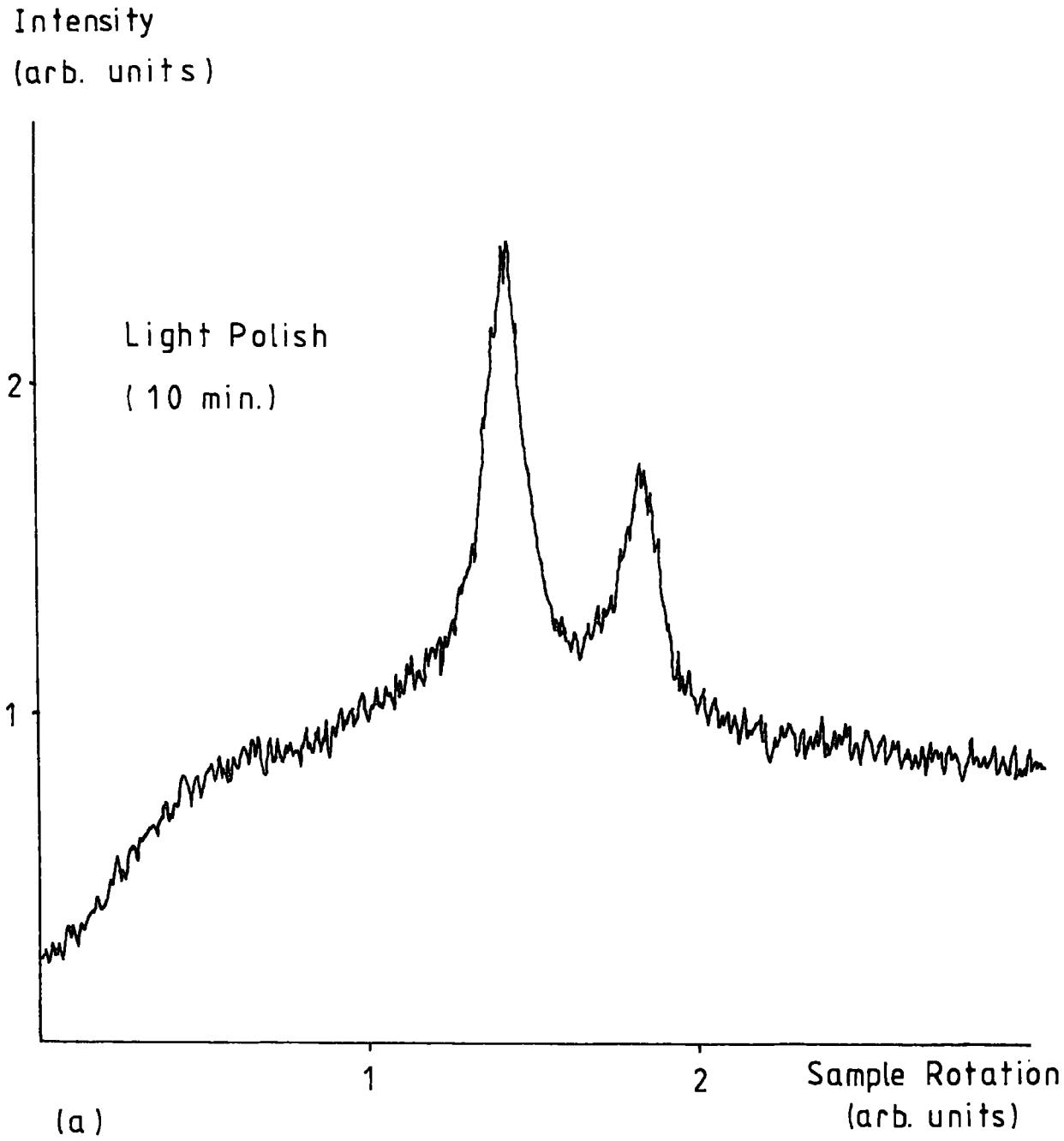
Intensity
(arb. units)
Light Polish
(10 min.)
2
1
1
2
Sample Rotation
(arb. units)
(a)

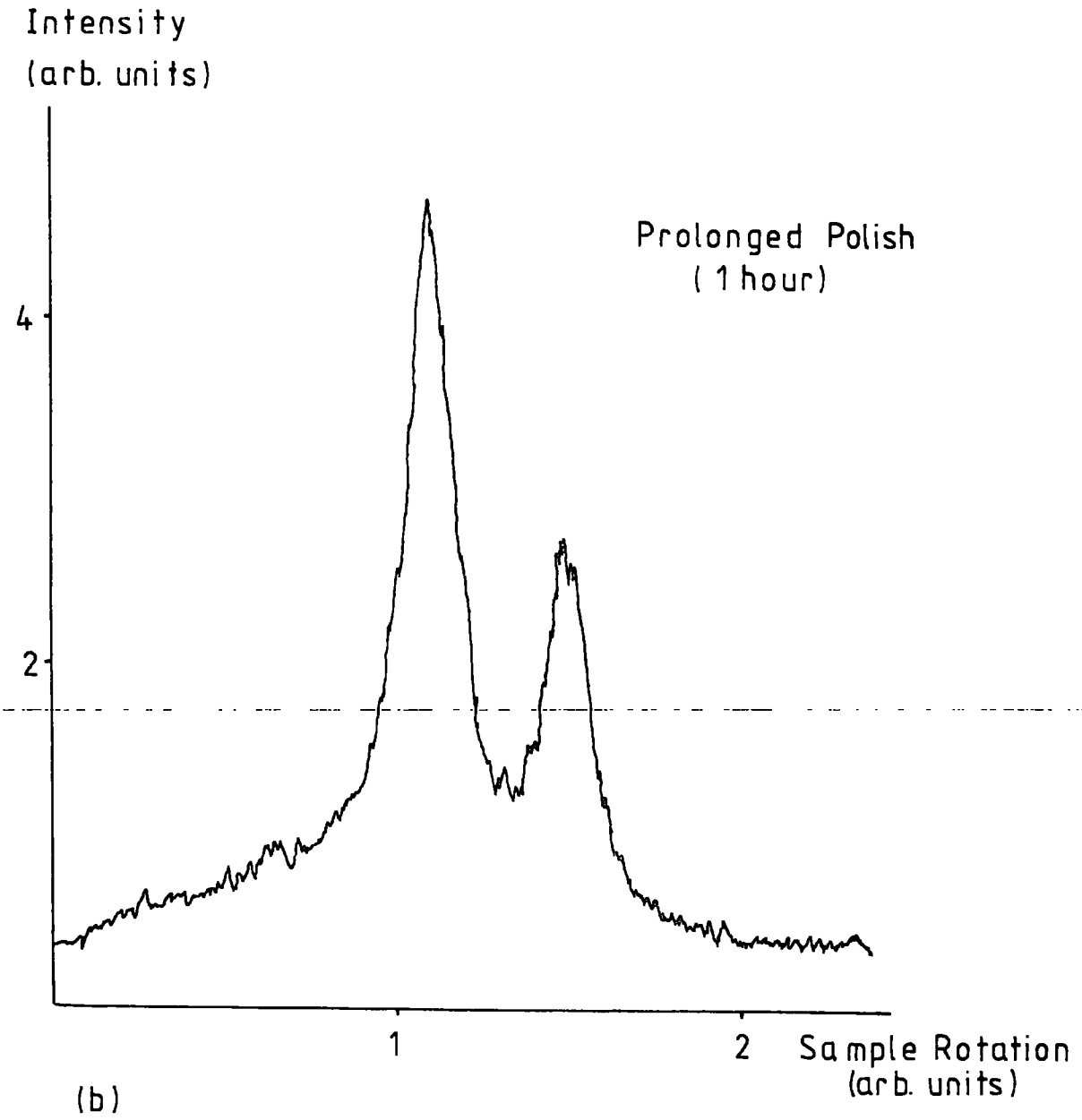

Fig. 7.14 Rocking Curves. Effect of Chemical Polishing on Terbium ($3\bar{1}\bar{2}0$ Reflection Cu K_α)

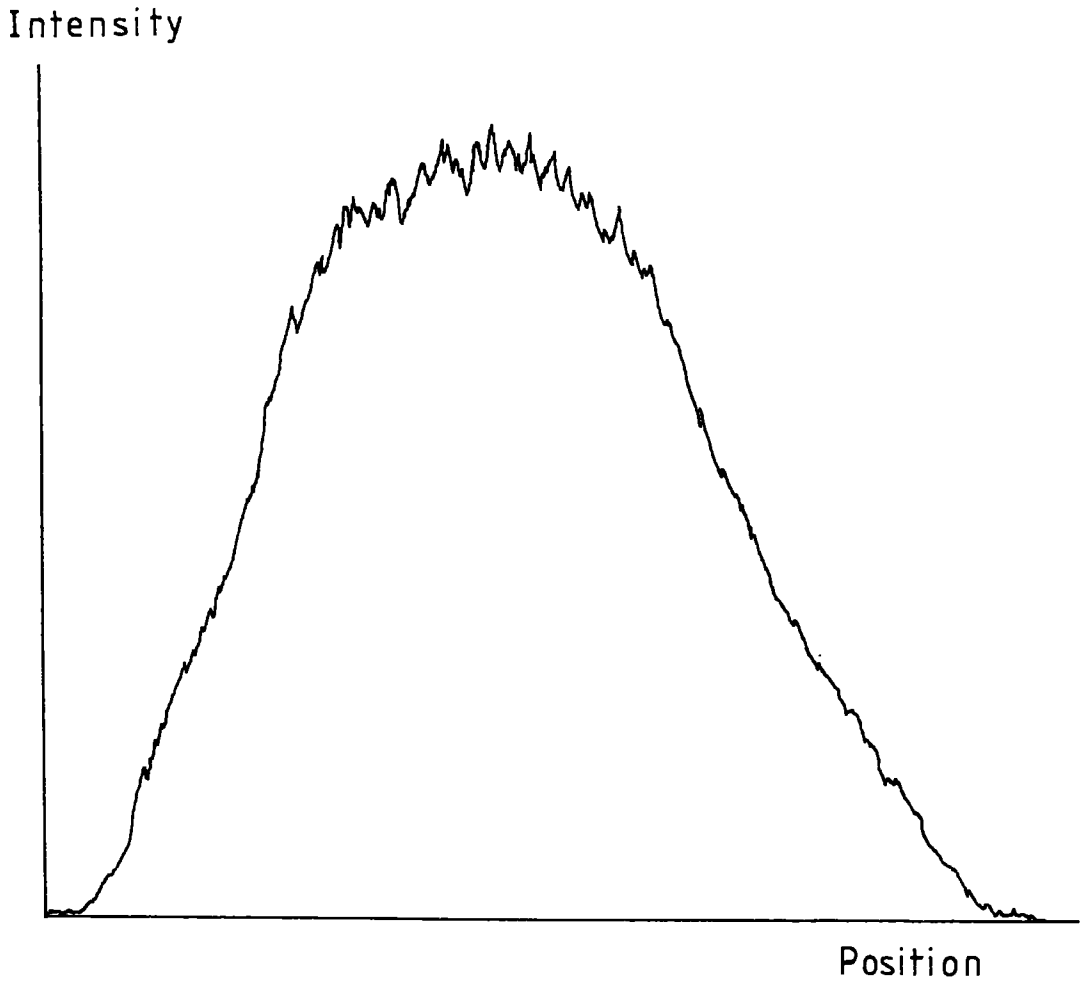

Fig. 7.15 Terbium X-Ray Intensity vs. Position

Fig. 7.16 Lang Topograph of Terbium
($3\bar{1}\bar{2}0$ Reflection Cu K_α)

of the sample could be obtained by use of the four adjustable feet of the cryostat holder enabling the Bragg planes to be set vertically. The desired Bragg reflection could be found in the normal manner prior to cooling the sample. Rocking curves were recorded at temperatures varying from above the Curie temperature to the lowest temperature available. The temperature was varied and maintained by means of a heating coil and measured by means of a silicon diode thermometer. Rocking curves were recorded for three different reflections, and two orientations of the sample in a number of cooling runs during both warming and cooling of the sample which was remounted between some experimental runs.

7.6 Analysis of Results

The angular splitting of an X-ray rocking curve due to reflection from equivalent planes in two different domains is given by

$$\Delta\theta = \frac{\Delta L}{L} \tan\theta \pm \Delta\theta_{rot} \qquad (7.4)$$

where $\Delta\theta_{rot}$ is the angular mis-orientation of the lattice planes between the two different domains.

Using the orthogonal co-ordinate system shown in fig 7.1 direction cosines for the three possible magnetization directions can be substituted into the magnetostriction expression along with the direction cosines for each measuring direction. This gives rise to expressions for the magnetostrictive change in lattice parameter along the measuring directions for each easy direction. These expressions are tabulated in table 7.2.

The mis-orientation of the lattice in directions parallel

Table 7.2

Reflection $30\bar{3}0$

Magnetization Direction

$[0\ 1\ \bar{1}\ 0]$	$-\frac{1}{4}\lambda_2^{\gamma} + \frac{1}{28}\,{}^1\lambda_4^{\gamma} + \frac{1}{2}\,{}^2\lambda_4^{\gamma}$ + Constant
$[1\ \bar{1}\ 0\ 0]$	$-\frac{1}{4}\lambda_2^{\gamma} + \frac{1}{28}\,{}^1\lambda_4^{\gamma} + \frac{1}{2}\,{}^2\lambda_4^{\gamma}$ + Constant
$[1\ 0\ \bar{1}\ 0]$	$\frac{1}{2}\lambda_2^{\gamma} - \frac{1}{14}\,{}^1\lambda_4^{\gamma} - {}^2\lambda_4^{\gamma}$ + Constant

Reflection $3\bar{1}\bar{2}0$

Magnetization Direction

$[0\ 1\ \bar{1}\ 0]$	$-\frac{13}{28}\lambda_2^{\gamma} + \frac{13}{196}\,{}^1\lambda_4^{\gamma} + \frac{26}{28}\,{}^2\lambda_4^{\gamma}$ + Constant
$[1\ \bar{1}\ 0\ 0]$	$\frac{1}{14}\lambda_2^{\gamma} - \frac{1}{98}\,{}^1\lambda_4^{\gamma} - \frac{1}{7}\,{}^2\lambda_4^{\gamma}$ + Constant
$[1\ 0\ \bar{1}\ 0]$	$\frac{11}{28}\lambda_2^{\gamma} - \frac{11}{196}\,{}^1\lambda_4^{\gamma} - \frac{22}{28}\,{}^2\lambda_4^{\gamma}$ + Constant

Reflection $5\bar{1}\bar{4}0$

$[0\ 1\ \bar{1}\ 0]$	$-\frac{11}{28}\lambda_2^{\gamma} + \frac{11}{196}\,{}^1\lambda_4^{\gamma} + \frac{22}{28}\,{}^2\lambda_4^{\gamma}$ + Constant
$[1\ \bar{1}\ 0\ 0]$	$-\frac{2}{28}\lambda_2^{\gamma} + \frac{2}{196}\,{}^1\lambda_4^{\gamma} + \frac{4}{28}\,{}^2\lambda_4^{\gamma}$ + Constant
$[1\ 0\ \bar{1}\ 0]$	$\frac{13}{28}\lambda_2^{\gamma} - \frac{13}{196}\,{}^1\lambda_4^{\gamma} - \frac{26}{28}\,{}^2\lambda_4^{\gamma}$ + Constant

Magnetization direction perpendicular to a direction $-\frac{1}{2}\lambda_2^{\gamma} + \frac{1}{14}\,{}^1\lambda_4^{\gamma} + {}^2\lambda_4^{\gamma}$ + Constant

Magnetization direction at 30° to a direction $\frac{1}{4}\lambda_2^{\gamma} - \frac{1}{28}\,{}^1\lambda_4^{\gamma} - \frac{1}{2}\,{}^2\lambda_4^{\gamma}$ + Constant

Constant $= {}^1\lambda_0^{\alpha} - \frac{1}{3}\,{}^2\lambda_0^{\alpha} - \frac{1}{3}\,{}^1\lambda_2^{\alpha} + \frac{1}{9}\,{}^2\lambda_2^{\alpha} + \frac{3}{5}\,{}^1\lambda_4^{\alpha} - \frac{1}{5}\,{}^2\lambda_4^{\alpha}$

and perpendicular to the c axis will not be the same. From the domain model of Corner and Al-Bassam lattice mis-orientation parallel to the c axis is not expected. The lattice parameter parallel to the c axis will be the same in all domains and throughout all Bloch walls. Bloch walls perpendicular to the basal plane are not expected because of the high axial anisotropy energy. The discontinuity in lattice parameter between domains can then only be accommodated by a relative twist of the lattice about the c axis. It can be argued from magnetostatic energy considerations that only domains with magnetization along $\pm[1\bar{1}00]$ and $\pm[01\bar{1}0]$ directions are expected. From these considerations it is expected that for symmetric or asymmetric surface reflection rocking curves with the c axis horizontal no splitting of the rocking curve will occur, and for symmetric surface reflection rocking curves with the c axis vertical the observed splitting will be entirely due to domain mis-orientation permitting a direct measure of the lattice mis-orientation.

Any splitting of the rocking curve from asymmetric surface reflections with the c axis vertical will be due, in part, to the lattice mis-orientation and in part to the difference in lattice parameter. The difference in lattice parameter may be obtained in terms of the magnetostriction constants from table 7.2. The lattice mis-orientation and the angular splitting of the rocking curve can be measured directly enabling a linear combination of $\lambda_{2,1}^{\gamma}\lambda_4^{\delta}$ and ${}_2\lambda_4^{\delta}$ to be calculated from equation 7.4.

Fig 7.17 is a schematic representation of the lattice mis-orientation. In the real crystal the two domains will be

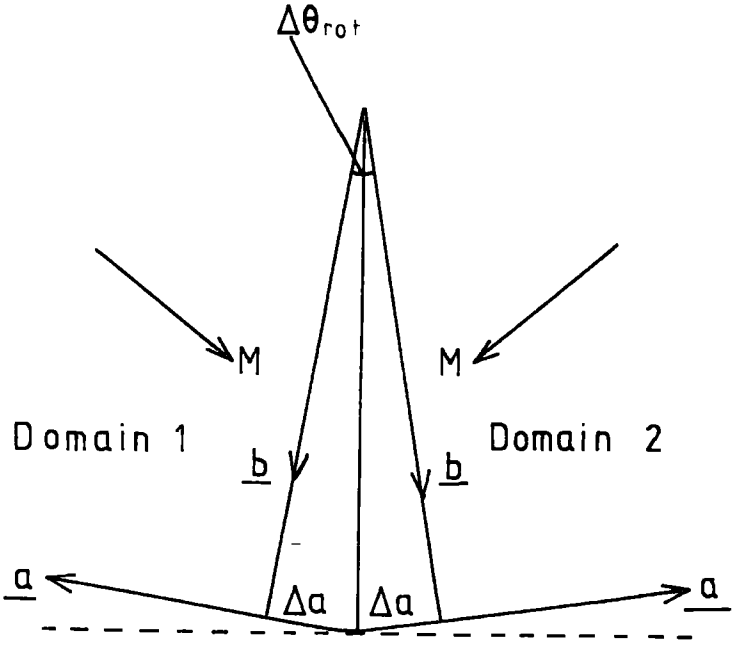

Fig. 7.17 Domain Misorientation (Schematic)

platelets lying parallel to the basal plane with a Bloch type domain wall parallel to the basal plane. The two domains are shown in the same plane for convenience. From the geometry of the figure, to a first-order approximation, the lattice mis-orientation is given by

$$\frac{1}{2}\Delta\theta_{rot} = \frac{\Delta a}{b} \qquad (7.5)$$

where b is the terbium lattice parameter along the b direction and Δa is the magnetostrictive change in lattice parameter along the a direction parallel to the crystal surface. This enables a value of the linear combination of magnetostriction constants shown in table 7.2 to be calculated.

7.7 Results and Discussion

Part of a typical sequence of rocking curves from the $5\bar{1}\bar{4}0$ reflection obtained from one cooling run using molybdenum K_{α} radiation is shown in fig 7.18. These, like all other cooling runs with the c axis vertical, show two distinct sets of peaks below the Curie temperature with a splitting between peaks of up to 0.6^{o} at temperatures down to 135K. The presence of two sets of peaks clearly indicates that domains are present with magnetization lying along two of the three easy directions, confirming Corner and Al-Bassam's (1971) model. The equal amplitudes of the two sets of peaks indicates that the volumes of crystal with magnetization along each of these easy directions are equal. The splittings between peaks, measured from rocking curves such as these, as a function of temperature are

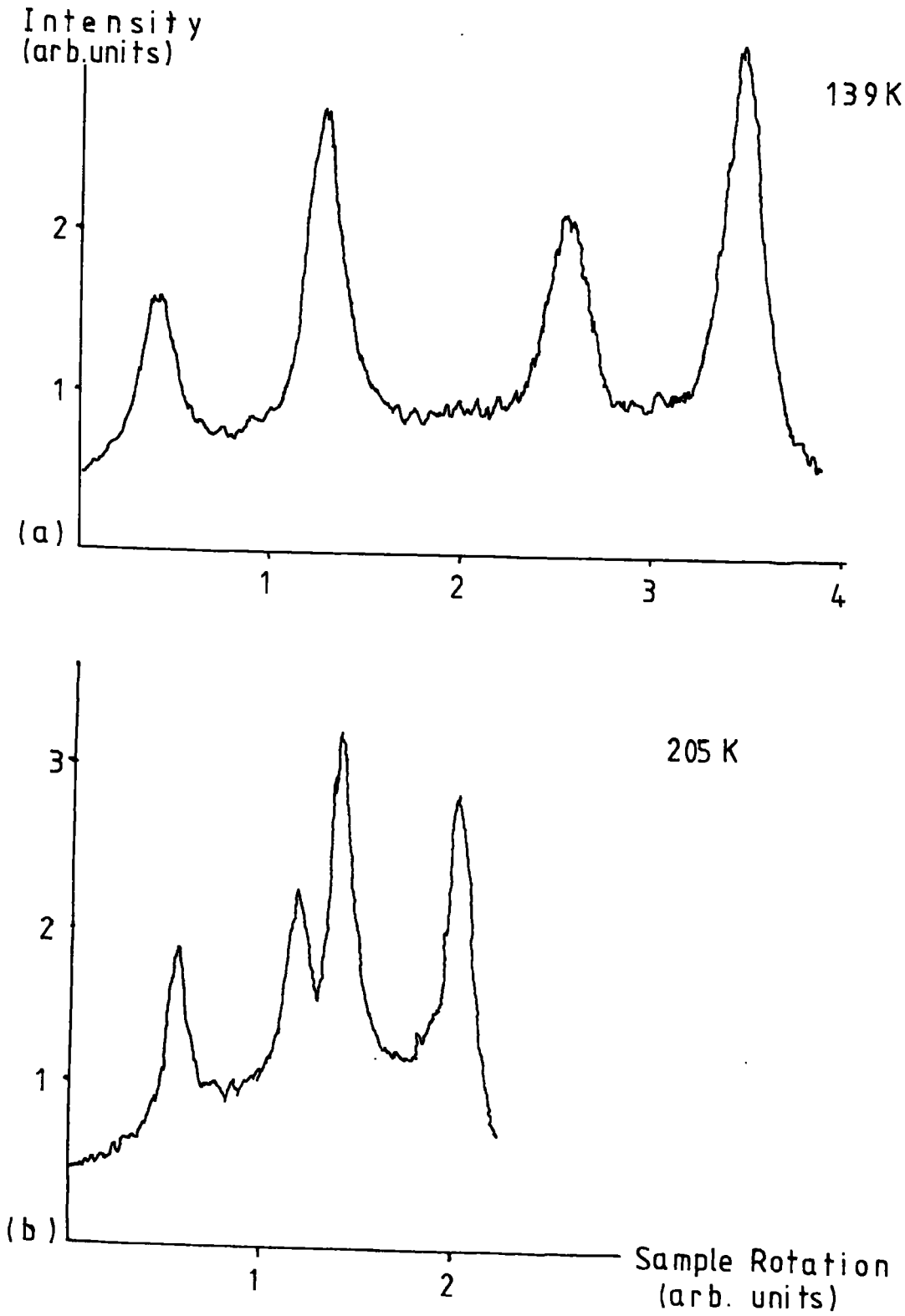
Intensity
(arb.units)
139 K
2
1
(a)
1
2
3
4
3
2
1
(b)
205 K
1
2
Sample Rotation
(arb. units)

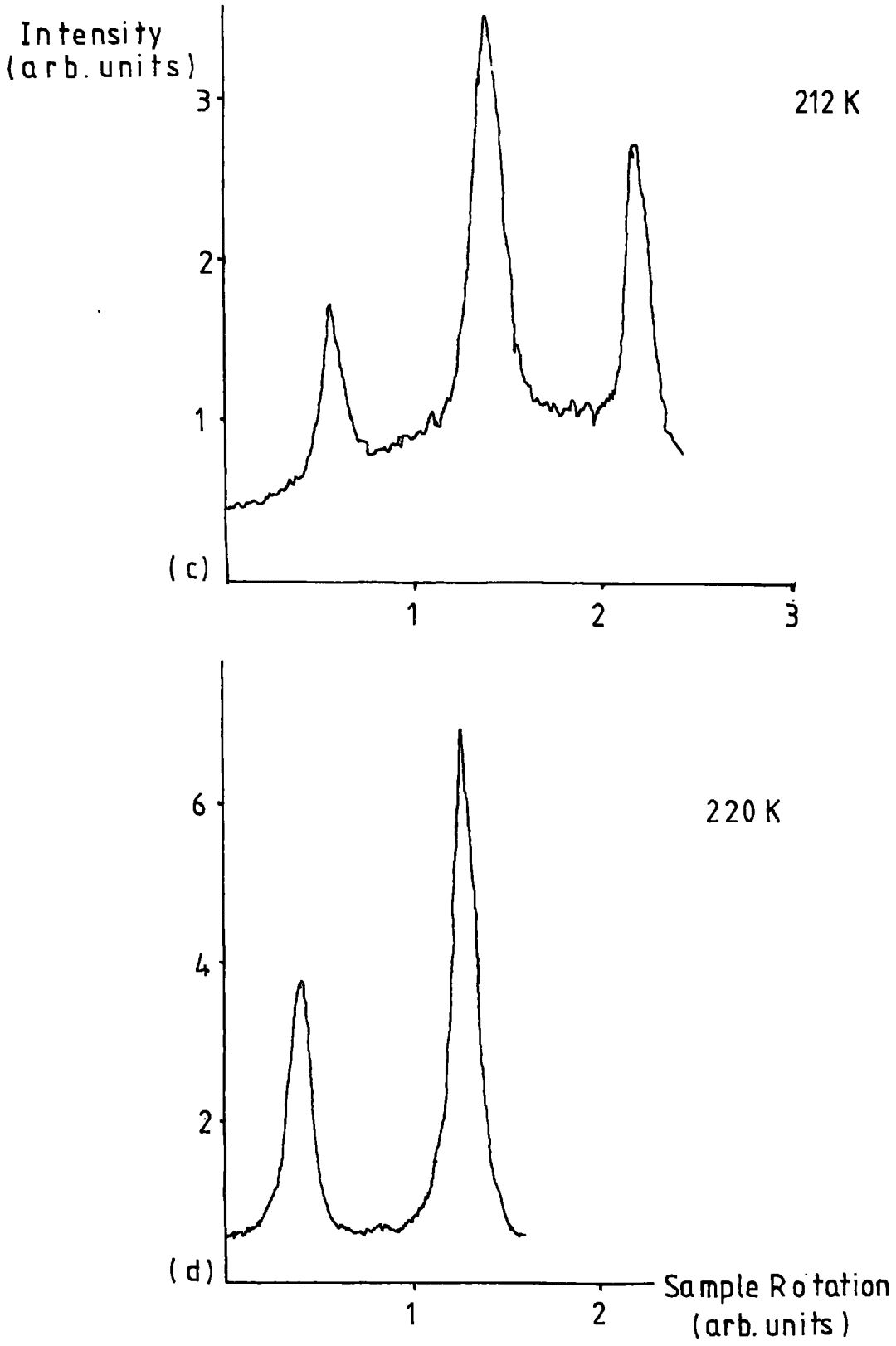

Fig. 7.18 Terbium Rocking Curves $5\bar{1}\bar{4}0$ Reflection

(c axis perpendicular to the diffraction vector)

shown for two different reflections in fig 7.19.

Symmetric surface reflection rocking curves with the c axis horizontal do not exhibit any splitting below the Curie temperature. This is expected for a sample containing slab-like domains with the magnetization along $\pm[1\bar{1}00]$ and $\pm[01\bar{1}0]$ directions with Bloch type domain walls lying parallel to the basal plane. If a third set of domains were present, or if one set of domains possessed a magnetization along the $\pm[10\bar{1}0]$ direction, then a splitting due to lattice parameter differences would be expected, (see table 7.2). No such splitting was observed. Symmetric surface reflection rocking curves with the c axis vertical do exhibit splitting, (see fig 7.19) It is thus concluded that the magnetostrictive deformation of the lattice is accommodated by a twisting of the lattice about the c axis.

The technique will not differentiate between domains with magnetization lying in opposite senses along one easy axis. The lattice parameter and orientation of such domains will be the same. There are thus four possible domain types allowing 60°, 120° and 180° Bloch walls. The presence of 180° Bloch walls is not detectable by the technique and 60° and 120° Bloch walls are not distinguishable.

The value of the Curie temperature obtained from all but one of the cooling runs was 218.9 ± 0.5K. This was characterized by the onset of the splitting of the rocking curve. The remaining experimental run gave a Curie temperature of 214.1 ± 0.5 K, and the difference is probably due to variations in the mounting

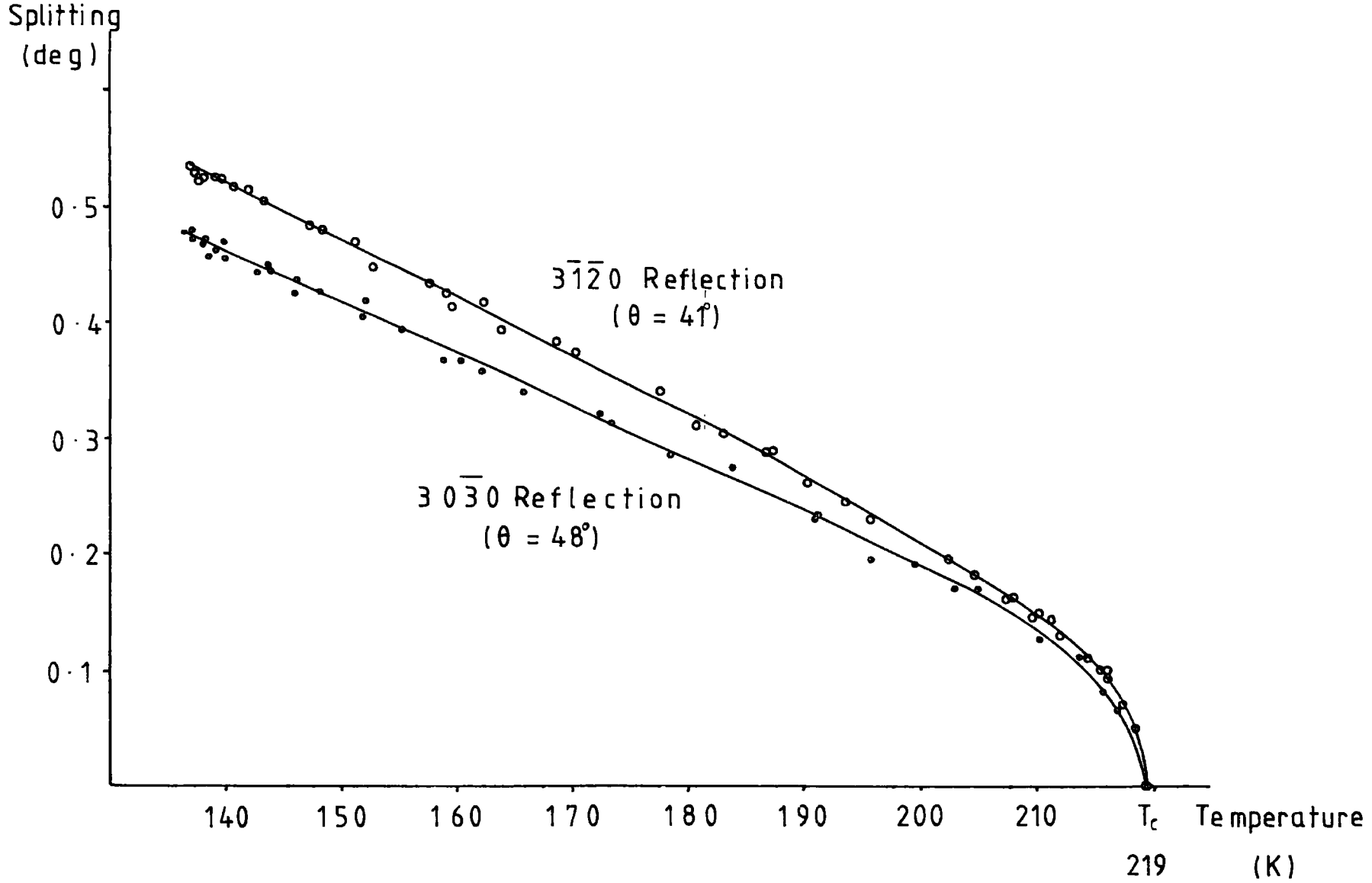

Fig. 7.19 Terbium Rocking Curve Splitting vs. Temperature

conditions resulting in different strains upon cooling the sample. The width of the rocking curves, fig 7.20, on this latter occasion were very much broader indicating the presence of strain within the crystal. This strain was not noticeable in the room temperature rocking curves prior to cooling the crystal and was probably due to poor mounting conditions. This made it extremely difficult to obtain reasonably accurate measurements of the separation of the peaks, and hence data from this experimental run could not be included in the measurement of the magnetostriction constants.

The rate of cooling of the sample can affect the domain structure. When the sample was cooled rapidly from room temperature to below its Curie temperature over a period of about one minute, sharply defined peaks were obtained similar to those shown in fig 7.18. When cooled more slowly to below the Curie temperature over a period of about 10 minutes very ill-defined peaks were obtained, fig 7.21. In both cases the domain structure is due to domains with spins along $\pm[1\bar{1}00]$ and $\pm[01\bar{1}0]$ directions. Slow cooling results either in very broad domain walls comparable with the domain widths or in very narrow domain widths comparable with the domain wall width. Rapid cooling of the sample results in abrupt domains with the majority of the spins along one of the two easy directions and hence discrete peaks are obtained in the rocking curves. These abrupt barriers probably cause scattering of ultra-sonic waves resulting in poor acoustic data. Slow cooling of the sample results in less well defined barriers giving better acoustic data and poor X-ray data. The ultra-sonic data of Palmer (1979, 1980), were obtained by cooling the sample very slowly. The X-ray data reported here were

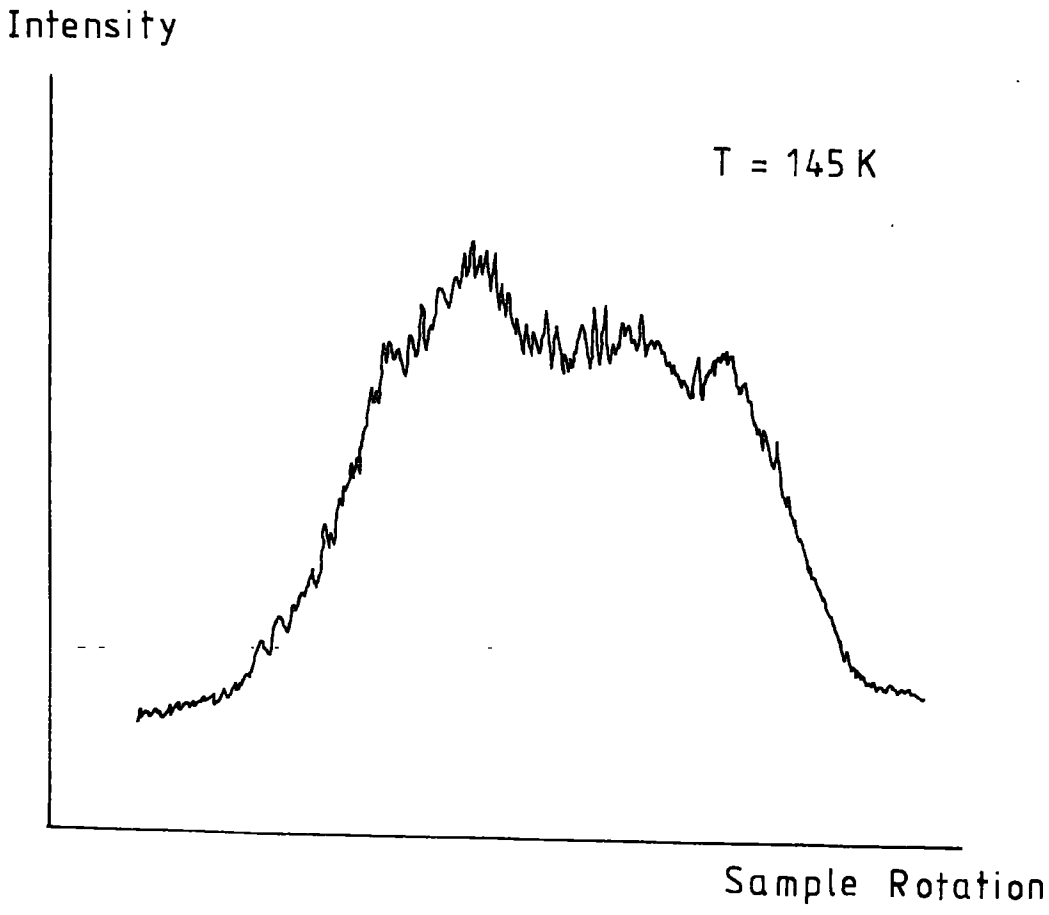

Fig. 7.20 Broad Rocking Curve of Sample Strained on Mounting

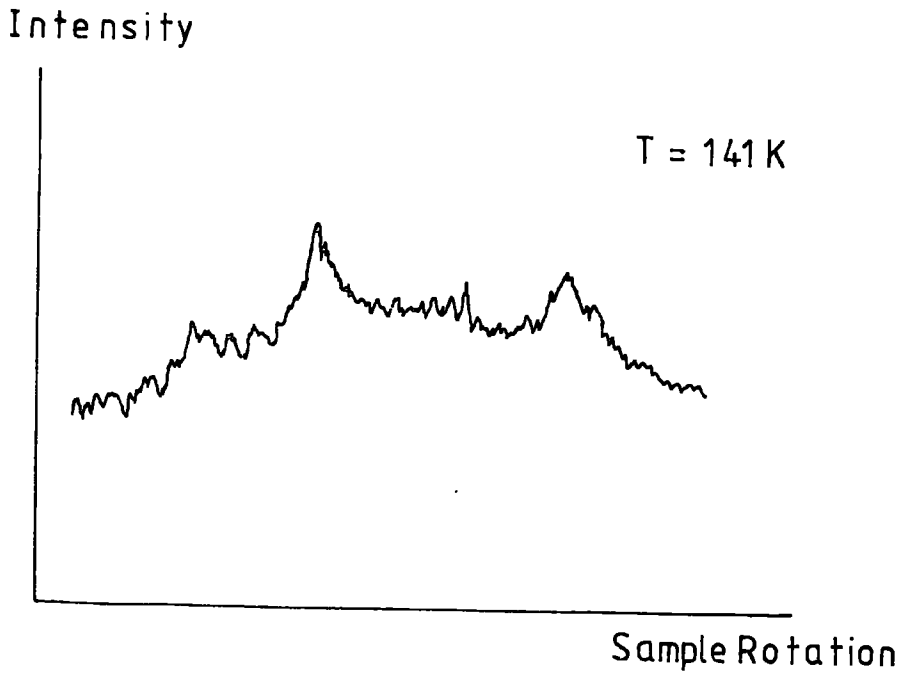

Fig . 7.21 Rocking Curve of Sample Cooled Slowly

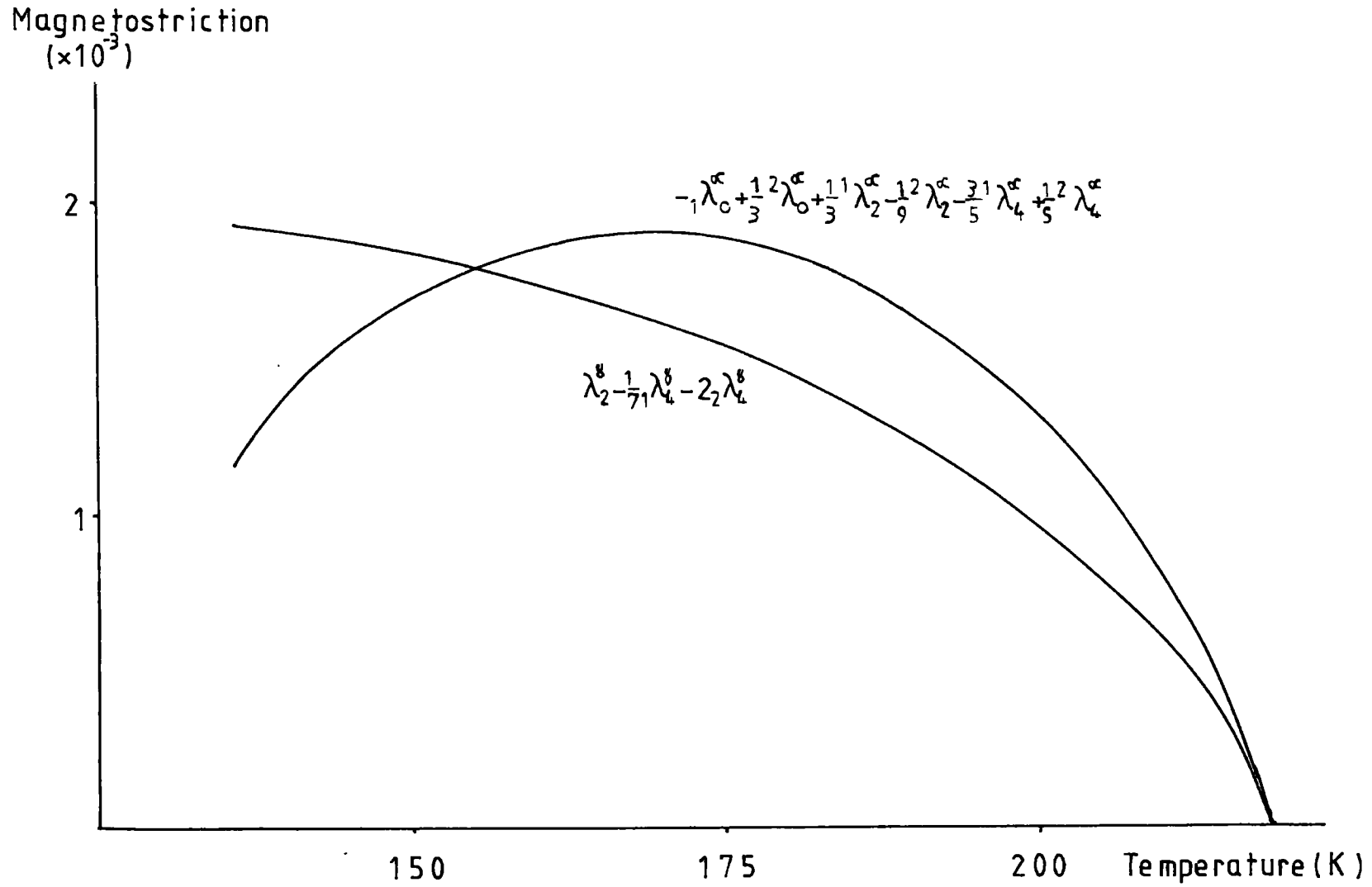

Fig. 7.22 Terbium Spontaneous Magnetostriction

obtained by cooling the sample rapidly. Some evidence has been seen that maintaining the sample below its Curie temperature for long periods results in less abrupt domains; however, rapid variations in the temperature of the sample tend to destroy this effect.

A third possibilty is that Néel walls may also be present. Inconclusive evidence for the existence of Néel walls perpendicular to the basal plane of this sample, when the sample is cooled rapidly, have been obtained by Bareham (1980) using the dry colloid technique to observe the domains. Bareham's results also indicate domain walls parallel to the basal plane. The rate of cooling the sample may affect the width of these domains separated by Néel walls and may thus affect the X-ray and ultra-sonic data as described above. No evidence is yet available as to whether the rate of cooling affects the domains separated by Bloch or Néel walls.

The spontaneous magnetostriction constants obtained by applying equations 7.4 and 7.5 to the data shown in fig 7.19 are shown in fig 7.22. The value of $\lambda_2^\gamma - \frac{1}{7}\lambda_4^\gamma - 2\lambda_4^\gamma$ obtained by this method is a factor of about two smaller than previously reported results, (see section 7.4). Previous results also indicate a non-zero value of the magnetostriction constants above the Curie temperature. Rhyne and Legvold (1965) extrapolated their results to zero field(see fig 7.23) These results are again higher and non-zero at the Curie temperature. From this it is concluded that the presence of an applied magnetic field induces ferromagnetic ordering above the Curie temperature. A field of 3 tesla raises the effective Curie temperature to about 260K

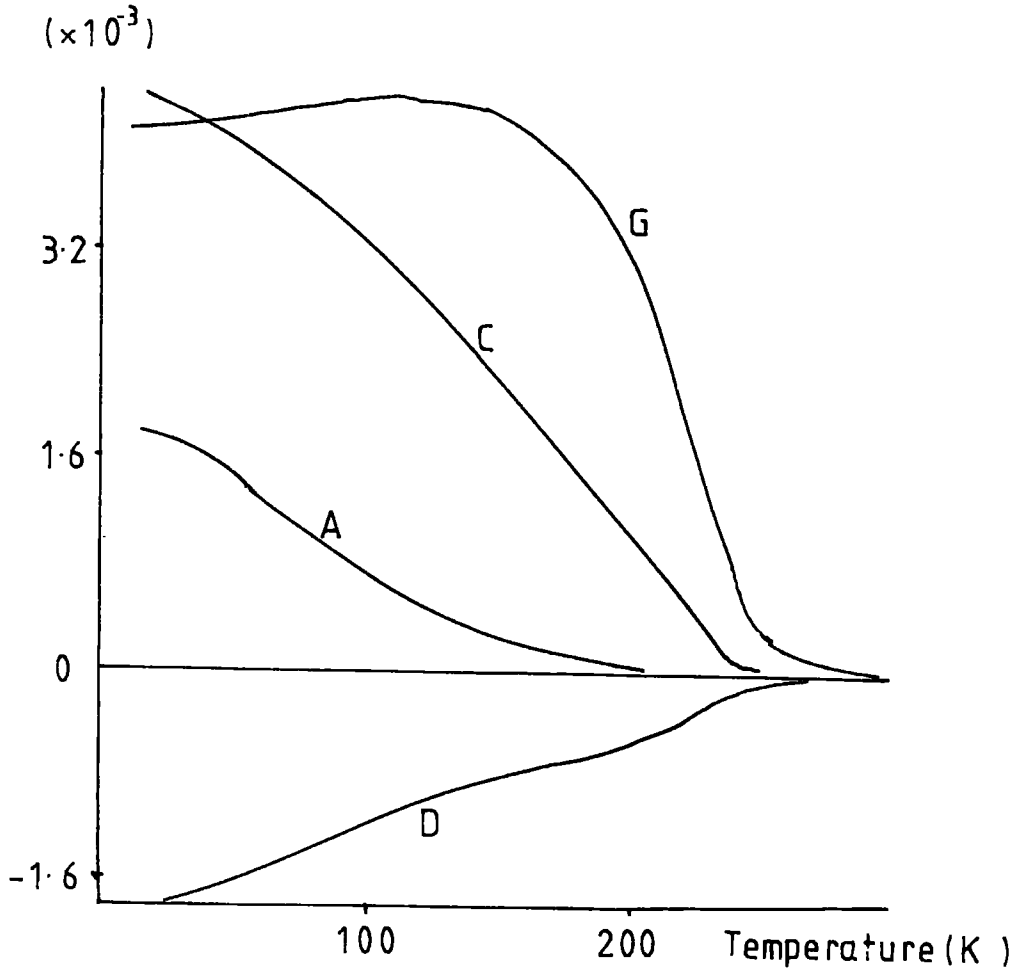

Fig. 7.23 Extrapolated Zero Field Magnetostriction
(Rhyne and Legvold 1965)

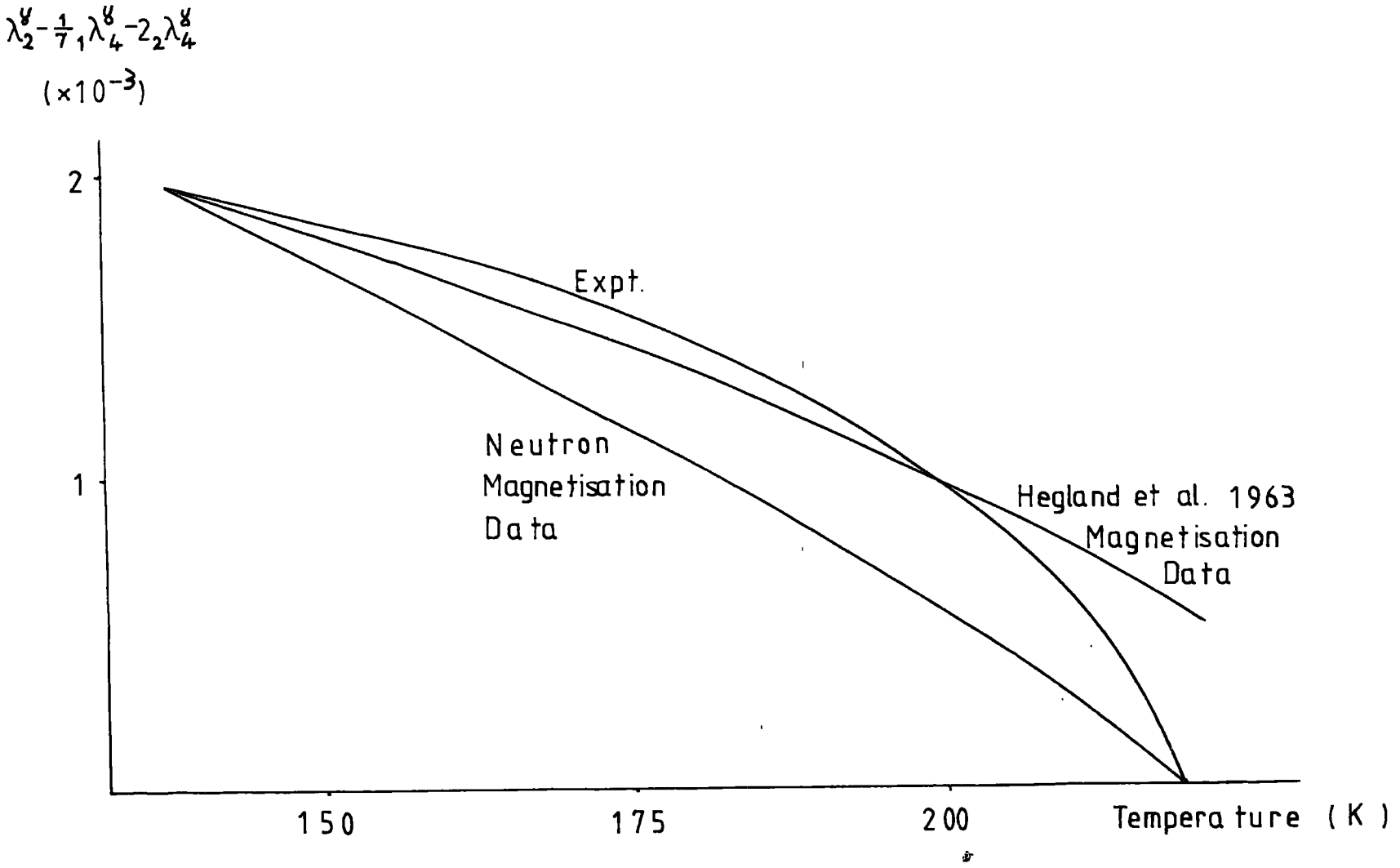

Fig. 7.24 Magnetostriction Data Single—Ion Fit

(data from Rhyne and Legvold 1965)

Attempts have been made to fit the data for $\lambda_2^{\gamma} - \frac{1}{7}{}_1\lambda_4^{\gamma} - 2_2\lambda_4^{\gamma}$ to a single-ion interaction model using bulk magnetization data and neutron diffraction magnetization data. In both cases the fit is extremely poor (see fig 7.24). The data have however been fitted to a single-ion plus two-ion interaction model. Using high field bulk magnetization data the fit is again poor; however, excellent agreement is obtained for the single-ion plus two-ion interaction model using the neutron diffraction magnetization data (see fig 7.25).

Theoretical fits for the temperature dependence of the constants have in the past been performed on values of the saturated magnetostriction constants employing values of the saturated magnetization obtained from high field bulk magnetic measurements which, again, has a non-zero value above the Curie temperature. The induced ferromagnetic ordering renders the values of the constants questionable although the general trend of the temperature of the saturated and spontaneous magnetostriction constants is similar over the temperature range for which results are available. Unfortunately, with this technique, it is not possible to obtain a value of ${}_2\lambda_4^{\gamma}$ independently from λ_2^{γ} and ${}_1\lambda_4^{\gamma}$ and hence only combinations of these results can be compared. Attempting to extend the measurements down to liquid helium temperatures proved extremly difficult. The limited wavelengths available from convential X-ray sources, along with the geometrical constraints imposed on the Bragg angle by the MERIC cryostat did not allow such measurements to be made. The introduction of the new synchrotron radiation

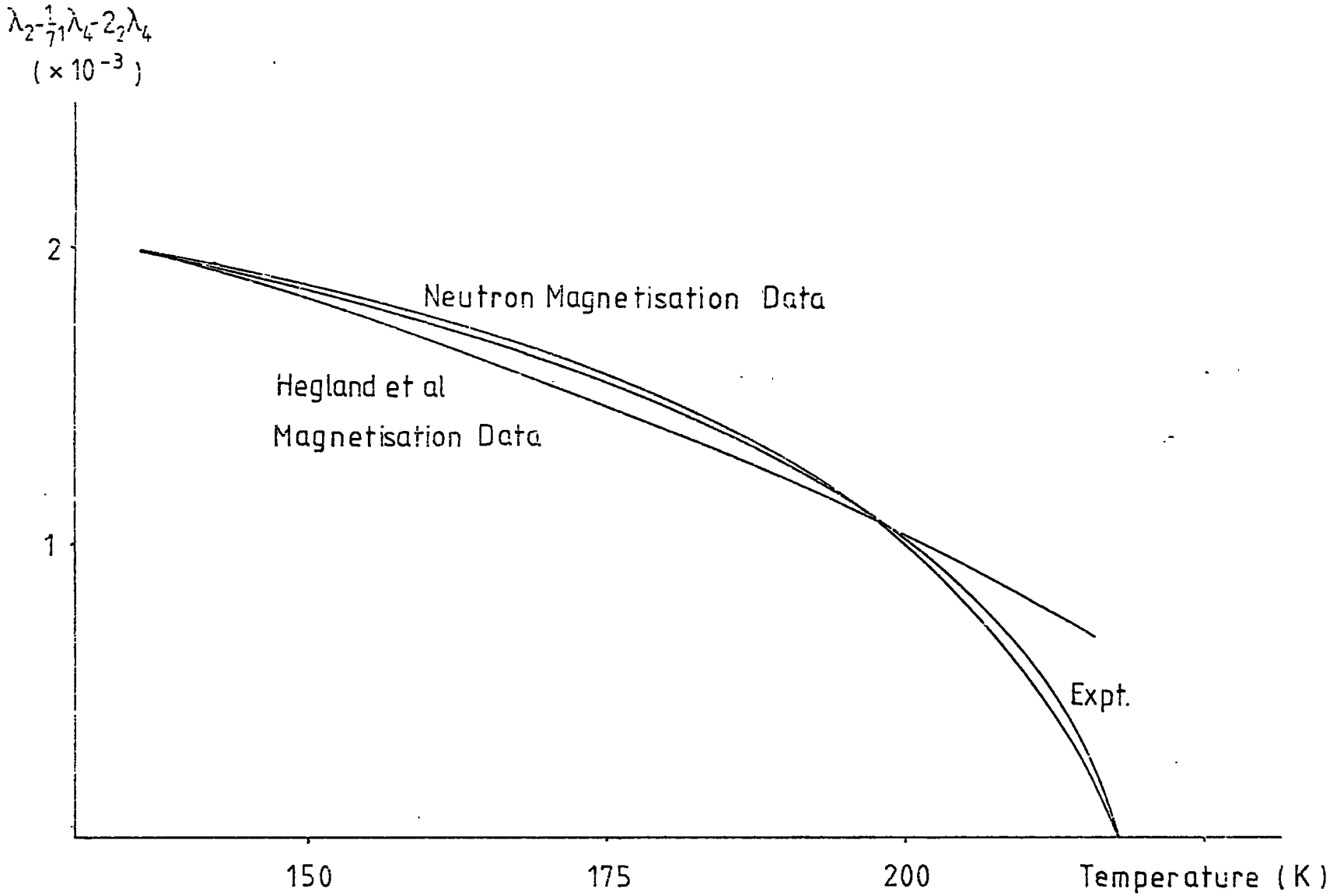

Fig 7.25 Magnetostriction Data Two - Ion Fit

source at Daresbury with facilities for white and tuned monochromatic X-ray topography should allow such measurements to be made and enable topographs of the domain structure to be recorded.

CHAPTER EIGHT

Synchrotron X-ray Topography Studies of the Magnetization Process in $Tb_{0.27}Dy_{0.73}Fe_2$

8.1 Introduction

8.2 Magnetic Properties of Terfernol

8.3 Experimental Observations of Magnetic Domains

8.4 Zero-Field Results

8.5 Applied-Field Results

8.6 Summary of Domain Wall Boundary Planes

8.7 Calculations of Domain Wall Energies and Widths

CHAPTER EIGHT

Synchrotron X-ray Topography Studies of the Magnetization Process in $Tb_{0.27}Dy_{0.73}Fe_2$

8.1 Introduction

The giant magnetostrictions of the rare-earth metals are of little technical value as their Curie temperatures are much less than room temperature. The production of rare-earth iron Laves phase compounds has stimulated considerable interest as these also have giant magnetostrictions and are ferromagnetic at room temperature, thus making them potentially useful. By varying the composition of rare-earth transition metal alloys it is possible to optimise desired magnetic properties for specific technical applications. Attempts have been made to make use of the giant magnetostriction of terfernol, $Tb_{0.27}Dy_{0.73}Fe_2$, as an ultra-sonic transducer, (Meeks and Timme 1977, Timme 1978). Problems have been encountered due to the necessity of employing high magnetic fields in order to saturate the material. As a single crystal became available and very few domain studies have been carried out on <111> easy axis ferromagnets, it was decided to undertake direct observations of the magnetic domain structure in order to understand the magnetization process.

8.2 Magnetic Properties of Terfernol

The rare-earth iron two compounds are cubic Laves phase

compounds with the $MgCu_2$ - type structure,(Bushow and Van Stapele 1970), with a large magnetostrictive rhombohedral distortion, (Dwight and Kimball 1974), (see fig 8.1). Little or no tetragonal distortion is allowed (Clark et al. 1975).

The composition of terfernol was chosen in order to minimise the magnetocrystalline anisotropy and maximise the magnetostriction, (Clark et al. 1975). $TbFe_2$ and $DyFe_2$ possess enormous magnetic anisotropy energies, predicted by Clark (1973), with anisotropy constants of opposite sign, (Clark et al.1975 . and Clark 1976). The opposite sign of the anisotropy constants of $TbFe_2$ and $DyFe_2$ allows an alloy of these two materials to be produced in which the anisotropy energies compensate at room temperature, producing a material with the maximum magnetostriction-to-anisotropy energy ratio, (Savage et al. 1975).

The magnetostriction of $Tb_{1-x}Dy_xFe_2$ at room temperature as a function of composition has been measured, (Clark et al. 1975), and is shown in fig 8.2. These measurements were made using X-ray techniques to measure the precise lattice parameter. Further measurements of the magnetostriction, at room temperature, with varying applied magnetic fields have been made by Clark (1976), see fig 8.3, who also reports measurements on the magnetostriction of other rare-earth iron Laves phase compounds, fig 8.4, and reports on the temperature dependence of the magnetostriction of $TbFe_2$, fig 8.5. Fig 8.6 compares the temperature dependence of λ_{100} for $DyFe_2$ with the temperature dependence of λ_{111} for $TbFe_2$, Clark et al. (1977). A room temperature value of λ_{111} for $DyFe_2$ has been reported,(Clark

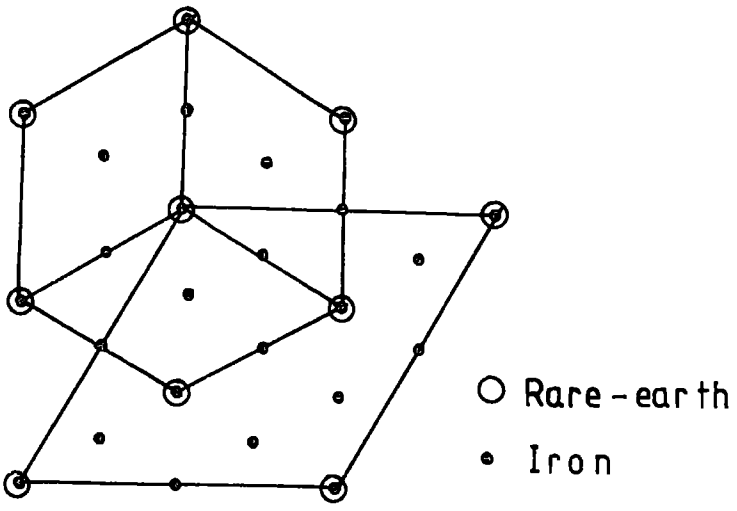

Fig. 8.1 Laves Phase Structure
(Dwight and Kimball 1974)

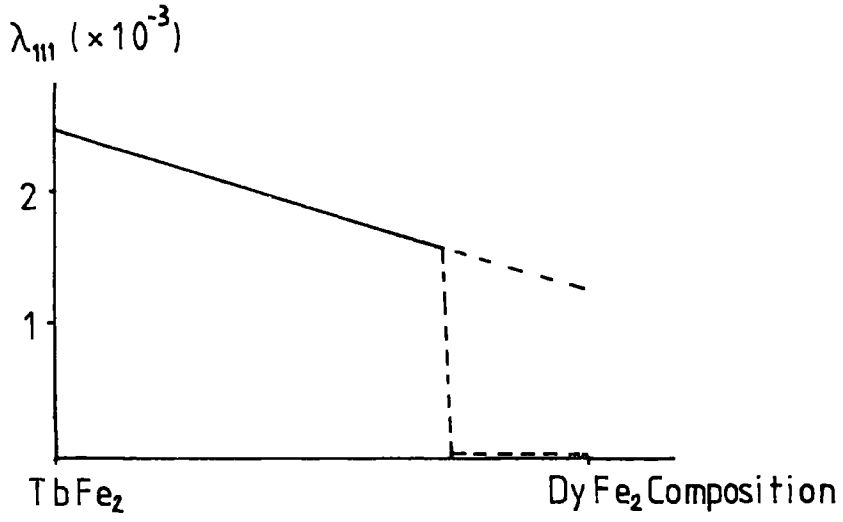

Fig. 8.2 λ_{111} for $Tb_{1-x}Dy_xFe_2$

(Clark et al. 1975)

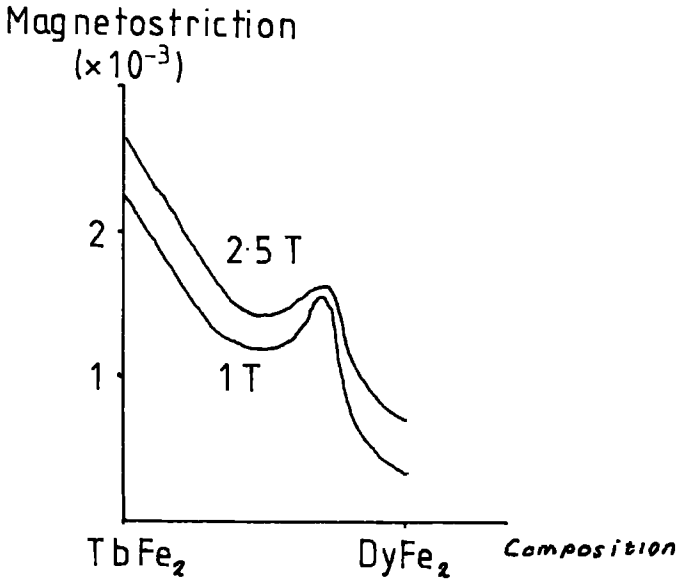

Fig. 8.3 Magnetostriction of $Tb_{1-x}Dy_xFe_2$

(Clark 1976)

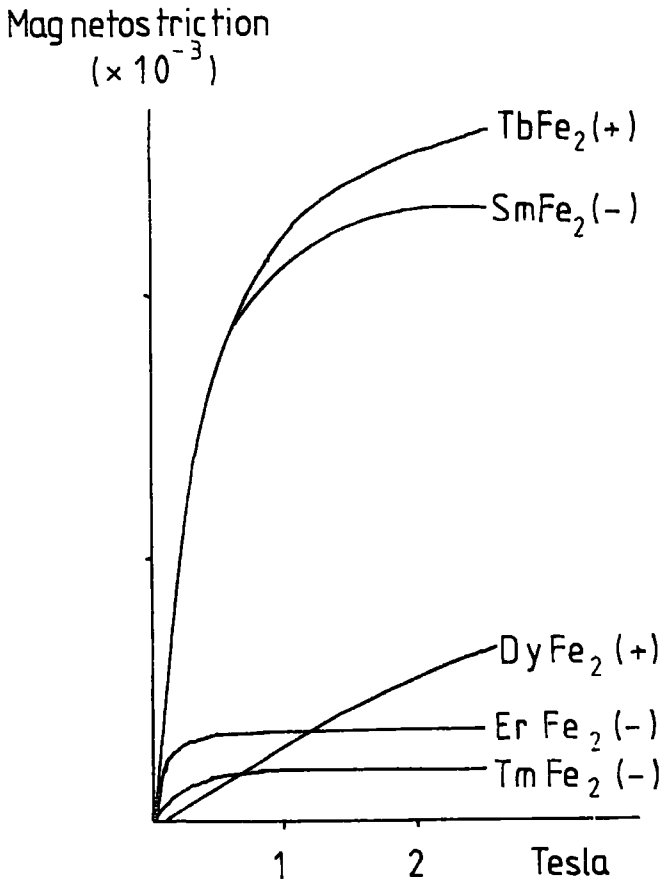

Fig. 84 Magnetostriction of RFe_2

(Clark 1976)

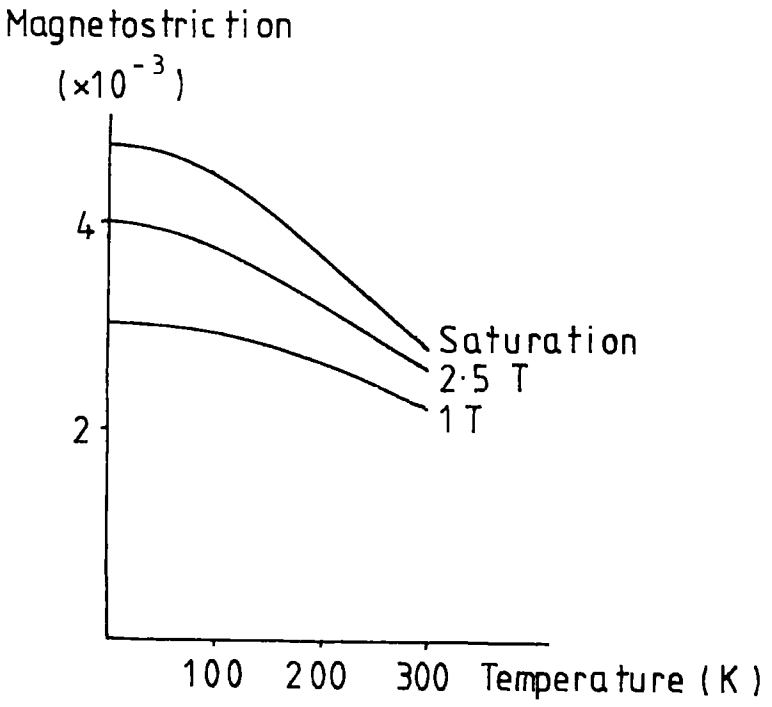

Fig. 8.5 Magnetostriction of $TbFe_2$
(Clark 1976)

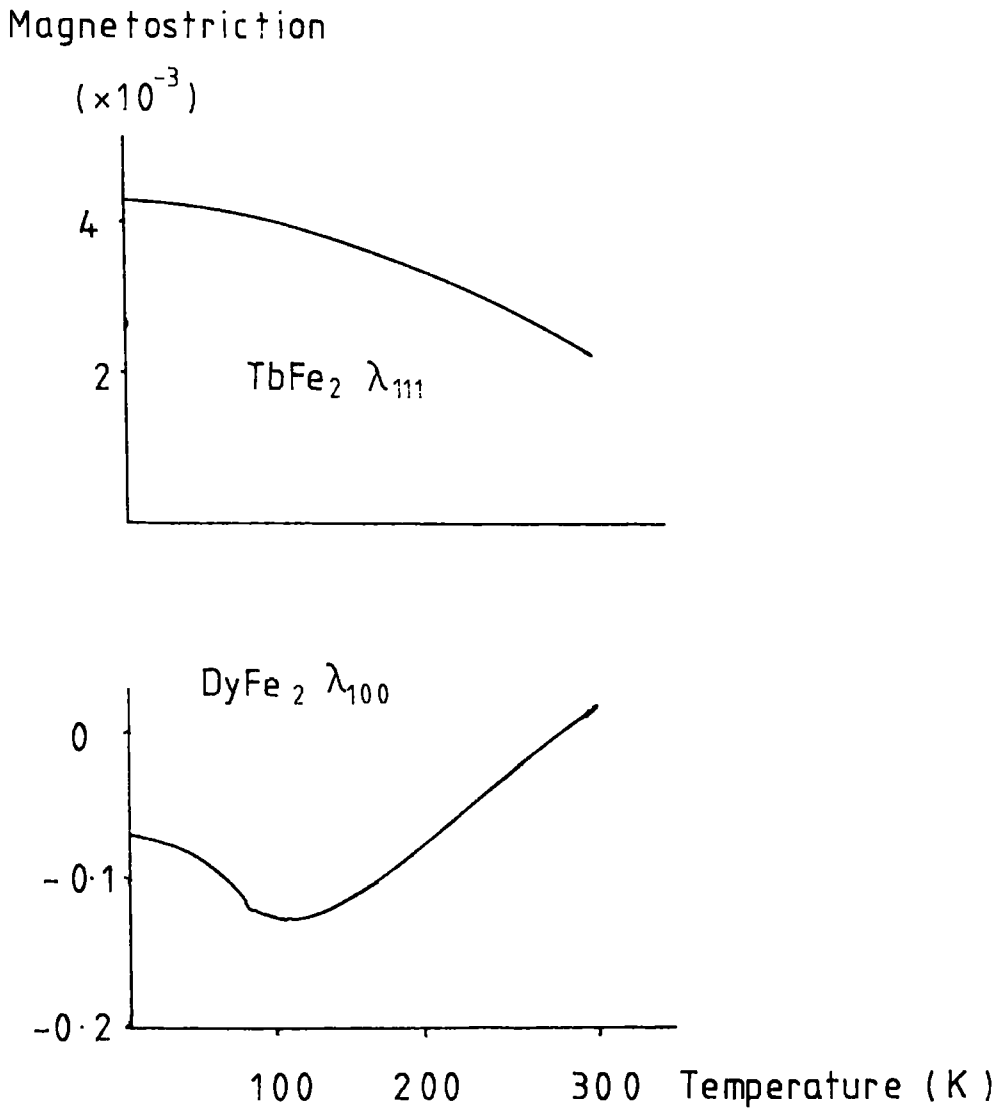

Fig. 8.6 Magnetostriction of $TbFe_2$ and $DyFe_2$ (Clark et al. 1977)

et al. 1975), to be 1260 x 10^{-6} about half the value for $TbFe_2$ of 2460 x 10^{-6}. Other measurements on the magnetostriction and magnetization of polycrystalline $TbFe_2$ and $DyFe_2$ have been reported by Clark and Belson,(1972) and Melville and Al-Rawi, (1978).

The elastic constants of rare-earth iron two compounds have been measured by Blessing (1976) who finds that they are nearly elastically isotropic. The magnetomechanical coupling factors for $Tb_xDy_{1-x}Fe_2$ have been measured by Savage et al. (1975) and maximum coupling is found for the terbium-to-dysposium ratio used in terfernol. This is one of the highest measured values for any material indicating the potential useful ness of this material as a transducer.

Values of various magnetic and elastic constants for terfernol are given in table 8.1. Near room temperature some of these values are very susceptible to small variations in temperature and composition, (Savage 1978 and Williams and Koon 1978).

Bulk magnetic anisotropy energy constants for a variety of rare-earth iron two compounds have been reported by Dariel and Atzmony (1973). Dariel et al. (1976) report the first observation of the domain structure in a rare-earth iron compound. The domain structure, revealed through the Kerr effect, appears to be the typical maze pattern associated with a strained sample. Different domain widths are apparent within different grains of the sample whose orientations are not recorded. This is claimed to be due to different structure variants in their polycrystalline Tb_2Fe_{17} sample.

Table 8.1

Anisotropy constants* x 10^4 ergs cm^{-3}

K_o	K_1	K_2	Temp(K)
0	120	-490	285
0	55	-410	295
6	24	-380	300
20	-24	-320	310

Elastic constants + x 10^{11} dynes cm^{-2} (room temperature)

C_{11}	C_{12}	C_{44}
14.1	6.5	4.87

Curie temperature * 700K

Magnetization * $4\pi M_s$ = 9800 G

Ion moment * per iron atom 1.6 μ_B at OK

per rare-earth atom 9.7μ_B at OK

Magnetostriction at room temperature $\lambda_{111} = 1.5 \times 10^{-3}$, $\lambda_{100} \simeq 10^{-4}$

* Savage (1977)

\+ Clark (1978)

8.3 Experimental Observations of Magnetic Domains

The principal method employed to observe the domain structure of terfernol was synchrotron X-ray topography. A limited amount of additional information was obtained by employing the well-known wet colloid technique first developed by Bitter (1931) and independantly by Von Hamos and Thiessen (1931). It proved impossible to image the crystal,made available by Dr H.T.Savage, with conventional X-ray topographic techniques. The presence of subgrain boundaries with a mis-orientation of three minutes of arc, permitted only small areas of the crystal to be imaged with one setting. The situation was however worse than this with the large number of dislocations resulting in a bending of the lattice within the subgrains.

The techniques of synchrotron X-ray topography have been described in chapter two. The useful properties relating to the domain observations are briefly recalled here.

1. It is a white-radiation technique which enables imperfect crystals to be imaged in reflection. Each part of the continuously bent lattice selects its own wavelength from the incident radiation.

2. The very high natural collimation of the source and large source-to-specimen distance allows the entire crystal to be imaged without scanning and permits a fairly large specimen-to-plate distance, (10-20cm), without serious loss of resolution. This enables the sample to be placed between the pole pieces of an electro-magnet.

3. The high intensity of the source results in short exposure times permitting quasi-dynamical experiments on a realistic time scale.

4. In principle it is possible to determine the change in magnetization across a domain wall from the invisibility criterion,

$$\Delta \underline{M}.\underline{g} = 0$$

5. Relatively simple polishing techniques to produce a strain free surface are sufficient. The surface does not have to be as flat as required for Kerr effect or Bitter technique studies.

The sample employed was an irregular sided single crystal disc of $Tb_{0.27}Dy_{0.73}Fe_2$ about 7mm. long 4mm. wide and 1.5mm. thick. One surface was cut and mechanically polished to within a few degrees of (110). It was then electro-polished in a 2% perchloric acid-methanol solution in a dry ice and acetone bath to remove surface strain. Before each experiment surface tarnishing was removed by light etching in a 2% glacial acetic acid, 5% nitric acid in methanol solution.

The domain pattern on the (110) surface of terfernol was revealed by surface reflection synchrotron X-ray topography using the 5 GeV electron synchrotron NINA at Daresbury, England and the 7.2 GeV electron synchrotron DESY at Hamburg, West Germany. The best topographs obtained were the symmetric 110 type reflections, as image distortion associated with other reflections made them difficult to interpret. The Bragg angle employed was about 45° giving a penetration depth of about 40 microns for wavelengths of less than one angstrom. (see appendix)

Topographs were recorded in zero field and in increasing steps of magnetic field with the field applied along the principal directions which lie in the sample surface [001], [$1\bar{1}0$] and

$[1\bar{1}1]$, A topograph was also recorded at about 273K below the temperature at which an easy axis change from <111> to <100> was expected to occur. Between each application of the magnetic field the sample was demagnetized by cooling below this transition temperature and allowed to warm up in the absence of a magnetic field.

8.4 Zero Field Results

In this material, at room temperature, K_1 is positive and K_2 is less than $-9K_1$, where K_1 and K_2 are coefficients of the magneto-crystalline anisotropy. The resulting <111> easy directions lead to a variety of wall planes and 70.57°, 109.43° and 180° walls are all possible, where the angles are the angles through which the spins must rotate from one easy direction to another across the wall.

The (110) surface contains two easy directions, $[\bar{1}11]$ and $[1\bar{1}1]$. We expect from magneto-static considerations that these two magnetization directions will be favoured. From the diffraction conditions employed for the symmetric surface reflection topographs, we do not expect to see contrast between domains with their magnetization directions lying in the surface of the sample if the domain walls behave as coherent twins. For these domains $\Delta\underline{M}$ would also lie in the surface and $\Delta\underline{M}.\underline{g}$ would be zero. There is no lattice distortion across 180° domain walls, hence contrast is not expected between these domains either. However, due to the large

Fig 8.7 Symmetric Surface Reflection Synchrotron Topograph of Terfernol (NINA 5Gev 5ma 5min 10μmL 4)

magnetostriction surface relaxation effects could result in such domains becoming visible, (Lang 1970).

Fig 8.7 is a symmetric surface reflection synchrotron topograph. Wall traces can be seen by orientation contrast along [001], [1$\bar{1}$0], [1$\bar{1}$1], [1$\bar{1}$2] and [1$\bar{1}$3] directions of typical domain spacing 30 to 40 microns. $<1\bar{1}3>$ wall traces can arise from only 109° $\{112\}$ wall planes and must be between two domains, one with its magnetization vector in the surface of the sample and one with magnetization vector inclined to the surface. (Table 8.2) $<112>$ wall traces must arise from 109° $\{111\}$ wall planes with magnetizations in both domains inclined to the sample surface. $<111>$ wall traces have several possibilities; a 109° $\{112\}$ wall plane with at least one magnetization direction inclined to the surface of the sample, or a $\{110\}$ wall plane which could be either a 71° or 109° wall. Either of these must have one domain with its magnetization direction inclined to the surface. The [1$\bar{1}$0] wall trace can arise from $\{100\}$ or $\{110\}$ wall planes which can be either 71° or 109° walls. Here the 109° $\{100\}$ wall will be between domains both of which have their magnetization direction inclined to the surface. The other wall types will have one domain with its magnetization inclined to the surface. [001] wall traces can again arise from 71° or 109° $\{100\}$ or $\{110\}$ wall planes. All can arise between domains, one of which has its magnetization inclined to the surface. In addition 71° $\{100\}$ and 109° $\{110\}$ walls can be between two domains both with magnetization directions inclined to the sample surface.

180° walls may have either $\{110\}$ or $\{112\}$ wall planes.

{110} wall planes will result in [111] and <1$\bar{1}$0>wall traces with both magnetizations lying in the surface, or inclined to the surface of the sample. 180° {110} wall planes can also result in an [001] wall trace with the magnetization directions in both domains inclined to the surface. 180° {112} wall planes may result in <111>wall traces with the magnetization direction lying in the surface of the sample and in [1$\bar{1}$0] and <113> wall traces with magnetization direction inclined to the sample surface. If the magnetization directions in both domains lie in the surface of the sample 71° walls from {100} and {110} wall planes will result in an [001] wall trace and 109° walls from {100}, {111} and {112} wall planes will result in [1$\bar{1}$0] wall traces.

Parts of the crystal show no apparent wall trace or only very faint wall traces. Wall traces may be present which, owing to the diffraction conditions, satisfy the invisibility criterion. The faint wall traces may be due to surface relaxation effects for otherwise invisible wall traces. Other parts of the crystal show an overlapping domain structure or a parallelogram-net pattern first observed on a curved (110) surface in nickel, (Yamamoto and Iwata 1953), which was interpreted as being due to the small value of the domain wall energy in nickel and is not unusual for <111>easy axes materials (Carey and Isaac 1966).

The magneto-crystalline anisotropy data indicate that an easy axis change from <111>to <100>occurs just below room temperature. In order to observe this change the crystal was cooled to about 273K by packing dry ice around the goniometer.

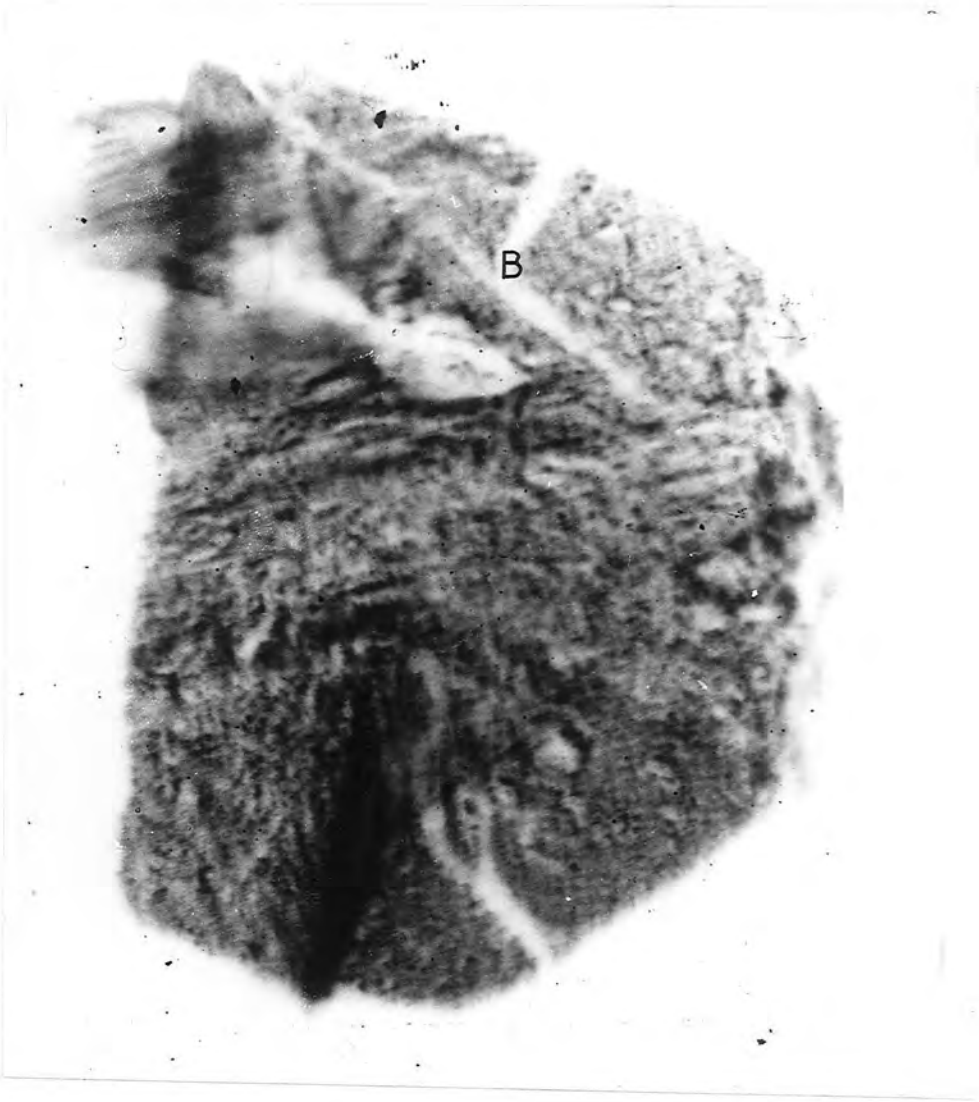

Fig 8.8 Symmetric Surface Reflection Synchrotron Topograph of Terfern at 0°C (NINA 5Gev 5ma 5min 10μm L4

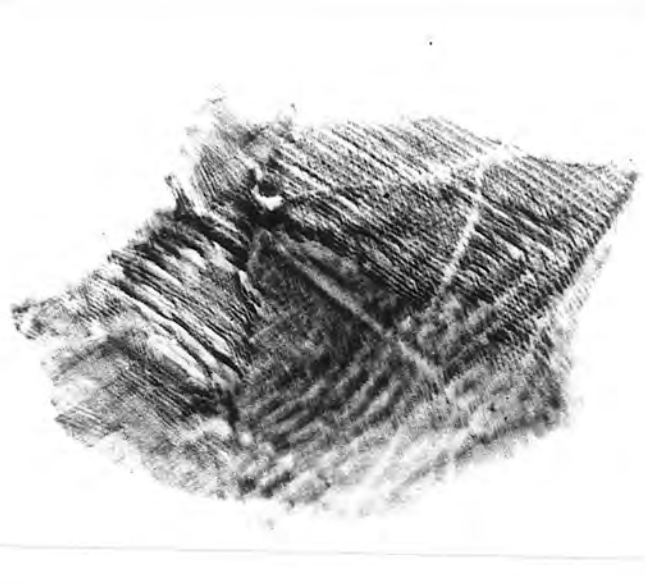

(a) Zero Field

1mm

[$\bar{1}$11](H)

[1$\bar{1}$0]

[001]

(b) 0.05 T

(c) 0.06 T

The resulting topograph is shown in fig 8.8. Due to the very small value of λ_{100} compared with λ_{111} no definite domain pattern is observable. Any orientation contrast associated with a domain structure is masked by the general strain within the crystal. In any case a 180° wall structure parallel to [001] is expected in a (110) disc. The disappearance of the original domain structure clearly indicates that such a change does take place. The faint streaking along the [001] and $[1\bar{1}0]$ directions could possibly be associated with a domain structure. Upon rewarming the sample a new domain pattern was obtained. This cooling cycle was used to demagnetize the sample between applications of a magnetic field.

The white bands on the topograph, B, are areas of reduced intensity due to a small mis-orientation between subgrains. This mis-orientation is calculated to be about 3 minutes of arc from a measure of the width of the bands, corrected for image distortion, and a knowledge of the specimen to plate distance.

Attempts were made to observe the domain structure using the Bitter technique. Clear results were not obtained due to the difficulty of preparing a suitable surface. Some evidence of the domain structure was seen which was similar to that observed by X-ray topography. Contrast visible in some parts of the sample was area contrast as opposed to simply delineating walls, which was confirmed by a reversal of the contrast when a small bias field, applied perpendicular to the surface of the sample, was reversed As this indicates the presence of free poles on the surface, these results provide some evidence that a stable domain structure with

at least some of the magnetization directions inclined to the sample surface is possible within this material.

8.5 Applied Field Results

A magnetic field was applied parallel to the surface of the crystal and along each of the three principal directions [001], $[1\bar{1}0]$ and $[\bar{1}11]$. This produced wall traces parallel to the field direction for fields in excess of 0.14 tesla along the easy direction and slightly higher fields along other directions which remained up to the highest fields available, (about 0.3 tesla) at the synchrotron source.

Estimates of the magnetization as a function of field in this sample indicate a rapid change in the magnetization for fields up to 0.15 tesla along the easy direction and saturation, (or very small changes in the magnetization) for fields in excess of 0.4 tesla, with slightly higher fields being required along the [001] and $[1\bar{1}0]$ directions. Due to the varying demagnetizing factors quantitative evaluation of the data was not possible.

Figure 8.9 shows part of a sequence of topographs taken in increasing steps of magnetic field with the field applied along the $[\bar{1}11]$ direction. The initial domain pattern consists mostly of $[1\bar{1}0]$ wall traces with a large area showing no wall traces. This remains fairly constant up to a field of 0.05 tesla though however, some $[1\bar{1}0]$ wall traces do disappear. At 0.05 tesla $\langle\bar{1}11\rangle$ wall traces are apparent over much of the surface, often with $[\bar{1}10]$ wall traces as well. The region which previously

(b) 0.05 T

(c) 0.06 T

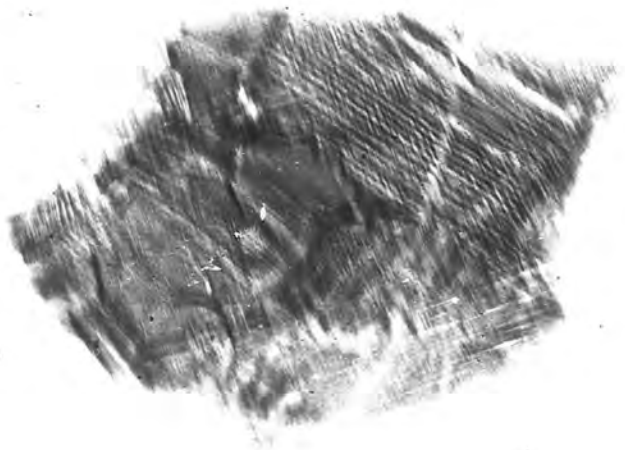

(b) 0.05 T

(c) 0.06 T

(d) 0.08 T

(e) 0.14 T

Fig 8.9 Symmetric Surface Reflection Synchrotron Topographs of Terfernol in Increasing Magnetic Fields along [$\bar{1}11$] (DESY 7Gev 5ma 4min 10μm L 4)

showed no wall traces shows a mixture of [$\bar{1}11$] and[$\bar{1}10$] wall traces. At 0.06 tesla [$\bar{1}11$] and [$\bar{1}10$] wall traces cover most of the crystal. By 0.08 tesla the [$\bar{1}10$] wall traces have started to disappear with weaker contrast of the remaining wall traces. Further increases in field up to 0.14 tesla result in a gradual diminution of the [$\bar{1}10$] wall traces until finally only [$\bar{1}11$] wall traces remain, which remain unchanged up to 0.3 tesla, and upon reducing the field to zero.

The remaining wall traces cannot be 180° walls between [$\bar{1}11$] and [$1\bar{1}\bar{1}$] magnetization directions in spite of lying along the [$\bar{1}11$] direction. The force exerted by the field on this type of domain wall would be greater than on any other domain wall and hence such walls would be expected to disappear first. These walls must therefore be similar to the walls observed between inclined domains in nickel (Alex et al. 1974, Kuriyama et al. 1977, Boettinger et al. 1977)

The immobility of these wall traces implies the magnetic energy is identical within the two sets of domains. With the field applied along the [$\bar{1}11$] direction the wall trace must result from a ($1\bar{1}2$) wall plane between domains with magnetization directions along [111] and [$\bar{1}\bar{1}1$]. This is the 109° wall shown in fig 8.10. The components of the magnetization along the [$\bar{1}11$] direction from the two domains is identical. When the field is applied along the [001] direction the 71° (100) and (010) wall planes between domains magnetized along [111] and [$\bar{1}\bar{1}1$] directions will result in an [001] wall trace with identical components of magnetization along the field direction. Similarly the 109° ($1\bar{1}0$) wall between

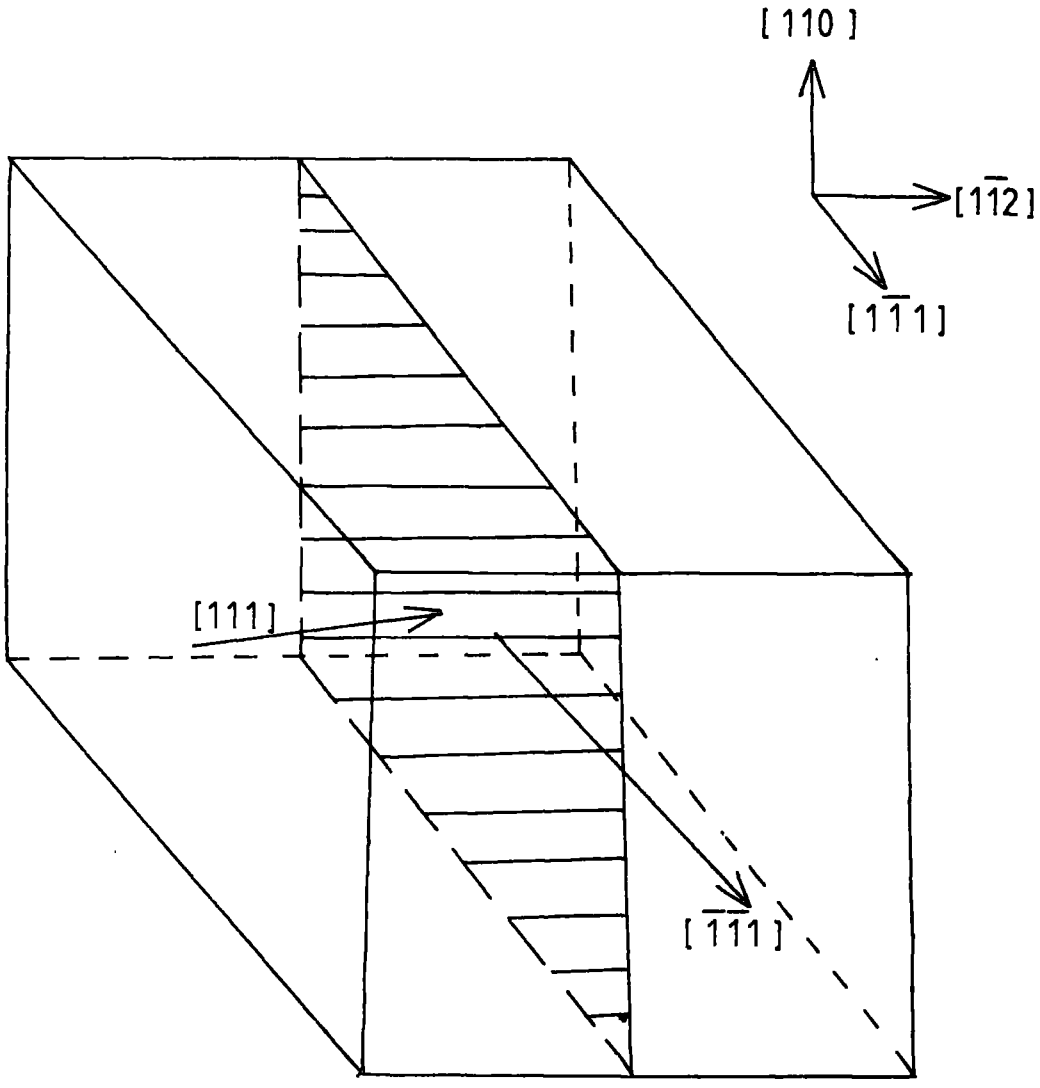

Fig. 8.10 (1$\bar{1}$2) Wall Plane 109° Wall

[111] and [$\bar{1}\bar{1}$1] domains will give an [001] wall trace with identical components of magnetization along the field direction. When the field is applied along the [1$\bar{1}$0] direction the 109° (001) wall plane between [111] and [$\bar{1}\bar{1}$1] domains is the only wall with identical magnetization components along the field direction.

Any direction of applied field within the plane of the (110) surface sample can produce wall traces parallel to the field direction between [111] and [$\bar{1}\bar{1}$1] domains with a zero force exerted on the domain wall. The field will cause the magnetizations within the Bloch-type domain walls to lie parallel to the field direction causing a rotation of the domain walls to lie parallel to the field. This domain structure will then remain locked. Any increase in field cannot result in the growth of one type of domain at the expense of another, but will result in the magnetization directions within the bulk of the domains tending to rotate towards the field direction. This will be accompanied by a small change in the magnetization of the sample compared with the rather large changes associated with the re-orientation of the original domain structure. There will be no observable change in the domain structure until the field is sufficiently strong to cause saturation of the sample with the magnetization direction within the entire sample along the field direction.

Since the domain structure remains constant when the field is reduced to zero, it can only be concluded that despite the magnetostatic energy associated with free surface poles a domain structure

with magnetization directions inclined to the sample surface is stable for this material.

8.6 Summary of Domain Wall Boundary Planes

The various types of domain wall boundary can be considered with reference to figure 8.11. All 71° {100} boundaries are similar to the (001) boundary between domains magnetized along [$\bar{1}$11] ,VO, and [1$\bar{1}$1] , OD. All 109° {100} boundaries are similar to the (001) boundary between domains magnetized along [$\bar{1}$11] , and [$\bar{1}\bar{1}$1] , OA. Further, all 180° {110} boundaries are similar to the (110) boundary between domains magnetized along [$\bar{1}$11] , VO, and [1$\bar{1}\bar{1}$] , OV, and all 109° {110} boundaries are similar to the (110) boundary between domains magnetized along [$\bar{1}$11] , VO and [1$\bar{1}$1] , OD. There are two possible 71° {110} boundaries. These are similar to the (110) boundary between domains magnetized along [$\bar{1}$11] , VO, and [$\bar{1}$1$\bar{1}$] , OT, and between domains magnetized along [111] , SO and [11$\bar{1}$] OU.

All {111} boundaries are 109° boundaries similar to the (111) boundary between domains magnetized along [$\bar{1}$11] , VO, and [1$\bar{1}$1] , OD, all 180° {112} boundaries are similar to the (1$\bar{1}$2) boundary between domains magnetized along [$\bar{1}$11] , VO, and [1$\bar{1}\bar{1}$] , OV and all 109° {112} boundaries are similar to the (1$\bar{1}$2) boundary between domains magnetized along [$\bar{1}\bar{1}$1] , UO, and [111] , OC. These are summarised in table 8.2 along with the possible wall traces on the (110) plane for given wall boundary planes.

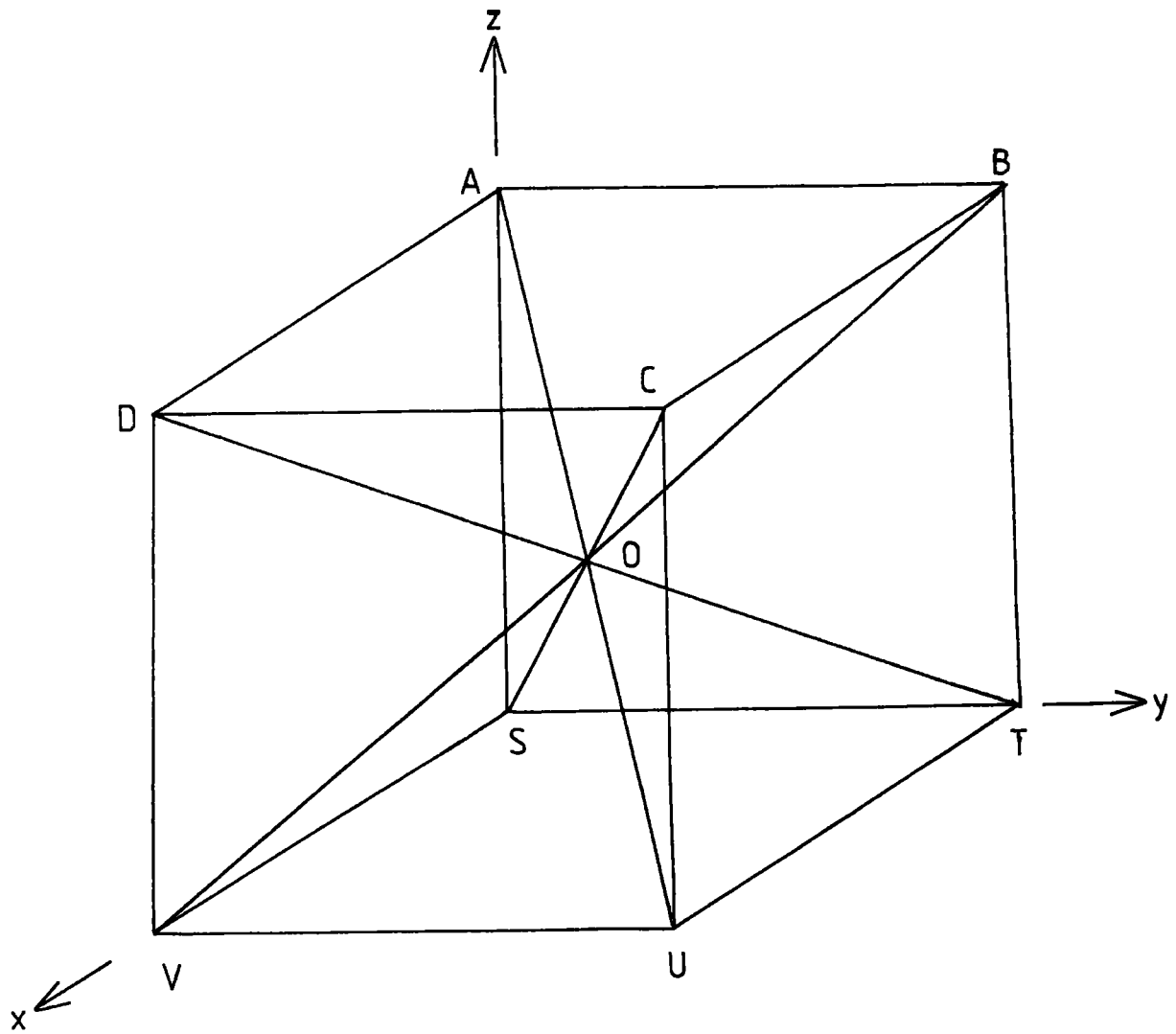

Fig. 8.11 Illustration of Domain Walls (see text and table 8.2

Table 8.2

M_1	M_2	Wall Type	Wall plane
$[\bar{1}11]$	$[1\bar{1}1]$	71°	(001)
$[\bar{1}11]$	$[\bar{1}\bar{1}1]$	109°	(001)
$[\bar{1}11]$	$[1\bar{1}\bar{1}]$	180°	(110)
$[\bar{1}11]$	$[1\bar{1}1]$	109°	(110)
$[\bar{1}11]$	$[\bar{1}1\bar{1}]$	71°	(110)
[111]	$[11\bar{1}]$	71°	(110)
$[\bar{1}11]$	$[1\bar{1}1]$	109°	(111)
$[\bar{1}11]$	$[1\bar{1}\bar{1}]$	180°	$(1\bar{1}2)$
$[\bar{1}\bar{1}1]$	[111]	109°	$(1\bar{1}2)$

Wall plane	Wall trace on (110) plane
$\{001\}$	$[001]$, $[1\bar{1}0]$
$\{110\}$	$[001]$, $[1\bar{1}0]$, $<111>$
$\{111\}$	$<112>$
$\{112\}$	$<111>$, $<113>$

Higher index domain wall boundary planes are also possible. Any plane rotated about the [001] axis can form a 71° domain wall boundary between domains magnetized along [111] and [$\bar{1}\bar{1}$1] directions that is any plane in the [001] zone. Also any plane within the [110] zone can form a 109° wall boundary plane between domains magnetized along [111] and [11$\bar{1}$] directions. This allows wall traces to be visible along any direction within the crystal surface. However, lower index wall planes are expected to have lower wall energies and are thus more probable unless the crystal is influenced by the presence of an applied magnetic field.

8.7 Calculations of Domain Wall Energies and Widths

Assuming the boundaries between the domains are conventional Bloch (1932) walls it is possible to estimate the thickness and energies of these walls. A variety of early estimates on various materials have been performed, Bloch (1932), Landau and Lifshitz (1935), Néel (1944), Lifshitz (1944) and Lilley (1950), only the latter considering the case of $<111>$ easy axis material.

The domain wall boundary is the transition region in which the spontaneous magnetization vector changes from its direction in one domain to its direction in an adjacent domain. In order to avoid the formation of free poles on this boundary layer, the normal component of the magnetization vector must be constant in both domains and throughout the wall, (Néel 1944). The direction of the magnetization at any point within the boundary can be specified by (θ, ψ). Where θ is the angle between the magnetization and the

boundary normal and is constant for any particular boundary and ψ is the angle between the projection of the magnetization on the boundary plane and a selected zero direction within this plane.

Following the treatment of Lilley (1950), the free energy per unit volume of crystal in zero applied field is

$$F = F_a + F_e \qquad (8.1)$$

where F_a is the anisotropy energy

and F_e the exchange energy.

The energies and effective widths of the boundaries can be determined from the condition that F integrated over the range in which ψ changes from one easy direction to another is a minimum.

The anisotropy energy consists of a magnetocrystalline, F_k and magnetoelastic, F_m, terms. In order to determine the excess wall energy reduced energy terms are obtained by subtracting constant terms from F_k and F_m to make each zero when the magnetization lies along an easy direction hence

$$f_a = f_k + f_m \qquad (8.2)$$

If the boundary is considered to be in the yz plane with its normal along Ox and Oy is the zero direction for measurement of ψ then the angle between spins in the adjacent layers according to Néel (1944) and Stoner (1950) is

$$\Delta\varphi = \sin\theta\,\Delta\psi \qquad (8.3)$$

and the exchange energy which is proportional to $1-\cos\varphi$ may be written

$$F_e = \alpha a^2 \sin^2\theta \left(\frac{d\psi}{dx}\right)^2 \qquad (8.4)$$

where α is proportional to the exchange energy for parallel spins and will be estimated later and a is the lattice constant.

The energy per unit area of the boundary is then given by

$$\gamma = \int \left(\alpha a^2 \sin\theta \left(\frac{d\psi}{dx}\right)^2 + f_a\right) dx \qquad (8.5)$$

Then for γ to have a minimum value a variational treatment (Kittel 1949) gives

$$f_a = \alpha a^2 \sin^2\theta \left(\frac{d\psi}{dx}\right)^2 \qquad (8.6)$$

i.e. the exchange and anisotropy contributions to the energy are equal (Becker and Doring 1939, Néel 1944, and Stoner 1950). Rewriting equation 8.6 gives

$$\frac{dx}{d\psi} = \alpha^{1/2} a \sin\theta f_a^{-1/2} \qquad (8.7)$$

and rewriting equation 8.5 taking into account 8.6 and 8.7 gives

$$\gamma = 2\alpha^{1/2} a \sin\theta \int_{\psi_1}^{\psi_2} f_a^{1/2} \, d\psi \qquad (8.8)$$

where ψ_1 and ψ_2 are the values of ψ for magnetization along the easy directions on either side of the domain wall. Equations 8.7 and 8.8 can be used to estimate domain wall widths and energies.

The form of the anisotropy energy terms are well known and can be found from any standard text eg. Chikazumi (1964). The expression for magnetocrystalline anisotropy energy of a cubic crystal is, to second order,

$$F_K = K_0 + K_1(\alpha_1^2\alpha_2^2 + \alpha_2^2\alpha_3^2 + \alpha_1^2\alpha_3^2) + K_2\alpha_1^2\alpha_2^2\alpha_3^2 \ldots (8.9)$$

where the α_i's are the direction cosines of the magnetization vector

and the K_i's are the anisotropy coefficients.

The magnetoelastic energy is the sum of the magnetostriction and elastic energy terms

$$\begin{aligned} F_m = & -\tfrac{3}{2}\lambda_{100}(C_{11}-C_{12})[e_{xx}(\alpha_1^2-\tfrac{1}{3}) \\ & + e_{yy}(\alpha_2^2-\tfrac{1}{3}) + e_{zz}(\alpha_3^2-\tfrac{1}{3})] \\ & - 3C_{44}\lambda_{111}[e_{xy}\alpha_1\alpha_2 + e_{yz}\alpha_2\alpha_3 + e_{xz}\alpha_1\alpha_3] \\ & + \tfrac{1}{2}C_{11}(e_{xx}^2 + e_{yy}^2 + e_{zz}^2) \\ & + \tfrac{1}{2}C_{44}(e_{xy}^2 + e_{yz}^2 + e_{xz}^2) \\ & + C_{12}(e_{yy}e_{zz} + e_{xx}e_{yy} + e_{xx}e_{zz}) \end{aligned} \quad (8.10)$$

where $e_{xx} = \frac{3}{2}\lambda_{100}(\alpha_1^2 - \frac{1}{3})$ etc (8.11)

$e_{xy} = 3\lambda_{111}\alpha_1\alpha_2$ etc (8.12)

the C's are the elsatic constants and the λ's are the magnetostriction constants.

The reduced value of F_K is obtained directly by the inclusion of the K_0 term, the reduced value of F_m is found by putting $\alpha_1 = \alpha_2 = \alpha_3 = \frac{1}{3}$; (<111> easy direction) into equation 8.10 and subtracting the resulting value from F_m.

The direction cosines for the magnetostriction vector throughout any domain wall can be determined in terms of θ and ψ with respect to a co-ordinate system in which the wall plane becomes the $y-z$ plane and the wall normal the Ox direction. A transformation of co-ordinates allows these to be transposed to the normal crystallographic co-ordinate system. These expressions are

tabulated for the domain walls under consideration in table 8.3.

The exchange constant, α , can be estimated from the Weiss treatment of ferromagnetism as outlined by Chikazumi (1964)

$$\alpha = \frac{1}{2} N_w I_o^2 \qquad (8.13)$$

where I_o is the saturation magnetization and N_w is the molecular field coefficient

$$N_w = \frac{3 k_B T_c}{N \mu^2} \qquad (8.14)$$

where N is the number of spins per unit volume

k_B is Boltzmann's constant

T_c is the Curie temperature

μ is the atomic magnetic moment

Applying a suitable weighting for the atomic magnetic moments for the rare-earth and iron atoms gives a value of the exchange constant of $\alpha = 5.07 \times 10^8$ in c.g.s. units.

Numerical integration of equation 8.8, taking into account the above considerations, enables the estimates of domain wall energies to be calculated. The results are presented in Table 8.3.

The angle between the magnetization directions between adjacent layers within the domain wall is not constant, but will be greater where the direction of the magnetization results in a higher anisotropy energy. There is thus no sharply defined boundary width. A measure of the boundary width is thus taken from the gradient associated with the point of inflexion of the function of the change in angle between magnetization directions with distance through the domain wall. fig 8.12. Where only one point of inflexion exists the boundary width is

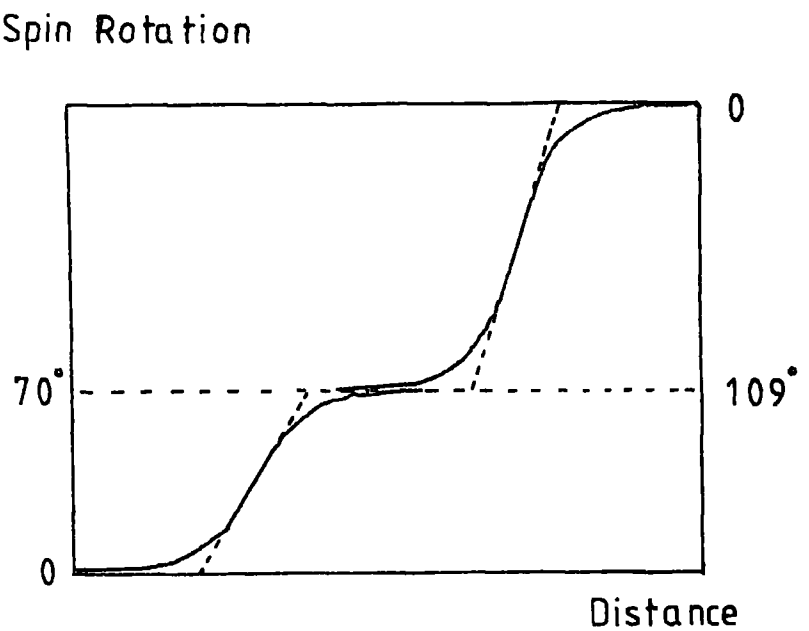

Fig 8.12 Domain Boundary Widths

(Lilley 1950)

Wall Plane	Wall Type	$\sin\theta$	ψ_1	ψ_2	α_1	α_2	α_3	γ ergscm^{-2}	ψ_{Inf}	Wall Width $\times 10^{-8}$m
(001)	71°	$\sqrt{\frac{2}{3}}$	0	$\frac{1}{2}\pi$	$-\frac{1}{\sqrt{3}}\cos\psi + \frac{1}{\sqrt{3}}\sin\psi$	$\frac{1}{\sqrt{3}}\cos\psi + \frac{1}{\sqrt{3}}\sin\psi$	$\frac{1}{\sqrt{3}}$	2.196	$\frac{1}{4}\pi$	2.590
(001)	109°	$\sqrt{\frac{2}{3}}$	0	π	$-\frac{1}{\sqrt{3}}\cos\psi + \frac{1}{\sqrt{3}}\sin\psi$	$\frac{1}{\sqrt{3}}\cos\psi + \frac{1}{\sqrt{3}}\sin\psi$	$\frac{1}{\sqrt{3}}$	4.393	/	
(110)	180°	1	β	$\pi+\beta$	$-\frac{1}{\sqrt{2}}\cos\psi$	$\frac{1}{\sqrt{2}}\cos\psi$	$\sin\psi$	7.125	/	
(110)	109°	1	β	$\pi-\beta$	$-\frac{1}{\sqrt{2}}\cos\psi$	$\frac{1}{\sqrt{2}}\cos\psi$	$\sin\psi$	5.209	$\frac{1}{\sqrt{2}}\pi+\beta$	4.513
(110)	71°	1	β	$-\beta$	$-\frac{1}{\sqrt{2}}\cos\psi$	$\frac{1}{\sqrt{2}}\cos\psi$	$\sin\psi$	1.912	0	2.775
(110)	71°	$\frac{1}{\sqrt{3}}$	$-\frac{1}{2}\pi$	$\frac{1}{2}\pi$	$-\frac{1}{\sqrt{3}} + \frac{1}{\sqrt{6}}\cos\psi$	$\frac{1}{\sqrt{3}} + \frac{1}{\sqrt{6}}\cos\psi$	$\frac{1}{\sqrt{3}}\sin\psi$	4.654	0	2.357
(111)	109°	$\frac{2\sqrt{2}}{3}$	$\frac{1}{6}\pi$	$\frac{5}{6}\pi$	$\frac{1}{3\sqrt{3}} - \frac{2}{3}\cos\psi - \frac{2}{3\sqrt{3}}\sin\psi$	$\frac{1}{3\sqrt{3}} + \frac{2}{3}\cos\psi - \frac{2}{3\sqrt{3}}\sin\psi$	$\frac{1}{3\sqrt{3}} + \frac{4}{3\sqrt{3}}\sin\psi$	4.984	$\frac{1}{2}\pi$	2.769
(112)	180°	1	0	π	$\frac{1}{\sqrt{3}}\cos\psi + \frac{1}{\sqrt{2}}\sin\psi$	$-\frac{1}{\sqrt{3}}\cos\psi + \frac{1}{\sqrt{2}}\sin\psi$	$-\frac{1}{\sqrt{3}}\cos\psi$	7.866	$\frac{1}{2}\pi$	7.034
(112)	109°	$\sqrt{\frac{14}{18}}$	$-\delta$	δ	$\frac{1}{27} + \sqrt{\frac{14}{54}}\cos\psi + \sqrt{\frac{7}{18}}\sin\psi$	$-\frac{1}{\sqrt{27}} + \sqrt{\frac{14}{54}}\cos\psi + \sqrt{\frac{7}{18}}\sin\psi$	$-\sqrt{\frac{4}{54}} - \sqrt{\frac{14}{54}}\cos\psi$	4.606	0	3.652

$\beta = \sin^{-1}\frac{1}{\sqrt{3}}$ $\qquad$ $\delta = \tan^{-1}\sqrt{6}$

$$b = (\psi_1 - \psi_2)\left(\frac{dx}{d\psi}\right)_{Inflexion} \qquad (8.15)$$

This expression has been used to estimate the width of all boundaries, (see table 8.3) except the $\{001\}$ 109° and $\{110\}$ 180° boundaries, both of which have three points of inflexion and can be made up of two other boundaries. Values obtained for the boundary widths are listed in table 8.3.

The domain wall energy calculations clearly indicate that the most probable domain walls are the $\{001\}$ and $\{110\}$ 71° walls which will result in [001] [1$\bar{1}$0] and <111> wall traces which are the predominant wall traces observed. Other wall traces do occur, but only over small areas of the sample surface. The $\{112\}$ wall planes have presumably been induced by the application of a magnetic field. These wall planes remain when the field is removed indicating that once formed they provide a stable, or at least meta-stable domain structure.

Conclusions and Suggestions for Further Work

Synchrotron topographs of the rare-earth germanates showed the high quality of these flux grown crystals. The properties of synchrotron radiation enabled topographs of these bent crystals to be recorded which was impossible using convential topographic techniques. The rapidity with which the topographs were taken enabled a large number of crystals to be examined in a realistic time. Synchrotron topography thus allows an entire batch of crystals to be examined rather than a selected few and is thus a useful tool in crystal growth assessment programme. Work is already continuing on the assessment of large numbers of natural fluorite crystals from Weardale.

The holmium gallium garnet results show that neutron topography can be used to study thick crystals which could not be studied by X-ray techniques. However since dislocations known to exist were not always apparent on the topographs, care has to be taken in interpreting the results. The unusual contrast observed on these topographs is not yet understood, hence more work is required to understand the contrast mechanisms. The long exposure times did not allow sufficient topographs to be recorded to conclusively confirm the correlation between dislocations and vicinal features.The apparent invisibility of dislocations in many reflections meant that section topographs would be required to analyse the Burgers vectors. Insufficient time was available

for such experiments. The difficulties and expense of performing these lengthy experiments at a distant institution has not allowed this work to be completed. The work has however given a further insight into the possibilities and limitations of the neutron topography.

The work on the motion of antiferromagnetic domain walls in $KCoF_3$ under an applied stress, once again shows the possibilities of synchrotron topography enabling simple apparatus to be used to perform experiments impossible to perform with conventional techniques. The understanding obtained from the synchrotron topography results enabled additional data to be obtained with conventional techniques. If similar experiments are performed on the motion of domain walls in $KNiF_3$, for which magnetic field data is available, some further understanding on the origin of the restoring force on the domain walls may be obtained.

The discrepances in the measurement of the magnetostriction of terbium between this and other works, suggest that these zero field results on solid state electrotransport material should be verified by another technique, preferably absolute lattice parameter measurements. The results also require extending down to liquid helium temperatures. This should be possible using the tunability of synchrotron radiation as it will enable reflections and wavelengths to be chosen to allow the experiments to be performed in the MERIC cryostat. Results obtained from performing similar experiments in a non-saturating magnetic field may also prove interesting.

The results obtained on $Tb_{.27}Dy_{.73}Fe_2$ once again show the importance of synchrotron radiation in studying a crystal impossible to study with conventional topographic techniques. The magnetic field data enabled an understanding of the magnetization process to be obtained and with the aid of domain wall energy calculations allowed the zero field domain structure to be interpreted. The commissioning of the S.R.S. should enable these experiments to be continued with a magnetic field capable of saturating the sample. The possibility also exists of simultaneously recording topographs and measuring the magnetization of the sample.

REFERENCES

Aldred P.J.E. and Hart M: (1973) Proc. Roy. Soc. A 332 223

Alex V. Tikhonov L.V. Brümmer O: (1974) Kristall Und Technik 9 643

Alperin H. Brown P.J. Nathans R. and Pickart S.J: (1962)
Phys. Rev. Lett. 8 237

Ando M. and Hosoya S: (1972) Phys. Rev. Lett. 29 281

Armstrong R.W. and Wu C: (1975) Com. in Microstructural Analysis,
Tools and Techniques (Ed. McCall and Muller) (Plenum) 169

Armstrong R.W: (1980) Pro. of the Nato A.S.I. on Characterization
of Crystal Growth and Crystal Defects (Ed. Tanner and Bowen) (Plenum)

Austermann S.B. and Newkirk J.B: (1967) Adv. in X-ray Analysis 10 134

Authier A: (1961) Bull.Soc France Minér. Crist. 84 51

Authier A: (1966) J. Phys. 27 57

Authier A: (1967) Adv. in X-ray Analysis 10 9

Authier A: (1970) Modd. Diff. and Imaging Techniques in Materials
Science (Eds. Amelinckx, Gevers, Remaut, Van Landuyt)(N. Holland)

Authier A: (1970)in Adv. in Structure Research by Diff. Meth. 3
(Ed, Brill and Mason) 1

Balchin A.A. and Whitehouse C.R: (1974) Phys. Ed. 9 53

Bardsley W. and Cockayne B: (1967) Proc. Int. Conf. Cryst. Growth(1966)
J. Phys. Chem. Sol. Supp. No 1 109

Barrett C.S: (1945) Trans. AIME. 161 15

Barth H. and Hosemann R: (1958) Z. Naturforschung 13a 792

Baruchel J: (1974) Ph.D. Thesis from L'université Scientifique et Médicale de Grenoble

Baruchel J. Schlenker M. Zarka A. and Petroff.JF(1978) J. Cryst.Growth 44 356

Bates L.F. and Neale F.E: (1949) Physica 15 220

Batterman B.W. and Cole H: (1964) Rev. Mod. Phys. 36 681

Becker R. and Döring W: (1939) Ferromagnetismus (Springer)

Belov N.V: (1958) Sov. Phys. Crystallogr. 3 222

Belov K.P. Levitin R.Z. and Nikitin S.A: (1961) Bull. Acad. Sci. U.S.S.R. Phys. Ser. 25 1394

Belt R.F: (1969) J. App. Phys. 40 1644

Berg W.F: (1931) Naturwissenschaften 19 391

Berger H: (1971) Ann. Rev. Nucl. Sci. 21 335

Berger H: (1973) Nucl. Techn. 19 188

Birss R.R: (1964) Symmetry and Magnetism (North Holland)

Birss R.R. Keeler G.J. Pearson P and Potton R.J: (1978) J. Phys. E 11 928

Bitter F: (1931) Phys. Rev. 38 1903

Bleaney B. I. and Bleaney B: (1976) Electricity and Magnetism (3rd Ed) (Oxford)

Blessing G: (1976) Acoustical Soc. of America Bull. 92nd meeting San Diego Cal.

Bloch F: (1932) Z. Fur Phys. 74 295

Bly P.H. Corner W.D. and Taylor K.N.R: (1968) J. Appl. Phys. 39 1336

Bly P.H. Corner W.D. and Taylor K.N.R: (1969) J. Appl.Phys. 40 4787

Bobeck A.H: (1967) Bell Syst. Tech.J. 46 1901

Boettinger W.J. Burdette H.E. and Kuriyama M: (1977)
Phil. Mag. 36 763

Boeuf A. Lagomarsino S. Rustichelli F. Baruchel J. and Schlenker M:
(1975) Phys. Stat. Sol. a31 K91

Bond W.L. and Andrus J: (1952) Amer. Mineralogist 37 622

Bondar I.A. Petrova M.A. and Toropov N.A: (1970)
Science of Ceramics 5 3

Bonse U. and Kappler E: (1958) Z. Naturforschung 13a 348

Bonse U: (1962) In Direct Observations of Imperfections in Crystals.
(Ed. Newkirk and Wernick) (Wiley) 431

Bonse U. Hart M. and Newkirk J.B: (1967) Adv. in X-ray Analysis 10 1

Bordas J. Glazer A.M. and Hauser H: (1975) Phil. Mag. 32 471

Bushow K.H.J. and Van Stapele: (1970) J Appl. Phys 41 4066

Carey R. and Isaac E.D: (1966) Magnetic Domains and Techniques
for their Observation (Univ. Press)

Chikawa J: Proceedings of the Nato A.S.I. on Characterization of
Crystal Growth and Crystal Defects (1979) (Ed. Tanner and
Bowen) to be published (plenum)

Chikawa J. and Fujimoto I: (1968) Appl. Phys. Lett. 13 387

Chikawa J. Fusimoto I: (1974) N.H.K. Tech. Res. Lab. Tech.
Monograph No 33

Chikazumi S: (1964) Physics of Magnetism (Wiley)

Clark A.E: (1973) A.I.P. Conf. Proc. 10 794

Clark A.E: (1976) A.I.P. Conf. Proc. 18 1015

Clark A.E: (1978) Unpublished. Obtained via Rare-earth Information Centre Ames

Clark A.E. Abbundi R. Savage H.T. McMasters O.D: (1977) Physica 86 - 88 B 73

Clark A.E. and Belson H.S: (1972) Phys. Rev. B 5 3642

Clark A.E. and Cullen J.R. McMasters O.D. and Cullen E.R: (1975) A.I.P. Conf. Proc. 29 192

Clark A.E. Cullen J.R. and Sato K: (1975) A.I.P. Conf. Proc. 24 670

Clark A.E. De Savage B.F. and Bozorth R: (1963) Phys. Lett 5 100

Clark A.E. De Savage B.F. and Bozorth R. (1965) Phys. Rev. 138 A216

Codling K. (1973) Rept. Prog. Phys. 36 541

Colas G. and Zarka A: (1973) Bull. Soc. Fr. Min. Crist. 96 274

Cooke A.H. Swithenby S.J. and Wells M: (1973) Measurements reported by Wanklyn (1973)

Cooper B.R: (1968) Phys. Rev. 169 281

Cooper B.R. (1968) Solid States Phys. 21 393

Coqblin B: (1977)The Electronic Structure of Rare-earth Metals and Alloys (Academic Press)

Corner W.D. and Al Bassam T.S: (1971) J. Phys. C 4 47

Crangle J: (1977) The Magnetic Properties of Solids (Arnold)

Crangle J: (1979) Communicated via Palmer S.

Cullity B.D: (1956) Elements of X-ray Diffraction (Addison-Wesley)

Dariel M.P. and Atzmony U: (1973) Int. J Magnetism 4 213

Dariel M.P. Holthuis J.T. Pickus M.R: (1976) J. Less Common Metals 45 91

Darnell F.J.: (1963) Phys. Rev. 132 128

Darwin C.G: (1914) Phil. Mag. 27 315

Darwin C.G: (1914) Phil. Mag, 27 675

Darwin C.G: (1922) Phil. Mag. 43 800

Davidson J.B: (1976) Proc. Conf. Neutron Scattering
Gatlinburg Conf. 760601

Davidson J.B.,Werner S.A. and Arrott A.P: (1974)
A.I.P. Conf. Proc. 18 396

Dietrich O.W. and Als-Nielsen J: (1967) Phys. Rev. 162 315

Dionne G: (1967) J. Appl. Phys. 38 4094

Doi K., Minakawa N., Motashashi H., Mosaki N: (1971)
J. appl. Cryst. 4 528

Donnay J.D.H. and Ondik H.M: (1973) Cryst. Data Determanitive Tables
(3rd Ed.) Vol. 2 (U.S. Dept. of Commerce, National Bureau of
Standards, Joint Committee on Powder Diff. Standards)

Dwight A.E. and Kimball C.W: (1974) Acta. Cryst. B30 2791

ElliottR.J: (1972) Magnetic Properties of Rare-earths (Plenum)

Englander M: (1976) Phil. Mag. 33 743

Ewald P.P: (1916) Ann. Phys. Lpz. 49 1

Ewald P.P: (1916) Ann. Phys. Lpz. 49 117

Ewald P.P: (1917) Ann. Phys. Lpz. 54 519

Féron J.L: Huy G. and Pauthenet R. Les Elements des Terres Rares

Ferré J., Briat B., Petit R.H., Pisarev R.H. and Nouet (1976)
J. de Phys. 37 503

Garrard B.J., Smith S.H., Wanklyn B.M. and Gorton G:
(1975) J.Cryst. Growth 29 301

Garrard B.J., Wanklyn B.M. and Smith S.H:
(1974) J.Cryst. Growth 22 169

Glushkova V.B., Duvtjan I.A. and Keler E.K:
(1967) Inorganic Materials 3 96

Goldman J.R: (1947) Phys. Rev. 72 529

Goldman J.R. and Smoluchowski R: (1949) Phys. Rev. 75 140

Goodenough J.B: (1956) Phys. Rev. 102 356

Green Jr.R.E: (1971) Ad. in X-ray Analysis 14 311

Green Jr.R.E: (1977) Adv. in X-ray Analysis 20 221

Guinier A. and Tennevin J: (1949) Acta Cryst. 2 133

Von Hamos L., Theissen P.A: (1931) Zeit Für Phys. 49 619

Hart M: (1968) Science Progress 56 429 (Oxford)

Hart M: (1975) J.Appl. Cryst. 8 436

Hartmann W: (1977) X-ray Optics (Ed. Queisser)
Topics in Adv. Physics 22 191 (Springer)

Hartmann W: Proceedings Nato A.S.I. (1979) Characterization of
Crystal Growth and Crystal Defects (Eds. Tanner and Bowen)
To be published (Plenum)

Hartmann W., Markewitz G., Rettenmaier U. and Queisser H.T:
(1975) App. Phys. Lett. 27 308

Haruta K: (1965) J.Appl. Phys. 36 1789

Hashizume H., Kohra K., Yamaguchi T. and Kinoshita K:
(1971) App. Phys. Lett. 18 213

Hegland D.E., Legvold S. and Spedding F.H: (1963) Phys. Rev. 131 158

Heisenberg W: (1928) Z Phys. 49 619

Herring C.P. and Jakubovics J.P: (1973) J. Phys. F 3 157

Hirakawa K., Hirakawa K. and Hashimoto T: (1960)
J.Phys. Soc. Jap. 15 2063

Hirakawa K., Hashimoto T. and Hirakawa K: (1961) J. Phys.
Soc. Jap. 16 1934

Hosoya S: (1968) Jap. J. Appl. Phys. 7 1

Houmann J.C.G. and Nicklow R.M: (1970) Phys. Rev. B1 3943

Huber E.E., Smith D.O. and Goodenough J.B: (1958)
J. Appl. Phys. 29 294

Isherwood B.J. and Wallace C.A: (1974) Phys. in Techn. 5 244

James R.W: (1948) The Optical Principles of the Diffraction
of X-rays (Bell)

Jones D.W., Farrani S.P. Fort D. and Jordan R.G: (1977) Proc.
Conf. Rare-earths and Actinides. Inst. of Phys. Conf.
Ser. 37 (Ed. Corner and Tanner)

Jones G.A: (1976) Science Progress 63 219

Jordan R.G: (1974) Contemp. Phys. 15 375

Jordan C. and Gastaldi J: (1979) Phys. Stat. Sol. a 52 139

Julliard J. and Nouet J: (1975) Rev. Phys. Appl. 10 325

Kasuya T: (1956) Prog. Theor. Physics Japan 16 45

Kittel C. (1949) Rev. Mod. Phys. 21 541

Kittel C. (1971) Intro. to Solid State Phys. (4th Ed.) (Wiley)

Koehler W.C: (1965) J.Appl. Phys. 36 1078

Koehler W.C. (1967) Trans. Am. Cryst. Assoc. (Ed. Smith)

Koehler W.C., Cable J.W., Wollan E.O. and Wilkinson M.K: (1962)
J. Phys. Soc. Jap. 17 Suppl. B - III 32

Koehler W.C., Child H.R., Wollan E.O. and Cable J.W: (1963)
J. Appl. Phys. Suppl. 34M 1335

Komatsu H., Homma S., Kimuru S., Miyazawa Y. And Shindo I: (1974)
J. Cryst. Growth

Komatsu H. and Sunagawa I: (1964) Minerological J. 4 203

Kramers H: (1934) Physica 1 182

Kuriyama M., Boettinger W.J. and Burdette E: (1977)
J. Mat. Sci. 12 353

Landau L. and Lifshitz E: (1935) Phys. Z. Sowjet 8 153

Lang A.R: (1957) Acta Met. 5 358

Lang A.R: (1958) J. App. Phys. 29 597

Lang A.R: (1959) Acta Cryst. 12 249

Lang A.R: (1959) J. Appl. Phys. 30 1748

Lang A.R: (1963) Brit. J. Appl. Phys. 14 904

Lang A.R: (1970) Modd. Diff. and Imaging Techniques in Material Sci.
(Ed. Amelinckx, Gevers, Remaut and Van Landuyt (N.Holland) 407

Von Laue M: (1931) Ergeb Der Exact Naturwiss 10 133

Lefever R.A., Chase A.B: (1962) J. Am. Ceram. Soc. 45 32

Lefever R.A., Chase A.B. and Torpy J.W: (1961)
J. Am. Ceram. Soc. 44 141

Lefever R.A., Chase A.B. and Wickersheim K.A: (1962)
J. Appl. Phys. 33 2249

Levitin R.Z., Ponomarev B.K: (1968) Sov. Phys. J.E.T.P. 26 1121

Liénard A: (1898) L'Éclairage Électr. 16 5

Lifshitz E: (1944) J. Phys. U.S.S.R. 8 337

Lilley B.A: (1950) Phil. Mag. 41 792

MacCormack I.B., and Tanner B.K: (1978) J. Appl. Cryst. 11 40

Malgrange C., Petroff J.F., Sauvage M. and Zarka A
(1976) Phil Mag. 33 743

Marmeggi J.C. and Baruchel J: Unpublished

Marmeggi J.C., Baruchel J., Schlenker M. and Bertault E.F: (1977)
Coll. Abstr. 4th Europ. Crystal. Meeting B 957

Mason W.P: (1954) Phys. Rev. 96 302

Mathiot A., Petroff J.F. and Barnard Y: (1973)
Phys. Stat. Sol. a 20 k 1

McEwan K.A. and Touborg P: (1973) J. Phys. F 3 1903

Meeks S.W. and Timme R.W: (1977) J. Am. Acoustic Soc. 62 1158

Melville D. and Al Rawi K.M: (1978) I.O.P. Conf. ser. 37 (Ed. Corner
and Tanner) 293

Merlini A. and Guinier A: (1957) Bull. Soc. Franc. Minér.
Crist. 80 147

Merzk M: (1960) J. Appl. Phys. 31 147

Midgley D: (1978) Ph.D. Thesis Univ. of Durham

Middelhoek S: (1963) J. Appl. Phys. 35 1054

Miltat J. and Kleman M: Proc. Joint Intermag - M.M.M.Conf. (1979)
J. Appl. Phys.

Miriam Abdul Gani S. (1979) Private Communication

Morimoto S. and Ito A: (1977) Jap. J. Appl. Phys. 16 85

Nagamiya T: (1958) Second Welch Foundation Conference (Texas)

Nagamiya T: (1962) J. Appl. Phys. 33 1029

Néel L: (1932) Ann. de Phys. 17 64

Néel L: (1944) Ca hiers de Phys. 25 1

Néel L: (1954) Proc. Conf. on Theoretical Physics. Kyoto
(Science Council of Japan) 701

Néel L:. (1955) Compt Rend Acad. Sci. Paris 241 533

Okazaki A. and Suemune Y:(1961) J.Phys. Soc. Jap. 16 671

Okazaki A, Suemune Y. and Fuchikemi T: (1959)
J.Phys. Soc. Jap. 14 1823

Palmer S.B: (1980) Private Communication

Palmer S.B., Jiles D., Isci C. (1979) J. de Phys. 40 C5 - 33

Polcarova M: (1969) I.E.E.E. Trans. on Magn. 5 536

Polcarova M. and Lang A.R: (1962) Appl. Phys. Lett. 1 13

Polcarova M. and Lang A.R: (1968) Bull. Soc. France Minér Crist. 91 645

Polcarova M. and Gemperlova J: (1969) J.Phys. Stat. Sol. 32 769

Rhyne J.J. and Clark A.E: (1967) J.App. Phys. 38 1379

Rhyne J.J. and Legvold S: (1965) Phys. Rev. 138 A507

Rhyne J.J., McGuire T.R: (1972) I.E.E.E. Trans. Mag, 8 105

Roessler B: (1967) Phys. Stat. Sol. 20 713

Roth W.L: (1960) J.Appl. Phys. 31 2000

Rousseau M., Nouet J. and Zarembowitch A: (1974)
J. Phys. Chem. Solids 35 921

Rozgonyi G.A., Hasko S.E:, Statile J.C: (1970)
App. Phys. Lett. 16 443

Rudermann M.A.and Kittel C: (1954) Phys. Rev. 96 99

Safa M: (1977) Ph.D. Thesis Univ. of Durham

Safa M., Midgley D. and Tanner B.K: (1975)
Phys. Stat. Sol. a 28 K89

Safa M., and Tanner B.K: (1977) Physica 86 - 88 B 1347

Safa M., and Tanner B.K: (1978) Phil. Mag. B37 739

Safa M.,Tanner B.K., Klapper H. and Wanklyn B.M. (1977) Phil. Mag.

Safa M., Tanner B.K., Wanklyn B.M. and Garrard B.J: (1977)
J. Cryst. Growth.

Saito S., Nakahigashika K. and Shimomura Y: (1966)
J. Phys. Soc. Jap. 21 850

Sauvage M: Proceedings NATO A.S.I. on Characterization of Crystal Growth and Crystal Defects (1979) To be published (Plenum)

Sauvage M. and Petroff J.F: (1979) In Synchrotron Radiation Research (Ed. Donioch and Winick) (Plenum)

Savage H.T: (1977) Private communication

Savage H.T: (1978) Private communication

Savage H.T., Clark A.E. and Powers J.M: (1975)
I.E.E.E. Trans. Mag. 11 1355

Scatturin V., Corliss L., Elliot N. and Hastings J: (1961)
Acta. Cryst. 14 19

Schlenker M: (1975) Phys. Stat. Sol. a 31 K91

Schlenker M. and Baruchel J: (1978) J.App. Phys. 49 1996

Schlenker M., Baruchel J. and Nouet J:

(1974) Pro. Int. Conf. Magnetism (Moscow) 368

Schlenker M., Baruchel J., Petroff J.F. and Yelol W.B:

(1974) App. Phys. Lett. 25 382

Schlenker M. and Shull C.G: (1973) J.App. Phys. 44 4181

Schwinger J: (1946) Phys. Rev. 70 798

Schwinger J: (1949) Phys. Rev. 75 1912

Schulz L.G: (1954) J. Metals 6 1082

Shull C.G., Strauser W.A. and Wollan E.O:

(1951) Phys. Rev. 83 333

Slack G.A: (1960) J.Appl. Phys. 31 1571

Smith H.G: (1962) Rev. Sci. Instr. 33 128

Smith R.L: (1978) Ph.D. Thesis University of Durham.

Smolin and Yu I: (1970) Sov. Phys. Cryst. 15 36

Spencer E.G., LeCraw R.C. and Reggia F:

(1956) Proc. I.R.E. 44 790

Stoner E.C: (1950) Phys. Soc. Rep. Prog. Phys. 13 83

Suller V.P: (1973) Daresbury Laboratory Internal Report DL/TM 118

Sunagawa I: (1967) J.Cryst. Growth 1 102

Tanner B.K: (1976) X-ray Diffraction Topography (Pergamon)

Tanner B.K: (1977) Prog. Cryst. Growth Charact. 1 23

Tanner B.K: (1979) Contemp. Phys. 20 187

Tanner B.K. and Bowen D.K: (Eds.) Proceedings of the Nato A.S.I.

on Characterization of Crystal Growth and Crystal Defects

(Plenum) to be Published

Tanner B.K. and Humphreys C.J: (1970) J.Phys. D 3 1144

Tanner B.K., Safa M.and Midgely D: (1977) J.Appl. Cryst. 10 91

Tanner B.K., Safa M. and Midgely D: (1977) J.Appl. Cryst. 10 281

Tanner B.K., Safa M., Midgely D. and Bordas J:
(1976) J.Magn. Mag. Mat. 1 337

Taylor K.N.R: (1970) Contemp. Phys. 11 423

Taylor K.N.R: (1971) Adv. in Phys. 20 551

Taylor K.N.R. and Derby M.I. (1972) Phys. of Rare-earth Solids
(Chapman and Hall)

Thompson D.J. et al. (1975) Daresbury Laboratory Report DL/SRF/RT

Timme R.W: (1978)Proc.int. Colloq.C.N.R.S. Grenoble (1978) J.de Phys.

Tuomi T., Naukkarinen K. and Rabe P: (1974) Phys. Stat. Sol. a 25 93

Ubain G., Weiss P. and Trombe F: (1935) C.R. Acad. Sci. Paris 200 2132

Uchida E., Kondo H., Nakazumi Y. and Nagamiya T:
(1960) J. Phys. Soc. Jap. 15 466

Van Vleck J.H: (1932) The Theory of Electric and Magnetic
Susceptibilities (Oxford)

Van Vleck J.H., Frank A: (1929) Phys. Rev. 34 1494

Wang F.F.Y: (1973) Physical and Chemical Properties of Garnets
in Treatise on Materials Science Vol.2 (Ed. Herman)
(Academic Press) 279

Wang S.P., Schull C.G. and Phillips W.C: (1962) Rev. Sci. Instr.
33 126

Wanklyn B.M: (1969) J.Cryst. Growth 5 279

Wanklyn B.M: (1973) J.Mater. Sci. 8 649

Wanklyn B.M: (1975) J.Mater. Sci. 10 1487

Wanklyn B.M: (1975) Crystal Growth (Ed. Pamplin) (Pergamon)

Wanklyn B.M: (1978) J.Cryst. Growth 43 336

Warren B.E: (1969) X-ray Diffraction (Addison-Wesley)

Wyckoff R.W.G:(1965) Crystal Structures (Vol. 3) (2nd Ed.)(Wiley)

Weiss P: (1907) J.Phys. et Rad. 6 661

Williams C.M. and Koon N.C: (1978) I.O.P. Conf. Ser. no 37
(Eds. Corner and Tanner)

Williams H.J. and Shokley W: (1949) Phys. Rev. 75 178

Wooster N. and Wooster W.A: (1945) Nature 155 786

Wu C.C.M. and Armstrong R.W: (1975) J.Appl. Cryst. 8 29

Yamamoto M. and Iwata T: (1953) Sci. Rep. R.I.T.U. A5 433

Yosida K: (1957) Phys. Rev. 106 893

Zacharieson W.H: (1945) Theory of X-ray Diff. in Crystals (Wiley)

Anderson P.W: (1950) Phys. Rev. 79 350

Bareham H: (1980) Private Communication

Bates L.F. and Neale F.E: (1950) Proc. Phys. Soc. A 63 374

Gschneidner K.A. and Eyring L: (1976) Handbook of the Rare Earths (North-Holland)

Methfessel S., Middelhoek A. and Thomas H: (1960) J. Appl. Phys. 31 3025

Morrish A.H: (1965) The Physical Principles of Magnetism (Wiley)

Pauthenet R: (1956) C. R. Acad. Sci. 242 1859

Smith R.L., Corner W.D. and Tanner B.K: J. Phys. F 7 1229

Tanner B.K: (1977) Spec. Periodical Reports of the Chemical Society p. 280

Appendices

A1 Holmium Gallium Garnet Neutron Structure Factors

Reflection	Bragg angle (deg)	F
400	8.3	26.1
800	16.8	39.3
440	11.8	12.4
880	24.2	38.9
444	14.5	30.4
640	15.1	41.1
642	15.7	30.4
10 8 4	29.0	32.9
10 10 4	32.1	31.5
12 2 2	26.5	30.2

(Provided by staff from the I.L.L.)

A.2 $KCoF_3$ Structure Factors

Reflection	F	$\lambda = 0.7107$ Å		$\lambda = 0.5608$ Å	
		Bragg angle (deg)	ext. dist (microns)	Bragg angle (deg)	ext.dist (microns)
100	17.6	5.1	58.0	4	73.2
200	51.0	10.2	20.3	8	25.5
300	3.3	15.4	322.0	12.1	399.5
400	29.4	20.7	37.8	15.6	45.7
110	29.7	7.2	34.6	5.7	43.5
220	40.3	14.3	26.2	11.4	32.6
111	11.0	8.8	93.2	6.9	117.0

A3 $Tb_{0.27}Dy_{0.73}Fe_2$ Structure Factors

Bragg angle 45°

Reflection	λ(Å)	F	ext.dist. (microns)
440	1.8	559	3
660	1.2	180	14
880	0.9	346	10
10 10 0	0.7	125	34
12 12 0	0.6	240	21
14 14 0	0.5	93	64
16 16 0	0.46	191	35